LIVE-CELL VISUALISATION OF CHROMATIN FOR THE STUDY OF RADIATION-INDUCED CHROMOSOME ABERRATIONS

A thesis submitted for the degree of Master of Philosophy by

GEORGIOS MALIS

CENTRE FOR CELL AND CHROMOSOME BIOLOGY

SCHOOL OF HEALTH SCIENCES AND SOCIAL CARE

BRUNEL UNIVERSITY

AUGUST   2011

<u>ABSTRACT</u>

Chromosomes can be visualised during the metaphase stage of the cell cycle however, there are various limitations associated with the visualisation of chromatin during interphase. This is due to the fact that during that stage of the cell cycle, chromatin is decondensed and difficult to resolve by using standard techniques. The employment of fluorescence microscopy has provided great insight into the examination of the structure and dynamics of fluorescently tagged chromatin regions in living cells during interphase. Thus the *in vivo* stable expression of fluorescent proteins such as Enhanced Green Fluorescent Protein (EGFP) has the potential to address questions that lead to understanding dynamic responses of chromatin in response to DNA damage. In this study, chromatin sites within the nuclei of Chinese Hamster Ovary (CHO) cells were fluorescently labelled using the lac operon system, which works on the principle that EGFP-lac repressor protein will bind to sites of integrated lac operator sequence. To achieve this, CHO cells were transfected with pSV2-DHFR8.32 (lac operator) and p3'SSdimerClonEGFP (lac repressor-EGFP fusion protein) plasmids by calcium phosphate transfection. 68 stable transfectants were stored and clone CHO-R-O-25 cells were used for further experimental analysis based on these cells containing discrete and intense fluorescent spots. It was shown that the physiological and functional characteristics of CHO-R-O-25 cells were comparable to those of control CHO DG44 cells. Time-lapse fluorescence microscopy was used to examine for any alterations in the physical structure of chromatin in response to DNA damage that was induced by radiation and a range of different chemicals. It was demonstrated that in cells exposed to DNA damaging agents, chromatin diffusion and expansions revealed by alterations in the intensity and size of the fluorescent spots within the nuclei of cells are owed to relaxation of chromatin structures in response to genome insults. The potential for this tool to study the organisational responses of chromatin in response to damage and the ulitimate relevance of any physical alterations to mechanisms for chromosome exchange formation, are described.

TABLE OF CONTENTS

CHAPTER 5: DNA DAMAGE EVENTS AND REPAIR PROCESSES REVEALED BY TIME-LAPSE MICROSCOPY..201

LIST OF TABLES

LIST OF FIGURES

ABBREVIATIONS

α-particles: alpha-particles

γ-H2AX: Phosphorylated histone H2AX

γ-IR: Gamma-irradiation

εdAdo: $1, N^6$-etheno-2'-deoxyadenosine

μg: microgram

μm: micrometre

μM: Micromolar

2-D: Two-dimensional

3-D: Three-dimensional

^{3}HdUrd: Tritiated deoxyuridine

4-D: Four-dimensional

53 BP1:   p53 binding protein 1

53BP1-RFP: p53 binding protein 1- Red fluorescent protein

8-oxodGuo: 8-oxo7,8-dihydro-2'-deoxyguanosine

A: Adenine

ADLs: Aldehydic DNA Lesions

AFM: Atomic Force Microscopy

Amp R: Ampicillin Resistance

Arg: Arginine

A-T: Adenine-Thymine

AT: Ataxia Telangiectasia

ATM: Ataxia Telangiectasia Mutated

ATP: Adenosine triphosphate

ATR: ATM and Rad-3 related

Aza: Azacytidine

BLM: Bleomycin

bp: base pairs

Brca 1: Breast cancer associated protein 1

BRCT: Brca-1 C-terminal domains

BrdU: bromodeoxyuridine

BSA: Bovine Serum Albumin

Bsr: Blasticidin resistance

C.M.: Complete Media

C: Cytosine

Ca^{2+} ion: calcium ion

Ca_2PO_4: Calcium phosphate

$CaCl_2$: Calcium chloride

CCD camera: Charge-Coupled Device camera

CDKs: Cyclin-dependent kinases

cDNA: complementary DNA

CENP-A: Centromere protein A

CENP-B: Centromere protein B

CENPB-GFP: Centromere protein B - GFP

CFP: Cyanide Fluorescent Protein

CGE: Circadian Gene Express

CGNs: Cerebellar Granule Neurons

cGy: centi-Gray

CHF: Chinese Hamster Fibroblasts

CHO DG44 cells: Chinese Hamster Ovary cells containing a double deletion for the DHFR locus

CHO: Chinese Hamster Ovary

CHO-R cells: CHO cells stably transfected with p3'SSdimerClonEGFP plasmid

CHO-R-O cells: CHO cells stable transfected with p3'SSdimerClonEGFP and pSV2-DHFR 8.32 plasmids

CK2: Casein Kinase 2

CldU: chlorodeoxyuridine

CLEM: Correlative Light-Electron Microscopy

CLSM: Confocal Laser Scanning Microscopy

Co (II) : cobalt ion

CO_2: Carbon dioxide

Co-60: Cobalt-60

C-terminal: COOH - terminal

CTs: Chromosome Territories

Cu^{2+} / Cu (II) : copper ion

Cy3-AP3-dUTP: [cyanine dye (Cy3) conjugated to 5-amino-propargyl-2'-deoxyuridine 5'-triphosphate (AP3-dUTP)]

DAPI: 4',6-diamidino-2-phenylindole

DEPC: diethyl pyrocarbonate

Der: Derivative chromosomes

DFO: Desferioxamine

dH_2O: Distilled water

DHFR locus: Dihydrofolate reductase locus

DIC: Differential Interference Contrast

DiOC6(3):   3, 3' dihexyloxacarbocyanine iodide

DMSO: dimethyl sulfoxide

DNA-PK: DNA – Protein Kinase

dNTP: Deoxyribonucleotide triphosphates

DPBS: Distilled Phosphate Buffered Saline

DSBs: Double Strand Breaks

dsDNA: Double stranded DNA

dTTP: Thymidine Triphosphate

dUTP: deoxyuridine 5'-triphosphate

EDTA: EthylenediamineTetra Acetic Acid Disodium Salt Dihydrate

EGFP: Enhanced Green Fluorescent Protein

EM: Electron Microscopy

EMEM: Eagle's Minimum Essential Medium

ERK: Extracellular signal-Regulated Kinases

EtBr: ethidium bromide

Eth: Ethionine

EtMes: Ethyl Methanesulfonate

EtOH: Ethanol

FBS: Fetal Bovine Serum

FC: Fibrillar Centre

FCS: Fluorescence Correlation Spectroscopy

FCS: Fluorocarbons

FCS: Fetal Calf Serum

FdU: fluorodeoxyuridine

Fe^{2+} ion: Ferrous ion

Fe^{3+} :   Ferric ion

FHA/BRCT: Forkhead Associated domain on the N-terminal of Nbs-1 and

                   Brca-1 C-terminal domains (BRCT) domains

FHA: Forkhead Associated

FISH: Fluorescence In Situ Hybridisation

FITC: Fluorescein isothiocyanate

FLIP: Fluorescence Loss In Photobleaching

FM: epifluorescence microscopy

FOV: Fields Of View

FPs: Fluorescent proteins

FRAP: Fluorescence Recovery After Photobleaching

FRET: Fluorescence Resonance Energy Transfer

G: Guanine

G_0 phase: gap 0 or resting quiescence phase

G_1 phase: gap or growth 1 phase

G_2 phase: gap or growth 2 phase

G-banding: Giemsa - banding

GFP: Green Fluorescent Protein

GGHG complex: Cu(II)-glycylglycylhistidylglycine complex

GHHG complex: Cu^{2+}-glycylhistidylhistidylglycine complex

GLs: Giant Loops

GR: Glucocorticoid Receptor

Gy: Gray

H2A: histone H2A

H2AX:	Histone variant
H2B:	histone H2B
H2B-GFP:	histone H2B-Green Fluorescent protein
H_2O_2:	Hydrogen peroxide
H3:	histone H3
H4:	histone H4
HBEP:	Human Bronchial Epithelial Primary
HBSS:	Hepes Buffered Saline Solution
HCl:	hydrochloric acid
HDF:	Human Diploid Fibroblasts
HEPES:	4-(2-hydroxyethyl)-1-piperazineethanesulfonic acid
HMG proteins:	High Mobility Group proteins
hnRNPs:	heterogeneous ribonucleoprotein particles
HR:	Homologous Recombination
HSA:	Homo Sapiens
HSRs:	Homogeneously Staining Regions
HU:	Hydroxyurea
Hyg R:	Hygromycin Resistance
IC:	Interchromatin Compartment
ICD:	Interchromosome Domain
ICN:	Interchromatin Channel
IdU:	iododeoxyuridine
Ig:	Immunoglobulin
IGCs:	Interchromatin Granule Clusters

iGFP:	improved GFP
ITS:	Interstitial Telomeric Sequences
KAP-1:	KRAB-associated protein 1
kb:	Kilobases
kbp:	Kilobase pairs
KCl:	Potassium chloride
kDa:	Kilo Dalton
kHz:	Kilo Hertz
Lac I:	Lac repressor
Lac O:	Lac operator
LCLs:	Llymphoblastoid Cell Lines
LET:	Linear Energy Transfer
LM:	Light Microscopy
LN_2:	Liquid Nitrogen
LPC:	Lysophosphatidylcholine
Lys:	Lysine
M phase:	mitotic phase
M.I.:	Mitotic Index
M:AA	Mehanol : Acetic Acid
MAPK:	Mitogen-Activated Protein Kinases
MARs:	Matrix Attachment Regions
MBF:	MacBiophotonics
Mbp:	Megabase pairs
MDC1:	Mediator of DNA damage Checkpoint protein 1

MEFs:	Mouse Embryonic Fibroblasts
mFPs:	monomeric Fluorescent proteins
Mg^{2+} ion:	magnesium ion
$MgCl_2$:	Magnesium chloride
$MgSO_4$:	Magnesium sulfate
mM:	Millimolar
MMC:	Mitomycin-C
MP:	Multi-Photon
MRN complex:	Mre11-Rad50-Nbs1 complex
mRNA:	messenger RNA
MTX:	Methotrexate
N.A.	Numerical Aperture
Na acetate:	Sodium acetate
NaB:	Sodium butyrate
NaCl:	Sodium chloride
NCS:	Newborn Calf Serum
NHEJ:	Non-Homologous End Joining
NHFs:	Normal Human Fibroblasts
NLS:	Nuclear Localisation Signal
nm:	nanometer
NRK:	Normal Rat Kidney
N-terminal:	NH_2 – terminal
Nu:	Nucleoli
O_2^- :	superoxide anion
O_2 :	oxygen

OH⁻ radical: hydroxyl radical

P/S: Penicillin/Streptomycin

PAGFP: Photoactivatable GFP

PBL: Peripheral Blood Lymphocytes

PBS: Phosphate Buffered Saline

PCC: Premature Chromosome Condensation

PCNA: Proliferating Cell Nuclear Antigen

PFs: Perichromatin Fibrils

PI-3K: Phosphatidylinositol -3-OH-Kinase

PML bodies: Promyelocytic Leukaemia bodies

PNA-FISH: Peptide Nucleic Acid - FISH

Pol I enzyme: DNA Polymerase I enzyme

PP2A: Protein Phosphatase 2 A

PP4:   Protein Phosphatase 4

PR: Perichromatin Region

pre-mRNA: pre-messanger RNA

PSFE: Point Spread Function Engineering

PTC: Papillary Thyroid Cancer

Pur: Purine

Pyr: Pyrimidine

r^2 r – squared

rDNA: ribosimal DNA

RFP: Red Fluorescent Protein

ROI: Region of Interest

ROS:	Reactive Oxygen Species
rpm:	rounds per minute
rRNA:	ribosomal RNA
RT:	Room Temperature
RW/GL:	Random Walk/Giant Loop
S phase:	synthesis phase
S:N ratio:	Signal:Noise ratio
S65T:	Serine 65 to Threonine mutation
SCE:	Sister Chromatid Exchange
SDC:	Spinning Disk Confocal
SDS:	Sodium Dodecyl Sulfate
Ser 139 residue:	Serine 139 residue
SLs:	Small-scale chromatin Loops
SMI:	Spatially Modulated Illumination
SOD1:	Superoxide dismutase 1
SPDM:	Spectral Precision Distance Microscopy
SPT:	Single-Particle Tracking
SSA:	Single-Strand Annealing
SSBs:	Single Strand Breaks
SSC:	Saline-Sodium Citrate buffer
ssDNA:	single stranded DNA
SV40 promoter:	Simian Virus 40 promoter
T:	Thymine
TBP:	TATA box binding proteins
TE buffer:	10 mM Tris-Cl, 1 mM EDTA, pH 8.0

tet O:	Tetracycline Operator
TR:	Texas Red
TRITC:	Tetramethyl Rhodamine Isothiocyanate
U.V.:	Ultraviolet
VE:	Video Enhanced
VE-DIC:	Video Enhanced Differential Interference Contrast
WF:	Wide-field
w/v:	weight/volume
x g:	gravity (measuring centrifugal force)
YFP:	Yellow Fluorescent Protein
Z:	Z group chromosomes
Zn (II):	zink ion

ACKNOWLEDGEMENTS

DECLARATION

I DECLARE THAT UNLESS OTHERWISE STATED I AM THE ONLY BEARER OF THE WORK THAT IS PRESENTED IN THIS THESIS

1. INTRODUCTION

1.1 THE CELL CYCLE

The eukaryotic cell cycle describes the process of DNA replication and the formation of two daughter cells from a single parent cell (figure 1.1). The duration of the cell cycle is variable in different types of cells, albeit in most cell types it is approximately 24 hours and comprised of two distinct stages: interphase and mitosis (M). The duration of interphase which accounts for most of that time interval is 22 hours, whereas M phase lasts for approximately two hours.
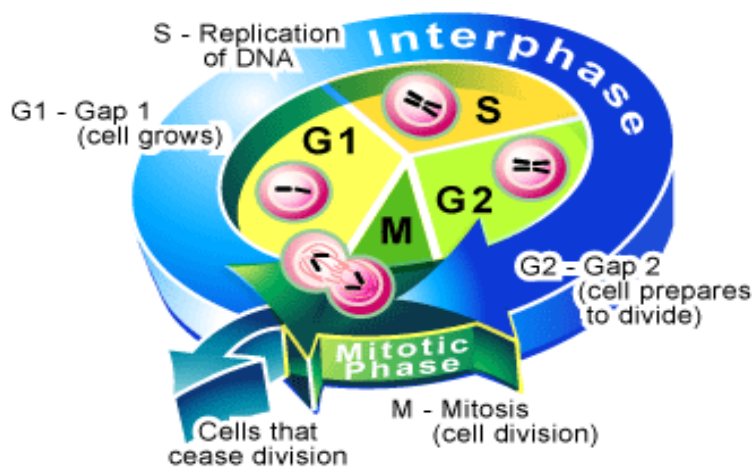
Figure 1.1: Schematic representation of the cell cycle
(341. David Secko. The cell cycle: A universal cellular division program. The Science creative Quarterly, August 2003)

Several processes that take place during interphase are associated with chromosomal function. These include the decondensation of chromosomes into chromatin as 30 nanometer (nm) chromatin fibers (1, 2), the association of regulatory factors with chromatin, RNA synthesis and splicing, DNA replication and repair of DNA damage. Interphase is sub-divided in three major phases called G_1 (gap or growth 1 phase), S (synthesis) phase and G_2 (gap or growth 2 phase). During G_1 phase, proteins, RNA and intracellular organelles are synthesized resulting in the active growth of the cell in preparation for the subsequent S phase. Non-dividing or senescent cells enter G_0 (gap 0 or else called resting quiescence phase) instead of progressing to the S phase. During S phase replication of a cell's DNA occurs,

resulting in the generation of two sister chromatids from a single G_1 phase chromatid. During G_2 phase the cell is characterised by a fast growth rate in preparation for M phase. The rate of growth of a cell during this stage is faster than that of G_1 phase and also the duration of G_2 is shorter than that of G_1.

M phase is sub-divided into four main phases; prophase, metaphase, anaphase and telophase. Briefly, during prophase, the compaction of chromatin into higher-order structures results in the formation of condensed chromosomes, consisting of two sister chromatids and the centromere, which is the common attachment point for the two sister chromatids. The next phase is metaphase and during that phase chromosomes are aligned at the metaphase plate, which is located at the equator of the cell and the nuclear envelope is disintegrated. In anaphase, the action of the microtubules results in the pulling of sister chromatids to opposite poles of the cell. Telophase signals the end of mitosis and during this stage, the nuclear envelope is reformed and chromosomes become decondensed again resulting in the appearance of chromatin.

1.2 ALTERATIONS IN CONDENSATION OF CHROMATIN DURING INTERPHASE

The basic structural unit of chromatin is the nucleosome, which is composed of 146 bp of DNA wound around an octamer of core histones, which in turn consists of two copies of H2A, H2B, H3 and H4 histones (3-5), appearing as a 11 nm fibre of 'beads on a string' under the microscope (4). It has been proposed that the surface of the octamer of histones regulates higher-order chromatin organisation by modulating the compaction and self-association of chromatin fibres (6, 7). Nucleosomal sedimentation procedures have revealed that the presence of Mg^{2+} cations on nucleosomal surfaces is critical for their self-association and the overall nucleosomal condensation (7). It is this nucleosome compaction of DNA from interphase to metaphase that results in the formation of fully condensed chromosomes at metaphase (4, 7).

It is well documented that the higher order chromatin organisation consists of several levels of packaging [as reviewed in (3, 8), (9-12)]. Nucleosomal arrays are

initially folded into 30 nm chromatin fibres (1, 2) and then into even more condensed chromatin structures. Initial evidence supporting this argument was provided by Pienta et al (1984) in human cells through the proposal of the radial loop model (11, 13). The authors demonstrated that 30 nm chromatin fibres are folded into loops 60 – 200 kilobases (kb) in size. The nuclear matrix was proposed to serve as the attachment structure for each one of these loops. Higher-order folding of 18 of these loops in a radial orientation results in the formation of a chromosome structure that was termed miniband. The latter was predicted to accommodate approximately 1 million base pairs of DNA. Subsequently, further packaging of roughly 106 minibands results in the formation of the chromatid (11). In a later study, Belmont et al (1987) provided evidence for the hierarchical non-random organisation of higher-order chromatin structures through the development of three-dimensional (3-D) reconstructions of *Drosophila melanogaster* mitotic chromosomes. It was suggested that the basic building block of mitotic chromosomes is a fibre that has a diameter of 10-14 nm. The complex coiling of this fibre gives rise to higher-order structural domains that have a diameter of 22-26, 40-50 and 80-100 nm (9). Based on the prediction that the approaches used for the visualisation of mitotic chromosomes in *Drosophila* models could also be applied to the visualisation of interphase chromosomes in mammalian cells (9), Belmont and Bruce (1994) assessed chromatin packaging characteristics in Chinese Hamster Ovary (CHO) cells (10). They used an approach that permeabilises cells and removes nucleoplasmic background staining through the use of non-ionic detergents in polyamine or divalent cation buffers. It was demonstrated that the higher-order large – scale chromatin organisation within the interphase nucleus of mammalian cells consists of successive packaging of the 30 nm chromatin fibres to 60 – 80 nm fibres, followed by folding into 100 – 130 nm 'chromonema' fibres and finally 200 – 240 nm fibres that are characteristic of G_1 chromatids [(10); figure 1.2].
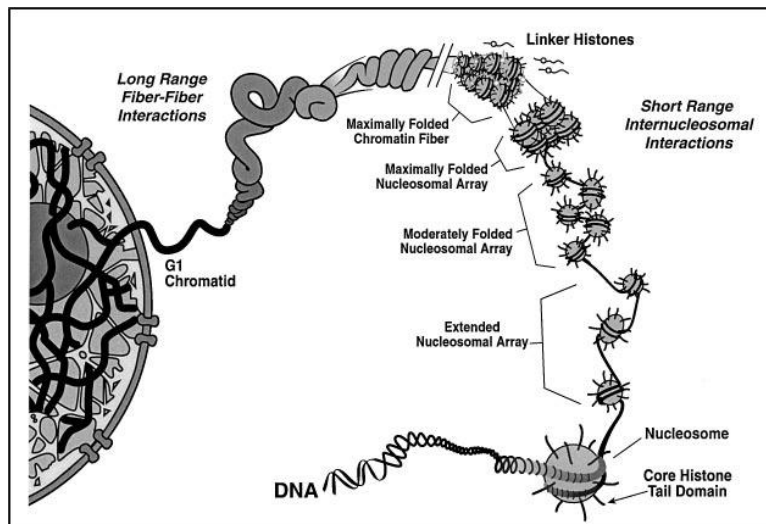
Figure 1.2 Higher order chromatin folding from the DNA level to G_1 chromatids

(3. Hansen J.C. Annu Rev Biophys Biomol Struct. 2002; 31: 361-92)

Interestingly, 3-D imaging of serial thin sections provided evidence for large-scale chromatin decondensation during progression from G_1 to S phase that was concomitant with its uniform spreading into the interior of nuclei. It was found that initially, early in G_1, 30 nm chromatin fibres are folded into 100 - 130 nm 'chromonema' fibres, before uncoiling into 60 - 80 nm fibres at a later stage of G_1 (figure 1.3). As the cells progressed through G_1 and reached the transition to S-phase, these 60 - 80 nm fibres became more prominent and at local regions further decondensed 30 nm chromatin fibres could be visualised using a combination of serial thin-section electron and light microscopy. In addition, concomitant to the chromatin uncoiling phenomenon at that stage was the linearisation of chromonema fibres. The separation of these chromatids could be visualised at the metaphase stage of the cell cycle, when mitotic chromosomes appeared as condensed structures (10). Further evidence for higher-order chromatin folding has been derived from cryoelectron microscopy observations of nucleosomes in fixed chicken erythrocyte nuclei in which chromatin condensation was induced by increasing salt concentrations (12). At low salt concentrations nucleosomes were shown to be condensed in a 3-D 'zig-zag' conformation. The application of higher concentrations resulted in further nucleosome compaction, as evidenced by the decrease in the angle distance between the two linker DNA segments (12).
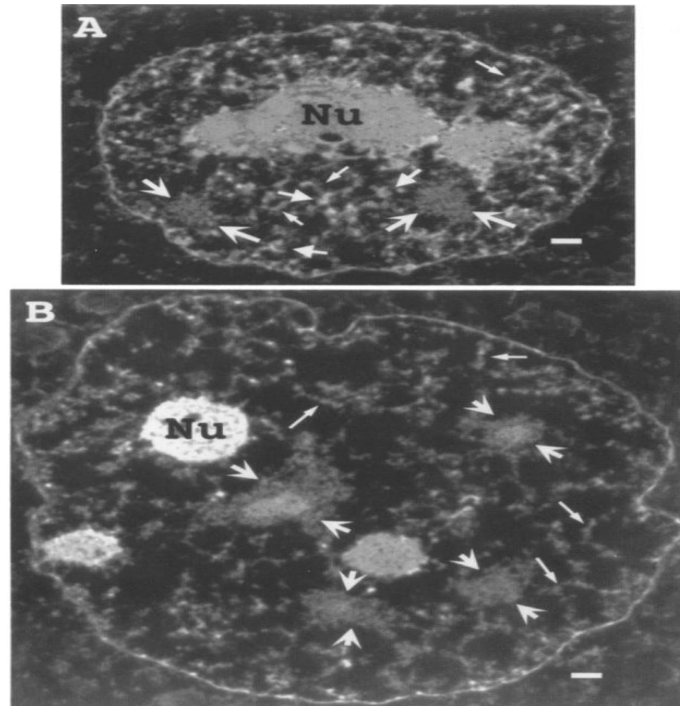
Figure 1.3: (A) Evidence for the presence of 100-130 nm chromonema fibres in early G_1 phase nuclei (thin arrows). Thick arrows correspond to 100-130 nm chromonema fibres that are extensively folded. (B) Evidence for the presence of more decondensed 60-80 nm chromonema fibres in late G_1/early S phase nuclei (thin arrows). (A and B) Thick arrows with curved heads point to interchromatin granule clusters (IGCs). Note that Nu=nucleoli

(10. Belmont AS, Bruce K, J Cell Biol. 1994 Oct; 127(2): 287-302).

The results from this work are consistent with the chromatin compaction (14, 15) and large – scale chromatin decondensation associated with intranuclear movement of transgene arrays (16) that have been reported by other live-cellular microscopic studies. Interestingly, the visualisation of decondensed chromatin fibres in CHO cells has unveiled interactions between lamin B and decondensed chromatin fibres in the vicinity of the nuclear envelope, where lamin B overlies these chromatin domains (17).

1.3 CHROMOSOME TERRITORIES: FUNCTIONAL IMPLICATIONS AND MODELS ASSOCIATED WITH THE ORGANISATION OF CHROMOSOME TERRITORIES

Intranuclear structures are characterised by a significant extent of compartmentalisation. The nucleolus is a strikingly compartmentalised nuclear component, which contains ribosomal DNA (rDNA) genes that are attached to the fibrillar centre (FC). Within the nucleolus, ribosome production, pre-mRNA processing events and transcription of rRNA take place [reviewed in (18, 19)]. Nuclear proteins and RNAs are also compartmentalised structures and studies have shown that a number of cell functions including DNA synthesis, gene expression alterations and progression through the cell cycle are linked to this specific organisation [as reviewed in(20, 21)]. *In situ* hybridisation experiments have provided evidence for the specific and cell-type dependent localisation of centromeric and telomeric sequences at defined sub compartments of the nucleus in *Drosophila* and mammalian cells [reviewed in (13)]. In addition, experiments with micro-nucleated Chinese hamster fibroblast (CHF) cells proved that compartmentalisation of DNA either to the nuclear interior or the nuclear periphery during interphase occurs for each individual chromosome, suggesting that it is a process that is not dependent on chromosome number (22).

Similarly, evidence has been provided for the fact that chromosomes are highly compartmentalised structures within the interphase nucleus and occupy distinct chromosome territories (CTs) (23-31). It has been proposed that CTs are composed of 10-30 nm and 60-130 nm chromonema fibres (10, 32) that are compacted by being coiled within their respective CTs [reviewed in (30)]. In their attempt to explain the organisation and properties of CTs, two research groups have proposed the basic constituents of CTs to be chromatin rosettes that are composed of small-scale chromatin loops (SLs) that have a size of approximately 50-200 kilobase pairs (kbp) (30, 33). Other scientists believe that giant loops (GLs) of one to several Megabase pairs (Mbp) are the basic building blocks of CTs (34-36), while a third proposal is that both SLs and GLs are the building components of CTs (30, 33, 37). Several models have attempted to explain the organisation of CTs within the

interphase nucleus. These include the interchromosome domain (ICD) (38), the random walk/giant loop (RW/GL) (34) and the interchromatin channel (ICN) (26) models (figure 1.4).
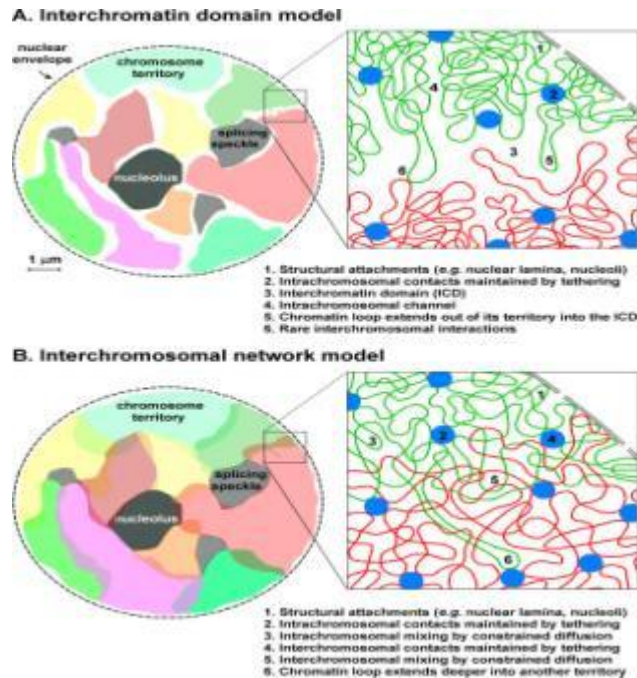
Figure 1.4: Comparison between the ICD (shown in A) and the ICN models (shown in B). The white space that separates the chromatin domains, the nucleolus, the CTs and the spliceosomes in A is the IC. This space is absent in B. Also note that in B, chromatin loops from CTs intermingle extensively with chromatin loops from other CTs by confined diffusion, which is not the case in A.

 (26. Branco MR, Pombo A., PLoS Biol. 2006 May; 4(5): e138).

1.3.1 The ICD model

Initial studies leading to the formulation of the ICD model were performed by Zirbel et al (1993). These authors suggested that a network of nuclear matrix channels within CTs expanding towards the nuclear pores facilitates the import/export of proteins and processed mRNAs. Splicing of mRNAs and transcription were proposed to take place within these channels. Based on the fact that the constituents of the splicing apparatus and the transcripts were absent from the interior of CTs, it was shown that this compartment is present at the borders of CTs and it was therefore termed the interchromosome domain (ICD) (38). Subsequent studies

revealed that CTs consist of a hierarchy of chromatin domains with the most basic constituent being the ~100 kb chromatin loop domains. A series of these ~100 kb chromatin loop domains form small chromatin clumps that correspond to ~1Mbp chromatin domains, which are also linked to each other in higher-order entities (31). According to the ICD model, the architecture of CTs appears to resemble a sponge that is composed of compacted higher-order chromatin fibres and domains. Within CTs, regions of condensed ~1 Mbp chromatin domains are separated from the boundaries of other CTs by the ICD which was renamed by Cremer and Cremer (2001) as the interchromatin compartment (IC) (25, 30, 31). The latter is a continuous and interconnected system of lacunas and channels that is present in the border zone of each CT and extends into its own and other CTs. The lacunas and channels are devoid of DNA and lay between these higher-order chromatin structures. In this way, the chromatin loops from adjacent CTs and ~1 Megabase (Mb) chromatin domains are allowed to intermingle with each other by expanding into the IC territory. This has been substantiated by the observed protrusion of small and larger chromatin clumps from their respective CTs in the form of finger-like extensions and the subsequent invasion of adjacent CTs (25).

In certain regions of CTs the presence of the IC is not a requirement for the association of chromatin fibres. Direct interactions between chromatin fibres extending from ~1Mb chromatin domains that are directly contacting each other and are not separated by the IC, have been reported (25). This view is different from the original proposal of Zirbel et al (1993) that the IC space can expand in an outward direction only between the exterior surfaces of CTs, which by extension implicates that rosette-like chromatin loops that are present within CTs can intermingle with loops that are contained in other CTs only at sites where the two neighbouring CTs directly touch each other (38). Finally, the ICD model states that CTs have a smooth surface and active genes that are located at the periphery of CTs enable the interactions between the constituents of the IC such as IGCs, repair proteins, nuclear speckles and nuclear bodies, such as Promyelocytic Leukaemia (PML) bodies and Cajal coiled bodies (25).

Initial evidence for the presence of DNA-free channels was obtained by the detection of lamin B staining in CHO cells (17). In order to examine these channels, Belmont et al (1993) employed a combination of optical sectioning light microscopy,

immunogold staining, intermediate voltage electron microscopy (EM) and EM tomography (17). An intense staining was observed at the chromatin surfaces that were in close proximity with the nuclear envelope and weaker staining was observed in regions where nuclear pores were present. This covering of large-scale chromatin domains by high concentrations of lamin staining was shown to result in the clustering of these domains, which was in turn proposed to allow the formation of nuclear pores in regions between these clustered domains. In this way, nuclear pores corresponding to channels that are devoid of DNA and invade the nuclear space were proposed to be generated (17). Consistent with this, Cremer et al (2004) have also reviewed that the IC between chromatin clumps is chromatin free (39) and immunogold experiments have shown that DNA-specific antibodies did not produce a signal within this compartment, thereby verifying this argument (25).

1.3.2 The RW/GL model

The random walk/giant loop (RW/GL) model states that there is no IC and that extensive intermingling between GLs of chromatin that are present within the same or different CTs occurs in the interphase nucleus (34). Initial evidence that led to the formulation of this model was derived from Van den Engh et al (1992) who studied the compaction characteristics of chromatin by employing a statistical measurement method with fluorescent probes that were present at specific sites of human chromosome 4, within a region of ~4 Mbp. The results of this work demonstrated that over genomic distances of 100 kbp to ~ 2 Mbp, chromatin coiling and diffusion are represented by random walk characteristics which are very similar to that of linear polymers. The latter are extended molecular chains that themselves fold in a random fashion. The finding that at genomic distances greater than 2 Mbp chromatin deviated from the linear polymer-behaviour suggested that unknown limitations do not allow further random chromatin diffusion within the interphase nucleus to take place (40).

According to Sach's (1995) and Yokota's (1998) predictions, chromatin is coiled in flexible and loosely folded GLs that have a length of several Mbp. The GLs are formed through the interconnection of genomic sites that are positioned several Mbp away from each other within each strand. Furthermore, the bases of the GLs are attached to a flexible backbone structure through the loop attachment

points. Within each loop, the motion of chromatin takes place in a random walk manner (34, 35). More specifically, it was found that at distances between the range of 2 and 4 Mbp the mean interphase (physical) distance between the chromosomal points was decreasing as the genomic separation was increasing. In addition, the average separation between distant chromosomal points (global scale factor) was found to be much lower than that of proximally positioned chromosomal points (local scale factor) with the scale factors being $0.065\mu m^2/Mbp$ and $1.9\mu m^2/Mbp$, respectively. It was suggested that these findings can only be consistent with the localization of chromosomal points on GLs. Moreover, the observation that the distances between points on the same chromosome were increasing in an infinite fashion without constraints, suggested that the volume of each CT is not restricted by a border such as the IC (35).

Based on the RW/GL model, the intermingling of GLs from different CTs is based on random diffusive motions exhibited by these GLs (35). This model supports the view that gene-poor and gene-rich nuclear areas are not compartmentalised. It also states that GLs are approximately 10 Mbp long (36), have a diameter of 30 nm and are built up by continuous chromatin fibres that are 50-200 kbp long and are in turn separated from each other by a 200 kb chromatin linker present within the same CT (30, 34). GLs walk randomly in the CTs and invade other CTs to intermingle with other GLs from different CTs (34). Nuclear speckles and nuclear bodies are formed in expanded areas where overlapping and decondensed GLs are present. The generation of these nuclear speckles and bodies possibly accounts for the departure of flanking chromatin regions from these areas. The degree of dispersion or condensation of chromatin is regulated by the size of either the GLs or the linkers that separate them [as reviewed in (30)]. In addition, this model does not refer to any correlations between the organisation of a CT and the functional activity of that CT (28). Further evidence supporting this model has been provided by Solovjeva et al (1998) who used Van den Engh's and Yokota's approach to study the characteristics of replicated chromosomal segments within replication foci in normal proliferating human cells during S phase. The results indicated that there were no confinements in the local arrangement of chromosomal segments, thereby providing evidence for the random walk behaviour of GLs during S phase (36).

The degree of compaction of individual GLs is still under scrutiny, far from resolved. 3-D Fluorescence In Situ Hybridisation (FISH) analysis of the gene-dense region on human chromosome HSA 11p15.5 suggested that GLs are higher-order chromatin fibres that are characterised by a compaction ratio between the ranges of 1:30-1:40 [as reviewed in (30)]. However, Albiez et al (2006) examined the same gene-rich region of HSA 11p15.5 and found chromatin extensions that appeared as finger-like structures rather than GLs that protrude from the periphery of CTs. These finger-like chromatin extensions were shown to have a compaction ratio of 1:300 rather than 1:30- 1:40 (25).

1.3.3 The ICN model

Branco and Pombo (2006) performed chromosome painting of CTs on ultrathin cryosections of human lymphocyte nuclei by using different fluorochromes and then they analysed the chromosomal areas where the colours were overlapping. Their proposed ICN model, consistent with the RW/GL model contradicts the existence of the IC. However, unlike both ICD and RW/GL models, the ICN model argues against the presence of condensed ~1 Mbp chromatin domains within CTs (26). This model states that the chromatin loops penetrate freely into other CTs and intermingle with the chromatin loops of other CTs, with the highest level of intermingling occurring at the borders of different CTs. According to the ICN model, the dynamic properties of chromatin explain its ability to diffuse into different CTs, with the extent of intermingling confined to proximally located CTs by the nuclear envelope, nuclear structures and nearby CTs. Moreover, the physical characteristics of individual CTs and the functional interactions between these CTs play an important role in the determination of the extent of intermingling (26). Evidence that supports the argument that there is no IC between CTs comes from the microscopic examination of all of the heterologous CTs in nuclei of G_0 and early S phase stage human fibroblasts by 3-D FISH. These observations reveal that there is a close spatial proximity between individual CTs with no visible IC space between CTs separating them (41). On the other hand, the findings that chromatin fibres from gene - dense chromosome regions characterised by high transcriptional activities in human cells expand outside CTs in nuclear areas in a transcription-dependent fashion (42) in conjunction with the proposal that genes are preferentially localised at the peripheral surfaces of CTs in order to be readily exposed to the components of the transcription

apparatus, contradict this statement (38, 43). While Zirbel et al (1993) have suggested that the IC at the periphery and surfaces of CTs is the site of splicing and transcription events (38), Kurz et al (1996) have implicated the IC as the site of localisation for both expressed and non-expressed genes, independent of their transcriptional status (43).

1.4 CHROMOSOME TERRITORIES IN RELATION TO FUNCTION

Chromatin structure changes according to functional processes such as transcription and DNA replication (13, 19, 25, 28, 30, 44-55). For instance, during transcription different levels of chromatin folding occur to facilitate interactions between DNA and DNA binding proteins (13). Initial evidence supporting the direct correlation between the chromatin structure characteristics and transcription has been provided from studies that employed DNase I, which is an enzyme causing double strand breaks (DSBs) (13, 44, 45). It was shown that the transcription of the early-immediate proto-oncogenes c-myc and c-fos enhances the access DNase I to their sequences and their digestion by DNase I (45). Inversely, the inhibition of transcription makes the sequences of these genes inaccessible to DNase I (44).

At the interface of the IC, between the condensed internal chromatin domains and the IC, the perichromatin region (PR) is observed to be present. The PR has been characterised as a 100-200 nm wide boundary zone of decondensed chromatin that outlines the periphery of chromatin domains and contains components of both transcription and splicing machinery. It is generally accepted that the PR is the nuclear subcompartment where DNA replication and transcription (RNA synthesis) take place (25, 46). The PR has been suggested to separate but at the same time connect the 3-D network of condensed chromatin domains and the interconnected IC channel network both structurally and functionally, by being located between these two networks. In addition, it has been suggested that proteins are either transported from the PR to the interior of condensed ~1Mb chromatin domains or transported to the nuclear pores for export (25). Actively transcribed sequences are found at the surface of CTs at the chromatin-free PR, which is present between the ICD and condensed chromatin domains (19). Electron microscopic autoradiographic analyses

have demonstrated that the perichromatin fibrils (PFs) associate with splicing factors, RNA polymerase II and other transcription factors (19, 47). The PFs are regarded as *in situ* forms of active heterogeneous ribonucleoprotein particles (hnRNP) transcripts that are formed at the PR. Transcription factors and factors that are involved in pre-mRNA processing events accumulate at the PFs which surround compact chromatin domains, indicating that PFs represent the *in situ* active transcripts and that pre-mRNA processing takes place at the PFs. Studies indicated that transription is a process that takes place at discrete sites rather than at transcription factories, as it had formerly been proposed (46). By using antibodies against RNA polymerase II, it has been shown that a strong signal is obtained at the PFs within the PR, demonstrating that they represent the main sites of transcription in the nucleus (39, 46).

The chromatin component of each CT is specifically compacted so that the transcriptionally active chromatin regions are exposed near the surface of compact chromatin domains and as a consequence of that the interaction between these sites and the transcriptional machinery is facilitated. Upon gene activation, condensed chromatin regions that are neighbouring the IC are decondensed (47). Despite the fact that during interphase chromosomes are restricted in non-overlapping CTs, they are proximally positioned in a way that enables their mutual associations to occur. Decondensed loops of chromatin that contain actively transcribed genes have been shown to extend into the IC, in order for the genes to interact with the transcription factors that are present within this compartment (25, 47). Moreover, evidence has suggested that active genes that are located on chromatin loops interact with genes that are located on other chromatin loops via the expansion of the loops out of their respective CTs and the intermingling with each other at CT borders [as reviewed in (39)].

A growing body of evidence has also demonstrated that chromatin structure is linked to DNA replication process (22, 28, 30, 38, 43, 48-57). The incorporation of fluorescently labelled nucleotides, such as halogenated thymidine analogues bromodeoxyuridine (BrdU), iododeoxyuridine (IdU), chlorodeoxyuridine (CldU) and fluorodeoxyuridine (FdU), into the nuclei of living cells during S phase is accomplished by using DNA polymerase enzymes. In this way, the DNA content of the cells becomes fluorescent (22, 48). It has been shown that active DNA

polymerases become accumulated at subchromosomal foci 400-800 nm in diameter that correspond to ~ 1Mbp chromatin domains. These foci, the presence of which is maintained throughout subsequent interphase stages and cell cycles of descendant cells after the end of S phase, are known as replication foci (28, 30, 50-52, 56). Furthermore, it has been suggested that roughly 0.3-1.5 Mbp of DNA is contained within each one of these foci (28, 52). The replication foci have also been shown to be relatively immobile and compartmentalised to distinct nuclear regions during interphase (49, 55, 57). In human diploid fibroblast (HDF) cells these foci are preferentially positioned towards the periphery of the nucleus (49). In contrast, during mitosis they are largely mobile. Furthermore, their specific arrangements within the nucleus are transmitted to subsequent cell generations (50). The finding that segregation of DNA into compartments is induced before or at the very early stages of G_1 phase has led to the conclusion that DNA replication is not solely responsible for the compartmentalisation of DNA (22, 53, 54).

Visser et al (1998) analysed DNA that had been produced at two distinct stages of S phase in the same nuclei of human fibroblasts, by employing replication double labelling with IdU and CldU, in conjunction with chromosome painting. These two cytochemical approaches were used with the aim of revealing whether DNA replication occurs at the surface of CTs or it covers the entire volume of CTs in the transcriptionally active Xα and transcriptionally inactive Xi CTs of female fibroblasts and in the CTs of chromosome 8 and chromosome X of male fibroblasts. The fixation of the cells at mid-late S phase of the cell cycle revealed that at this stage intense replication occurs within Xi and not Xα CT. The latter is known to replicate its DNA early in S phase. In general terms, the chromatin regions where replication was taking place during early S phase were compartmentalised at spatially distinct regions from those where replication was taking place during late S phase. However, apart from Xi CT in which most of the early replicating chromatin was distributed towards the nuclear periphery, almost equal concentrations of each of early-replicating and late-replicating chromatin regions were found to be present throughout the whole volume of CTs corresponding to male chromosomes 8, X and female chromosome Xα. It was therefore concluded that with the exception of Xi CT, replication generally occurs at both the interior and the peripheral surface of CTs (51). This argument contradicts the predictions of other studies that replication

processes take place exclusively proximal to the peripheral surface of CTs (22, 38, 43).

In order to determine whether subchromosomal foci exist in living cells, the fluorescently labelled thymidine analogue Cy3-AP3-dUTP [cyanine dye (Cy3) conjugated to 5-amino-propargyl-2'-deoxyuridine 5'-triphosphate (AP3-dUTP)], has been microinjected into nuclei of HeLa cells, HDFs and human neuroblastoma cells (28). Following several cell cycles, nuclei of all cell types exhibited segregated chromatid territories that were replication labelled, implicating that the nuclei that had stably integrated the fluorescent label managed to grow and undergo cell division. Four-dimensional (4-D, or alternatively called 3-D + time) analyses that were performed in Cy3-AP3-dUTP-labelled and segregated chromatid territories in the nuclei of HeLa and neuroblastoma cells allowed the observation of migrations of nuclei and entire cells as well as the detection of dynamic movements of chromatid territories and replication foci. Differences between the patterns of extensions and foldings could be observed between different replication foci. The results of this study led to the hypothesis that subchromosomal foci found within CTs are higher-order functional structures that play a role in the regulation of both DNA replication and transcription. It was also suggested that they are functionally different from each other and that their functions are conserved throughout subsequent cell cycles (28). Finally, it should be mentioned that the microinjection of fluorescently labelled thymidine analogue biotin-11-dUTP within the nuclei of HDF cells has shed light into the relationship between the localisation of freshly produced DNA and proliferating cell nuclear antigen (PCNA) during S phase (49).

1.5 DYNAMICS OF CHROMATIN MOTION

The motion of chromatin within the interphase CTs has been shown to be a requirement for several important cellular processes such as differentiation, progression through the cell cycle, alterations in cellular physiology and gene transcription processes [reviewed in (29, 58)]. In addition, according to several studies it is involved in chromosomal translocation events following DNA damage induction (342), recombination (59), pairing between homologous chromosomes

during meiosis (60) and chromatin compaction (59). CTs are subdivided into distinct chromosomal domains such as telomeric, chromosome arm and band-like and centromeric domains (43, 61). Centromeric domains are known to possess relatively stable positions during interphase and perform only slow and selective movements, as evidenced by the labelling of α-satellite DNA domains in the centromeres of living human cells with Centromere protein B - GFP (CENPB-GFP) fluorescent fusion protein (62). CENP-B is a protein present in the centromeres that is known to bind to satellite DNA regions of the genome. The possibility that these occasional movements could be directed by motor proteins has also been speculated (62).

Two different levels of motion are thought to exist within CTs of living cells: short-range/confined (29, 57, 59, 63, 64, 64, 65) and large-scale motion [(29, 57, 63, 66); figure 1.5]. Controversy surrounds the identity of these motions. Some researchers believe that chromatin motions are random (29, 59), whereas others have stated that they are directed towards specific nuclear sites (29, 57, 66). The confined area of chromatin motion corresponds to 1% of the total nuclear volume and the restricted chromatin motion has been reported to be in the order of 10^{12} to 10^{11} cm² per second (59). A number of studies have suggested that diffusion-driven mechanisms result in Brownian motions of chromatin (29, 57, 59, 63). However, in two of these studies it has been proposed that these motions occur in conjunction with active motility-based mechanisms. Examples of these mechanisms include the microtubule-based motility system that positions chromosomes across the metaphase plate during mitosis or motor-protein driven mechanisms (57, 63).
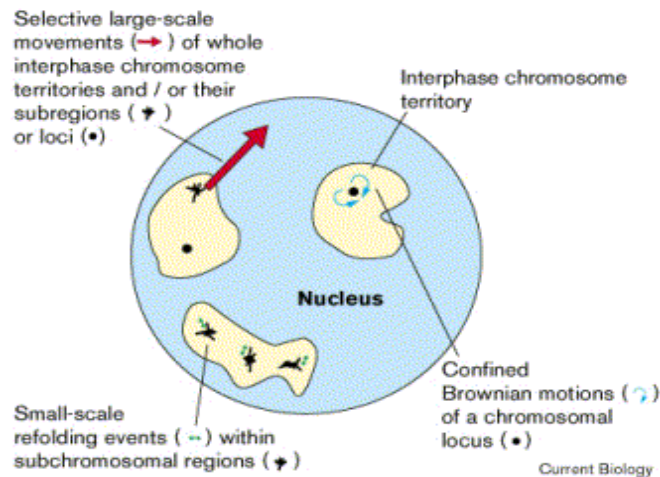
Figure 1.5: Schematic illustration of the different types of chromatin motion within CTs of the interphase nucleus

(29. Zink D, Cremer T, Curr Biol. 1998 Apr 23;8(9):R321-4).

During interphase, constrained Brownian motions can be regarded as diffusive movements of chromosomal subregions within a CT that is stable in terms of position. Quantitative analyses of yeast and *Drosophila* cell nuclei have suggested that constrained Brownian (diffusive) motions of chromosomal loci take place within the nuclei of these cells. These movements were demonstrated to cover nuclear areas with a radius of 0.3 μm and 0.9 μm in yeast and *Drosophila* nuclei, respectively (29, 59). Marshall et al (1997) used a 3-D time-resolved detecting approach in conjunction with quantitative motion analysis to examine the diffusive motion of chromatin regions within the interphase nucleus. The end conclusions of this investigation highlighted that within overlapping regions of chromatin motion restriction that are present in the CTs of interphase cells, limited and diffusive Brownian chromatin movements occur through the random collision of chromatin sites within these regions. It was also established that chromatin diffusion is fast enough to carry out processes associated with chromatin motion such as recombination (59). Bornfleth et al (1999) used 4-D microscopy to gain insight into the different types of chromatin motion in human cells. In order to achieve this, they employed fluorescent labelling of newly replicated DNA to generate and analyse simultaneously many signals of subchromosomal size within the same nucleus of living cells [as described in (28)]. The labelled chromosomes were subsequently

segregated into the nuclei of descendant cells and in this way, distinct subchromosomal foci could be examined. In summary, this study provided evidence for the existence of a highly compartmentalised, complex nuclear landscape. Restricted, correlated and diffusive motions were assessed as being constrained to a subpart of the nucleus. However, it was also demonstrated that seldom directed and slow chromatin movements occur within CTs. The authors did not exclude the possibility that these motions could be driven by motor proteins (57). Subsequent experiments with living human cells agreed with the constraint of chromatin motion within the nucleus and suggested that this motion restriction is more pronounced in nuclear regions in close proximity with nucleoli and within the nuclear periphery. Based on these findings it was proposed that the higher-order nuclear landscape is responsible for imposing these constraints. Furthermore, the chromatin motion restriction at the nuclear periphery was attributed to the presence of compact heterochromatic sequences in this nuclear compartment (64).

On the other hand, selective large-scale movements are believed to be specific for the cell type, the cell state, the locus and the species from which cells originate and it has been postulated that the whole underlying CT will have to be deconstructed in order for such movements of individual loci to occur. An alternative way in which these movements could occur is their coupling with similar movements that might occur in certain regions of the entire CTs. It is likely that large-scale movements occur only in cases where the functional state of the cell has been changed. For instance, such movements could occur only during cell differentiation [reviewed in (29)]. Selective large-scale redistributions of the single chromosomal locus 93 D during transcription have been observed by Buchenau et al (1997) within the polyploid nuclei of *Drosophila* embryos. Over a time interval of 10 minutes, several 93D loci were observed to move at a high speed that exceeded 3μm, whereas other 93D loci that were present within the same nucleus were found to exhibit a random walk leaping behaviour of moderate speed (66). In addition, Shelby et al (1996) have recorded large-scale redistribution of α-satellite DNA sequences over the range of 7 - 10 μm in 60 minutes (62). It has been suggested that selective large-scale movements are rare compared to Brownian motions (57, 62, 63), despite the fact that chromosome loci of interphase nuclei are characterised by both selective large-scale and Brownian motions (29, 57, 63).

Vazquez et al (2001) analysed the motion of fluorescently labelled chromosomal regions in developing spermatocyte nuclei of *Drosophila* cells during G_2 stage of interphase, by using a combination of single-particle tracking (SPT) analysis and Lac operon labelling system. The results of this work argued for the presence of significant short and long distance Brownian motions that existed together with the rapid alteration of the nuclear design. The long-range chromatin motion, which was proposed to reflect a random walk motion, was shown to correspond to distances as large as 4-5 µm per hour, whereas the short-range motion was reported to be more significant and corresponded to 0.3 µm approximately every second. The short-range motion was fast as it lasted 1 -2 seconds, whereas the long-range motion was slow. Overall, the results of this study supported the notion that despite the long-distance chromatin motion that was observed in many occasions, the chromatin component of chromosomes is stably restricted to particular regions of CTs. Both long and short distance chromatin movements were proposed to correspond to different levels of higher-order folding of the chromatin fibres and alterations of the nuclear landscape. It was also suggested that the cell cycle stage plays an important role in the specificity of these motions, as long-range movements were abolished at later stages of G_2 phase (63).

Bornfleth et al (1999) have provided a separate body of evidence supporting the notion that both random and occasional directional motions occur within the nuclei of human cells. The results of this work have demonstrated that subchromosomal foci within CTs are occasionally characterised by an alteration from random to non-random directional motion relative to the territory centre of mass. SPT analysis was employed to study the diffusive motion of CTs. It was found that within the observed time interval, a free diffusion of subchromosomal foci was taking place with low diffusion coefficients. The diffusion coefficients of foci positioned at different CTs were low, but still higher than the corresponding coefficients of foci positioned within the same CTs (57).

It has been proposed that the confinement of chromatin motion is the consequence of the tethering of chromatin to positionally stable intracellular structures such as the nuclear envelope, the cytoskeleton, the nucleolus, microtubules and the matrix attachment regions (MARs) on the nuclear matrix (29, 57, 59, 63, 65). In addition, it has been suggested that the proximity between

chromatin fibres and their interactions put constraints on chromatin motion (63, 65). The anchorage of chromatin fibres to nuclear structures was initially supported by Abney et al (1997). The authors studied chromatin mobility characteristics in nuclei of Swiss 3T3 fibroblasts and HeLa cells during interphase after the fluorescent labelling of chromatin with dihydroethidium. The maintenance of the resulting fluorescent spots after Fluorescence Recovery After Photobleaching (FRAP) experiments for periods greater than 60 minutes suggested that chromatin was stationary during interphase for distances lower or equal to 0.4 μm. The authors concluded that the confinement of chromatin motion could either be due to interactions between chromatin fibres or macromolecules within the nucleus or due to the attachment of chromatin fibres to the nucleolus, nuclear matrix or lamina (65). Studies on yeast and *Drosophila* cell nuclei have demonstrated that microtubules play a role in the confinement of these movements of chromosomal loci to particular areas within the nucleus. In addition, consistent with the predictions of Vazquez et al (2001) and based on experiments that assessed the diffusion rate of loci on plasmids that had been introduced in yeast nuclei, it has been suggested that the restriction of diffusion is the result of such a tethering of chromosomal sites to either the nuclear matrix or the nuclear envelope (29, 59, 63). The application of the analysis procedures to the 4-D analysis of experimentally obtained confocal 3-D images of human cell nuclei that contained replication-labelled CTs indicated that in general terms, the motion of CTs and the constituents of CTs are both restricted by the nuclear envelope and the CTs themselves. The nuclear envelope was suggested to restrict the motion of both entire CTs and subchromosomal foci and CTs were suggested to restrict the motion of their components (57). However, the proposal that selective large scale movements could be the result of Brownian motions or the result of the action of motor proteins such as actin or myosin, implies that apart from confined motions, large-scale motions could also be driven by the anchoring of chromosomal loci to an immobile structure (29, 57, 62). The results of Vazquez et al (2001) led to the proposal of a model which states that local interactions which take place within the interphase nucleus drive the diffusive chromatin motion which in turn determines the dynamic organisation of chromatin within the interphase nucleus, in a higher-order manner. According to this model, within the interphase CTs, chromatin regions are tethered to specific anchoring sites. In early G_2 phase nuclei, only a small number of anchoring sites are present within large chromosomal

regions. In this way, chromosomal loci are able to explore a large nuclear area, without altering the stable position of individual chromosomes within the nucleus. In contrast however, in late G_2 nuclei, a much higher number of anchoring sites is present within the same large chromosomal regions. This increase in the anchoring sites restricts the motion of the chromosomal loci to a much more confined nuclear area. Therefore, it was concluded that alterations in the number of anchoring sites, the stability of the interactions and the spatial relationship of chromatin fibres play a crucial role in the regulation of the distance over which chromatin can move and the rate at which it is able to move (63).

1.6 CHROMATIN CHARACTERISTICS IN RESPONSE TO DNA DAMAGE AND REPAIR IN MAMMALIAN CELLS

1.6.1 BACKGROUND

Induction of DNA damage is responsible for the formation of DNA lesions, including base damage, single-strand breaks (SSBs) and double strand breaks (DSBs). If left unrepaired, DSBs will result in cell death. Accordingly, cellular systems have very sophisticasted repair pathways that can result in the successful, error-free repair of the lesion. Erroneous repair results in the formation of chromosomal aberrations such as chromosomal breaks, deletions, inversions, duplications and exchanges. Ultimately, one consequence of these aberrations could be the initiation and/or progression of carcinogenesis (67). Chromosomal aberrations can either be intrachromosomal (involving one chromosome) or interchromosomal involving two or more chromosomes (68). Regarding intrachromosomal aberrations, the erroneous rejoining of broken genomic material leads to paracentric inversions, pericentric inversions and intra-arm deletions. In interchromosomal aberrations chromosomal translocations that involve two DSB ends from two distinct chromosomes, dicentrics or more complex rearrangements between ≥ 3 breaks in two or more chromosomes may be formed (69, 70). While exposure of cells to ultraviolet (U.V.) light most frequently accounts for the formation of pyrimidine dimers and SSBs (68), exposure of cells to ionising radiation such as x-rays or α-particles and genotoxic chemical agents are intimately associated with the formation of DSBs. Endogenous formation of DSBs arises as a consequence of free radicals

produced by oxidative metabolism, during meiotic processes or V(D)J recombination during genetic reprogramming of B and T lymphocytes (67, 71).

1.6.2 DNA DAMAGING AGENTS

It is well documented that DNA damaging agents such as the radiomimetic drug bleomycin, reactive oxygen agent hydrogen peroxide and ionising radiation have a negative impact on DNA integrity by producing DSBs (67 - 172).

<u>1.6.2.1 Bleomycin</u>

Bleomycin (BLM) is a member of metal-binding glycopeptides antibiotic family (72) isolated from the bacterial species *Streptomyces verticillus* (73), which cleaves DNA in a sequence-specific fashion. The cleavage of φX174 DNA restriction fragment by BLM and subsequent autoradiographic analysis has revealed that it preferentially fragments double stranded DNA (dsDNA) at the pyrimidine base positioned to the 3' end of every guanine (G) (74) in the presence of ferrous (Fe^{2+}) ion and oxygen (74, 75). In this way, SSBs and DSBs are formed, resulting in the release of free bases with carbons at the 4' and 5' positions of the deoxyribose moiety and a chromogenic compound termed malondialdehyde (75). In addition, other released products can be propenal base (thymine and other bases with three carbons present in the released product). The two other possibilities are that a combination of the aforementioned products or no product is released (75). Line of evidence has suggested that there is a ratio-based relationship between free base and base propenal release (76, 77). Müller et al (1972) have demonstrated that for every released free base, 0.58 base propenal is produced (ratio 1: 0.58) (77). Since BLM recognises DNA at guanine-thymine (G-T) and guanine-cytosine (G-C) sequences, these are the preferential cleavage sites. In this respect, the presence of a pyrimidine at the 3' end of every guanine is critical for cleavage, as sequences possessing the reverse polarity with the guanine present at the 3' end of pyrimidine (T-G) and (C-G) could not be cleaved (74). It has been demonstrated that BLM-induced DSB formation is the consequence of SSB induction on Pyr-G-C (directed from 5' – 3') and Pur-C-G (directed from 3' – 5') sequences that are positioned opposite each other on the two strands of the double helix (78). The Fe^{2+} ion is oxidised to Fe^{3+} thereby reducing oxygen and producing superoxide anion (O_2^-) and hydroxyl (OH^-) radicals that subsequently attack the DNA double helix (79, 80). The consequence of

this attack is the radical-induced disruption of the 3' - 4' bond between the carbons on the ring leading to G-T and G-C base pair cleavage, base propenal (74, 81) and free base release (82). The attack is also associated with the conversion of the 3' and 5' end DNA groups to the phosphate ester of glycolic acid and a free phosphate ester, respectively (74, 81). Therefore, the presence of Fe^{2+} ion and O_2 are absolutely necessary for bleomycin induced cleavage of DNA (79, 80). Evidence supporting this argument has also been provided by the fact that in the coexistence of Fe^{2+} ion and chelating agents such as Cu (II), Co (II) and Zn (II), cleavage by BLM is abolished (83). BLM possesses two groups termed bithiazole and dimethylsulfonium that are involved in the binding of the antibiotic to DNA by acting as intercalating agents. Takeshita et al (1978) proposed a model for BLM-induced strand scission of DNA according to which the bithiazole groups of bleomycin recognise, intercalate and thus disrupt G-T and G-C base pair bondages along dsDNA. This intercalation is believed to be maintained by the attraction between the positive and negative charges of disulfonium ion and DNA, respectively (74).

Autoradiographic analysis of the purified human α-DNA has suggested that BLM exerts its degrading action upon the linker region of the nucleosomes that are present in chromatin. It was also shown that at the cellular level the pattern of BLM-induced cleavage was almost identical to the *in vitro* pattern, despite the fact that the same cleavage efficiency was obtained using a higher amount of BLM compared to the *in vitro* experiments. This observation was not consistent with expectations, as the chromatin conformation is more compact at certain regions and chromatin associated proteins such as histones would be expected to interfere with the binding of the antibiotic on DNA. Therefore the two suggestions were that nucleosomes are randomly positioned on chromatin and that the sequence compositions of DNA rather than higher order chromatin structure determine BLM cleavage sites and the resulting DNA integrity (84).

Thus, the structure of chromatin has been suggested to be a determinant of the extent of damage induced by BLM. Southern blotting analysis of DNA extracted from hen cells and exposed to BLM support this by revealing that actively transcribed ovalbumin and globin genes from oviduct and erythrocyte nuclei respectively are more prone to BLM-induced DNA damage compared to the same genes in the transcriptionally inactive state. Therefore, there is a greater sensitivity to

BLM in more relaxed chromatin regions of actively transcribed genes, compared to regions in which the chromatin conformation is more compact (85). It has also been shown that sodium butyrate (NaB) - induced chromatin unwinding of ATC-15 mosquito cells in conjunction with BLM exposure results in an increased number of DNA breaks compared to CHO cells treated with BLM only. Both cell types show the same BLM-induced break frequency in the absence of further treatment, which is interesting because chromatin structure of ATC-15 cells is more compact than that of CHO cells. Intuitively, the frequency of SSB and DSB in these cells should be lower compared to that of CHO cells. However, it was speculated that the compact conformation of ATC-15 cells is due to the presence of shorter linker DNA segments that interconnect the nucleosomes, thereby reflecting the reduced efficiency of BLM intercalation within these cells (86). This prediction was supported by the finding that in mammalian cells BLM degrades DNA by binding to the linker stretches of DNA between individual nucleosomes (87).

The extent of chromosome damage and cell growth arrest following BLM exposure is cell type and donor specific. Evidence for this has come from the comparison between the chromatid break frequencies of BLM-exposed peripheral blood lymphocytes (PBL), oral fibroblasts and primary oral keratinocytes with those of normal lymphocytes (88). The repair processes that occur following BLM exposure have also been shown to differ between different cell types. Experimental data have suggested that p53 protein, which is responsible for cell cycle arrest following damage induction assisted by p21waf1/cip1, is involved in DNA damage repair in the crypt and villi cells of the small intestine and lung cells in mice following BLM-induced damage induction (89). However, differences in the damage response and repair were recorded between intestine and lung cells. More specifically, apoptotic cell death was recorded only in intestinal cells and was absent in lung cells. Even between villi and crypt cells of the small intestine there were differences. While in crypt intestinal cells apoptosis was found to be induced by both p53-dependent and p53-independent pathways (with the p53 pathway being more prominent), in villi cells it was solely induced by a p53-independent pathway (89).

As noted above, chromosomal structure plays a role in BLM-induced aberration formation. However, Hittelman et al (1974) have argued that cell cycle stage is also important. Their work involved the fusion of mitotic and interphase

cells by employing the premature chromosome condensation (PCC) method in order to examine BLM-induced DNA damage in CHO cells present in interphase of the cell cycle. The results of this study revealed that the formation of chromosomal aberrations after BLM treatment was substantially enhanced in PCC chromosomes at G_2 phase of the cell cycle compared to the appearance of the same PCC chromosomes at the mitotic stage. While the transition from mitosis to G_1 phase was not affected, the progression from S and G_2 phases of the cell cycle was considerably delayed. In addition, it was shown that 44 % of CHO cells containing aberrant PCC chromosomes were prevented from entering mitosis, thereby confirming the notion that extensive damage causes cell cycle arrest at G_2/M checkpoint and that chromosomal breaks and gaps are repaired within the first hour after BLM exposure (90). The BLM-induced prevention of entry into mitosis has been reported after histological analysis of the small intestine crypt cells of the mouse following intravenous injection of the agent (91). Similarly, in asynchronised CHO cells exposed to BLM it was demonstrated that cells undergoing mitosis at the time of the addition of the agent were characterised by the highest degree of cell death, followed by cells that were present in G_2 phase of the cell cycle. Less sensitive to the agent were the cells in S phase, whereas the most resistant were those that were present in G_1 phase. The cells were found to be arrested only at the G_2/M transition point and not at G_1/S. The arrest at G_2/M checkpoint was proposed to be due to RNA synthesis inhibition during transcription (92). A further line of evidence verifying the delay in progression from G_2 phase to mitosis following BLM exposure was provided from studies in mouse L-cells. The delay was proposed to take place early in G_2 phase, as the proportion of cells with the ability to enter the mitotic stage of the cell cycle showed a significant decline only 90 - 100 minutes following BLM addition in metaphase-arrested cells (93).

The action of BLM is responsible for the generation of aberrations at chromosomal sites where interstitial telomeric sequences (ITS) are present in CHO cells, which in their highest proportion involve the formation of dicentrics and acentric pieces of DNA. In addition, translocations and amplification of telomeric sequences within the genome of these cells has been recorded. More specifically, the performance of FISH revealed that telomeric sequences were involved in 18.1 % and 9.5 % of the BLM-induced chromosomal aberrations in G_1 and G_2 phases of the cell

cycle, respectively. It was also proposed that the action of BLM results in damage induction at ITS of the centromeres and that heterochromatic sequences are involved in the formation of aberrations (94). Experiments on confluent human fibroblasts have suggested that treatment with BLM results in only a proportion of BLM penetrating the cell membrane and thus entering the cells. More specifically, the permeabilisation of the cell membrane using lysophosphatidylcholine (LPC) in these cells resulted in the increase of the fraction damaged cells and cells undergoing damage repair from 5 % in untreated cells to approximately 86 %. It was suggested that the cell membrane acts as a barrier that prevents BLM from entering the cell nucleus. BLM exposed cells not treated with LPC were found to form aggregates that were characterised by higher extents of damage and repair at their cores compared to their extremities. This observation led to the speculation that BLM is initially taken up by the cells that are located at the centre of these clusters and then transferred to the cytoplasmic space of adjacent cells via the gap junctions that are present at the cytoplasmic borders that separate the cells (95).

1.6.2.2 Hydrogen Peroxide

In mammalian cells, agents such as potassium superoxide (96), cumene hydroperoxide (97), hydrogen peroxide (H_2O_2) and the reactive products of BLM are responsible for the generation of reactive oxygen species (ROS) resulting in the induction of DNA damage. ROS include O_2^- and OH^- radicals (96, 98). Evidence for the radiomimetic properties of ROS has been provided by experiments with wild-type CHO-K1-BH$_4$ and AS52 cells that were transformed into irradiation oversensitive cells. It was shown that the degree of mutations induced in the AS52 cells was comparable following treatment with both x-ray and neutron irradiation and ROS (96).

H_2O_2 is a radiomimetic ROS chemical (96, 99) that has been extensively implicated in DNA damage induction resulting in the generation of SSBs, DSBs and DNA adduct formation (97, 99-110). Studies on mouse lymphoma L5178Ytk$^{+/-}$ cells have revealed that exposure to H_2O_2 can result in the formation of 8-oxo7,8-dihydro-2'-deoxyguanosine (8-oxodGuo) and 1, N^6-etheno-2'-deoxyadenosine (εdAdo) DNA adducts at the estimated ranges of 500 - 1000 8-oxodGuo and 50 – 90 εdAdo adducts

every 10^9 nucleotides. Increasing concentrations of ROS results in the increase of the levels of DNA SSBs and DSBs and gene mutation, but not adduct levels (97).

The intracellular mechanism by which H_2O_2 induces DNA damage has been proposed to involve Fe^{2+} ion in a Haber-Weiss reaction, part of which is a Fenton type reaction. More specifically, Fe^{3+} is initially reduced to Fe^{2+} upon interaction with oxygen ($Fe^{3+} + O_2^- \rightarrow Fe^{2+} + O_2$; reaction 1). The interaction of H_2O_2 with Fe^{2+} results in the production of OH^- radical species which is highly reactive and can attack the DNA structure. This Fenton-type reaction is: $H_2O_2 + Fe^{2+} \rightarrow OH^- + OH^- + Fe^{3+}$ (reaction 2) (99-101). Initial studies using the iron chelator EDTA on human fibroblasts revealed that a metal-containing complex was responsible for DNA damage induction by OH^- radical formation following exposure to H_2O_2 (99, 100). Subsequently this metal was shown to be Fe^{2+} (102). Evidence for the participation of OH^- radical in the damage was demonstrated by carrying out OH^- radical scavenger studies (100) and by employing EDTA which is a chelator of Fe^{2+} ion. It has been shown that upon complexing, the OH^- radical is unable to induce DNA damage (99). Iliakis et al (1992) have more recently verified the notion that the presence of Fe^{2+} ions in close proximity to the DNA structure is essential for the formation of chromosomal damage by studying the interphase chromosome damage in CHO cells. Evidence for that was provided by the finding that H_2O_2 concentrations higher than 1 mM resulted in a reduced fraction of cells containing chromosomal aberrations, implying that this was due to the depletion of Fe^{2+} ions proximal to the double helix. In the absence Fe^{2+}, H_2O_2 alone is unable to induce DNA damage (104). However, separate line of evidence has contradicted the notion that the initial interaction between iron molecules and H_2O_2 that results in DNA damage takes place on the double helix and has suggested that it occurs in the lysosomes, cellular compartments that are rich in redox-active iron (103, 105, 111-113). Doulias et al (2003) provided evidence supporting this in HeLa cells and they also supported the view that redox-active iron molecules are subsequently transported into the nucleus where they exert their effect on DNA after inducing damage in the lysosomal compartment. They also proved that the chelation of iron by desferioxamine (DFO) in the lysosomes or the endosomes interferes with cell cycle progression, indicating that iron molecules in the lysosomal and endosomal compartments play an important role in cell division (103). Likewise, experiments

with primary rat hepatocytes (111) and J774 murine macrophage cells (112, 113) have identified the lysosomal compartment as the cellular storage area of iron, enhancing OH^- radical production due to interaction of iron with DNA damaging agents napthazarin (111) and H_2O_2 (112, 113). Studies in which Jurkat cells were exposed to glucose oxidase that is known to result in the continuous intracellular production of H_2O_2 have suggested that the subsequent interaction between intracellular iron that is concentrated at these cellular structures and H_2O_2 results in rupturing of the lysosomal membranes, followed by the release of iron to the cytosol and the nucleus where it plays a role in initiation of the apoptotic process and DNA damage induction, respectively (105).

Cu^{2+} is another divalent cation that is important in DNA damage induction. In the presence of ascorbic acid or cysteine and other biological reductants, Cu^{2+} in Cu^{2+}-glycylglycylhistidylglycine (GGHG) and Cu^{2+}-glycylhistidylhistidylglycine (GHHG) complexes is reduced to Cu. Subsequently, Cu acts in a Fenton type reaction (reaction 2) resulting in the production of OH^- radicals that subsequently attack and damage DNA (106). Further evidence for the damaging action of Cu^{2+}-H_2O_2 complexes on DNA has been provided by immunospin trapping detection of superoxide dismutase (SOD1) radicals. SOD1 is a class of enzymes that have binding sites for metals such as copper and zinc. In the presence of H_2O_2 and the absence of anions such as bicarbonate that are known to bind to SOD1 enzyme active site, copper has been reported to react with H_2O_2 resulting in the production of SOD1-centered radicals and the degradation of SOD1 through oxidation of SOD1 active site (114). Finally, research with rat cerebellar granule neuron (CGN) cells has indicated that the combined effect of Cu^{2+} and H_2O_2 resulted in a considerably higher level of cell death compared to exposure to H_2O_2 alone. In the presence of mannitol which is known to scavenge OH^- radicals, these increased cell death levels were maintained (115).

Cell death after exposure to H_2O_2 has been reported to be executed by both apoptotic and necrotic pathways (115-119). The treatment of human eosinophils with 1 mM of H_2O_2 resulted in the activation of caspase-3 apoptotic effector and an elevation in the fraction of apoptotic cells, whereas addition of the ROS scavenger NAC resulted in the repression of apoptosis in these cells by interfering with the action of H_2O_2 (116). The mitogen-activated protein kinases (MAPK) extracellular

signal-regulated kinases (ERK) 1 and 2 were also shown to become phosphorylated in the presence of H_2O_2 (116). It is worth noting that mitochondrial respiration was found to play an essential role for the execution of apoptosis in these cells (116). Experimental evidence has suggested that while caspase-3 is responsible for fragmentation of DNA and shrinkage of nuclei, cell death can be induced in the absence of caspase-3. These findings supported the notion that cell death can also take place via necrosis (119). In contrast however, other studies have suggested that the process of cell death is solely dependent on necrosis as the apoptotic pathway is inhibited by H_2O_2 (120). More specifically, experiments with Jurkat cells have shown that while the steps preceding the activation of procaspase-9, namely translocation of cytochrome c from the mitochondria to the cytosol and the assembly of procaspase-9 on the apoptotic bodies were not affected by the presence of continuously generated H_2O_2, activation of caspase-9 was actually repressed (120). It was suggested that this inactivation was attributed to the oxidation of cysteine residues on procaspase-9 apoptotic effector by OH^- radicals, generated by the combined effect of intracellular iron and H_2O_2. The addition of iron chelator DFO resulted in the apoptotic process taking place normally, thereby supporting this notion (120).

While SSBs are known to be formed by H_2O_2 alone, the formation of DSBs by H_2O_2 has been reported to require the presence of the amino acid histidine in a number of mammalian cell lines including human, mouse, monkey and hamster. In addition, the enhancement of histidine-induced cell death is the direct consequence of DSB formation (107, 110, 121). Under conditions that are known to slow down DNA damage repair (incubation of cells at 4 ^{o}C), it has been shown that the number of DSBs and non-viable cells are the same as the corresponding number of DSBs and non-viable cells at the temperature of 37 ^{o}C. Therefore, neither energy-propelled processes that are involved in damage repair nor cellular metabolism play a role in the histidine-assisted degree of DSB generation and cell death occurrence by H_2O_2 (108, 109). The CHO cell line AG8 (AA8 CHO cell line derivative) is remarkably tolerant to H_2O_2 (122) partly due to the high levels of catalase activity within their genome (110). Experiments in which these cells were subjected to the combined effect of histidine and H_2O_2 have revealed that while the abolition of catalase activity by the inhibitor aminotriazole was accompanied by the maintenance of resistance to

H$_2$O$_2$ alone, the combination of histidine and H$_2$O$_2$ resulted in the elevated level of DSB formation, which was also directly correlated with the level of cell death in these cells (110).

1.6.3 DNA DAMAGE REPAIR

There are two pathways by which DSBs can be detected and repaired in mammalian cells, namely homologous recombination (HR) and non-homologous end joining (NHEJ). During the process of HR which occurs in S and G$_2$ phases of the cell cycle, a broken DNA end is repaired using an intact homologous DNA sequence of the genome as a template. This DNA sequence is usually the other sister chromatid or a homologous chromosome. Other pathways are associated with illegitimate exchange between broken DNA segments that share homology such as single-strand annealing (SSA), which takes place between two random homologous DNA sequences and can result in tumourigenic translocations (67, 123-125). Sequence homology is not a requirement for NHEJ that predominantly occurs in G$_0$ and G$_1$ phases of the cell cycle and during which the broken chromosome end is repaired using a random non-homologous damaged DNA end as a template. NHEJ is generally perceived as a repair pathway that results in a higher frequency of chromosomal rearrangements compared to HR (67, 123, 124).

In human and mouse cells, following exposure to ionising radiation histone γ-H2AX is rapidly phosphorylated on serine 139 of its C-terminal tail in response to DSB formation (126-128). H2AX is phosphorylated by Ataxia Telangiectasia Mutated (ATM) and DNA – Protein Kinase (DNA-PK), which belong to the phosphatidylinositol -3-OH-kinase (PI-3K) like family (126, 127, 129-132). On average, 35 DSBs are formed per every Gy of irradiation in hamster and human cell lines within the total of 6 x 10^9 bp of DNA within the genome of cells and the damage has been calculated to afflict 1.8 – 3.5 x 10^6 bp of DNA following exposure to γ-irradiation (126). Rogakou et al (1998) have also reported that within 1 minute following irradiation exposure the level of γ-H2AX foci formation within the genome of cells reaches its half maximal value, whereas the maximal peak is reached 10 – 30 minutes post-irradiation (126, 133). In the most recent work of An et al (2010) it was shown that 15 minutes after the exposure of HeLa cells to a dose of 4 Gy of γ-irradiation, the level of γ-H2AX reaches its maximum value (128). Paull et

al (2000) have likewise demonstrated that within the first 3 minutes following exposure to ionising irradiation γ-H2AX foci are formed over large genomic regions (127). Following microbeam laser-induced exposure of normal IMR90 human fibroblasts, Indian Muntjac cells and MCF7 breast cancer cells to ionising irradiation, the formation of γ-H2AX foci was shown to be expanded in Megabase regions of chromatin flanking the DSBs. This response of the genome was shown to be evolutionary conserved, as it was similarly found to operate in *Drosophila melanogaster, Xenopus laevis and Saccharomyces cerevisiae* cells (133). In addition, it has been suggested that p53 binding protein 1 (53 BP1) foci are formed almost immediately following DSB induction (127, 130). In human bronchial epithelial primary (HBEP) cells it has been shown that during the first 30 minutes following exposure to 2 Gy of γ-irradiation there is an abrupt increase in the levels of 53 BP1 foci in chromatin regions marked with γ-H2AX, followed by a gradual decline during the next 6 hours (Andrew McVean; Brunel University – personal communication). Paull et al (2000) have shown that there is a co-localisation between Mre11-Rad50-Nbs1 (MRN) complex, Breast cancer associated protein 1 (Brca 1), Rad 51 and γ-H2AX foci in MCF 7 breast tumour human cells, thereby suggesting that Brca 1 and the MRN complex are involved in the repair process following DSB formation. In addition, based on the fact that the abolishment of γ-H2AX foci appearance by kinase inhibitor wortmannin also resulted in the failure of MRN complex and Brca1 foci formation, it was proved that the formation of the aforementioned foci is downstream of γ-H2AX foci appearance and that the signal for their emergence is γ-H2AX foci formation. More specifically, Brca1 foci were shown to accumulate at the damaged sites hours after insult detection. To this extent, it was also demonstrated that Brca 1 is assembled at γ-H2AX foci considerably earlier than Rad 51 and the MRN complex (127). In human fibroblasts, the recruitment of the MRN complex at DSB sites is believed to occur in the first 30 minutes following exposure to ultrasoft x-ray irradiation, whereas the failure of Rad51 and Mre11 to co-localise has indicated that these two repair proteins are involved in distinct repair pathways (134). It has also been speculated that PI-3K family members such as ATM and DNA-PK play a role in the emergence of γ-H2AX foci, as γ-H2AX foci formation was minimal in a cell line lacking ATM and DNA-PK and in cells where their activity was blocked by wortmannin (127). Stiff et al (2004) have shown that in ATM-deficient DT 40 chicken cells and mouse

embryonic fibroblasts (MEFs), the inactivation of DNA-PK by a specific inhibitor of this PI-3K like kinase results in the abolishment of H2AX phosphorylation and thus γ-H2AX foci formation following γ-irradiation exposure. These authors have also demonstrated that in MEFs, human fibroblasts and DT40 chicken cells, the functions of ATM and DNA-PK are overlapping. In the absence of ATM (ATM$^{-/-}$ cells), DNA-PK is fully capable of phosphorylating H2AX and likewise in the absence of DNA-PK (DNA-PK$^{-/-}$ cells), ATM is able to phosphorylate H2AX (129). RNA interference on the catalytic subunit of DNA-PK has indicated that it is essential for H2AX phosphorylation, as abolition of its function resulted in a considerable decline of the level of H2AX phosphorylation. In addition, in two cell lines that were lacking ATM, increased levels of H2AX phosphorylation were recorded apparently due to DNA-PK induced H2AX phosphorylation. In one of these cell lines, inhibition of ATM and DNA-PK by specific inhibitors, diminished the level of phosphorylated H2AX. It has also been shown that DNA-PK is required for exit from the G_1 / S phase DNA damage checkpoint and progression into mitosis (128). Based on the finding that in ATM-deficient MEFs and human fibroblast cells the kinetics of γ-H2AX foci formation was somewhat delayed, it was suggested that regarding these particular parameters ATM is the primary inducer of phosphorylation. In addition, the observation that in confluent Ataxia Telangiectasia (AT) lymphoblastoid cell lines (LCLs) specifically, but not in AT human fibroblasts that have reached the plateau phase H2AX phosphorylation by ATM failed to take place indicated that under certain growth parameters ATM is the major inducer of γ-H2AX foci formation. While DNA-PK in this study was assessed as incapable of phosphorylating the chromatin associated protein Rad 17, it was found to be able to support the recruitment of 53 BP1 and mediator of DNA damage checkpoint protein 1 (MDC1) DNA damage repair proteins following damage induction, 1 hour after the end of exposure to γ-irradiation (129).

It is well documented that the formation of γ-H2AX foci signals the assembly of 53 BP1, Brca1, Nbs1 proteins and MDC1 mediator protein at the damaged sites and that these repair proteins are able to interact with the conserved SQE repeat that is present on H2AX (127, 135-138). Despite the fact that the presence of H2AX is not absolutely necessary for the initial recruitment of ATM, 53BP1, Brca1 and Nbs1 component of the MRN complex, it is required for the

amplification of the amount of protein assembled, their expansion at more distant chromatin sites surrounding the damaged sites and their maintenance at these sites (126, 130). Evidence for this was provided by immunofluorescence experiments performed by Celeste et al (2003) with H2AX wild type and knockout (H2AX$^{+/+}$ and H2AX$^{-/-}$) immortal MEFs and H2AX-deficient MEFs containing a mutated form of H2AX that abolishes γ-H2AX formation, in which certain amounts of these repair factors corresponding to spots were assembled at DSB sites. However, it was found that although the aforementioned factors are recruited at DSB sites they are unable to form foci in response to ionising irradiation (130). Commenting on 53 BP1, evidence supporting this statement was provided from immunofluorescence detection of 53 BP1 in H2AX$^{+/+}$ and H2AX$^{-/-}$ MEFs. While in H2AX$^{+/+}$ cells 53 BP1 foci that were formed were retained and amplified at damaged sites for 4 hours post-irradiation, the intensity 53 BP1 spots that were observed in H2AX$^{-/-}$ cells was decreased during the time period of 30 – 60 minutes after the end of irradiation. Moreover, regarding ATM and Nbs1, experiments in which the phosphorylation of H2AX was abrogated by mutation of H2AX phosphorylation site at Ser 139 residue and ATM gene was doubly deleted supported this notion, as these defects did not interfere with the ability of initial amounts of Nbs1 (and thus the MRN complex) to be assembled at the damaged sites. It was therefore concluded that following insult formation PI-3K like family members such as ATM, DNA-PK and ATM and Rad-3 related (ATR) sense the damage and are immediately assembled at the damaged sites. Following their assembly, they signal γ-H2AX formation over large chromatin regions flanking DSBs (126, 130). These findings have led to the speculation that γ-H2AX dependent chromatin unwinding plays a central role in the recruitment of repair factors at DSB sites and thus facilitates the execution of repair. It achieves that by maintaining a favourable chromatin environment for the orchestrated assembly of repair factors at the secondary DNA damage response stage (139). The initial escort of minimal amounts of 53 BP1, Brca1 and MRN complex proteins at the damaged sites occurs regardless of the H2AX phosphorylation status and the chronic sequence of this event is also independent of γ-H2AX formation. However, the phosphorylation of H2AX is indeed a requirement for the recruitment of greater amounts of DNA damage repair proteins and their expansion and maintenance at surrounding chromatin regions that are distant from the damaged site (130).

Other immunofluorescence experiments on human fibroblast cells have provided evidence supporting the co-localisation of γ-H2AX and phosphorylated ATM foci upon DSB formation. In these experiments normal and DNA repair defective quiescent cells were exposed to γ-irradiation doses as low as 5, 10 and 25 cGy and following a period of 24 hours during which repair was allowed to take place immunofluorescence was performed. The results indicated that regarding repair of DNA damage there were more considerable variations for cells derived from different individuals at low doses (5 and 10 cGy), despite the fact that there were no differences in insult induction. In addition, it should be noted that across individuals there was a lower variation in the ionising radiation-induced foci formation compared to spontaneous foci formation (0.15 foci/cGy at peak timepoints of 10 and 30 minutes compared to a range of 0.2-2.6 foci/cell, respectively). Interestingly, following exposure of cells to 25 cGy of γ-irradiation, repair was shown to be most effective in cells where focus formation had been assessed as slower (131).

Evidence supporting the notion that Nbs1 directly interacts with phosphorylated H2AX has been provided by Kobayashi et al (2002), who have shown that the presence of a combination of forkhead associated (FHA) domain on the N-terminal of Nbs 1 and Brca 1 C-terminal domains (BRCT; FHA/BRCT domains) is absolutely essential for this association, which is not dependent on the other two components of the MRN complex Mre11 and Rad50 or Brca 1. Immunoprecipitation experiments proved that in cells where the binding site of γ-H2AX had been occupied by a specific antibody against H2AX and in AT cells where phosphorylation of H2AX could not be achieved, the aforementioned interaction was abolished. These findings indicated that Nbs1 acts downstream of γ-H2AX formed after insult detection (138). Furthermore, research has revealed that following DSB formation the recruitment of the MRN complex at DSB sites is mediated by MDC1 nuclear protein (135, 137, 140, 141). The latter has been shown to achieve that through its interaction with γ-H2AX (132). More specifically, the presence of a FHA domain on the N-terminal domain of NBS1 is critical for the interaction between MDC1 and MRN complex and the recruitment and maintenance of the MRN complex at chromatin areas where γ-H2AX foci have been formed (135, 140, 141). According to Spycher et al (2008), the presence of tandem acidic

sequence SDT motifs on a region of MDC1 is critical for the recruitment of the MRN complex at damaged nuclear sites, as this motif is phosphorylated by casein kinase 2 (CK2). In light of these results, the authors proposed a model which explains the cellular response to DSB formation. According to this model, DSB formation in the genome is the signal for the initial assembly of a small proportion of the MRN complex at DSB sites, where it processes and binds to broken ends in order to propel ATM signalling activation. Following the activation of ATM, it phosphorylates H2AX. The resulting γ-H2AX foci formation provides the signal for the complexing of MDC1 and the remainder of MRN component that is associated with γ-H2AX (132). In this way, the fraction of MRN complex recruited at chromatin regions surrounding the damaged sites is increased (141). The authors further hypothesized that the recruitment of MDC1-MRN complex concomitant with the expansion of γ-H2AX foci in large chromatin regions flanking the damaged sites may serve as a positive feedback loop resulting in the phosphorylation of downstream targets, as a consequence of a wider response to DSB formation (132).

The formation of DSBs is not the only signal for γ-H2AX foci formation. Evidence has suggested that in response to replication stress following treatment of human cells with replication inhibitor hydroxyurea (HU) and U.V. light, H2AX is phosphorylated forming foci at stalled forks of replication in S phase checkpoint arrested cells. These foci have been observed to be located at the same nuclear positions as Brca1, 53 BP1 and PCNA foci. The mode in which the response to this replication stress occurs has been proposed to be identical to that following DSB formation. Chromatin relaxation takes place following the sensing of the stress thereby promoting H2AX phosphorylation and the subsequent assembly of DNA damage repair proteins 53 BP1 and Brca 1 to the damaged sites. Apart from ATM, another PI-3K like family kinase that has been reported to induce H2AX phosphorylation in this response is ATR (126, 142).

1.6.4 IMPORTANCE OF CHROMATIN STRUCTURE IN REPAIR

Research performed over the past years has linked post-translational epigenetic alterations in chromatin with chromosomal aberration leading to tumourigenesis (143-145). For instance, in cancerous human lymphocyte cells purified histone H4 analysis revealed that these cells show significant decreases in the levels of single and triple acetyl group addition on Lys16 and Lys 20 residues, respectively. On the other hand, these epigenetic modifications were shown to occur normally in healthy lymphocytes. Further analysis revealed that these abnormal features of the malignant cells were owed to significant decreases in methylation level of DNA repetitive sequences (144). In addition, immunohistochemical experiments in which five histone modifications, namely acetylation on histone H3 residue Lys9 (K9), histone H3 Lys18 (K18), histone H4 Lys12 (K12) and the dimethylation on histone H3 residue Lys4 (K4) and histone H4 residue Arg3 (R3) in cancerous prostate tissues were studied, indicated that predictions associated with malignancy can be made and patients can be separated in different groups according to specific combinations of histone modifications (145). Chromatin configuration has been reported to become more relaxed following DSB formation (139, 146-148). Evidence supporting this argument comes from the fact that after exposure of mammalian cells to X-ray irradiation, DSB-induced γ-H2AX foci were observed to be preferentially present in euchromatic regions of the genome and were absent from nuclear areas that were stained with markers labelling heterochromatin such as HP1α and H3K9Me3 in MCF7 human cells. It was suggested that the closed configuration of heterochromatin is inaccessible to DNA damage repair proteins and epigenetic modifications in its structure are responsible for this phenomenon (146). Furthermore, Falk et al (2007) have demonstrated that following γ-irradiation induced DSB formation in MCF7 and human fibroblast cells chromatin relaxation occurs. This was evident by the elevated levels of H4K5 acetylation and the decreased levels of H3K9 methylation at DSB sites during 15 - 40 minutes after γ-irradiation induction that resulted in the diffusion of the TOPRO-3 and H2B-GFP fluorescent signals at these sites (147).

Evidence has revealed that ATP-induced chromatin rearrangement in conformation plays a role in repair. More specifically, Kruhlak et al (2006) have shown that in ATP-depleted living cells chromatin unfolding was abolished as

judged by the poor extension of H2B-GFP in these areas, compared to wild-type cells. Although the diffusive movements of 53 BP1 and Nbs1 were not affected, these repair factors failed to become optimally assembled at the damaged sites, further implying that chromatin structure at the damaged sites acts as anchorage points for repair factors. In addition, it was suggested that this ATP-dependent chromatin decondensation is owed to proteins that are involved in the sensing of damage, thereby altering chromatin structure upstream of repair factor recruitment (139). Ziv et al (2006) have similarly provided evidence supporting the notion that chromatin becomes decondensed at DSB sites following DNA damage. Immunofluorescence analysis performed by these authors has indicated that this chromatin decondensation is mediated by KRAB-associated protein 1 (KAP-1) phosphorylation by ATM on Ser 824 residue of KAP-1. Following this event, phosphorylated KAP-1 is instantly expanded from the sites of DSBs to the entire chromatin component of the nucleus thereby inducing relaxation of chromatin structure (148).

While phosphorylation of H2AX acts as a mark of damaged chromatin that triggers the initiation of DSB repair, after the end of repair a phosphatase-dependent mechanism exists which ensures that chromatin is unmarked and DSB repair proteins are removed from the DSB sites (149-151). The co-localisation and co-immunoprecipitation between γ-H2AX and the catalytic subunit of protein phosphatase 2 A (PP2A) in immunofluorescence and immunoprecipitation experiments on HeLa, mouse endothelial and K562 cells have proved that following exogenously induced DSB formation, PP2A is responsible for the dephosphorylation of H2AX and thus the elimination of γ-H2AX foci after the end of repair. In addition, it should be noted that RNA interference experiments have supported this argument by showing that the abolition of PP2A expression results in failure of removal of γ-H2AX foci from damaged sites and DNA damage susceptibility (149). Nakada et al (2008) have subsequently proved that PP4 plays a role in the removal of γ-H2AX foci from chromatin in U2OS human osteosarcoma cells exposed to X-ray irradiation. Furthermore, these authors have performed immunofluorescence and immunoprecipitation experiments which have shown that PP4 is the major effector of H2AX dephosphorylation (151).

1.6.5 MECHANISMS OF CHROMOSOMAL ABERRATION FORMATION

Cells damaged in G_0 and G_1 phases of the cell cycle prior to S phase express any resulting aberrations as chromosome-type, while chromatid aberrations occur when damage is induced in G_2 phase of the cell cycle (152). The mechanism of formation of chromosomal and chromatid aberrations has been extensively examined over the years leading to the proposal of the mis-recombination (153, 154) and transcription-based (155) models explaining chromosomal aberration formation and signal model (156) explaining chromatid aberration formation. The exchange (157), breakage-first (342) and contact-first (343) models have been applied to the explanation of both chromosome and chromatid aberrations.

The 'mis-recombination' model predicts that following DSB induction chromosomal exchanges occur between homologous chromosomes, driven by the process of recombination of the damaged DSB end with another DSB that it shares homology with (152-154). Regarding chromatid aberrations, this model suggests that looped damaged chromatin domains associate with each other in the regions where they come in contact [as reviewed in (152)]. On the other hand, the 'transcription-based' model states that during the process of transcription a generated DSB associates with topoisomerase I molecule, thereby forming a complex which then associates and cleaves another topoisomerase I molecule that is present either on the same or on a distinct chromosome. The consequence of this interaction is the formation of chromosomal exchanges (152, 155). According to the chromosome 'exchange model', following chromosomal exchanges that occur by exposure to Carbon-K X-rays the damaged chromosome uses an undamaged chromosome in order to be repaired. This model predicts that SSBs are only produced by the X-rays (152, 157). The 'signal' model, which is a modification of the exchange model for chromatid aberrations within the same chromosome, states that damage occurring in a region of looped chromatin domains results in the generation of a signal that leads to the breakage and illegitimate exchange of the DNA strands at their contact points, possibly due to topoisomerase II-driven deconcatenation. A consequence of this misjoining would be the formation of a Ω-shaped looped chromatin domain caused by their inversion. These Ω-shaped chromatin domains are then sealed in order for the repair process to be completed. Contrary to the exchange model, the signal model

postulates that the erroneous rejoining is not expected to be followed by strand exchange (152, 156).

The 'breakage-first' theory states that broken ends explore areas within the nuclear territory in search for appropriate partners to interact with before producing a translocation (342). According to this model, broken chromatin ends perform significant large-scale migrations within the nuclear space (158). Initial evidence favouring the 'breakage-first' model was obtained from studies with the yeast species *Saccharomyces cerevisiae*. The conclusions of these studies pointed out that the ability of broken mitotic chromosomal ends to explore the nuclear space searching for partners to interact with is unlimited and that in yeast, chromosome territories that confine chromosome movement within a certain nuclear space do not exist. Evidence supporting this argument was provided by the fact that the proportion of broken ends interacting with partners showing homology at the same chromosome was comparable to chromosomal translocations taking place between different proximally positioned chromosomes (159). Additional evidence was provided by time-lapse studies on the same species which revealed that the repair of multiple DSB ends occurs in Rad52 foci that act as repair factories, with chromosomal ends migrating to these repair centres [(160), as reviewed in (125)]. In mammalian cells, the 'breakage-first' translocation theory has also been supported by immunofluorescence experiments in which HeLa cells were exposed to α-particle irradiation. The analysis of the track pattern of γ-H2AX foci in chromosomal regions in which they were present initially revealed that they were characterised by clustered and non-clustered morphologies or a mixture of both and they were therefore separated into distinct categories. In the non-clustered foci there were unoccupied spaces between individual foci along the tracks. Based on the finding that one of the two categories of chromosomal domains containing γ-H2AX contained both clustered and non-clustered foci at 15 minutes following the end of exposure, it was suggested that the γ-H2AX foci marking the DSBs were mobile and that their motion along the tracks accounted for the formation of aggregated and non-aggregated foci (161). In addition, the observation that in the non-aggregated category of foci within chromosome domains linear and non-linear trajectories of foci existed indicated that DSBs are characterised by small motions (161). However, the fact that a proportion of the trajectories in which foci were mobile was devoid of

clustering implied that the motion of broken chromatin fragments is not the sole explanation for clustering and that there must be a means of attachment between the chromosomal domains containing the γ-H2AX foci. The observation that CHO cell nuclei unable to induce either HR or NHEJ repair were characterised by the presence of both aggregated and non-aggregated tracks of foci, suggested that the motion and tethering of DSB ends is either irrelevant or takes place before repair (161). Finally, it should be noted that an updated version of the 'breakage-first' model supports the notion that the migration distance of two DSBs that produce an interchromosomal exchange is limited within 1 μm within the nuclear area (162).

On the other side of the spectrum, according to the 'contact-first' hypothesis following a DSB event the two broken ends can interact only when they are positioned at close proximity at the time of the insult (343). Several lines of evidence are in favour of the NHEJ based repair of DSBs, thereby supporting the chromosomal translocation model. These studies challenge the existence of repair factories in which DSBs are recruited and support the notion that repair proteins are recruited to factories, while only DSBs that are located at a close distance from these factories migrate towards them by constrained movement exclusively after the migration of repair proteins to these factories (70, 147, 158, 163, 164). Savage et al (1996) had initially reviewed findings which had suggested that interactions between DSB ends resulting in complex chromosomal rearrangements involving exchanges occur when these ends are closely associated, being separated by distances of only hundreds of nanometers from each other [reviewed in (165)]. During the process of HR in mammalian cells it was also shown that repair is more efficient for broken DNA fragments that are positioned on the same chromosome (and thus in more proximal locations), compared to DNA ends that are parts of distinct chromosomes [reviewed in (125)]. Experimental evidence for this was provided by studies in mouse embryonic stem cells (166), CHO-K1 and their descendant xrs-6 cells that are defective for DSB repair (167).

Phosphorylated histone H2AX has been implicated in the facilitation of recruitment and action of DNA damage repair proteins to damaged DSB ends by keeping these ends at close proximity after damage induction. In order to achieve that, it modulates higher-order chromatin organisation thereby establishing more favourable chromatin conformations that act as anchors for the broken pieces of

DNA that are to be repaired (168, 169). Regarding the repair of the damage, the significance of this property of γ-H2AX is high as it condenses chromatin and prevents chromosomal exchanges and translocations, which would otherwise take place in case the broken ends were not closely associated with each other (71). Evidence supporting these arguments has been provided after γ-irradiation exposure of H2AX$^{+/-}$ and H2AX$^{-/-}$ MEFs and lymph node T cells, which resulted in an increase of the chromosomal aberrations that were formed, involving exchanges. It was suggested that the failure of H2AX to keep broken chromosomal ends at close proximity was the cause of these chromosomal exchanges that took place during aberrant repair of the damage. A second docking function of γ-H2AX foci is associated with the promotion of assembly of DNA damage repair proteins, as it has been proposed that the presence of such foci at chromatin regions that are located at a distance from the damaged site plays a role in the recognition and anchorage of DNA damage repair proteins (169). It has also been speculated that the scaffolding property of γ-H2AX is crucial for the prevention of chromosomal exchanges between broken ends that have been left unrepaired at specific stages of the cell cycle and could combine at later stages. For instance, DSBs generated in ATM$^{-/-}$ cells in G_1 phase of the cell cycle that have not been repaired due to lack of p53-dependent pathway activation by ATM could then be subsequently repaired in S-phase following the phosphorylation of H2AX by ATR, as long as the broken ends are held together without having been dissociated (71). A separate body of evidence in favour of the 'contact-first' model has been derived from exposure of PBL to α-particle irradiation (70). The repair of the resulting complex chromosome translocations was proposed to take place by the limited movement of DSBs to repair factories at nearby interchromatin compartments that separate CTs within the nucleus (70). Repair was speculated to occur as predicted by the 'mis-recombination' model using an undamaged chromosome as a template (70, 153, 154).

More recently, Soutoglou et al (2007) have provided *in vivo* evidence favouring the 'contact-first' hypothesis as a means of chromosomal translocation formation (170). The notions that broken chromosomal ends migrate within the nucleus searching for appropriate partners to interact with or that they move into factories to be repaired were contradicted. NIH3T3 cells and MEFs deficient for H2AX were stably transfected with a construct containing the 256-copy lac operator

(lac O) repeat and the tetracycline (tet) response element. The binding of the lac repressor-CFP and tet repressor-YFP to the lac O and tet O arrays respectively resulted in the fluorescent labelling and visualisation of the arrays. The induction of DSBs was achieved following the development of glucocorticoid receptor (GR) ligand binding region. Upon activation of the GR by the ligand triamcinolone acetonide, the construct is redistributed from the cytoplasm to the nucleus, thereby resulting in DSB formation. The peak in the fraction of cells containing a DSB was observed as early as 5 minutes after receptor activation and was even further increased at 15 minutes. Following the employment of multicolour fluorescence labelling, the mobility of the broken chromosomal ends was assessed. The finding that the lac repressor-CFP and tet repressor-YFP remained in close proximity (as judged by the close association of CFP and YFP) within 24 hours after GR activation suggested that DSBs were relatively immobile within the damaged nuclei. Limited diffusive movements were recorded only at the local level. Further RNA interference experiments unveiled that in cells deficient for H2AX, NBS1, MRE11, RAD50 and SMC1, the positional proximity between the DSBs is retained up to 24 hours after DSB formation and is only lost in cells deficient for Ku80. It should also be mentioned that in Ku80 deficient cells the local diffusion rates of the damaged ends were increased. These results indicated that while H2AX, Nbs1, Mre11 and Rad50 are not involved in the maintenance of local positional proximity between the damaged ends, Ku80 is (170). Ku is a heterodimeric complex that consists of two 70 kilo Dalton (kDa) and 80 kDa subunits termed as Ku70 and Ku80, respectively. That Ku associates with DNA and is involved in the DNA damage repair response has been demonstrated by the fact that it is able to bind to blunt and sticky dsDNA ends and DSB ends that are generated following ionising irradiation treatment of cells. The way in which Ku binds to DNA has been reported to resemble the encircling of a doughnut shaped ring on a string. The C-terminal domain of Ku80 has been reported to tightly interact with the catalytic subunit of DNA-PK and by doing so it plays a role in NHEJ repair of DNA damage in mammalian cells [as reviewed in (171)]. Evidence for the role of Ku80 in NHEJ has also been provided by the fact that the Ku80 deficient xrs-2 (CHO-K1 descendant) cells are unable to repair damaged DNA via this end-joining route (167). The performance of FISH by Soutoglou et al (2007) suggested that 18% of the signals were indicative of a translocation event. The most frequent chromosomal exchange event observed was

between the array containing dicentric chromosome 3 and t (8:17) chromosome that had been observed to be positioned at close distances within the interphase nuclei of cells. Based on these findings, the authors supported the predictions of the 'contact-first theory' which suggests that in order for a translocation to take place the broken ends must be closely associated at the time of breakage (170).

Further evidence supporting the 'contact-first' model had been previously provided by Nikiforova et al (2000), who revealed that the RET/PTC1 gene rearrangement and the resulting chromosome 10 inversion that is responsible for the emergence of papillary thyroid cancer (PTC) is due to the random recombination between RET and H4 genes. Two-colour FISH followed by 3-D microscopic observations in human thyroid cells derived from four individuals suggested that despite the fact that these two genes are separated on the linear map of chromosome 10 by a distance of 30 Mb, their close abutment within the interphase nucleus allowed a rearrangement to occur. Evidence for this was provided by the significantly higher percentage of proximally positioned RET and H4 gene loci compared to the proximity between RET and another gene locus (D10S539). The subsequent finding that the distances between RET and H4 gene loci do not conform to the Rayleigh distribution model in contrast with the distances between RET and D10S539 loci, confirmed the notion that the RET and H4 genes are positioned on chromosomes present at close distances within the interphase nucleus (172). It has been shown that following ultrasoft x-ray exposure of human fibroblasts DSB formation results in local repair within a limited spatial nuclear region, during which broken chromosomal ends remain immobile and DNA damage repair proteins are assembled at the damaged sites. The co-localisation between DSB sites labelled with BrdU and hMre11 foci during the subsequent 30 minutes after the end of exposure revealed that the human Mre11-Rad50 complex is escorted at the damaged sites, excluding the possibility that the DSB ends reach the repair proteins. Additional evidence supporting this statement was provided by the fact that in DNA damage repair defective cells, where foci are maintained for long time periods, hMre11-BrdU staining was retained for 5 hours after exposure (134). Chromatin motion characteristics have been examined in living MEF cells using real-time fluorescence microscopy to track the photoactivatable version of H2B-GFP. The results have indicated that following microirradiation with U.V. light and γ-irradiation on the

microscope stage, the chromatin movements are diffusive and confined within small local intranuclear areas and have excluded the possibility that DSB ends migrate to repair factories by performing pre-determined directional movements. Apparently, the enlargement of foci following DSB formation was owed to amplification of the response to damage signalled by the expansion of γ-H2AX foci marks on chromatin and could not be attributed to aggregation between the resulting foci caused by their movement. While the γ-H2AX marked chromatin regions at the damaged nuclear areas were more decondensed, it was speculated that the borders of repair are determined by the presence of more compact chromatin regions flanking that unfolded chromatin component of the nucleus (139). Branco and Pombo (2006) have suggested that the degree of chromatin fibre intermingling between neighbouring CTs is a predictor of the possibility that two broken DSB ends will be involved in a translocation or an exchange event. What becomes apparent following this proposal is that associating chromatin fibres from two adjacent CTs are more likely to produce a chromosomal translocation upon damage induction, compared to chromatin fibres from two distant CTs (26). Finally, a recent line of evidence in favour of the 'contact-first' model has been derived from the work of Falk et al (2007), who employed fluorescent labelling against chromatin and 53 BP1 repair protein in MCF7 and human fibroblast cells (147). The insignificant mobility and close association of 53BP1-RFP foci in relaxed chromatin regions neighbouring condensed chromatin areas provided evidence supporting the view that following damage occurrence, DSB ends are relatively immobile and that their repair takes place in nuclear areas proximal to their generation (147).

1.7 VISUALISATION OF CHROMATIN IN LIVING CELLS USING TECHNIQUES THAT EMPLOY FLUORESCENCE MICROSCOPY

In fixed cells, CTs can be visualised through the employment of fluorescence *in situ* hybridisation (FISH). It has been reported that FISH is well suited for the visualisation of the arrangement of specific chromosomal domains and gene loci within interphase nuclei (173). In addition, by using 3-D FISH the distribution of CTs within the nucleus and the positional properties of chromatin regions such as the ~ 1 Mb chromatin domains and centromeric chromatin regions within CTs are not perturbed and thus can be studied in detail at the light microscopic level (39, 174). Moreover, other nuclear constituents such as splicing apparatus components are only slightly affected (38, 39, 174). However, FISH does not provide clear evidence associated with the degree of subcompartment formation, intranuclear distribution and morphological characteristics such as shape, size and surface structure of CTs. In addition, since FISH is a chromatin visualisation procedure that is liable to the generation of artefacts, the extent of chromatin folding and decondensation in fixed cells cannot be efficiently assessed (28). The permeabilisation and fixation of cells, as well as the denaturation of DNA are essential steps of the FISH procedure and other *in situ* hybridisation methods that can result in the loss of the preservation of the ultrastructural details of chromatin (28, 173-175). The performance of FISH on human amniocyte cells has pointed out that the DNA denaturation step in particular results in the artificial expansion of the DAPI signal and has the most catastrophic events on the preservation of chromatin structural characteristics (175). Commonly, FISH studies include the fixation of cells and tissues either with paraformaldehyde derivatives or 3:1methanol:acetic acid (3:1 M:AA) that interfere with chromatin structure preservation (19, 61, 176-178). It has been demonstrated that fixation of mouse liver nuclei with 3:1 M:AA followed by thermal denaturation results in the dissociation of the two strands of DNA and 40 % loss of genetic material (179).

The imaging of cells *in vivo* through the fluorescent labelling of chromatin structures is a crucial step forward for the comprehension of the alteration in the intranuclear distribution of chromatin structures during various cell cycle stages and cell differentiation (39, 180). By using fluorescence microscopy, it has been shown

that the chromosomes of *Drosophila* cells are more elastic than the chromosomes of vertebrate cells, further suggesting that the distinct mechanical properties of chromosomes from cells of different organisms regulate their compaction properties and thus the cell cycle progression characteristics (181). In living cells, the labelling of chromosomes (180, 182) and histones (178) has been achieved by using Hoechst 33342 dye (183, 184) and fluorescent proteins of various colours (180). It should be mentioned however, that the major disadvantage of living cell observations in comparison to 3-D FISH is that thus far the technology has been limited to a small number of cell types (39).

1.7.1 GENERAL DNA STAIN - THE HOECHST DYE

The dye Hoechst 33342 is used to fluorescently tag chromosomes by specifically binding to A-T rich DNA sequences in mammalian cells. Taking into consideration the fact that the wavelengths that excite Hoechst 33342 are within the U.V.-wavelength spectrum (350 nm), care must be taken in order to avoid the phototoxic effects that are associated with this dye (176). In general terms, phototoxicity is represented by the excessive illumination of cells and the associated generation of free-radicals which cause cell cycle arrest at the G_2 phase of cell cycle in synchronised CHO and human fibroblast cells (185), defects in cell movement, cell structure damage and in certain occasions, apoptotic cell death. Phototoxicity is known to negatively affect the structure of chromatin by promoting the condensation of mitotic chromosomes. It has also been shown to prevent DNA replication from taking place (176, 177). Similarly, DNA replication is disrupted and DNA mutations emerge as a consequence of fluorescent tagging through the introduction of dihydroethidium and other agents that intercalate DNA structures within cells (186). In cases where low levels of Hoechst dye and illumination are used, Hoechst can be successfully applied, whereas in high-resolution analyses where high illumination levels are employed its use should be avoided and fluorescent proteins (FPs) should be used instead (176). However, in studies where a low level of excitation light is employed, only faint fluorescence signals can be obtained. Taking into consideration the fact that weak fluorescence signals can lead to unreliable and illusionary observations, great care has to be taken in the analysis of the methods that are based on the localisation of these signals, in order to avoid misinterpretation caused either by photon shot noise, possible optical merging or mistracking of targets (57) .

1.7.2 FUSION PROTEINS

1.7.2.1 Overview of different types of FPs

Twenty seven GFP-like proteins have been isolated up to date (187). The isolation of green fluorescent protein (GFP) from the jellyfish *Aequorea victoria* was achieved in 1962 by Shimomura et al (188, 189). In the following years, yellow, green, orange-red and purple-cyan GFP-like proteins have been isolated from other bioluminescent and non-bioluminescent Anthozoan species such as *Condylactis gigantea*, *Montastraea cavernosa, Heteractis crispa, Scolumia cubensis, Ricordea florida, Anemonia majano, Discosoma, Zoanthus* and *Clavularia* species (187, 190). The emitted colour of these proteins is determined by their different chromophores (187). Although their sequences are relatively different, a common characteristic between them is that they all possess a β-can fold structure that is believed to be of great importance in the emission of fluorescence (180, 190). The yellow fluorescent protein (YFP) and the cyanide fluorescent protein (CFP) are derived from GFP (39). In general terms, YFPs and CFPs are advantageous compared to other FPs in the sense that they do not aggregate within cells and thus they do not dimerize or tetramerize [reviewed in (180)]. However, in general terms the majority of YFPs mature in a long period of time due to the slow oxidisation of their chromophores and their overexpression negatively affects cellular structures and the overall visualisation process (39, 180). Venus and citrine are two YFP variants that mature in a short period of time (191, 192). Venus contains a single mutation which promotes the oxidisation of its chromophore, thereby resulting in its faster maturation (192). Likewise, citrine contains a single mutation that accelerates its maturation and enhances its photostability and expression status within cells compared to other YFPs (191). The fusion between either of these YFPs and a host protein has a positive effect on the folding of the host protein and results in the quick production of an intense fluorescent signal (191, 192).

Red fluorescent proteins (RFPs) that emit fluorescence at red or far-red wavelengths are particularly useful for being incorporated into cells of eukaryotic organisms, as the background fluorescence (autofluorescence) levels of fluorophores within cells other than the incorporated ones are very low at these wavelengths. In fluorescence resonance energy transfer (FRET) and multicolour experiments RFPs

can also be used in conjunction with other FPs that emit fluorescence at lower wavelengths (180). In addition, for multicolour experiments, less common proteins can be labelled with photostable and intensely glowing enhanced GFP (EGFP), whereas histones can be tagged with more weakly fluorescing monomers such as the red-FP 'mCherry' (176). Three well known RFPs are DsRed (193), which is excited at 558 nm and emits fluorescence at 583 nm, mRFP1 (194) which is excited at 584 nm and emitted at 607 nm and HcRed1 which is excited at 588 nm and emitted at 618 nm (180). DsRed provides an intense fluorescence and it is not negatively influenced by discrepancies in the pH level, photobleaching or the presence of denaturation agents. The inability of this protein to maintain a monomeric form within cells which is a consequence of its tetramerization and the fact that like YFPs it matures in long time periods, have been major drawbacks that could affect the feasibility of live-cell studies (193). However, an asset of the tetramerization of this protein is that it facilitates its fusion to the host protein (180). On the other hand, the monomeric fluorescent protein mRFP1 is advantageous compared to dsRed in the sense that it matures faster, is more spectrally distinct from other FPs and autofluorescence signals and can be incorporated into the host cell more efficiently (194). HcRed1 has been developed through the mutagenesis of another chromophore and it only provides a low fluorescence level. The FP that is characterised by one of the strongest emissions (611nm) is eqFP611, which has been derived from the sea anemone *Entacmaea quadricolor* (180).

1.7.2.2 Folding of fusion proteins

In order to generate a functional fusion protein that will facilitate the performance of successful live cell imaging, the following parameters should be taken into account. First of all, to ensure that the fluorescence signal is emitted and the functionality and localisation of the host protein are maintained, it is crucial that both the FP and the host protein are folded appropriately within the cell. In this regard, it is important that the FPs have matured (folded) appropriately before being fused to the host protein. The fusion of immature FPs to the host protein results in the production of a weak fluorescence signal and disrupts the structure and normal functioning of the host cell. The linker region that connects the FP to the host protein can be specifically manipulated to confer a high flexibility to the fusion protein, resulting in its ideal folding within the cell (180). In addition, it is equally important that the

stability of the insertion of the fusion protein is retained throughout subsequent cell generations. The amounts of FPs that are incorporated into living cells must be appropriate in order to minimize the signal-to-noise (S:N) ratio and avoid the perturbation of the normal functional processes of the cell. Thus, it is crucial that a high quality FP is employed. In addition, as mentioned above, the oligomerisation of a FP and its subsequent fusion to a host protein has been shown to negatively affect the function of the host protein (39, 180). Therefore, in order to prevent this and the resulting augmentation of chromatin structures, monomeric FPs (mFPs) should be preferred for live-cell studies (176, 194, 195). Finally, it should be mentioned that the choice of the terminal domain of the host protein where the FP should be fused is dependent upon the potential necessity to preserve the structural and functional characteristics of the terminal domain(s) of either the FP or the host protein (180).

1.7.3 GENERATION OF STABLE CELL LINES THROUGH FLUORESCENT TAGGING OF HISTONES

In order to study chromosome characteristics in living cells, it is common to generate stable cell lines that express fluorescently labelled histones. Within the mammalian cell nucleus, there are copious numbers of histones that are strongly attached to DNA. This in conjunction with the fact that the normal functioning of cells is not perturbed by the fluorescent tagging of histones, have made histone fluorescent labelling an extensively used approach (174, 176, 178, 182, 196). An intense fluorescent tagging of core histones can be performed at low levels of FP expression (176) .

In living *Drosophila* cells, histones that have been fluorescently tagged with rhodamine have been proved to be useful for the examination of chromosomes (197, 198) . The microinjection of fluorescently tagged histone proteins into living *Drosophila* embryos has provided clues associated with the relationship between cell and mitotic domain position that is irrelevant of cell progeny in these embryos (197). Likewise, chromatin compaction and decompaction characteristics have been assessed using fluorescent labelling of histones in conjunction with time-lapse microscopy in the same species (198). However, their use has not produced satisfactory results in living mammalian cells (178). On the other hand, GFP protein can be fused to histones and the resulting constructs have been proved to be useful

for the examination of specific chromosomal regions in living mammalian cells by fluorescently tagging these regions (174, 196). The H2B-GFP fusion protein is developed through the tagging of the C-terminal domain of H2B with GFP. This chimeric protein has been shown to be successfully incorporated into the nuclei of yeast, hamster, monkey and mouse cells and into the nucleosomes of human cells without having any negative effects on the progression of these cells through the cell cycle. In all of the cell types that have been transfected with H2B-GFP, chromatin and regions surrounding the nucleoli become brightly labelled and therefore they can be examined closely and in depth during interphase. The fact that in living cells, H2B-GFP has only been observed to be present within nuclear regions and it is excluded from cytoplasmic regions has suggested that this fusion protein specifically labels regions where chromatin is present (178). Unlike Hoechst 33342, which is excited with U.V.-light (350 nm), H2B-GFP is excited with blue light (490 nm), which preserves the ultrastructure of the cells (176, 178). In living human HeLa cells, the fusion of histones H2B, H3 and H4 to GFP and the subsequent generation of stably transfected cell lines has facilitated the examination of histone kinetics during interphase and mitosis, without perturbing the cell homeostasis and division (196). Similarly, in human neuroblastoma cells and primary skin fibroblasts the incorporation of H2B-GFP fusion construct within the nuclei of cells has permitted the examination of chromatin characteristics (174). In mammalian HeLa cells, the incorporation of FPs into histones has indicated that alterations in fluorescence brightness are analogous to alterations in chromosome condensation levels. Evidence for that was provided by the analysis of the arrangements of the fluorescence intensities of chromatin regions within selected pixels (178). Double labelling with H2B-GFP and antibodies against centromeres that have permitted the detection of specific centromeric domains combined with DAPI staining of chromosome spreads expressing H2B-GFP, have revealed that the degree of chromatin compaction and decondensation in distinct nuclear regions can be assessed by the integration of H2B-GFP into living cells (178).

Differential photobleaching can be performed in cells that contain histones tagged with two GFP proteins, by photobleaching only one GFP. A similar method involves the tagging of histones with photoactivatable GFP (PAGFP), resulting in the photolabelling of the histones. The advantage of this technique is that it is

characterised by a high S:N ratio. The two techniques mentioned above are used in order to distinguish between two fluorescently labelled regions that are present on the same histones. In addition, another technique that can be used to label distinct and distantly located chromosomal regions, such as telomeres or centromeres and regions of chromatin is the dual colour subchromosomal labelling. By using this approach, different GFP proteins can be used to tag centromeric or telomeric regions and the dye Hoechst 33342 can be used to tag the entire chromatin component of the nucleus [reviewed in (176)].

1.7.4 VISUALISATION OF GFP-LABELLED CHROMATIN REGIONS IN LIVING CELLS

Various microscopic methods can be employed in order to visualise GFP-labelled chromatin segments. These include deconvolution epifluorescence microscopy (FM) confocal laser scanning microscopy (CLSM), wide-field (WF), spinning disk confocal (SDC) and multi-photon (MP) approaches. With regard to the S:N ratio quality, it has been demonstrated that WF microscopy is the approach of choice for specimen of low thickness (< 30 μm), while SDC microscopy is preferred for thicker (30 - 70 μm) samples and MP microscopy for considerably thick specimen (usually tissues) with a depth higher than 500 μm (39, 199). CLSM and FM are the two strategies of choice for the examination of GFP-tagged chromatin regions in living cells. A combination of the aforementioned approaches can also be employed. A major asset of FM is that it can employ a combination of several differently coloured fluorochromes to perform multicolour fluorescent labelling and thus easily distinguish between distinct cellular structures (39). CLSM has the advantage over FM and WF microscopy that it provides the investigator with more unclouded and distinguishable light optical sections, due to its ability to prevent the out of focus fluorescence from being captured by the detector (199). However, the resolution level of both CLSM and FM are poor and therefore these visualisation methods do not allow nuclear structures that have small diameters such as the ~1Mb chromatin domains (~500 nm in diameter) to be detected. In FM the blurring of light optical sections can be reduced by employing deconvolution processes, thereby providing a more satisfying resolution. However, this improved resolution level is still inadequate for the detection of the aforementioned nuclear structures (39). Iterative deconvolution has been shown to be crucial in the optimisation of S:N ratio for

photosensitive samples (200). More specifically, these studies were carried out in living HeLa cells fused to GFP, where the acquisition of many images at short time intervals and weak fluorescence light was required (200). On the other hand, the asset of MP microscopy compared to other methods is that it confers a higher resistance to phototoxicity in cells by not allowing damage induced by the excitation light to be spread over large focal volumes (201). In deconvolution FM microscopy, both the focus and the out of focus fluorescence signals enter the detector and a computer-based processing step is required in order for the out of focus signal to be removed. By contrast, confocal microscopy is advantageous over deconvolution FM microscopy in terms of the efficiency in which the light is abducted by the objective of the microscope [as reviewed in (176, 199)].

Quantitative four dimensional (4-D) imaging of living cells and fluorescence microscopy have shed light into the properties of chromatin over the past few years. Fluorescence and interference microscopy, fluorescence correlation spectroscopy (FCS) and correlative light-electron microscopy (CLEM) are three visualisation strategies that have been employed to directly investigate chromatin distribution and structure within the nuclei of living cells. In CLEM the specimen is studied by using a mixture of improved resolution-electron microscopy (EM) and light microscopy (LM) (202). However, due to its complexity, this approach cannot be easily used (176). Quantitative 4-D imaging can provide useful information associated with the distributional properties of specific chromosomal structures, as it provides the investigator with images from many positions and dimensions. By using cell tracking and auto-focusing, cell motions and focus displacements can be recorded in experiments that last for long periods of time. The measurement of the total volume that contains fluorescently labelled chromatin can be carried out by the determination of the total spatial expansion of the fluorescence signal (176). These measurements have also been performed in Lac operator/Lac repressor-GFP tagged chromatin regions, in the study of large-scale chromatin condensation following transgene array incorporation in mouse erythroleukemia cells (16) and for the *in vivo* imaging of transcription and chromatin structure properties of CHO DG44 cells using the Lac operator/Lac repressor-VP16 acidic activation domain system (203).

Finally, it is worth mentioning that in live-cell imaging experiments, it is important that immersion objective lens with numerical aperture (N.A.) as high as

possible is used, in order to obtain ideal resolution levels. In addition, it is equally important that the detectors are sensitive enough to detect even weak fluorescence signals. This can be achieved by using sensitive charge-coupled device (CCD) cameras. In time-lapse experiments it is crucial that while the cells are on stage the temperature conditions are maintained at a constant level without fluctuations, in order to avoid potential movements of the microscopic stage and lens that would result in the defocusing of the sample under examination [reviewed in (199)].

1.7.5 TIME-LAPSE MICROSCOPY

Over the past few years, the employment of time-lapse microscopy has revolutionised our perception of cell cycle progression and chromosome structure and movements. The history of time-lapse microscopy began before 1965 when cinemicrographic movies of cell movements were released [reviewed in (344)], (345). The development of video enhanced differential interference contrast (VE-DIC) light microscopy enabled the tracking of the motion of microtubule associated motor proteins such as kinesin [as reviewed in (204)]. This bright-field microscopic method is based on the ability of the video camera to convert light intensity signals generated after the acquisition of the image to electric signals that in turn become video signals. Despite the fact that analogue contrast enhancement and background subtraction can increase the quality of the video images, two major setbacks of this method are the poor S:N ratio and the optics of the DIC microscope. In addition, fluorescence imaging cannot be performed by using this approach [as reviewed in (204)].

In order to perform a successful time-lapse experiment, it is crucial that cell viability and proliferation are maintained at maximum levels while the cells are on stage. In order to achieve that, the temperature and humidity conditions on the stage should be ideal (199). Commenting on the temperature control, built-in electronic microscope temperature controllers or similar devices outside the stage can be employed (205). In addition, the bathing medium should be appropriate to ensure the maintenance of cell physiology. It should contain nutrients and amino acids required for cell growth in addition to agents that maintain a stable pH level, such as medium supplemented with 10 – 15 % fetal calf serum (FCS) and HEPES buffer. The presence of pH indicators in the medium should be avoided as they result in

autofluorescence generation. In case no CO_2 supply is provided to the chamber, medium that maintains a stable CO_2 level should be administered (199). The pumping of medium into the chamber is common in time-lapse experiments but it must be checked for CO_2 levels, pre-warmed and carefully administered so that it does not interfere with cell viability (62, 199, 205). Another factor that contributes to successful acquisition is the choice of the chamber bearing the cells. The asset of closed chambers is that they prevent media evaporation and maintain stable temperature levels, but their drawback is that they labour the access of the cells to the investigator. On the other hand, the asset of open chambers is that they permit easy access to the cells.

The development of time-lapse microscopic movies of fluorescently tagged targets has aided in the better understanding of intracellular and chromosomal processes (59, 62, 66, 206-212). Straight et al (1996) employed the lac operon approach in order to study the separation of sister chromatids in living and fixed cells of the budding yeast *S. cerevisiae*, over time (211). In the same prokaryotic species and in *Drosophila*, Marshall et al (1997) performed wide-field deconvolution 3-D time-lapse microscopy in order to examine chromatin dynamics (59). In *Drosophila*, following topoisomerase II microinjection, the same microscopic approach enabled the 3-D tracking of chromatin mobility (59). Furthermore, Buchenau et al (1997) studied chromatin mobility at transcription sites in the same species using time-lapse CLSM, following the microinjection of rhodamine-labelled antibodies into living embryos. Time-lapse experiments involved the examination of 93 D chromosomal locus motion after heat shock at 37 ^{o}C and during recovery from the shock (66). In addition, another prokaryotic organism that has been studied through time-lapse microscopy is the cellular parasite *Toxoplasma gondii*. The motion characteristics and dynamics of this parasite in human fibroblasts have been assessed through the analysis of phase time-lapse videos at slow rates, leading to the conclusion that they are dependent on actin and myosin motor proteins (213).

In living mammalian cells, short-term time-lapse acquisitions have contributed to a better understanding of cellular, chromosomal and protein-associated processes (206-210). Murata-Hori (2002) performed short-term time-lapse experiments by examining the dynamics of Aurora B mitotic protein in living normal rat kidney (NRK) epithelial cells, after the fusion of this protein to GFP. These

experiments lasted for approximately 1 hour, which is the duration of mitosis in most cell types. Useful information associated with the role of microtubules and CDK1 in the dictation of Aurora B distribution during mitosis was obtained from this study (206). Using the same cell type, the role of CDK1 protein in the separation of sister chromatids during anaphase and cytokinesis has been investigated by employing live-cell time-lapse microscopy following microinjection of rhodamine - tubulin fluorescent label into cell nuclei (207). In CHO cells, time-lapse microscopy tracking of α4-GFP fusion protein has provided evidence for α4β1 integrin mediated lamellipodia extensions, after wound induced by the scraping of confluent cells. These expansions were irrelevant of the focal adhesion and focal complex formation of this protein (208). In P_tk_1 vertebrate somatic cells, time-lapse video enhanced (VE) microscopy has shed light into the manner in which kinetochores that have failed to become attached to the mitotic spindle inhibit the progression from metaphase to anaphase, revealing the presence of a checkpoint that controls this progression event. The intranuclear site of this inhibition was identified and information associated with the cleavage furrow was also obtained (209, 210).

Long-term time-lapse experiments require a sophisticated imaging method, in order to ensure cell viability, while at the same time investigating the cellular processes in question (62, 199, 212). Spindle formation during mitosis has been researched using digital time-lapse microscopy (212). Hinchcliffe et al (2005) have managed to monitor this process for ~ 3 days in monkey kidney epithelial BSC-1 cells that had been transfected with a plasmid containing the α-tubulin-GFP fusion construct. The overall imaging method was assessed as successful, as the cells remained viable and kept dividing for numerous cell cycles (212). In living human cells, the employment of a fusion between the centromeric binding protein CENPB and GFP has permitted the examination of centromere mobility. Using time-lapse confocal microscopy, time-lapse series have been obtained during metaphase, anaphase and telophase stages of the mitotic cycle and interphase from one focal plane in each series (62).

Recent advances in time-lapse microscopy have shed additional light into the cellular and chromosomal functions in the uninterrupted state (214-217), in response to abrogation of telomere protecting mechanism (218) and repair in response to exogenously induced damage by exposure to microscope laser beam irradiation

(219) and γ-irradiation (147). The development of single molecule time-lapse atomic force microscopy (AFM) has permitted the examination of chromatin structure with a resolution efficiency of nanometres (215, 216). The method employs silicon nitride cantilevers that detect force and optical changes on the samples. Data are obtained either from dried or liquid samples in the presence of buffers at certain kilo Hertz (kHz) frequencies (217). A major asset of this method is that it is flexible to modifications that avoid glutaraldehyde fixation, which is known to perturb chromatin structure (217). It is worth mentioning that nucleosomal unfolding details have been unveiled by time-lapse AFM, suggesting that this event is independent of ATP-mediated chromatin remodelling (214).

Finally, it should be mentioned that the quality of the software program that analyses the time-lapse sequences plays an important role in the interpretation of the biological features under examination. MacBiophotonics (MBF) Image J is a Java based image analysing program that is well suited in the analysis of various image formats. It contains a wide variety of image filters that produce high-quality background noise subtraction, image segmentation algorithms, plug-ins appropriate for image and z-stack deconvolution and plug-ins specific for the analysis of fluorescently labelled objects (220). The plug-ins of image J are developed by individual users, therefore the program entity represents the coordinative effort of the scientific community (346). There are numerous applications assigned to Image J program. First of all, it can be successfully applied in co-localisation studies enabling the discrimination between antibodies and microinjected BrUTP in transcriptional activity investigations within the nuclei of HDFs (221). Likewise, the analysis of protein-protein communication (222) and the extent of co-localisation between mineralocorticoid and glucocorticoid receptors within the nuclei of rat neuronal cells can be achieved by using this program (223). Despite the fact that image J was developed to perform analysis in two dimensions, the possession of plug-ins such as hyper-volume browser and Volume J enables it to accomplish 3-D and 4-D analysis (224). The suitability of this program in the analysis of time-lapse image sequences (218) in addition to images acquired by AFM and CLSM microscopy, that employ Volume J and Surface J plug-ins (225), has also been demonstrated. Apart from the intensity against time analysis of fluorescent proteins within the nuclei of cells, a number of regions of interest (ROI) can be analysed using MBF Image J ROI

manager, which greatly facilitates the performance of intensity against time analysis (220). Such analysing methods have been used in the examination of Ca^{2+} ion channel characteristics in the terminals of presynaptic nerves (226, 227). Regarding particle analysis, in addition to the determination of their lengths and widths, image J can also track their movements. Finally, more complex automated individual or sequence image analysis and modifications can be carried out by the Macro function of the program (220). More recently, it has been shown that the examination of daily mammalian cell movements is greatly facilitated by a software termed circadian gene express (CGE). This software is based on an algorithm which not only tracks cell movements by recording their trajectories, but also provides information about fluorescent protein expression levels. This was demonstrated by the transfection of confluent NIH3T3 mouse fibroblasts with a fluorescently tagged circadian reporter protein (228).

1.7.6 MICROINJECTION OF FLUOROCHROME-LABELLED PROTEINS AND ANTIBODIES

The microinjection of fluorochrome-labelled proteins and antibodies into living cells is a technique that has produced desirable results in yeast, *Drosophila* and mammals. (29, 49, 59, 197). Specific chromosomal sites or artificially incorporated chromosomal subregions can be visualised by 3-D time-resolved microscopy and quantitative analyses can be performed following the incorporation of fluorescently tagged antibodies or proteins into cells *in vivo*, without disrupting the normal functional or structural properties of the cell (29, 57, 59, 197, 229). More specifically, Minden et al (1989) fulfilled the assessment of the link between mitotic domain distribution and cell position in syncytial *Drosophila* embryos. The results of this study revealed that the origin of cell progenitors did not play a role in this specific positional relationship (197). In a subsequent study of living cells from *Drosophila* embryos, the microinjection of rhodamine labelled enzyme topoisomerase II during interphase resulted in the characterisation of specific chromosomal regions. This was achieved via the tracking of fluorescently tagged enzymes by time-lapse microscopy and unveiled a link between the distribution of the enzymes, chromosomal compaction and segregation (229). In addition, this approach has been used in conjunction with 3-D SPT analysis of the motion of chromatin within living cell nuclei of both *Saccharomyces cerevisiae* and

Drosophila embryos, in order to label the chromosomes that are contained within these nuclei. The results have revealed that the chromatin component in the nuclei of these cells exhibits a confined random walk diffusive motion (59). Buchenau et al (1993) studied the dynamics of chromatin motion and identified selective large-scale chromatin movements on the 93 D chromosome locus, following the microinjection of fluorescently tagged antibodies against protein Hrb57A into *Drosphila* embryos (66). Furthermore, studies have revealed that the microinjection of nuclei of human neuroblastoma, HDF and HeLa cells with the fluorescently tagged thymidine analogue Cy3-AP3-dUTP results in the production of fluorescence within the nuclei of these cells, enabling in this way the examination of replication foci (28, 57). Although the microinjection of fluorescently tagged proteins or antibodies into living cells is a useful approach for the investigation of specific chromosomal sites, the main drawback of this method is that it is not suitable for the detection of entire chromosomal regions (29).

1.7.7 INCORPORATION OF FLUOROCHROME-LABELLED NUCLEOTIDES DURING S PHASE

The introduction of fluorescently tagged nucleotides such as the thymidine analogues Cy3-AP3-dUTP, fluorescein-12-dUTP, Cy5-dUTP and BODIPY-TR-dUTP into living cells and the *in vivo* pulse-labelling of cells with the halogenated thymidine analogues BrdU, IdU, CldU and FdU are approaches that can be used to directly label an organism's DNA content (22, 28, 29, 36, 39, 50, 51, 230, 231). The cells are labelled with the fluorochrome labelled nucleotides during S phase and allowed to proceed through subsequent stages of the cell cycle. As soon as semiconservative replication has been completed, two tagged sister chromatids are obtained from each replicated chromosome. At the second mitosis following the labelling event, one of the two sister chromatids of each chromosome becomes labelled, whereas the other one remains unlabelled (28, 29, 230). Evidence supporting this finding was initially provided by Latt (1973), following the pulse labelling of peripheral human leukocytes with BrdU (230). After 5 to 10 subsequent cell cycles, the random segregation of sister chromatids that occurs during mitosis results in the appearance of living cells that possess fluorescently tagged CTs or entire chromosomes that can subsequently be detected (22). The subsequent examination of fixed and living cells has unveiled that the fluorescently tagged CTs are constituted from subchromosomal

foci 400 – 800 nm in diameter, typical of replication labelled territories in S phase (28, 29). The advantage of this method is that it allows the visualisation of entire chromosomal regions. Its disadvantage, however, is that it cannot be employed for the visualisation of specific and single chromosomal sites. In addition, another drawback of this approach is that its use results in the generation of unstable cell lines (29).

The glass bead method has been reported to load fluorescently tagged nucleotides and other large macromolecules into the nuclei of living mammalian cells (50, 231). This technique, which was originally developed by McNeil et al (1987) can be adapted for many different cell types and is characterised by a higher cell yield and a lower number of dead cells, compared to other approaches (231). Application of the glass beads results in the transient permeabilisation of the cellular plasma membrane that in turn allows the introduction of fluorescently tagged thymidine analogues such as fluorescein-12-dUTP, Cy5-dUTP, BODIPY-TR-dUTP and fluorescently tagged dextran molecules into the cell nucleus during S phase [(50, 231); figure 1.6]. Briefly, the coverslips are initially placed into petri dishes containing the culture medium and the cells are seeded onto the coverslips. The next step is to rinse the cells and sprinkle glass beads of different sizes onto the cells. Afterwards, cells are rinsed once again and the coverslips are placed back into the petri dishes, which are rocked in order for the glass beads to be evenly allocated over the surface of the coverslips. In order to incorporate the fluorescently labelled thymidine analogue into the nuclei of cells, a solution that contains the fluorescently tagged thymidine analogue replaces the normal culture medium. In this way, fluorescently labelled chromosomal regions become available during mitosis based on the aforementioned principle (231).
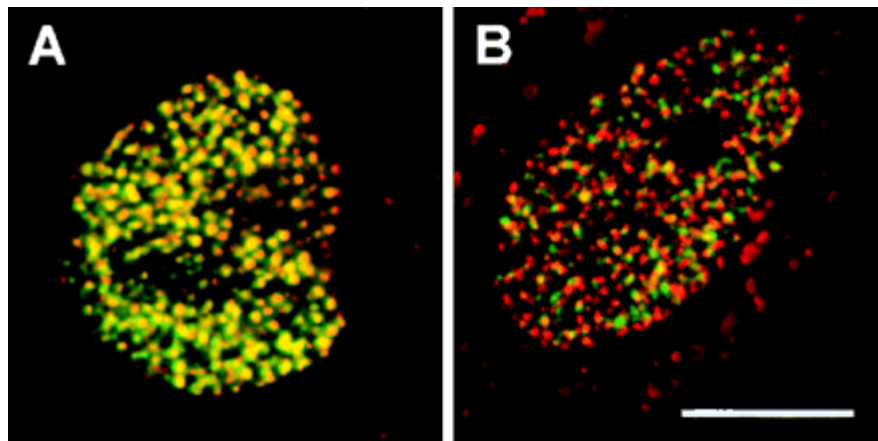
Figure 1.6: *In vivo* **fluorescent labelling of DNA regions. (A) The fluorescent tags that were delivered into the cells were BODIPY-TR-dUTP (represented by red colour) and fluorescein-12-dUTP (represented by green colour). The yellow colour in labelled nuclear sites is the consequence of the overlapping of the two tags that were incorporated into the cells simultaneously. (B) The two tags were introduced into the cells at different time points. The colours of the two labels can be distinguished from each other because the labels occupy distinct nuclear positions.**

(50. Manders EM, Kimura H, Cook PR, J Cell Biol. 1999 Mar 8; 144(5): 813-21).

The determination of the number of fluorescently labelled cells by flow cytofluorometry has demonstrated that more efficient permeabilisation of the plasma membrane and thus more successful dye loading can be performed, by using large 450 μm glass beads. However, care should be taken when loading these large and heavy beads, because they might damage the cells irreversibly (231). Zink et al (1998) demonstrated that the descendants of the cells that were fluorescently tagged with Cy3-AP3-dUTP maintained their morphological properties and were characterised by normal growth and transcriptional activity. No evidence for perturbations in cell viability and cell cycle progression was apparent following the completion of these studies (28). Manders et al (1999) further supported this argument by suggesting that the DNA repair machinery is somehow unable to recognise fluorescently labelled nucleotides that have been introduced into the cells. In this way, the cells are allowed to proceed throughout subsequent stages of the cell cycle without being arrested (50). In terms of the visualisation of CTs that are

present within the nuclei of fluorescently tagged living cells during S phase of the cell cycle, epifluorescence and phase-contrast living cell microscopy have been reported to be employed in these studies (28, 50, 231).

1.7.8 LAC OPERON TAGGING: GENERATION OF LAC OPERATOR-GFP TAGGED CHROMOSOMES

For more than 20 years, experimental evidence has unveiled that the lac repressor-lac operator system that is known to repress transcription in *Escherischia coli* bacterial cells, is also functional in mammalian cells (232, 233). Initially, the adaptability of the lac operon system for research purposes was promoted from the fact that lac repressor had been found to bind to nucleosomal operator sequences with high affinity (234). Subsequent experiments revealed that in living mammalian cells the binding of lac repressor to lac operator induces pSVlacO plasmid SV40 promoter dependent transcriptional inhibition (232) and that the expression of another transgene termed MSV-CAT can be switched off following this binding in mouse cells (233).

Single and specific chromosomal loci and transgenes can be examined in living cells by employing the lac repressor-EGFP/lac operator or collectively called lac operon system (39, 173, 235). This system is based on protein-DNA interactions which result in the specific binding of lac operator sequences by the lac repressor-GFP fusion proteins that have been introduced into the genome (173, 235). The lac operator repeats (Lac O) are present in a plasmid such as the pSV2-DHFR8.32, which is 15080 bp long (see figure 1.7, top). The expression of the lac operator repeats within nuclei is under the inducible control of the SV40 promoter sequence. The sequences that encode the dihydrofolate reductase (DHFR) locus and the ampicillin resistance (AmpR) gene respectively are also contained within the plasmid. The sequence that corresponds to the DHFR locus is flanked by the 'SV40 ori' and the 'SV40 small T intron' sequences of the promoter region (173). Expression of DHFR is driven by the 'SV40 ori' promoter region (236). The lac repressor (Lac I) and the GFP are contained in another plasmid, such as the p3'SSdimerClonEGFP, which has a total length of 7411 bp (figure 1.7, bottom). The Lac I sequence is fused to another sequence encoding the enhanced GFP (EGFP) (237). The difference of EGFP from GFP is that it contains two point mutations that make it more adaptable to different temperature and culture conditions compared to

GFP (177). Within the Lac I sequence, a nuclear localisation signal (NLS) sequence is also present (237). The fusion of LacI to NLS has been shown to confer greater flexibility to Lac I and more importantly to enhance the accumulation of the LacI-EGFP-NLS fusion protein inside the nuclei of cells (237, 238). Evidence (239) has suggested that the rapid interaction between the repressor and the operator is due to the strong attraction generated from the presence of a positively charged motif on the lac repressor protein and the negatively charged DNA double helix of the operator (239). The presence of NLS peptides within Lac I increases the affinity of the repressor for the operator, because they increase the positive charge of Lac I. In this way, the interaction between Lac I and Lac O becomes even faster (237). Based on the fact that the binding of the wild-type Lac I tetramer to the lac O repeat resulted in the poor stability of the Lac I-NLS fusion construct within CHO cells (177), dimerisation of Lac I was promoted through the truncation of 5 amino acids from its C-terminal domain resulting in the abolition of protein tetramerization (240). Robinett et al (1996) subsequently proved that this dimeric form of Lac I enhances the stability of the Lac I within CHO cells (173). Moreover, the fusion of the Lac I-NLS to the N-terminal domain of GFP was shown to retain the stability of the construct within the cells (177). The F9-1 polyoma promoter region which is also present in the plasmid drives the expression of the Lac I-EGFP construct. In addition, a sequence that encodes the hygromycin resistance (Hyg R) gene and a sequence that encodes the ampicillin resistance (Amp R) gene are contained within the plasmid (237).
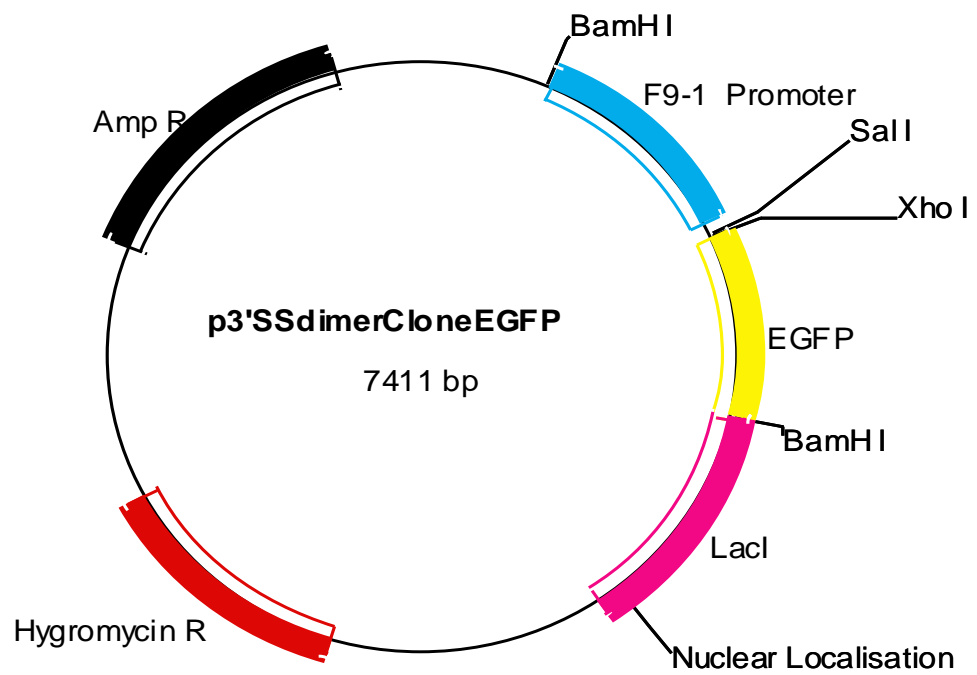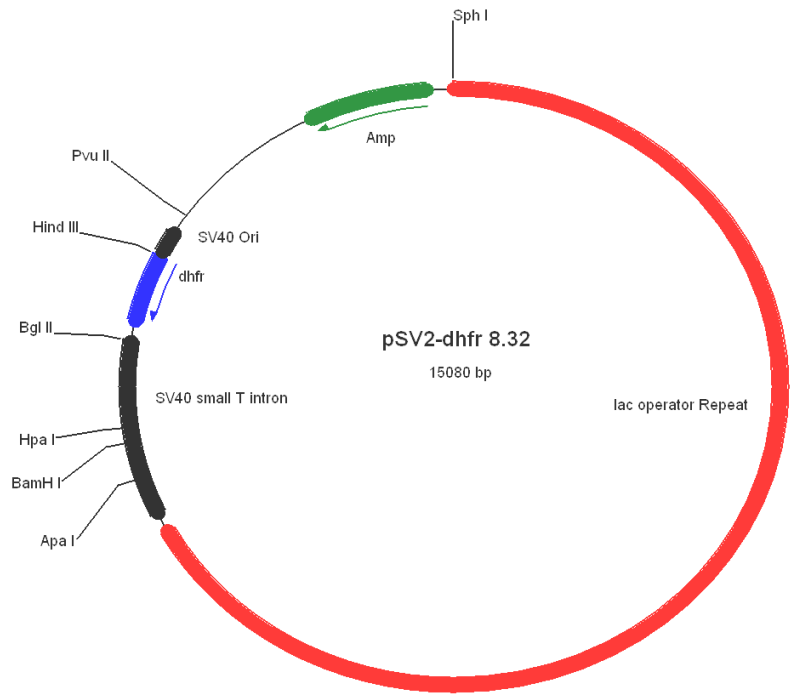
Figure 1.7: Top: pSV2-DHFR8.32 plasmid map. Bottom: p3´SS dimerClonEGFP map

There are two ways in which the lac repressor-GFP/lac operator system can be delivered within cells. One approach includes the establishment of a stable cell line expressing the lac repressor-GFP fusion protein followed by the introduction of the lac operator repeats, whereas a different approach is based on the initial establishment of the lac O repeats within the cells followed by the subsequent introduction of the lac repressor-GFP construct (figure 1.8). By using the first method, the detection of cell clones containing lac operator repeats can be accomplished in a short period of time. In this way, it becomes easier to select for cell clones containing unusual integrations, such as rare transgene insertions that are found at rare nuclear regions and arrangements. The employment of the second method results in the initial creation of control cell lines containing lac operator repeats. These cell lines are subsequently transfected with a plasmid containing the lac repressor and different GFP variants or other FPs or transcriptional activator constructs and as a consequence, the resulting cell lines that contain both lac operator and lac repressor-GFP are characterised by the production of fluorescence (238). In this way, the characteristics of the structure and the hierarchical folding pattern of large chromatin regions linked to specific cell processes can be examined at high resolution in living interphase cells, following the interaction between the lac operator and the lac repressor-GFP fusion protein. This then avoids the fixation of cells and disruption of genome integrity (173, 203, 241). In addition, positional shifts in the distribution of chromatin structures within interphase nuclei can be assessed by tagging those sites with the aid of the lac repressor-GFP/lac operator system and comparing the motion characteristics of these sites with untagged sites, by using 3-D/4 -D FISH (64, 235, 238, 241).

In living mammalian cells, the approach that is employed for the exploration of the organisation of chromatin is primarily based on the generation of a direct 256-copy Lac O repeat within a bacterial host, by using the directional cloning approach and the subsequent stable transfection of a mammalian expression vector such as CHO DG44 cells with a plasmid containing that 256-copy direct repeat. In this way, the repeat becomes incorporated at specific chromosomal sites (figure 1.8).
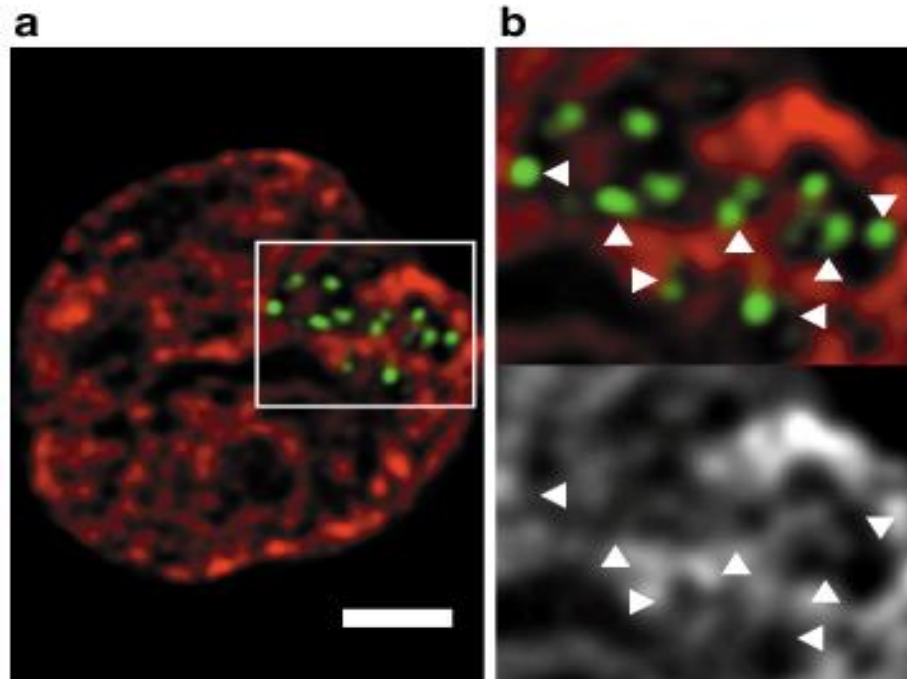
Figure 1.8: Lac operator incorporated within the nucleus of a CHO DG44-/- cell clone. This image shows the specific labelling of DNA-stained chromatin regions with lac repressor-GFP during interphase. DNA is stained in red, whereas the green dots represent GFP tagging. The boxed area that is seen in (a) is enlarged in (b). The arrows in (b) show the sites where the GFP label is present.

(245. S. Dietzel & A. Belmont; Nature Cell Biology, Vol. 3, p. 767-770, 2001)

It has been shown that the stability of Lac O inverted repeats within *E. coli* cells is poor (242). On the other hand, the advantage of direct over inverted repeats is that they are characterised by a lower level of recombination with the sequences of the bacterial host, thereby minimizing instability (177, 238). In addition, the finding that in linear DNA sequences only one Lac I tetramer binds on every 4 – 8 lac O repeats (242) suggested that the Lac O repeats would have to be retained at a certain distance, in order to prevent their instability within cell nuclei (177). In order to perform directional cloning, an octamer 36-bp lac operator repeat represented the starting point (242) and a direct 256-copy lac operator repeat that had a length of 10.1 kb was generated after five directional cloning cycles (238). By using this cloning approach, three restriction enzymes, two of which, named Sal1 and Xho1 possess compatible sticky ends are used, in order for the number of repeats to be doubled after the end of each cloning cycle (173, 177, 238). Gene amplification of

the Lac O repeat in the pSV2-DHFR plasmid (236) can then be used to augment chromosomal areas which flank the gene sequence that acts as a selectable marker, resulting in the generation of hundred to thousand base pair long Lac O repeat containing regions within the chromosomes (173, 177, 243). In order to select the cells in which gene amplification has been successful, the integration of the plasmid containing the DHFR gene into the chromosomes of CHO DG44 cells that are doubly deleted for the DHFR locus (244) is followed by the exposure to increasingly higher concentrations of the DHFR gene repressor methotrexate (MTX) (173, 177, 243). Following amplification, arrays of dots or curly continuous fibres become visible, indicative of the copy number of the plasmid that has been incorporated into the chromosomes (177, 245).

1.7.8.1 Transfection techniques

Following their isolation from the bacterial cells, the plasmids can be incorporated into mammalian cells by transfection. It has been shown that endocytotic or pinocytotic mechanisms contribute to the transfection of certain cell types. In order for efficient endocytosis or pinocytosis of the vectors into the mammalian host cells to be accomplished, the repulsive relationship between the negatively charged backbone of DNA and the equally negatively charged plasma membrane must be repressed (238). It is equally important that transfection is performed before confluency, on exponentially growing cells, because the vector DNA has been shown to enter the cells during mitosis. The success of transfection is strictly correlated with the fraction of cells that are present on the mitotic stage of the cell cycle at the moment of transfection (177, 238).

There are three main ways in which CHO and other mammalian cells can be transfected. These are calcium phosphate transfection, electroporation and lipofectamine transformation (177, 238). Electroporation is generally used in cases where transfected cells that contain a single copy of the lac operator-containing plasmid construct are to be obtained (177, 246). However, the fast and efficient delivery of high-copy number plasmid into CHO cell nuclei has also been reported. The plasmid incorporation within the chromosomes has been shown to be stable (247). During this process, the plasma membrane is temporarily permeabilised by intense electric pulses. In this way, DNA is free to move into the nucleus. In fact, it

has been suggested that this permeabilisation is due to the destabilisation of lipid and protein structures on the plasma membrane, which generates pores on the membrane following electric field pulse induction (248). However, the disadvantage of this method is that in certain occasions it leads to the unstable expression of the repeats inside the plasmid, resulting in unsuccessful cloning. Lipofectamine transformation, or alternatively called lipofection, is based on the creation of macromolecular assemblies between DNA and micelles. The latter are lipids that are positively charged. More specifically, the positive charge of the lipid micelles enables them to interact with the negatively charged membranes of vector DNA. The micelles surround DNA molecules and the resulting micelle-DNA complexes are able to enter the nuclear space. Apart from lipid micelles, lipofection can also exploit positively charged polypeptides and proteins that similarly complex with DNA molecules.

During the calcium phosphate transfection process, an insoluble precipitate between DNA molecules and hydroxyapatite molecules is formed. This precipitate subsequently enters the cells by endocytotic mechanisms (238). By using this approach, numerous copies of the vector can be integrated into the chromosomes (238, 249). However, it has been suggested that despite the fact that high copy plasmid integrations lead to increased fluorescence expression, they have a negative effect on cell division and survival (249). Although the calcium phosphate transfection is a relatively efficient approach, its dependence on multiple factors including the pH and CO_2 levels, temperature (250) and duration of incubation of $CaCl_2$-DNA precipitate particles, amount and form of DNA delivered into the cells, renders this method less successful in comparison with lipofectamine transformation (177, 238, 251). For the majority of mammalian cell types, the incorporation of the p3'SS dimerClonEGFP plasmid that contains the lac repressor fused to EGFP as well as other lac repressor-GFP fusion proteins into the chromosomes can be successfully achieved by using the lipofection approach (177). The fluorescent signal obtained by the expression of the lac repressor-EGFP that is present in the p3'SS dimerClonEGFP plasmid after lipofection, has been reported to be ideal for the detection of Lac O repeats (238). However, it has been suggested that for stable transfection of mammalian cells, the efficiency of the calcium phosphate method is higher compared to other approaches that are better applied in transient transfections (251). In addition, it is widely recognised that regarding the generation of stably

transfected CHO cells specifically, calcium phosphate transfection produces better results than the lipofection approach (173, 238).

Transformation of cells with circular DNA has been shown to be significantly more efficient in the generation of stable transfectants compared to that using linear DNA (251). The relative inefficiency of linearised plasmids in stable transfectant development has been attributed to nuclease dependent cleavage of these plasmids within the cell after endocytosis or before cellular uptake by nucleases that are present within the culture medium. Another speculation that has been put forth is that linear is not as capable as circular DNA in the formation of $CaCl_2$-DNA precipitates (251). Likewise, Strukov et al (2005) have predicted that the conversion of circular DNA to linear and the resulting interference with lac repressor-EGFP transgene expression could be responsible for the existence of clones lacking expression (238).

1.7.8.2 Selection of stable tranfectants

Based on the fact that the p3'SS dimerClonEGFP plasmid contains the Hyg R gene, cells that have been stably transfected with the plasmid can be selected by the addition of the antibiotic hygromycin B into complete F-12 HAM medium, where they are normally cultured. The medium should be replaced with fresh F-12 HAM medium supplemented with hygromycin B at regular time intervals, because hygromycin B has a short half-life period (177). On the other hand, cells that have been stably transfected with the pSV2-DHFR8.32 plasmid can be selected through their culture in medium that lacks the products of the DHFR gene thymidine and hypoxanthine (173, 177, 238). A combination of the aforementioned selection parameters has to be applied for cells that have been transfected with both plasmids.

1.7.8.3 Detection approaches

There are three major ways in which the detection of the 256-copy lac operator repeat can be accomplished. First of all, in fixed cells it can be achieved through the introduction of the purified lac repressor into the cells followed by the employment of immunostaining methods. Second, in living cells the direct 256-copy repeat of the lac operator can be localised indirectly by the incorporation of the lac repressor-NLS fusion protein into the cells followed by their subsequent fixation and visualisation

of the repeat by using immunostaining methods through the employment of electron microscopy. Third, the instant detection of direct Lac O repeat can occur by the integration of lac repressor-GFP-NLS into chromosomes *in vivo* followed by microscopic examination of the inserted construct [(173, 177); figure 1.9].
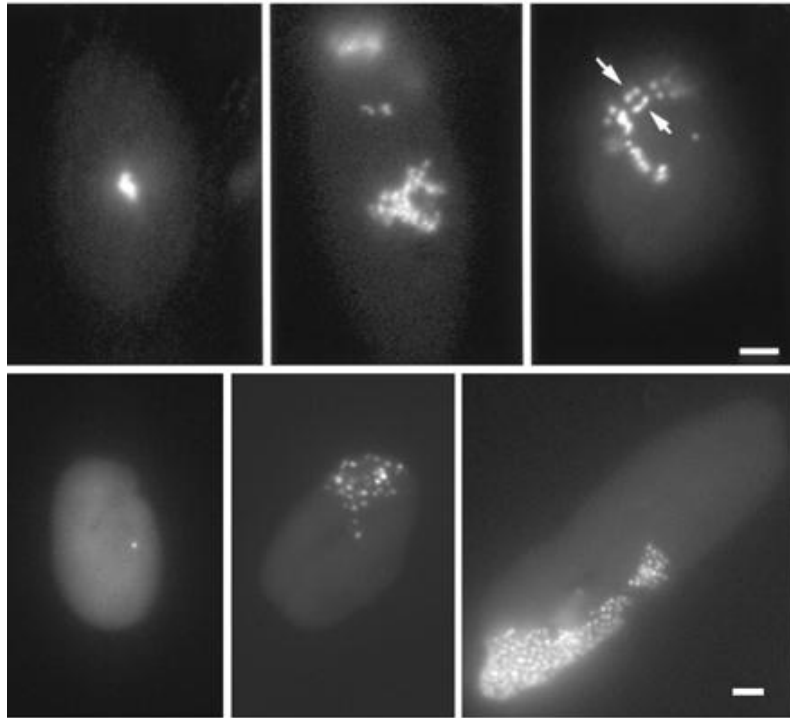
Figure 1.9 Incorporation of lac repressor-GFP into living cells stably transfected with lac operator repeats resulting in the visualisation of the repeats. Top, left: A03 cell containing an augmented chromosomal area. Top, middle: PDC cell containing an augmented chromosomal area that in turn possesses highly folded chromatin fibres. Top, right: Bb cell that possesses expanded fibrillar chromatin structures. The arrows point at presumed sister chromatids. Bottom, left: Single copy integration of the plasmid containing the lac operator repeat into an EP1-4 cell. Bottom, middle: Chromosomal areas that have undergone gene amplification by MTX. Bottom, right: Further amplified chromosomal areas detected at later stages of gene amplification by MTX.

(238. Strukov YG, Belmont AS. Chapter 25, Live Cell Imaging [edited by Robert D. Goldman and David L. Spector] Cold Spring Harbor Laboratory Press, 2005)

Taking into account the fact that both nuclear background fluorescence level and the degree of expression of lac repressor-GFP fusion protein play a role in the efficiency of detection of the lac operator repeats, the level of construct expression should be

intermediate. In this way, all of the lac operator sites are bound by the lac repressor-GFP construct, while maintaining a satisfactory S:N ratio (238).

Robinett et al (1996) attempted to visualise specific chromosomal regions of CHO cells by using the lac repressor-GFP/lac operator labelling system. The staining of the lac repressor was established by using the three different methods that are mentioned above. The imaging process was based on light and electron microscopy. The light microscope was equipped with a CCD camera and deconvolution of images was also performed. Cells that were characterised by high gene amplification efficiency were demonstrated to possess nuclei that in turn contained a high number of homogeneously staining regions (HSRs). The regions that became stained reflected condensed chromatin constituted of packed fibres 0.2-0.3 μm in diameter attached at the periphery of these regions. Consistent with previous studies (10, 183), the results suggested that the compaction ratio of chromatin folding is significantly higher than the 30 nm chromatin fibre, as assessed by the staining of the fibrous chromatin structures. In addition, it was confirmed that the chromonema fibres represent the building blocks of non-random large-scale chromatin architecture (173). The conclusions that were drawn from the examination of HSR morphological characteristics were very similar for all three methods, in which it was demonstrated that the overall distribution of the HSR large-scale chromatin structures is not altered and remains stable. Intense signals that could be recapitulated were obtained by all three methods. The most informative approach was the one that included the direct *in vivo* lac repressor-GFP-NLS fusion protein detection, despite the fact that it was characterised by a signal that was not as intense as the one that was obtained from the other two approaches. In this method, the initial S:N ratio following the acquisition of the images was low, due to the fact that the fluorescence intensity was poor and the background staining of the nuclei was high. However the performance of background subtraction (9) resulted in the dramatic improvement of S:N ratio (173). The fixation and staining of the cells with purified lac repressor had no negative effects on the positioning and morphological characteristics of the amplified chromosomal areas. However, blurry images of the fibrous chromatin structures were obtained as a consequence of the fixation of cells, caused by the decompaction of chromosomes that was in turn a consequence of the DNA denaturation step. On the other hand, by performing direct *in vivo* visualisation of these chromatin

structures through the introduction of lac repressor-GFP-NLS construct into the cells, no such problem was encountered.

Overall, these experimental procedures succeeded in the localisation of single CHO cell chromosomal sites, where numerous copies of the vector DNA that contained the lac operator repeat had been incorporated. The use of lac repressor-GFP-NLS fusion protein allowed the visualisation of a single copy in the stably transfected CHO cell clone EP1-4. The latter was created by transfection with the pSV2-DHFR 8.32 plasmid. Before gene amplification, the optical sectioning of EP1-4 cells containing lac repressor-GFP had revealed that one label spot is present in each one of the EP1-4 nuclei (figure 1.9; bottom, left). After gene amplification, many spots appeared to be present on HSRs (figure 1.9; bottom, middle and bottom, right). These spots corresponded to regions surrounding the sites of the vector integration. Southern blotting and restriction digestion indicated that the insertion of the vector corresponded to one copy. It was therefore proved that single copies of the direct 256-copy lac operator repeat can be detected in CHO and mammalian cells in general (173).

More currently, Chubb et al (2002) have used the approach developed by Robinett et al (1996) in order to study chromatin mobility characteristics in living human cells. Following the binding of lac repressor-EGFP fusion construct on the 128-copy lac O repeat that had been previously used to transfect the cells, detection was achieved using confocal microscopy. The results of this work revealed that chromatin motion is largely confined, especially at areas proximal to the nucleolus and at the nuclear periphery (64).

The lac repressor-GFP/lac operator tagging system is believed to have great future potential for a wide range of applications. The condensation and decondensation properties of chromatin structure during interphase and vital processes of cell function such as replication, transcription, recombination (173, 177) and DNA damage repair can be studied in great depth by using this system. Novel GFP variants and FPs continue to become commercially available and their use could permit the concomitant labelling and detection of many different sequences (177). The simultaneous examination of different chromosomal sites could also be accomplished through the employment of other operator labelling systems that are

based on similar protein-DNA interactions (235). Advances in biochemistry are expected to facilitate the purification of chromatin structures from distinct and specific chromosomal areas and the performance of genetic screening by using the lac repressor-GFP/lac operator system (177, 235). The lac repressor-GFP construct induction of expression by the tetracycline and enhanced UAS-Gal4 promoters(Clontech) has produced promising results associated with the stability of the lac repressor-GFP/lac operator system within mammalian and *Drosophila* cells, respectively (177). In addition, the lac repressor-GFP/lac operator tagging method could be used in conjunction with other *in situ* hybridisation approaches such as 3-D FISH, in order to compare the characteristics of distinct chromatin structures and develop an overall better understanding of the *in vivo* chromatin properties through the employment of EM, LM and FM approaches (173, 235).

The recent discovery of new nanoscopy methods is believed to contribute to the improvement of the resolution and magnification level of FM. One of these methods is point spread function engineering (PSFE) (252), which includes methods such as spatially modulated illumination (SMI) (253). By using SMI and PSFE, the axial resolution of the sample under investigation has been greatly increased [as reviewed in (39)]. Following excitation, the visualisation of focal spots has suggested that PSFE allows the performance of far-field microscopy with axial resolution between objects at 33 nm (252). In SMI, the axial nanometre distances between fluorescently labelled objects can be precisely determined, with a standard deviation average of ~2 nm. With regard to lateral measurements precision is lower, as the standard deviation has been found to be ~5 nm. It has been suggested that these deviations are the consequence of spatial alterations in fluorescent label intensity, the non-parallel orientation of the wave fronts relative to the object slides and low S:N ratio partly due to the CCD camera (253). An additional approach which involves the performance of epifluorescence and laser scanning microscopy (LSM), has provided satisfactory results associated with the precise determination of the distances between differentially labelled fluorescent gravity centres (254, 255). Dietzel et al (1998) has employed glass spheres that displayed the fluorescent signals of different colours at their cores, in order to determine the 3-D distances between probes in the X chromosome territories of human amniotic fluid cells. The standard error for these measurements corresponded to 70 nm (254). Esa et al (2001)

employed spectral precision distance microscopy (SPDM) combined with mean 3-D distance measurements of Euclides, in order to measure 3-D distances between loci on the heavy chain of the immunoglobulin gene cluster (IgH) in B lymphocytes and other cell types. The resolution quality of confocal laser scanning microscope was optimised by labelling each locus with at least two fluorochromes of different emission wavelengths. By using SPDM, an axial and lateral resolution level of 50 nm was accomplished (255). Hopefully, in future days developments in various light optical detection approaches including interferometric methods, FRET image analysis and the solving of refractive index problems, will result in the acquisition of more clear and informative images of intranuclear structures and chromatin regions under investigation [as reviewed in (39)].

1.8 CONCLUSION AND AIMS OF PROJECT

Overall, in the past few years the fluorescent labelling of chromatin has revolutionised our understanding regarding chromatin structure and function in the unperturbed cell state and following DNA damage induction. The evidence provided in the sections above has highlighted that time-lapse microscopy is capable of enabling the short-term and long-term examination of cell and chromatin characteristics in living cells. The main aim of this study was the accomplishment of the visualisation of single and specific chromatin regions in living CHO and other mammalian cells during interphase, following DNA damage induction by BLM, H_2O_2 and γ-irradiation. In order to achieve this, the lac operon method was employed. CHO cells were stably transfected with both p3'SS dimerClonEGFP and pSV2-DHFR8.32 plasmids, that contained the lac repressor-EGFP construct and the 256-copy lac O repeat, respectively. Following the generation of stable transfectant cells and the characterisation of a number of different clones, the ultimate goal was the determination of the relationship between the behaviour of chromatin and DSB formation within the nuclei of cells through the employment of time-lapse microscopy and immunostaining experiments.

2. MATERIALS AND METHODS

2.1 DNA PREPARATIONS

2.1.1 PRECIPITATION AND RESUSPENSION OF p3'SSdimerClonEGFP AND pSV2-DHFR 8.32 PLASMID DNA SAMPLES

0.25 µg of the p3'SS dimerClonEGFP and pSV2-DHFR8.32 plasmid DNA (figure 1.7), kindly provided by A. Belmont (Department of Cell and Structural Biology, University of Illinois, Urbana-Champaign) were stored in 100% ethanol (EtOH; Hayman) at -20°C. The plasmid DNA samples were precipitated and dissolved in 10 mM Tris buffer (pH 8.0) until required.

2.1.2 DNA PRECIPITATION

In order to bulk up DNA for samples containing <1 µg of DNA, 1 µl of glycogen (Sigma-Aldrich) was initially added to DNA and flick mixed. For all DNA samples, 3M sodium acetate (1/10 of total volume) was added to the eppendorf containing DNA on ice. In order to precipitate the DNA, 2.5 volumes of (-20°C) cold 100% EtOH was added and the sample left at -20 ^{o}C for 1 hour, in preparation for dissolving the DNA.

2.1.3 DISSOLVING DNA

Precipitated DNA was centrifuged at 11300 x g for 30 minutes at 4°C, after which time the supernatant was removed and stored at -20°C based on the fact that it might have contained traces of the pellet. In order to wash away any unwanted salts, 500 µl of RT 70% EtOH was added and the tube vortexed and centrifuged again at 11300 x g for 10 minutes at room temperature (RT). The supernatant was discarded and 500 µl of RT 100% EtOH was added in order for any traces of residual water to be removed. A further centrifugation at 11300 x g for 10 minutes at RT was performed and the supernatant removed. The tube was left on the bench for 15-20 minutes in order for the DNA pellet to air-dry and finally, the pellet was dissolved in 10 mM TE buffer [10 mM Tris-Cl, 1 mM EthylenediamineTetra Acetic Acid Disodium Salt Dihydrate (EDTA), pH 8.0] and the tube stored in the fridge at 4°C. Alternatively, DNA could have been re-suspended in sterile dH$_2$O. In order to calculate the

volumes (µl) in which DNA samples of known concentrations should be dissolved in, the following formula was used: [amount of DNA (µg) / concentration of DNA (µg/µl)] = required volume (µl) of DNA sample.

2.1.4 DETERMINATION OF DNA CONCENTRATION

2.1.4.1 'EPPENDORF BIOPHOTOMETER' SPECTROPHOTOMETER

Double stranded (ds) DNA concentration was determined by spectrophotometry (Eppendorf Bio photometer). Two cuvettes were labelled as "blank" and "sample". 100 µl of distilled water (dH$_2$O) were added to the "blank" cuvette and 90 µl of dH$_2$O were added to the "sample" cuvette. 10 µl of the DNA sample were added to the "sample" cuvette, making up a total volume of 100 µl. The spectrophotometer was blanked, the "sample" cuvette was inserted into the device and the reading was recorded. After having determined the dsDNA concentration, the plasmid was aliquoted into 30 µg fractions and stored at -20 ^{o}C.

2.1.4.2 'ND-1000' SPECTROPHOTOMETER

The ND-1000 spectrophotometer (Nanodrop; version v3.2.1) was used as another means to determine dsDNA concentration. After logging on, the 'ND-1000' and then the 'Nucleic Acid' options were selected on the computer. The reader was cleaned by the addition of 1 µl of dH$_2$O and then wiped with tissue. The lid was closed and the 'OK' icon was clicked. The Nanodrop was blanked with the addition of 1 µl of dH$_2$O. The 'Blank' option was selected and 1 µl of sample DNA was added. After having named the sample, the 'Measure' option was selected and the reading appeared on the screen of the computer. The reader was finally rinsed with dH$_2$O and wiped with tissue.

2.2 BACTERIAL CELL TRANSFORMATIONS

2.2.1 TRANSFORMATION OF DH5α CELLS WITH p3'SSdimerClonEGFP PLASMID

In order to transform DH5α (Invitrogen) bacterial cells with p3'SS dimerClonEGFP plasmid, 50µl of DH5α cell suspension was incubated with either 2.5µl of control DH5α DNA or 1 µl (10 ng) of p3'SS dimerClonEGFP plasmid DNA. After having mixed the contents of the tubes gently, they were immediately placed on ice for 30

minutes, incubated at 42 ^{o}C for 20 seconds and then again placed on ice for 2 minutes. Afterwards, 950 µl of RT SOC medium [20 g of tryptone (Oxoid), 5 g of yeast extract (Fisher BioReagents), 2 ml of 5M NaCl (Acros Organics), 2.5ml of 1M KCl (Fisher Scientific), 10ml of 1M MgCl$_2$ (Sigma-Aldrich), 10ml of 1M MgSO$_4$ (Sigma-Aldrich) and 20ml of 1M glucose (BDH) dissolved in 1L of sterile dH$_2$O] was added to the transfected control and bacterial cells. The cells were subsequently placed on a shaker at 37 ^{o}C for 1 hour. The respective control and p3'SSdimerClonEGFP-transfected cell cultures were then used to inoculate LB agar plates [10 g of tryptone, 5 g of yeast (Fisher BioReagents), 10 g of NaCl and 15 g / L of agar in 1 L of dH$_2$O] containing 100 µg/ml of ampicillin [1 ml of 100 mg/ml ampicillin (Gibco) in 1 L of LB medium] and after spreading the cells over the LB agar, the plates were incubated at 37 ^{o}C overnight. 24 hours later, glycerol stocks were prepared by mixing 800 µl of each bacterial suspension with 200 µl of 80% glycerol (80 ml of glycerol mixed with 20 ml of dH$_2$O; Acros Organics). The glycerol stocks were then immediately stored in the freezer at -80 ^{o}C.

2.2.2 TRANSFORMATION OF Stbl-2 BACTERIAL CELLS WITH pSV2-DHFR 8.32 PLASMID

In order to transform Max Efficiency Stbl-2 (Invitrogen) competent cells with pSV2-DHFR 8.32 plasmid, 100 µl of Stbl-2 bacterial cells was incubated with either 5 µl of control pUC19 plasmid or with 0.47 µl (50 ng) of pSV2-DHFR 8.32 plasmid. Following the gentle mixing of the contents of the tubes, they were immediately placed on ice for 30 minutes and incubated at 42 ^{o}C for 20 seconds, before being placed again on ice for 2 minutes. Afterwards, 900 µl of RT SOC medium was added and the transfected control and bacterial cells were incubated at 30°C for 90 minutes. Inoculations of 1:10 diluted and 1:100 diluted control pUC19-transformed cells, as well as inoculations of pSV2-DHFR 8.32 plasmid- transfected bacterial cells were transferred to LB agar plates containing 100 µg/ml of ampicillin and they were spread over the LB agar. The LB agar plates that contained the control pUC19-transformed cells were incubated at 37°C overnight, whereas the pSV2-DHFR 8.32 plasmid-transfected bacterial cells were incubated at 30 ^{o}C for 72 hours. 24 hours later, glycerol stocks were prepared and stored as described in section 2.2.1 above.

2.3 CELL CULTURING

2.3.1 BACTERIAL CELL CULTURING

2.3.1.1 BULKING THE p3'SS dimerClonEGFP AND pSV2-DHFR 8.32
PLASMIDS IN BACTERIAL CELLS AND PICKING UP COLONIES

5 ml of LB media containing 100 μg/ml of ampicillin were inoculated with small
amounts of p3'SS dimerClonEGFP and pSV2-DHFR8.32 plasmid glycerol stocks,
while the stocks were still frozen. Following the ejection of the tips into their
corresponding universal containers, the DH5α and Stbl-2 inoculated cultures were
incubated on a shaking platform at 220 rpm overnight at 37 ^{o}C and 30 ^{o}C,
respectively. Afterwards, 100 μl of each bacterial culture was used to inoculate each
of two vessels containing 250 ml of LB medium and 100 μg/ml of ampicillin. The
vessels were placed in the incubator shaking at 220 rpm overnight at 37 ^{o}C and 30 ^{o}C
for DH5α and Stbl-2 cells, respectively. After 24 hours on the shaking platform, the
p3'SS dimerClonEGFP and pSV2-DHFR8.32 plasmids were extracted from the
DH5α and Stbl-2 cells respectively, using the NucleoSpin plasmid extraction kit to
perform a Mini prep (QIAGEN - see section 2.4.1.1 below) before extracting the entire
plasmid by performing a Maxi prep as described in section 2.4.1.2 below.

2.3.2 MAMMALIAN CELL CULTURING

2.3.2.1 AGO1522 AND 1 HD HUMAN FIBROBLASTS

AGO1522 (Coriell Cell Repositories) and 1 HD human fibroblast cells [kindly
provided by J.M. Bridger (256)] were cultured in complete media [C.M.; Eagle's
Minimum Essential Medium (EMEM; Sigma-Aldrich) supplemented with 15%
Foetal Bovine Serum (FBS; Lonza), 1 % Penicillin/Streptomycin (P/S; Gibco) and 2
mM Glutamine (Gibco)] at 37 ^{o}C, in 95% air/5% CO_2. The medium was replaced
with fresh C.M. twice a week. Cells were passaged at 90-100% confluency.

2.3.2.2 CHINESE HAMSTER OVARY (CHO) CELLS

Chinese Hamster Ovary (CHO) cells (Invitrogen) were cultured in complete F-12
HAM medium (Gibco) containing L-glutamine and supplemented with 15% FBS
and 1 % Penicillin/Streptomycin (P/S), at the same conditions as described in section
2.3.2.1, above. Medium was replaced with fresh complete F-12 HAM medium twice

a week. Cells were passaged at 90 – 100% confluency as described in section 2.3.3.2 below.

2.3.3 CELL PASSAGING

2.3.3.1 AGO1522 AND 1HD CELLS

Medium was removed, the cell sheet rinsed with versene and cells were passaged by using 10 x trypsin solution (Gibco) diluted 1:10 in versene [Phosphate Buffered Saline (PBS) and EDTA]. Following the addition of trypsin solution into the flask, it was incubated at 37°C in 95% air/5% CO_2 for 2 minutes. Following the detachment of cells from the bottom of the flask, trypsin was inactivated by the addition of double volume of C.M., the cells re-suspended thoroughly and counted as described in section 2.3.4 below. Following centrifugation at 250 x g, the pellet was re-suspended in the desired volume of C.M. and cells reseeded into fresh T75 flasks at the appropriate seeding densities.

2.3.3.2 CHO CELLS

Following the removal of medium, the cell sheet was rinsed with Distilled Phosphate Buffered Saline (DPBS; Gibco) and the cells passaged using 10 x trypsin solution diluted 1:10 in DPBS (Gibco), as described in section 2.3.3.1 above. Trypsin solution was inactivated by the addition of double volume of complete F-12 HAM medium and following centrifugation at 250 x g, the pellet was resuspended in complete F-12 HAM medium and cells reseeded into fresh T75 flasks at the appropriate seeding densities.

2.3.4 CELL COUNTING

The Improved Neubauer haemocytometer (depth: 0.1mm^{2}) was used. 100 μl of cell suspension was added and the number of cells counted in the 16 squares of regions 1, 2, 3 and 4 of both chambers as shown in figure 2.1, using phase contrast microscopy.
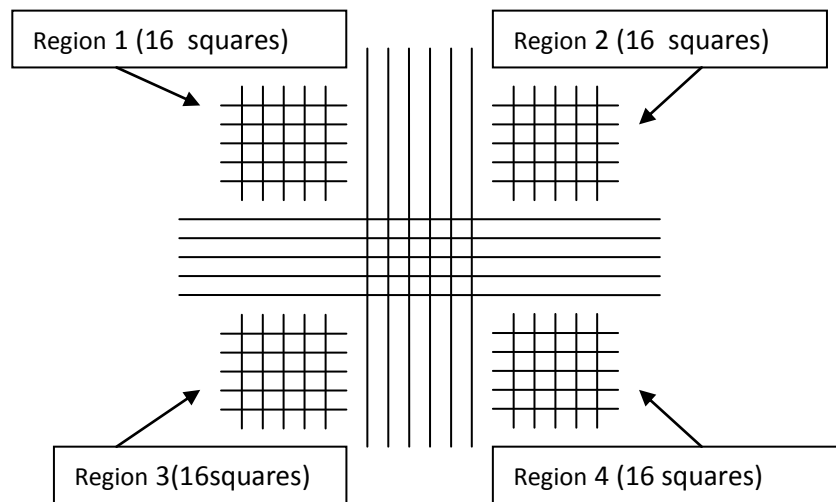
Figure 2.1 Schematic representation of the haemocytometer squares

The total average was calculated by using the following formula: (Total average/1x 10^{-4}) = number of cells per ml, where1x 10^{-4} represents the volume of each square of the haemocytometer. The total number of cells was determined by multiplying the number of cells per ml by the total volume of the cell suspension (number of cells per ml x total volume) = total number of cells.

2.3.5 TRYPAN BLUE EXCLUSION DYE EXPERIMENT

In order to assess the number of dead cells, 0.4 % trypan blue exclusion dye (Gibco) was used. 1:1 volume of trypan blue and cell suspension was added into an eppendorf tube. Following gentle mixing, the eppendorf was incubated at RT for 5 minutes, after which time 10 μl was added onto the haemocytometer and the number of dead cells determined by cell counting as described in section 2.3.4 above.

2.3.6 CRYOPRESERVATION

For long-term storage of cells, cryovials containing 1 ml aliquots of cell suspension supplemented with 5% dimethyl sulfoxide (DMSO; Sigma-Aldrich) were placed in the freezer at −80 ^{o}C overnight and subsequently stored in the liquid nitrogen (LN$_2$) container at -196 ^{o}C. To thaw, cells were taken out of the LN$_2$ container, immediately immersed into the water bath at 37°C and once thawed they were slowly pipetted up and added into a T25 flask that contained pre-warmed medium, in

a drop-wise fashion. Finally, the flask was placed in the incubator at 37°C in 95% air/5% CO_2.

2.4 DNA EXTRACTIONS

2.4.1 BACTERIAL CELLS

2.4.1.1 MINI PREP USING THE QIAGEN NUCLEOSPIN PLASMID EXTRACTION KIT

For each bacterial cell line, a Mini prep was performed in order to check whether a small amount of plasmid could be extracted from the cells. 4 ml of bulked DH5α cells containing the p3'SS dimerClonEGFP plasmid and 4 ml of bulked Stbl-2 cells containing the pSV2-DHFR 8.32 plasmid as described in section 2.3.1.1, were centrifuged at 11,000 x g for 30 seconds. The remaining volume was stored in the freezer at -80 ^{o}C as stock. The supernatant was discarded and the cells lysed by adding 250 µl of lysis buffer A1. The pellet was re-suspended through vigorous vortexing and 250 µl of lysis buffer A2 was added to the tube. The contents of the tube were mixed by inversion several times and the tube left on the bench at RT for 5 minutes. Afterwards, 300 µl of neutralisation buffer A3 was added and the contents of the tube mixed once again by inversion. The lysate was then clarified by centrifugation at 11,000x g for 10 min at RT. For DNA collection, the Nucleospin Plasmid Column was placed in a 2 ml collecting tube (also provided by the kit) and the supernatant was poured into the Nucleospin column. The collecting tube (containing the column), was then centrifuged for 1 min at 11,000 x g, and the flow-through discarded. In order to wash the silica membrane, 500 µl of washing buffer AW (pre-warmed at 50 ^{o}C), was added to the column and the collecting tube centrifuged for 1 minute at 11,000 x g. Afterwards, 600 µl of washing buffer A4 (supplemented with ethanol) was added to the column, which was centrifuged again for 1 min at 11,000 x g and the flow- through discarded. In order to ensure that the silica membrane had been dried properly, the Nucleospin Plasmid Column was further centrifuged for 2 min at 11,000 x g. Finally, for DNA elution, the Nucleospin Plasmid Column was placed in a 1.5 ml eppendorf and 50 µl of buffer AE (10 mM Tris-Cl, pH8.5) added to the column. The eppendorf containing the column was left on the bench at RT for 1 minute and then centrifuged for 1 min at 11,000x g. The 1.5

ml eppendorf containing the eluted DNA was subsequently stored into the freezer at -20 °C.

2.4.1.2 MAXI PREP USING THE QIAfilter MAXI KIT

DH5α and Stbl-2 cells bulked as described in section 2.3.1.1 were centrifuged at 6,000x g for 15 min at 4 °C. In order for the cells to be lysed, the pellet was resuspended in 10 ml of lysis buffer P1 and clumps of cells dissolved by vigorous pipetting. 10 ml of lysis buffer P2 was added to the tube and its contents mixed by vigorous inversion several times. The tube was then incubated at RT for 5 minutes. 10 ml of pre-chilled neutralisation buffer P3 was added to the cell lysate and the contents of the tube mixed immediately and thoroughly by vigorous inversion. The lysate was poured into the QIAfilter Maxi Cartridge and incubated at RT for 10 minutes. Then, the QIAGEN-tip was equilibrated and the plunger inserted carefully into the QIAfilter Maxi Cartridge. The cell lysate was filtered into the QIAGEN-tip and left to enter the resin by gravity flow. The QIAGEN-tip was washed twice with washing Buffer QC in order for any contaminants to be removed and then the plasmid DNA was eluted by the addition of 15 ml of elution buffer QF. DNA was precipitated by adding 10.5 ml of RT isopropyl alcohol to the eluted DNA and the contents of the tube mixed and centrifuged immediately at >15,000 x g for 30 minutes at 4 °C. The supernatant was removed and the DNA pellet washed with 5 ml of 70 % EtOH (RT). Then, the tube was centrifuged once again at >15,000 x g for 10 minutes. The supernatant was discarded and the tube left to air-dry for 10 minutes. Finally, the DNA pellet was dissolved in 5 ml of buffer QF (10mM Tris-Cl, pH8.5) and the tube containing the eluted DNA stored in the fridge at 4 °C.

2.4.2 MAMMALIAN CELLS

2.4.2.1 THE TRIzol METHOD

In order to perform homogenisation, the CHO cell pellet was re-suspended thoroughly in 1 ml of TRIzol reagent (Invitrogen). Afterwards, the contents of the tube were transferred to an eppendorf tube and left on the bench at RT for 5 minutes. Phase separation was carried out by the addition of 200 μl of chloroform (Sigma-Aldrich) and vigorous shaking of the tube by hand for 15 seconds. After incubation at RT for 3 minutes, the sample was centrifuged at 12000x g for 10 minutes at 4 °C.

Following centrifugation, a lower red phenol chloroform phase, an interphase (white) and a transparent upper aqueous phase could be observed. Since RNA remains exclusively in the aqueous phase, the upper phase was transferred to an RNase-free eppendorf tube. In order to precipitate RNA from the upper aqueous phase, 500 μl of isopropyl alcohol (Sigma-Aldrich) was added to the tube and it was left on the bench at RT for 10 minutes. Afterwards, centrifugation was performed at 12000x g for 10 minutes at 4 °C, resulting in the formation of a gel-like pellet at the bottom of the tube. In order to wash the RNA, the supernatant was removed and 1 ml of 75% EtOH [diluted in diethyl pyrocarbonate (DEPC) water (Fisher BioReagents)] added. The tube was then centrifuged at 7500x g for 5 minutes at 4 °C. Following the removal of supernatant, 1 ml of 100% EtOH was added to the tube, which was finally stored in the freezer at −80 °C.

DNA that was present in the interphase and lower red phenol chloroform phase was precipitated by the addition of 300 μl of 100% EtOH. After having mixed its contents by inversion, the tube was incubated at RT for 3 minutes and subsequently centrifuged at 2000x g for 5 minutes at 4 °C. The phenol-ethanol supernatant was removed and the DNA pellet washed by adding 1 ml of 0.1M sodium citrate in 10% EtOH [50 ml; 5 ml of 1 M sodium citrate (Fisher Scientific) mixed with 45 ml of 10% EtOH]. After having incubated the tube at RT for 30 minutes, it was centrifuged at 2000x g for 5 minutes at 4 °C. The supernatant was then removed and 1 ml of 0.1M sodium citrate in 10% EtOH added once again. After having incubated the tube at RT for 30 minutes, it was centrifuged at 2000x g for 5 minutes at 4 °C. The supernatant was removed, 1 ml of 75% EtOH was added and it was subsequently incubated at RT for 20 minutes. Afterwards, centrifugation at 2000x g for 5 minutes at 4 °C took place. The supernatant was removed and the tube left on the bench to air-dry for 15-20 minutes. Finally, DNA was re-dissolved in 50 μl of TE buffer (10 mM Tris-Cl, 1mM EDTA, pH 8.0) and the tube stored in the fridge at 4 °C.

2.4.2.2 PHENOL-CHLOROFORM DNA EXTRACTION

In order to prevent the shearing of DNA, the ends of the pipette tips were cut off. 1 ml of extraction buffer [0.1M EDTA (pH 8.0), 0.5 % (w/v) Sodium Dodecyl Sulfate (SDS) and 10mM Tris-Cl (pH 8.0) dissolved in 500 ml of sterile dH₂O and filter

sterilized] was added to the CHO cell pellet and the contents of the tube re-suspended thoroughly, resulting in the formation of a viscous solution. Afterwards, 400µg/ml of proteinase K solution (Sigma-Aldrich; stock concentration: 10 mg/ml) was added. A further 1 ml of extraction buffer was added and the contents re-suspended once again. The tube was placed in the water bath at 55 ^{o}C for 2 hours. 2 µl of RNase [Boehringer Mannheim; stock concentration: 10 mg/ml (100 mg of RNase dissolved in 10 ml of sterile dH$_2$O and then heated up to 100 ^{o}C for 15 minutes)] was then added and the tube was incubated in the water bath at 37 ^{o}C for 1 hour. During that period of time, equal volumes of phenol solution (Sigma-Aldrich) and chloroform (Sigma-Aldrich) were mixed in the fume cupboard, the tube inverted for a few times and the mixture left at RT for 1 hour to be equilibrated. After RNase incubation, equal volumes of DNA sample and phenol were mixed in each one of four eppendorf tubes, in the fume cupboard. After having mixed the contents of the tubes by gentle inversion, two phases became visible: the lower phase that contained phenol mixed with proteins and the upper aqueous phase that contained the DNA. In order for the two phases to separate completely from each other, the tubes were then centrifuged at 11300 x g for 10 minutes at RT. The upper aqueous phases that contained the DNA were transferred into 4 new eppendorfs slowly, by taking care not to remove any of the phenol that was present in the lower phases. Then, in the fume cupboard equal volumes of the phenol-chloroform mixture were added into each one of the eppendorfs. Following centrifugation at 11000 x g for 10 minutes, the upper aqueous phase from each eppendorf was carefully transferred to a 50 ml tube. DNA was precipitated by adding 2.5 x volumes of 100% EtOH and inversion of the tube several times. Afterwards, the supernatant was removed, an equal volume of 70% EtOH was added and the tube inverted again several times. The supernatant was discarded and the tube containing the DNA pellet left on the bench to air-dry for 15-20 minutes, after which time the pellet was dissolved in 500 µl of sterile dH$_2$O. Finally, the contents of the tube were transferred to a sterile eppendorf tube, which was stored in the fridge at 4 ^{o}C.

2.4.2.3 EXCISION OF THE LAC O BANDS FROM THE GEL

Based on the fact that prolonged exposure of the gel to U.V. light may result in the disruption of the hydrogen bonds that link the complementary bases of the probe to each other, a very quick picture of the gel was taken. After having recorded the

weight of a 1.5 ml eppendorf tube, the gel was placed on the U.V. transilluminator (UVP). Then, by wearing a face shield the bands were excised, by cutting off neat rectangle slices of the gel with the aid of a sterile scalpel blade and by avoiding cutting out any smear of DNA together with the bands. The U.V. transilluminator was turned off and with the aid of sterile forceps the bands were placed into the tubes. Afterwards, the weights of the bands were recorded and the tubes containing the bands were finally placed in the freezer at $-20\,^{\mathrm{o}}$C.

2.4.2.4 EXTRACTION AND PURIFICATION OF DNA FROM THE GEL SLICES

The MinElute Gel Extraction kit (QIAGEN) was used. 3x volume of solubilisation buffer QG was added to 1 x net weight of each gel slice. In order for the gel slices to be dissolved, the eppendorf tubes were placed in the water bath at $50\,^{\mathrm{o}}$C for 10 minutes. During this period of time, the contents of the tubes were mixed every 3 minutes by vortexing, in order to ensure that the agarose traces in the gel slices were dissolved completely. Solubilisation buffer QG contains a pH indicator that turns yellow at $pH \leq 7.5$, therefore a resulting yellow colour indicated that the gel slices had been dissolved completely. 1 x the weight of each gel slice of isopropyl alcohol was added and the contents of the tubes mixed by inversion. Then, the MinElute columns were placed into the 2 ml collection tubes. In order to bind DNA to the columns, the DNA samples were centrifuged at 11000x g for 1 minute at RT. The flow-through was discarded and the columns placed back into the 2 ml collection tubes. Afterwards, 500 μl of solubilisation buffer QG was added to the columns and they were centrifuged again at 11000x g for 1 minute at RT, in order for all traces of agarose to be removed. The flow-through was discarded and the columns placed back into the 2 ml collection tubes. DNA was washed by adding 750 μl of washing buffer PE to the columns and centrifugation at 11000x g for 1 minute at RT. After centrifugation, the flow-through was discarded and the columns centrifuged once again at 11000x g for 1 minute at RT, after which time they were placed into sterile 1.5 ml eppendorf tubes. For elution of DNA, 10 μl of sterile dH_2O was applied to the centre of the membranes that were present in the columns. The tubes containing the columns were then placed on the rack for 1 minute, after which time they were centrifuged at 11000x g for 1 minute at RT. The concentration of DNA was determined by spectrophotometry as described in section 2.1.4.1 and the eluted DNA sample finally stored in the freezer at $-20\,^{\mathrm{o}}$C.

2.5 DETERMINATION OF PLASMID SIZE

2.5.1 RESTRICTION DIGESTION

1 μg each of the p3'SS dimerClonEGFP and pSV2-DHFR 8.32 plasmid DNA samples was digested in each reaction mixture. The p3'SSdimerClonEGFP mixture 1 was prepared for the single digestion of 1 μg of plasmid DNA with restriction enzyme BamH1 (Sigma-Aldrich; stock concentration: 10 units/μl), whereas in reaction mixture 2, a double digestion of 1 μg of plasmid DNA was performed with restriction enzymes BamH1 and Xho1 (Qbiogene; stock concentration: 10 units/μl). The pSV2-DHFR8.32 reaction mixture 1 was prepared for the single digestion of 1μg of plasmid DNA with restriction enzyme Xho 1 (Qbiogene; stock concentration: 10 units/μl), whereas in pSV2-DHFR8.32 reaction mixture 2, a double digestion was performed with restriction enzymes Xho1 and Sal 1 (Qbiogene; stock concentration: 10 units/μl). Since 5 units of each enzyme are required to digest 1 μg of DNA, 0.5 μl of each enzyme was added to the corresponding reaction mixtures. Likewise, since the total volume of each reaction mixture was 20 μl, 2 μl of 10x buffer was added in each reaction mixture. Following the mixing of the contents of the tubes by vortexing, they were incubated in the water bath at 37 $^{\circ}$C for 1 hour and they were subsequently placed on the heater block at 65 $^{\circ}$C for 20 minutes in order for the enzymes to be inactivated. Afterwards, the appropriate amount of 5x glycerol dye (Nalgene) was added to the mixtures, which were vortexed briefly and loaded into the wells of the 1% (w/v) agarose mini gels (prepared as described in section 2.5.2 below). Along with the reaction mixtures that contained the restriction enzyme(s), undigested reaction mixtures were also loaded onto the gels. In addition, a small amount of 1kb Plus DNA ladder marker (Invitrogen; stock concentration: 0.1 μg/μl) was loaded on the gels.

2.5.2 PREPARATION OF AN AGAROSE GEL

The gel rig was set up using the appropriate combs and gel formers and 0.5 – 1.0 g (1 - 2% w/v) of agarose (Fisher Scientific) was dissolved in 50-100 ml of 1xTBE buffer (Fisher Scientific). The agarose was microwaved for 2 minutes and left to cool for a few minutes before adding 2 μl of ethidium bromide (EtBr, 10 mg/ml; Fisher Scientific) and pouring the gel into the gel rig (Fisherbrand). Once set, the comb and

the gel formers were removed, 1xTBE buffer was added and the samples that were digested as described in section 2.5.1 were loaded. Samples were finally electrophoresed for 2 hours at 40 volts.

2.6 CALCIUM PHOSPHATE (Ca$_2$PO$_4$) TRANSFECTION OF CHO CELLS

2.6.1 SINGLE TRANSFECTION WITH p3'SSdimerClonEGFP PLASMID

The desired amount of p3'SSdimerClonEGFP plasmid DNA was diluted as described in section 2.1.3. 24 hours before transfection, CHO cells were passaged and seeded into an appropriate number of flasks at the defined seeding density. The cells were left to settle overnight in the incubator at 37 ^{o}C and the plasmid DNA precipitated as described in section 2.1.2.

4 hours before transfection, the medium was replaced with fresh complete F-12 HAM medium. TR buffer [11.92 g of 50 mM HEPES (Acros Organics), 0.54 g of 1.5 mM Na$_2$HPO$_4$. 12 H$_2$O, 16.36 g of 0.28 M NaCl, 0.37 g of 5 mM KCl, 1.09 g of dextrose (Sigma-Aldrich) dissolved in dH$_2$O and adjusted to varying pH levels] of varying pH levels was initially added to the tubes. Plasmid DNA was dissolved in sterile dH$_2$O and incubated at 4°C for 30 minutes. The CaCl$_2$-DNA and CaCl$_2$- dH$_2$O mixtures were prepared by adding CaCl$_2$ [36.755 g of CaCl$_2$ (Fisher BioReagents) dissolved in 1 L of dH$_2$O and filter-sterilised] and 1/5 the total volume of the tube of plasmid DNA into tube A and CaCl$_2$ and 1/5 the total volume of the tube of dH$_2$O into tube B. Equal volumes of mixtures A and B were then added to tubes containing TR buffer at varying pH levels, in a drop-wise fashion (1drop/second) with continual vortexing (figure 2.2). The Ca$_2$PO$_4$ mixtures were incubated for 30 minutes at RT after which they were added to CHO cells drop-wise, by rotating each flask continuously. The culture flasks were then incubated for 24 hours at 37 ^{o}C. The transfection medium was replaced with complete F-12 HAM medium and the cells were incubated for an additional 24 hours at 37 ^{o}C. In order to select for CHO cells that had been stably transfected with p3'SS dimerClonEGFP plasmid, the medium that was present in Ca$_2$PO$_4$ -DNA containing culture flasks was replaced with complete F-12 HAM selective medium supplemented with the antibiotic hygromycin (200 µg/ml; stock concentration: 50 mg/ml; Invitrogen), whereas the medium that

was present in Ca_2PO_4- dH_2O containing culture flasks was replaced with normal complete F-12 HAM medium.
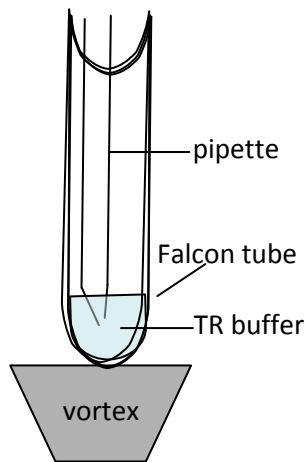
Figure 2.2 Schematic illustration of the calcium phosphate transfection process

2.6.2 DOUBLE TRANSFECTION WITH p3'SSdimerClonEGFP AND pSV2-DHFR 8.32 PLASMIDS

The procedure that was followed was similar to the one described above for single transfection. TR buffer of varying pH levels was initially added to the tubes. The $CaCl_2$- p3'SSdimerClonEGFP DNA and $CaCl_2$- pSV2-DHFR 8.32 DNA mixtures were prepared by adding $CaCl_2$ and 1/5 the total volume of the tube of p3'SSdimerClonEGFP plasmid DNA into tube A and $CaCl_2$ and 1/5 the total volume of the tube of pSV2-DHFR 8.32 DNA into tube B, respectively. The $CaCl_2$- dH_2O mixture was prepared by adding $CaCl_2$ and 1/5 the total volume of the tube of dH_2O to tube C. Equal volumes of mixtures A, B and C were then added to tubes containing TR buffer at varying pH levels, in a drop-wise fashion (1drop/second) with continual vortexing (figure 2.2).The Ca_2PO_4 mixtures were incubated for 30 minutes at RT after which they were added to CHO cells drop-wise, by rotating each flask continuously. The culture flasks were then incubated for 24 hours at 37 ^{o}C.

The transfection medium was replaced with complete F-12 HAM medium and cells were incubated for an additional 24 hours at 37 ^{o}C. In order to select for CHO cells that had been stably and doubly transfected with p3'SSdimerClonEGFP

and pSV2-DHFR 8.32 plasmids, the medium that was present in Ca_2PO_4 - p3'SSdimerClonEGFP and pSV2-DHFR 8.32 DNA containing culture flasks was replaced with ProCHO-AT (Lonza) selective medium supplemented with 1% P/S and the antibiotic hygromycin (200 µg/ml). In order to select for CHO cells that had been stably transfected with either p3'SSdimerClonEGFP or pSV2-DHFR 8.32 plasmids, the medium that was present in the Ca_2PO_4 - p3'SSdimerClonEGFP and Ca_2PO_4 - pSV2-DHFR 8.32 containing culture flasks was replaced with complete F-12 HAM medium supplemented with hygromycin and ProCHO-AT medium supplemented with 1% P/S and hygromycin, respectively. Finally, the medium that was present in control Ca_2PO_4- dH_2O containing culture flasks was replaced with complete F-12 HAM medium.

2.7 CLONING OF STABLE TRANSFECTANTS

2.7.1 FROM DISCRETE COLONIES

CHO cells were transfected with either p3'SSdimerClonEGFP plasmid (section 2.6.1) or both p3'SSdimerClonEGFP and pSV2-DHFR 8.32 plasmids (section 2.6.2), respectively. Colonies of cells that were present at distant regions of flasks where the possibility of cross-contamination was minimal were marked with the aid of a permanent marker. Using a glass pipette, cells were scraped from individual colonies and seeded into individual wells (24-well plate), containing 1 ml of complete F-12 HAM medium. In order to wash the cells off into the well, the pipette tip was inserted into a well of the 24-well plate, pipetting medium from the well several times into the tip. The same procedure was followed for the remaining colonies of cells. The 24-well plate was incubated at 37 ^{o}C for 24 hours before the addition of hygromycin for single transfected cells and ProCHO-AT medium + 1% P/S supplemented with hygromycin for doubly transfected cells. Then, cells were returned in the incubator for varying lengths of time. Expanded discrete colonies were picked up and bulked in 12-well plates, 6-well plates and T25 culture flasks. Fresh media containing hygromycin was added regularly. Each clone was subsequently frozen for long-term storage, once the T25 flask had reached approximately 80 % confluency.

2.7.2 FROM OVERLAPPING COLONIES

Cells were passaged and serially diluted in fresh complete F-12 HAM medium to obtain suspensions of 350, 35 and 3.5 cells/10 ml. A small volume from each cell suspension was then seeded into the 96-well plates. 24 hours later, 200 µg/ml of 1:100 diluted hygromycin in complete F-12 HAM medium (for single transfected cells), or 200 µg/ml of 1:100 diluted hygromycin in fresh ProCHO-AT medium (for doubly transfected cells) was added and the cells were subsequently incubated at 37 ^{o}C for varying lengths of time. Discrete colonies were expanded as described in section 2.7.1 above. At approximately 80% confluency, each clone was stored for long-term storage in LN_2 container.

2.8 SCREENING OF CLONES

2.8.1 PASSAGING AND RESEEDING CELLS ONTO COVERSLIPS INTO THE 24-WELL PLATE

The forceps were submerged in a beaker containing 70% EtOH. The autoclaved rounded coverslips were placed into the wells of a 24-well plate by using the forceps. 1 ml of complete F-12 HAM medium was added into each well and the plate was placed into the incubator for 2 hours in order for the medium to be pre-warmed. The cells were passaged from the wells of the 96-well plate to the wells of the 24-well plate by following the procedure that is described in section 2.3.3, with the differences being that smaller volumes of DPBS and 10 x trypsin 1:10 diluted in DPBS were used. Following the addition of cells into their corresponding wells of the 24-well plate, they were incubated at 37 ^{o}C for 3 hours in order to be settled onto the coverslips.

2.8.2 SEALING THE COVERSLIPS ONTO GLASS SLIDES

Using sterile forceps and a sterile hypodermic needle, the coverslips were taken out of the wells of the 24-well plate. A small volume of the medium that was present in each well was placed onto each glass slide (Thermo Scientific Superfrost) and each coverslip was placed onto its corresponding glass slide with cells facing the surfaces of the slides. Excess medium was blotted off from each slide and they were observed on Axiovert 200 M inverted fluorescence microscope. For each clone, four random

fields of view (FOV) were examined for EGFP expression using the Phase channel and the FITC excitation light and observations were recorded.

2.8.3 FLUORESCENCE MICROSCOPY AND IMAGE ACQUISITION

Cells seeded at the appropriate density in glass-bottom dishes (MatTek Corporation) were cultured for ~48 hours before image acquisition, whereas cells on coverslips were cultured and sealed onto glass slides as described in section 2.8.2 above. Image acquisition was performed on Axiovert 200 M inverted fluorescence microscope by employing the 63 x and 100 x objective lenses. Using the Multidimensional Acquisition tab on Axiovision 4.5 software, images were captured using the Phase channel and the FITC or DAPI excitation light, accordingly. The exposure time of cells to U.V. light was kept constant for all images, z-stack and time-lapse experiments at 3.5 seconds.

2.8.4 SCREENING OF CLONES AT 24-WELL PLATE STAGE

Clones at the 24-well plate stage were screened on Axiovert 200 M inverted fluorescence microscope for EGFP expression as described in section 2.8.3 and observations were recorded.

2.9 CYTOCHEMISTRY

2.9.1 DiOC6(3) CYTOPLASMIC STAINING

2 µl of 3, 3' dihexyloxacarbocyanine iodide [DiOC6(3); stock concentration: 0.5 mg/ml; a gift from Mark Hill, Oxford University] was added in 3 ml of medium that was present in the glass-bottom dish and the medium swirled. The dish was returned into the incubator at 37°C for 30 minutes, after which time it was covered with aluminium foil to protect it from the light and transferred to the inverted fluorescence microscope (Zeiss Axiovert 200 M). Images were acquired using the 63 x objective lens as described in section 2.8.3.

2.9.2 HOECHST 33342 DYE NUCLEAR STAINING

3 µl of Hoechst 33342 dye (stock concentration: 1 mg/ml; Invitrogen) was added to the dishes and they were subsequently incubated at 37 ^{o}C for 30 minutes. Following two washes in Hepes Buffered Saline Solution (HBSS; Lonza) the medium was

restored and images acquired on Zeiss Axiovert 200 M inverted fluorescence microscope as described in section 2.8.3 using the Phase and DAPI channels.

2.9.3 DIOC6(3) AND HOECHST 33342 DYE DUAL STAINING

3 µl of Hoechst 33342 dye was added and the medium swirled. Following incubation of the dish at 37 $^{\circ}$C for 30 minutes, the cells were washed twice with HBSS and the medium was restored. Afterwards, 2 µl of DiOC6(3) was added and the medium swirled. Following incubation at 37 $^{\circ}$C for 30 minutes the dish was covered with aluminium foil to protect it from the light and transferred to Zeiss Axiovert 200 M inverted fluorescence microscope. Images were acquired as described in section 2.8.3, using the Phase, DAPI and FITC channels.

2.10 IMMUNOSTAINING

2.10.1 STAINING FOR PROLIFERATING CELL NUCLEAR ANTIGEN (PCNA)

Sterile rounded coverslips were initially placed in 8.8 cm culture dishes and CHO-R-O-25 and control CHO DG44 cells were reseeded at the appropriate seeding densities in each one of the two dishes. Following incubation of the cells at 37 $^{\circ}$C for 72 hours, the medium was removed and the coverslips present in each dish washed three times with 1 x PBS. Afterwards, cells were fixed by the addition of 1:1 methanol:acetone (BDH) in each dish for 4 minutes. The fixative was removed and the cells washed three times with 1 x PBS. Then, PBS supplemented with 1% Newborn Calf Serum (NCS; Gibco) was added for 2 minutes. After having transferred the coverslips into the humidified chamber, 10 µl of human anti-PCNA primary antibody (1:10 diluted in PBS + 1% NCS; a gift from Dr. Ian Kill, Brunel University) was added onto each coverslip and they were then incubated at RT for 1 hour. Cells were washed by dipping each coverslip in 3 baths containing PBS for 3 times. 10 µl of goat anti-human secondary antibody conjugated to rhodamine isothiocyanate (1:40 diluted in PBS + 1% NCS; a gift from Dr. Ian Kill, Brunel University) was added onto each coverslip, before being incubated in the humidified chamber at RT for 1 hour. Cells were washed by dipping each coverslip in 3 baths containing 1 x PBS for 3 times and in a bath containing dH$_2$O after the end of the last wash in PBS. Following the addition of a small drop of mountant (mowiol +

buffer +DAPI anti-fade; MetaSystems GmbH) on each slide, each coverslip was applied on its corresponding pre-labelled slide with cells facing the surfaces of the slides. Finally, the slides were stored in the fridge at 4 ^{o}C until visualisation. The fractions of PCNA positive nuclei of CHO-R-O-25 and control CHO DG44 cells were determined by observation on the Zeiss Axioskop 2 fluorescence microscope. The 40 x objective lens was used and the DAPI and TRITC excitation wavelengths were employed.

2.10.2 STAINING FOR H2AX AT SITES OF DSBs

Cells were seeded onto slides at the appropriate seeding densities and treated with the appropriate doses of BLM, H_2O_2 and γ-IR DNA damaging agents for defined time intervals. For each treatment, unexposed cells were also stained. The cells on each slide were washed three times with cold 1 x PBS and then fixed using 4 % paraformaldehyde (PFA; Sigma-Aldrich) for 5 minutes at RT. Following three washes in 1 x PBS, cells were permeabilised at 4 ^{o}C for 5 minutes with permeabilisation buffer [0.5% Triton X-100 (Fluka) in 1 x PBS]. They were subsequently washed three times with cold 1 x PBS and blocking buffer (5% FBS in 1 x PBS) was added on each slide for 1 hour, during which time they were incubated at RT with occasional gentle agitation. Following the removal of blocking buffer, the cells were incubated with mouse anti-phospho-histone H2AX primary antibody (Upstate cell signaling solutions; 1:10000 diluted in blocking buffer) for 1 hour at RT. Following three washes in washing buffer (0.1% Triton X-100 in 1 x PBS) for 45 minutes (15 minutes incubation at RT for each wash), incubation took place at RT for 1 hour with rabbit anti-mouse AF480/FITC secondary antibody (Molecular Probes; 1:1000 diluted in blocking buffer), while covering the slides with an aluminum foil-wrapped beaker that prevented their exposure to light. The cells on each slide were then washed three times in washing buffer (0.1% Triton X-100 in 1 x PBS) for 45 minutes (15 minutes incubation at RT for each wash), after which time they were counterstained using Vectashield mounting medium for fluorescence containing 10 x DAPI (Vector Laboratories). A 22 x 40 coverslip was applied on each slide and nail varnish was used to seal the coverslips onto the slides. The slides were finally stored in the fridge at 4 ^{o}C until visualisation.

2.10.3 VISUALISATION

Numerous two-dimensional (2-D) images from each slide were acquired on Axiovert 200 M inverted fluorescence microscope as described in section 2.8.3, for presentation purposes and for script analysis (in collaboration with Andrew McVean; Brunel University). The images that were acquired for presentation purposes contained a high number of nuclei in close proximity with each other, whereas the images that were acquired for script analysis accounted for > 100 well separated nuclei. 10 images for each treatment or sham were captured, whereas for script analysis an appropriate number of images were acquired in order to exceed 100 nuclei for each treatment or sham. Information associated with the total number and percentages of γ-H2AX positive cells, the total number of γ-H2AX foci and the mean number of γ-H2AX foci / nucleus was provided after script analysis and the corresponding graphs were drawn.

2.11 FLUORESCENCE IN SITU HYBRIDISATION (FISH)

2.11.1 METAPHASE CHROMOSOME HARVEST

CHO-R-O-25 cells were reseeded in an appropriate number of flasks at defined seeding densities and the cells were incubated at 37 $^{\circ}$C for approximately 72 hours. 5 μl/ml of colcemid (Gibco) was added into the flasks for a time interval range of 2 hours and 40 minutes - 15 hours and 25 minutes. The medium was decanted and stored in a 50 ml tube, while cells were harvested using PBS, 1 x trypsin and medium as described in section 2.3.3, which were then also poured into the 50 ml tube. Following centrifugation at 250 x g for 10 minutes, the supernatant was discarded, the pellet flick-mixed thoroughly and pre-warmed 0.075 M KCl hypotonic solution (Fisher Scientific; 0.559 g of 1M KCl in 100 ml of dH$_2$O) was added slowly and drop-wise to the pellet whilst flick-mixing continuously. After having placed the tube in the water bath at 37 $^{\circ}$C for 8 minutes, 3 drops of freshly prepared 3:1 methanol:acetic acid (BDH, Fisher Scientific) fixative were added and centrifugation at 250 x g for 10 minutes was performed. The supernatant was removed, leaving only 0.5 ml in the tube. The cells were resuspended thoroughly by flick-mixing and whilst vortexing at an intermediate speed, 1 ml of freshly prepared 3:1 methanol:acetic acid was added to the tube slowly and drop-wise, before topping up

the volume to 8 ml with 3:1 methanol:acetic acid. After having mixed the contents of the tube by inversion, it was stored in the freezer at -20 ^{o}C for 30 minutes and the nuclei were then washed 3 times with freshly prepared 3:1 methanol:acetic acid. Following each wash, centrifugation at 250 x g for 10 minutes was being performed. The chromosome preparations were finally stored in the freezer at -20 ^{o}C and the slides prepared for dropping.

2.11.2 DROPPING SLIDES

Following 3 washes in fresh 3:1 methanol:acetic acid, the glass slide (Thermo Scientific Superfrost) was held at a distance from the pipette and 10 µl of the preparation was dropped onto its surface. In order for nuclei and chromosomes to become better spread on its surface, the slide was swirled around for a few seconds. The region of the slide where the drop was present was humidified by breathing on it and then it was air-dried by waving it in the air for a few seconds. The metaphase spreads were finally observed on the phase contrast microscope (Zeiss).

2.11.3 MITOTIC INDEX DETERMINATION

Metaphases were harvested using the procedure described in section 2.11.1 and the slides were dropped using the procedure described in section 2.11.2. The number of nuclei at metaphase stage of the mitotic cycle was determined by scoring a minimum of 200 nuclei from each metaphase chromosome preparation. The mitotic index (M.I.) was calculated by using the following formula:

M.I. = Total # of mitoses / (Total # of mitoses + Total # of nuclei in the FOV) x 100

In the formula above, the total number of mitoses represents the sum of metaphases observed in the FOV examined, whereas the total number of nuclei corresponds to the sum of the metaphase and interphase nuclei that were present in the same FOV.

2.11.4 NICK TRANSLATION FOR FLUORESCENT LABELLING OF LAC O PROBE

In order to fluorescently label the purified lac O probe DNA, nick translation was performed. On ice, 5 µl of dNTP Mix (without dTTP; Invitrogen), 1 µl of biotin-16-dUTP (Roche Diagnostics), 1 µg of lac O probe DNA and enough sterile dH$_2$O to reach a final total volume of 45 µl was added to an eppendorf and briefly flick-

mixed. 5 µl of Pol I / DNase I Mix (Invitrogen) was added, the eppendorf components were gently but thoroughly flick-mixed and spinned at 11300 x g for 5 seconds in the microcentrifuge (Eppendorf). The mixture was then incubated in the incubator at 15 ^{o}C overnight. In order to test whether DNA fragments of the desired length had been produced, 5 µl of the labelled product was loaded on a 2% gel and agarose gel electrophoresis was then performed. The unincorporated nucleotides were removed using the illustra^{TM} Microspin G-50 columns (GE Healthcare). The incorporated nucleotides were collected in an eppendorf tube and 50 µg of salmon sperm DNA (Sigma-Aldrich) was added. DNA was precipitated by the addition of 1/10 volume of 3M Na acetate and 2.5 volumes of ice-cold 100 % EtOH to the tube, which was then stored in the freezer at -80 ^{o}C for 1 hour. Following centrifugation at 11300 x g for 30 minutes, the DNA pellet was washed by the addition of 70% EtOH to the eppendorf. The supernatant was discarded and the pellet air-dried for 30 minutes. The pellet was finally dissolved in sterile dH$_2$O and the eppendorf placed in the fridge at 4 ^{o}C overnight. The next day it was transferred to the -20 ^{o}C freezer until required for FISH.

2.11.5 COT-1 DNA ISOLATION FROM CHO CELLS

Cot-1 DNA was manually extracted from control CHO DG44 cells by following the procedure described in (347).

2.11.5.1 CELL CULTURING

Cells were harvested from confluent T75 flasks as described in section 2.3.3 and the cell suspensions were distributed among three tubes (A, B and C). Following centrifugation of cells in all three tubes, the pelleted cells were re-suspended in DPBS by serial re-suspension of the pellets in tubes A, B and C and collection of all of the re-suspended cells in tube C. The remaining cells in tubes A and B were rinsed off using DPBS and transferred to tube C. Following centrifugation of tube C at 250 x g for 10 minutes and removal of the supernatant, the volume that was occupied by the pellet was determined by optical comparison with three other 50 ml tubes that contained 500 µl, 1 ml and 2ml of dH$_2$O, respectively.

2.11.5.2 ISOLATION OF NUCLEI

Initially, 5 x the volume of the pellet of ice-cold buffer A [0.35 M sucrose (Sigma-Aldrich), 0.05 M Tris-HCl (pH 7.5; Fisher BioReagents), 0.066 M EDTA (Fisher BioReagents), 0.003 M $CaCl_2$, 0.025 M KCl] was added and the contents of the tube mixed in a homogenizer. Following incubation on ice for 10 minutes, a 1% concentration of Triton X-100 was obtained in the tube by slowly adding drops from a 10 % solution of Triton X-100. The contents of the tube were transferred to a Sorvall tube and centrifuged at 800 x g for 5 minutes at 4 ^{o}C. The supernatant was discarded, the pellet washed using ice-cold buffer A and the contents of the tube re-suspended by gentle vortexing. Following centrifugation at 800 x g for 5 minutes at 4 ^{o}C, the supernatant was removed and the pellet washed for three additional times as described above.

2.11.5.3 NUCLEI LYSES AND PROTEINASE K TREATMENT

5 ml of buffer A were added and the pellet re-suspended gently. Afterwards, 20 ml of buffer B [0.05 M Tris-HCl (pH 7.5), 0.066 M EDTA, 0.1 M NaCl] containing 10 μg/ml of RNAse A was added and the contents of the tube split in two Sorval tubes. An equal amount of buffer B containing 0.4% SDS (Fisher BioReagents) and 0.1 mg/ml of proteinase K was added in each Sorvall tube and the contents of the tubes were then mixed by inversion, after which time they were incubated in the water bath at 65 ^{o}C for 2 hours, with occasional vortexing every 10 – 20 minutes.

2.11.5.4 ULTRASOUND DNA FRAGMENTATION

2.11.5.4.1 Optimisation

The ultrasonic homogenator (SoniPrep 150) was used to fragment DNA present in the tubes. Initially, a sonication test was performed in order to identify the duration of sonication and the number of pulses that result in the generation of DNA fragments of the desired size. Using two DNA samples, 5 - 20 μg were diluted in different volumes (100 μl - 1 ml) and sonication was performed by inducing 4 - 16 and 3 - 12 pulses to sample volumes of 100 μl for durations of 20 seconds each and 30 seconds each respectively and 6 pulses to sample volumes of 100 μl - 1 ml for a duration of 20 seconds each.

2.11.5.4.2 Operation of sonicator

The metallic bar of the sonicator was rinsed with dH_2O, the eppendorf attached firmly to the base of the sonicator and the screw used to adjust its position. The metallic bar was placed just below the surface of the sample and the door closed. After having worn the ear muffs, the 'supply' and 'start' buttons were pressed simultaneously in order to activate the sonicator, after having switched the amplitude to maximum. Following the completion of sonication, the DNA sample that had been heated up during the procedure was immediately placed on ice.

2.11.5.4.3 Sonication procedure

In order to generate DNA fragments of a length of ~500 bp, sonication was performed 24 – 30 times at maximum amplitude (22 amplitude microns) by inducing 30 second sonication pulses (24 -30 pulses x 30 sec). After each pulse and after the end of the procedure, the heated DNA samples were immediately placed on ice. The sizes of the generated fragments were checked by agarose gel electrophoresis on a 1% agarose gel, by following the procedure described in section 2.5.2.

2.11.5.5 ETHANOL PRECIPITATION

The contents of the two tubes were split in 4 Sorvall tubes. 1/10 the volume of 4 M NaCl was added in each tube in order to obtain a concentration of 0.4 M NaCl. DNA was precipitated as described in sections 2.1.2 – 2.1.3 with the differences being that all centrifugations were performed at 10000 x g and at 4 ^{o}C, larger volumes were used and the DNA pellet in each tube was washed in 70 % EtOH twice. The dissolved DNA samples were pooled in a 15 ml tube and the DNA concentration was determined using the spectrophotometer by following the procedure described in section 2.1.4.1. Following the loading of 2 µg of sample in a 1% agarose gel, electrophoresis was performed in order to confirm that ~500 bp DNA fragments had been produced after sonication.

2.11.5.6 DNA REANNEALING

The incubation time of the DNA sample in the water bath was determined based on the fact that repetitive DNA re-anneals into dsDNA first in 1.2 x SSC by incubation of 83 µg/ml of DNA at 60 ^{o}C for 1 hour (347). The formula that was used to

calculate the period of incubation was: t_0 = COTX x 4.98/C_0, where C_0 = initial concentration in $\mu g/\mu l$, t = incubation period, x =COT fraction (e.g.: COT1 = 1, COT2 = 2, etc.) and 4.98 = 60 min x 0.083. In order for DNA to be denatured, the lid of the tube was loosened and it was placed on the heater block of the magnetic stirrer at 95 ^{o}C for 10 minutes. A concentration of 1.2 x SSC was obtained by adding 1/10 the volume of the DNA sample of 12 x SSC. The tube was then incubated in the water bath at 60 ^{o}C for 4 hours and 39 minutes, based on the formula mentioned above.

2.11.5.7 S1-NUCLEASE HYDROLYSIS

After the end of incubation the tube was placed on ice. In order to degrade the remaining non-repetitive ssDNA fragments that had not re-annealed into dsDNA, 100 units / mg of DNA of S1- nuclease (Sigma-Aldrich; stock concentration: 405000 units/ml) were added and the tube was incubated in the water bath at 42 ^{o}C for 1 hour. After transferring the contents of the tube to a Sorvall tube, DNA was precipitated by the addition of 1/10 volume of 3M Na acetate (pH 5.2) and 0.8 x volume of isopropyl alcohol, followed by storage in the freezer at -20 ^{o}C overnight.

2.11.5.8 PURIFICATION

The pellet was washed twice in 70 % EtOH as described in section 2.11.5.5 above, air-dried and dissolved in 1ml of TE buffer, before being finally stored in the fridge at 4 ^{o}C. The following day, the DNA concentration was determined using the spectrophotometer as described in section 2.1.4.1.

2.11.6 FISH PROCEDURE

2.11.6.1 SLIDE PREPARATION

Slides were washed for 5 minutes in 2 x SSC on the rotating platform and then dehydrated by incubation in 3 coplin jars containing 70 % EtOH, 90% EtOH and 100% EtOH (Hayman) for 3 minutes each. The slides were air-dried on the bench for 5 minutes, after which time the chromosomes were denatured in freshly prepared denaturing solution [10 ml dH$_2$O; 5 ml 20xSSC (Fisher Scientific); 25 μl of 250 mM EDTA; 35 ml of 70% Formamide (Fisher Scientific); pH 7.0] in the water bath at 70 ^{o}C for 5 minutes. They were then washed for 5 minutes in ice-cold 2 x SSC on the

rotating platform and dehydrated once more by incubation in 3 coplin jars containing 70 % EtOH, 90% EtOH and 100% EtOH for 3 minutes each. Finally, the slides were air-dried for 5 minutes and left at RT until use.

2.11.6.2 TREATMENT OF THE PROBE FOLLOWING LABELLING

Initially, 250 ng of lac O probe DNA was mixed with 5 µg of Cot-1 DNA in a sterile eppendorf. DNA was air-dried using the vacuum dryer and then dissolved in hybridisation mixture [50% Formamide; 10% (w/v) Dextran Sulfate (Sigma-Aldrich); 1% Tween 20 (Fisher Scientific); 2xSSC (Fisher Scientific); pH 7.0]. DNA was then denatured by placing the eppendorf containing the hybridisation mixture in the water bath at 75 ^{o}C for 10 minutes. 12 µl of the dissolved denatured probe DNA was subsequently added on each slide.

2.11.6.3 HYBRIDISATION AND POST-HYBRIDISATION WASHES

Following the application of a 22 x 22 mm coverslip on each slide, bicycle glue was used to seal the coverslips onto the slides. The slides were placed in a moist chamber and incubated in the water bath at 42 ^{o}C overnight. The rubber solution was carefully removed from each slide with the aid of forceps and the coverslips removed from the slides via incubation in 2 x SSC for 5 minutes on the rotating platform. Afterwards, stringency washes were performed by incubating the slides in pre-warmed 0.4 x SSC in the water bath at 72 ^{o}C for 5 minutes and then in 2 x SSC on the rotating platform for 5 minutes at RT.

2.11.6.4 DETECTION: BIOTIN-LABELLED PROBES

150 µl of blocking solution {1.8 g of BSA [Bovine Serum Albumin (3% w/v ; Sigma-Aldrich)]; 60 ml of 4xSSC/Tween 20; 4xSSC/Tween 20: 1000 ml 4xSSC; 500 µl Tween 20 (0.05%)} was added onto each slide and they were then placed in the moist chamber to be incubated at 37 ^{o}C for 1 hour. 2 µg/ml of Avidin - Texas Red antibody (Vector laboratories; 1:667 diluted in blocking solution; stock concentration: 1.3 mg/ml) was added on each slide, which were subsequently placed in the moist chamber and incubated at 37 ^{o}C for 20 minutes. They were washed in 4 x SSC / Tween 20, 3 times for 3 minutes each and then 5 µg/ml of biotinylated anti-Avidin antibody (Vector laboratories; 1:100 diluted in blocking solution; stock concentration: 500 µg/ml) was added on each slide. Following their incubation in the

moist chamber in the water bath at 37 ^{o}C for 20 minutes, they were washed in 4 x SSC / Tween 20, 3 times for 3 minutes each. The amplification step was carried out by the addition of 2 μg/ml of Avidin - Texas Red antibody on each slide and further incubation in the water bath at 37 ^{o}C for 20 minutes. After having washed the slides in 4 x SSC / Tween 20, 2 times for 3 minutes each, they were placed in a coplin jar containing 1 x PBS and on the rotating platform to be washed for 10 minutes. For each slide, 15 μl of DAPI – Antifade (MetaSystems GmbH) was added, a 22 x 40 mm coverslip was carefully applied and the coverslips sealed onto the slides using nail varnish. The slides were finally stored in the fridge at 4 ^{o}C until visualisation.

2.11.6.5 VISUALISATION

In order to visualise and score the hybridised chromosomes, the CCD camera and computerized filter wheel-equipped Zeiss Axioplan 2 imaging confocal microscope was used. The Smart Capture 2 and MetaSystems capture software systems were used in order to carry out the capturing, storage and analysis of the pictures.

2.12 CHEMICAL TREATMENT OF CELLS

2.12.1 RECONSTITUTION OF BLEOMYCIN AND HYDROGEN PEROXIDE

Bleomycin (BLM) sulfate [Sigma-Aldrich; lyophilized powder isolated from *Streptomyces verticillus* (1 mg)] was reconstituted in 0.5 ml of sterile dH$_2$O, thus producing a final concentration of 1 mg/0.5 ml. In order to obtain the desired concentration of hydrogen peroxide [H$_2$O$_2$; Sigma-Aldrich; 30 % (w/v) solution in water] into the volume of the medium present in each glass-bottom dish or 6-well plate, the solution was diluted either 1:10 or 1:100 in sterile dH$_2$O before being administered to cells, according to the experiment requirements.

2.12.1.1 OPTIMISATION OF BLEOMYCIN (BLM) AND HYDROGEN PEROXIDE (H$_2$O$_2$) DOSE ADMINISTRATION

In order to identify the ideal dose of BLM sulfate that results in the production of DSBs within the genome of cells without interfering with cell viability, CHO-R-O-25 and control CHO DG44 cells growing in 6-well plates were exposed to concentration ranges of 0 - 20 μg/ml of BLM and 0 – 400 μM of H$_2$O$_2$. Cells treated

with BLM were exposed to the aforementioned range for 30 minutes at 37°C, washed twice with DPBS, medium was then restored and cells further incubated at 37°C for 3 hours, before being harvested. Cells exposed to H_2O_2 were treated with the dose range mentioned above, incubated at 37°C for 3 hours, washed twice with DPBS and harvested. For both treatments, the trypan blue exclusion dye experiment (section 2.3.5) was performed and followed by cell counts, in order to determine the numbers of nonviable cells.

2.13 TIME-LAPSE MICROSCOPY

2.13.1 BLEOMYCIN (BLM) AND HYDROGEN PEROXIDE (H_2O_2) EXPOSED CELLS

CHO-R-O-25 cells were reseeded at the appropriate seeding density in glass-bottom dishes and incubated at 37 ^{o}C for defined time intervals. The appropriate concentrations of BLM and H_2O_2 were added in sterile eppendorfs. A flamed needle was used to puncture a hole on the lid of the dishes and a piece of Para film was used to cover the hole on the lid of each dish. The medium in each dish was replaced with Opti-MEM medium supplemented with 30 mM HEPES buffer (pH 7.3), then a big drop of oil was added on the objective and the dishes placed onto the stage of the Zeiss Axiovert 200 M inverted fluorescence microscope. Following the identification of a cell containing a discrete and intense fluorescent spot within its nucleus, a syringe was used to add the appropriate concentration of BLM or H_2O_2 into the dishes, after having re-suspended the contents of the eppendorfs with a small amount of medium from the dishes. The 63 x objective lens was used and images began to be acquired immediately every 2 minutes over a period of 2 hours, as described in section 2.8.3. In two separate BLM and H_2O_2 experiments, acquisition was commenced and the drug was added at certain time points during acquisition, in order to facilitate comparison between the appearance of the spots before and after agent addition. The resulting time-lapse series were then analysed on image J program.

2.13.2 CELLS EXPOSED TO γ-IRRADIATION

CHO-R-O-25 cells were reseeded in glass-bottom dishes and cultured as stated in section 2.8.3. The medium was replaced with Opti-MEM medium supplemented with 30 mM HEPES buffer (pH 7.3) and cells were exposed to defined doses of γ-irradiation in the Cobalt – 60 (Co-60) irradiation facility. In order to determine the duration of exposure to γ-irradiation that results in the treatment of cells with the desired dose, the following formula was employed: Exposure Time = Distance from the source x Dose Rate. While the distance from the source is measured in cm, the dose rate is measured in Rad x min^{-1} and determined by observation of the table in Co-60 higher activity cell sheet where different Rad x min^{-1} doses are specified on a monthly basis, based on the isotope decay time elapsed and half-life. The dose that was chosen corresponded to the tabulated dose for the closest date to that of the performance of the experiment. In a separate experiment, cells were exposed to the defined dose of γ-irradiation while being incubated on ice, in order to slow down DNA damage repair until acquisition. The dish was removed from ice before being placed onto the microscope stage. Regarding all experiments, after the end of irradiation the dishes were immediately transferred to Zeiss Axiovert 200 M inverted fluorescence microscope and acquisition was performed as described in section 2.8.3, before analysing the time-lapse series on image J program.

2.13.3 UNTREATED CELLS

CHO-R-O-25 cells were reseeded in glass-bottom dishes and cultured as stated in section 2.8.3. The medium was replaced with Opti-MEM medium supplemented with 30 mM HEPES buffer (pH 7.3) and acquisition was performed as described in section 2.8.3.

2.13.4 INFLUNCE OF FOCAL PLANE ON EGFP SPOT APPEARANCE

CHO-R-O-25 cells were reseeded in glass-bottom dishes and cultured as stated in section 2.8.3. In order to exclude the possibility that the diffusion of the fluorescent spots observed during the course of time-lapse experiments was an artefact caused by defocusing of the cells of interest on the microscope, the focusing experiment was performed. Two cells containing fluorescent spots were identified and pictures were acquired at different focus positions. In addition, following the identification of two

separate cells, two z-stack experiments were performed in which 14 images were acquired at different depths of the nucleus within the range of 14 µm, with each image being separated from each other by a distance of 1µm. The focus positions, the z-positions and observation comments were recorded for all four cells of interest.

2.13.5 BACKGROUND CORRECTIONS USING IMARIS 572

Using Imaris 572 program, the background threshold from the Phase and FITC channels of each time-lapse series was adjusted in order to generate more presentable image sequences. This resulted in the removal of the background for each image, but also in the inevitable increase of the intensities of the fluorescent spots within the cells of interest. Initially, the time-lapse ZVI series were dragged into the program and the 'Slice' option was selected from the toolbar. The pictures in which the cell of interest was not captured by the camera of the microscope were deleted. Then, for each series the background threshold of each one of the two channels was adjusted by selecting the 'Edit' and then 'Show Display adjustment' options from the toolbar menu. In order to execute the background removal, the 'Image Processing', 'Thresholding' and 'Background Subtraction' options were sequentially selected and the filter width for background subtraction was adjusted to 30.5 µm. In addition, the time points at which the images were acquired were added to each individual image of each time-lapse series. The 'Animation' option was selected from the toolbar, followed by the selection of 'Edit', 'Image Properties' and 'All Equidistant' options and the starting point for the first picture was set to 00:00:00. Then, the time interval for the following pictures was set to 2 minutes, resulting in the time points underneath each image increasing by 2 minutes for every individual image. Novel videos were generated, by adjusting the number of frames based on the number of pictures that were present in each series and clicking on the 'REC' button. The image sequences were finally converted to tif series and stored on a CD.

2.13.6 ANALYSIS OF TIME-LAPSE SERIES ON IMAGE J PROGRAM

MacBiophotonics (MBF) image J program was used to obtain information associated with the intensity and the area of each spot in each cell of interest. The time-lapse series were initially converted from zvi to unmerged tif series and then they were imported into the program, after having been converted to 8-bit grayscale images. The two channel image sequences were de-interleaved, generating two separate

channel sequences (Phase and FITC) and the FITC channel image sequence was cropped. The pixel width, pixel height and voxel depth were all set to 1 from the properties selection and from the 'Analyse' window, the 'Set Measurements' option was selected. The Area, Min & Max gray value, Mean gray value and Perimeter boxes were ticked and then by selecting 'Analyse' and 'Tools' options, the ROI (region of interest) Manager option was selected. For each individual image in the series, the circle or the freehand tool was used in order to carefully encircle the spot around its edges and the spot coordinates added into the ROI manager. After having processed all images, the 'More' and then the 'MultiMeasure' options were selected. The results appeared on the screen of the computer with perimeter, Min & Max gray value and Mean gray value being measured in pixels and area in pixels^2. The results sheets were copied and pasted into Excel sheets and graphs associated with mean intensity and area value alterations over time were constructed. In addition, the total intensity values (mean intensity x area) were calculated for each time point and graphs showing total intensity value alterations over time were plotted.

3. RESULTS

CHAPTER 3: GENERATION OF CELL LINES CONTAINING FLUORESCENTLY TAGGED CHROMATIN SITES

In order to generate CHO cells containing fluorescently tagged chromatin sites, DNA stocks of p3'SSdimerClonEGFP and pSV2-DHFR 8.32 plasmids that were generously provided by A. Belmont were bulked in DH5α and Stbl-2 bacterial cells, respectively. Prior to double transfection of CHO cells with the plasmids, they were extracted by the performance of Maxi prep and their dsDNA concentration determined.

3.1 PREPARATION OF p3'SSdimerClonEGFP and pSV2-DHFR8.32 PLAMIDS FROM DNA STOCKS

The p3'SSdimerClonEGFP and pSV2-DHFR 8.32 plasmids were bulked and extracted as described on sections 2.2, 2.3.1 and 2.4.1 of Materials and Methods. A high number of bacterial colonies was obtained from control, p3'SS dimerClonEGFP plasmid-transformed DH5α cells and pSV2-DHFR 8.32 plasmid-transformed Stbl-2 cells. Along with the control bacterial colonies, one colony of p3'SS dimerClonEGFP plasmid-transformed DH5α cells and two colonies of pSV2-DHFR 8.32 plasmid-transformed Stbl-2 cells were picked and used to inoculate 5 ml of LB medium supplemented with 100 µg/ml of ampicillin. The universals containing the p3'SSdimerClonEGFP and pSV2-DHFR 8.32 transformed cells were then placed in the incubator at 37 °C and at 30 °C respectively, shaking at 220 rounds per minute (rpm) overnight. Following extraction (as described in section 2.4.1), a number of tests was carried out to determine whether the plasmids had been extracted successfully from the DH5α and Stbl-2 bacterial cells, respectively.

The dsDNA concentrations of p3'SS dimerClonEGFP and pSV2-DHFR 8.32 plasmids were determined by spectrophotometry (2.1.4.1). The dsDNA concentration of p3'SSdimerClonEGFP plasmid was found to be 0.185 µg/µl with an A_{260}/A_{280} ratio of 1.696, indicating that the quality of the DNA was of high standard. Based on this reading, the total amount of DNA was calculated to be 4990 µl x 0.185 µg/µl = 923.2 µg. The dsDNA concentrations of the two pSV2-DHFR 8.32 plasmid

DNA samples A and B (derived from the two individual colonies) were shown to be 0.112 µg/µl and 0.106 µg/µl, respectively. The total amount of DNA was calculated to be 934 µl x 0.112 µg/µl = 104.6 µg for sample A and 1133 µl x 0.106 µg/µl = 120.1 µg for sample B, respectively. The A_{260}/A_{280} ratios were 1.71 and 1.75, for samples A and B, respectively.

3.2 CONFIRMATION OF p3'SSdimerClonEGFP and pSV2-DHFR8.32 PLASMID EXTRACTIONS BY RESTRICTION DIGESTION

In order to confirm that the plasmids had been extracted successfully after Maxi prep, 1 µg each of p3'SSdimerClonEGFP and pSV2-DHFR 8.32 plasmid DNA samples was digested as described in section 2.5.1 of Materials and Methods. Based on the spectrophotometer readings above for p3'SSdimerClonEGFP and pSV2-DHFR 8.32 plasmids, 1 µg of DNA corresponded to 2.5 µl and 9.4 µl, respectively. The reaction mixtures for the single and double digestions of both plasmids are shown on tables 3.1 and 3.2, respectively. Regarding the single digestion of p3'SSdimerClonEGFP plasmid, restriction enzyme BamH1 was selected because it cleaves F9-1 polyoma promoter-EGFP DNA sequence, whereas for double digestion enzymes BamH1 and Xho1were used because they cut EGFP and F9-1 polyoma promoter out of the plasmid (see plasmid map on figure 1.7). Regarding the single digestion of pSV2-DHFR 8.32 plasmid, enzyme Xho1 was selected because it cuts downstream of the 256-copy lac O repeat, whereas for double digestion enzymes Xho1 and Sal1 were used because they cut the 256-copy lac O repeat out of the plasmid (see plasmid map on figure 1.7). In figures 3.1 and 3.2 below, the pictures of the gels for p3'SSdimerClonEGFP and pSV2-DHFR 8.32 digested DNA samples are presented.

Table 3.1 Reaction mixtures of single and double digestions of p3'SSdimerClonEGFP plasmid

	p3'SSdimerClonEGFP Reaction Mixture 1	p3'SSdimerClonEGFP Reaction mixture 2
Buffer x10	2 µl	2 µl
DNA	2.5 µl	2.5 µl
Enzyme BamH1	0.5 µl	0.5 µl
Enzyme Xho1	-------	0.5 µl
Distilled water	15 µl	14.5 µl
Total Volume	20 µl	20 µl

Table 3.1 above presents the reaction mixtures for single digestion of 1 µg of plasmid DNA with BamH1 and double digestion with BamH1 and Xho1

Table 3.2 Reaction mixtures of single and double digestions of pSV2-DHFR 8.32 plasmid

	pSV2-DHFR 8.32 Reaction mixture 1	pSV2-DHFR 8.32 Reaction mixture 2
Buffer x10	2 µl	2 µl
DNA	9.4 µl	9.4 µl
Enzyme Xho1	0.5 µl	0.5 µl
Enzyme Sal1	-------	0.5 µl
Distilled water	8.1 µl	7.6 µl
Total Volume	20 µl	20 µl

Table 3.2 above shows the reaction mixtures for single digestion of 1 µg of plasmid DNA with Xho1 and double digestion with Xho1 and Sal1

3.2.1 p3'SSdimerClonEGFP
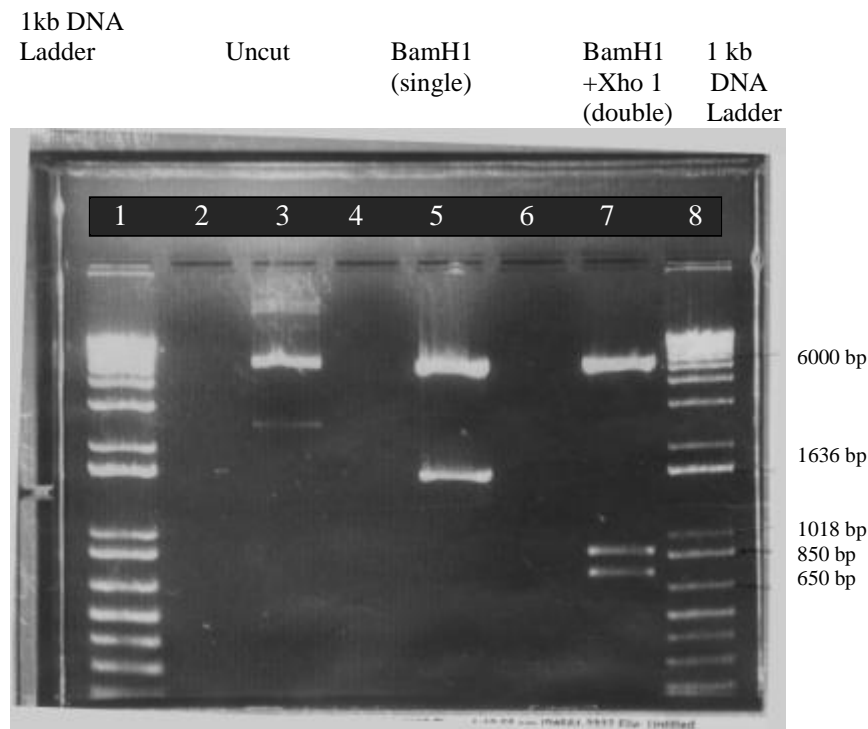
Figure 3.1 Restriction digestion of 1 μg of p3'SSdimerClonEGFP plasmid DNA

A digestion of 1 μg of p3'SSdimerClonEGFP plasmid DNA was performed (see figure 3.1). The sizes of the bands that appear on lane 5 where the reaction mixture that contained BamH1 restriction enzyme (single digestion) was loaded are approximately 1600 bp and 5800 bp. The band that is ~1600 bp corresponds to the F9-1 polyoma promoter-EGFP sequence, whereas the band that is ~5800 bp corresponds to the rest of the plasmid length (LacI-HygR-AmpR; see plasmid map in figure 1.7). The sizes of the bands that appear on lane 7 where the reaction mixture that contained both BamH1 and Xho1 restriction enzymes (double digestion) was loaded are approximately 750 bp, 900 bp and 5800 bp. The band that is ~750 bp represents the EGFP sequence, the band that is ~900 bp corresponds to the F9-1 polyoma promoter sequence and the band that is ~5800 bp corresponds to the rest of the plasmid length (LacI-HygR-AmpR; see plasmid map in figure 1.7). Based on the fact that these were the sizes of bands that were expected to appear on the picture of the gel before digestion, it was concluded that the plasmid had been extracted

successfully by Maxi prep and its components could also be cleaved efficiently by BamH1 and Xho1 restriction enzymes.

3.2.2 pSV2-DHFR 8.32
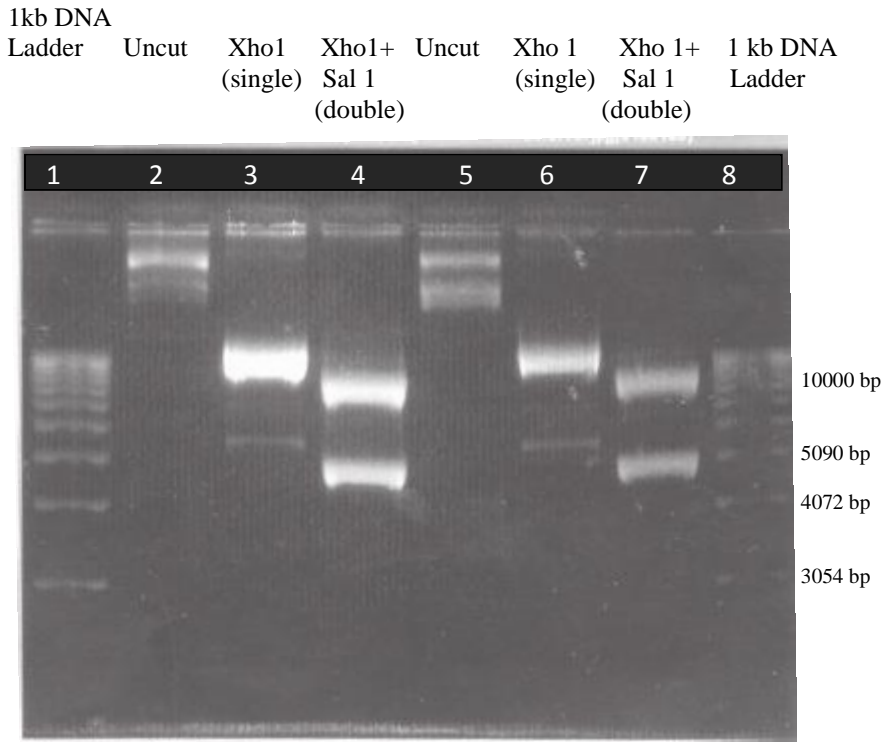
Figure 3.2 Restriction digestion of 1 μg of pSV2-DHFR 8.32 plasmid DNA

A restriction digestion of 1 μg of pSV2-DHFR 8.32 plasmid DNA (2.5.1) was carried out (figure 3.2). Examination of wells 2 and 5 where the uncut samples were loaded suggests that bands having a size of high molecular weight (>15 kb) are present. These bands correspond to the entire plasmid length. In wells 3 and 6, reaction mixtures containing plasmid DNA digested with Xho I restriction enzyme were loaded and the presence of bands possessing a size of >12 kb on lanes 3 and 6 confirms the identity of the plasmid that has a total length of 15080 bp (figure 1.7). The sizes of the bands that appear on lanes 4 and 7 where the reaction mixtures digested with both Xho I and Sal I enzymes were loaded are ~10 kb and ~5kb respectively, which is consistent with the expectations, since the 256-copy lac O repeat has a total length of 10 kb. The uppermost bands on these lanes correspond to the lac O repeat. The bands located underneath them correspond to the rest of plasmid length (5080 kb).

151

3.3 CALCIUM PHOSPHATE TRANSFECTION OF CHO CELLS WITH p3'SSdimerClonEGFP and pSV2-DHFR 8.32 PLASMIDS

3.3.1 GENERATION OF STABLE CHO CELL TRANSFECTANTS WITH p3'SSdimerClonEGFP PLASMID

CHO cells were seeded into the appropriate number of flasks at a seeding density of 1.25×10^4 cells / cm^2 in 20 ml of complete F-12 HAM medium and harvested as described in section 2.3.3.2, whereas the $CaCl_2$-DNA and $CaCl_2$-dH_2O solutions were prepared as described in section 2.6.1 of Materials and Methods. Calcium phosphate (Ca_2PO_4) single transfection was performed as described in section 2.6.1. In order to optimise the transfection efficiency, $CaCl_2$-p3'SSdimerClonEGFP plasmid DNA and $CaCl_2$-dH_2O mixtures were incubated in equal volumes of TR buffer of varying pH levels (pH 6.94 - 7.11), before being added to their corresponding flasks, as described on table 3.3 below.

Table 3.3 Calcium phosphate single transfection mixtures

Tube	TR buffer (0.5 ml)	$CaCl_2$ (0.5ml) mixed with	Flask	Selective medium Hygromycin
1	TR buffer pH 6.94	DNA	1	+
2	TR buffer pH 7.05	DNA	2	+
3	TR buffer pH 7.11	DNA	3	+
4	TR buffer pH 6.94	dH_2O	4	+
5	TR buffer pH 7.05	dH_2O	5	+
6	TR buffer pH 7.11	dH_2O	6	+
7	TR buffer pH 7.05	DNA	7	-
8	TR buffer pH 7.05	dH_2O	8	-
9 (control)	-	-	9	-

One day after transfection, cells were observed under the light microscope at high magnification. Although the morphology of the cells had not changed significantly,

inspection of the appearance of cells in T75 culture flasks 1-8 (table 3.3) revealed that calcium phosphate (Ca_2PO_4) particles had been successfully integrated into the cytoplasm of CHO cells. Evidence for this was provided by the fact that small black dots could be observed to be present within both rounded and spindle-shaped CHO cells and the overall colour of the cells had become darker. In culture flasks 1, 2 and 7, small particles that looked like precipitates could be spotted in regions devoid of cells. These particles possibly corresponded to $CaCl_2$-DNA precipitates. The density of the cells was very similar from flask to flask, in the time period of 4 days after transfection. No significant differences between the cell density of control flasks and that of transfected flasks had been observed up to that time point.

On the fifth day following transfection, the cell density in flasks 1, 2, 3 and 7 containing cells possessing the p3'SSdimerClonEGFP plasmid that in turn contained the Hygromycin resistance (Hyg R) gene, was much higher compared to that of flasks 4, 5, 6 and 8 that were transfected with the $CaCl_2$-dH_2O mixtures that did not contain the plasmid. The latter were characterised by extensive cell death that could not be observed in the rest of the flasks. In comparison with the cell density of control culture flask 9 that contained no hygromycin, the density in flasks 1, 2, 3 and 7 was slightly lower, whereas the corresponding density of flasks 4, 5, 6 and 8 was considerably lower. It should be mentioned that the efficiency of transfection in flask 7 was found to be poor compared to that of flasks 1-3, as the number of cell colonies that were present in this flask was low, compared to flasks 1-3. The same observations were drawn after the daily examination of the culture flasks for nearly a 2-week period.

13 days after hygromycin addition, discrete colonies of cells that were present at a small distance from each other began to emerge in culture flasks 1, 2, 3 and 7, indicating that these colonies corresponded to stable clones containing the p3'SSdimerClonEGFP plasmid. No such colonies could be observed to exist in flasks 4, 5, 6 and 8. The cells that were present in these flasks were characterised by a much lower cell density and a much higher observed extent of cell death compared to flask 9 (control).

3.3.2 DETERMINATION OF THE REQUIRED CONCENTRATION OF HYGROMYCIN

The effect of hygromycin on CHO cells was tested in order to determine the appropriate concentration of antibiotic for selection of transfected cells. 90% confluent CHO cells were passaged and reseeded in 3.5 cm diameter wells (total area : 9.6 cm^2), at a seeding density of 1.6 x 10^5 cells/well, in a total of 3 ml of complete F-12 HAM medium. After having incubated the cells at 37 ^{o}C overnight, a range of hygromycin concentrations was added to duplicate wells. The cultures were then returned into the incubator at 37 ^{o}C and the medium replaced with fresh complete F-12 HAM medium containing the appropriate amount of hygromycin twice a week. The number of nonviable cells in each well was assessed by visual inspection and Trypan blue exclusion dye (as described in section 2.3.5 of Materials and Methods) during a period of two weeks (see table 3.4 below). During this period of time, the cells were also observed daily under the light microscope.

Table 3.4 Results of the Trypan blue exclusion dye experiment for assessment of nonviable doubly transfected CHO-R-O cells following hygromycin exposure

Wells	1-2	3-4	5-6	7-8	9-10	11-12	13-14	15-16
Hygromycin concentration	50 µg/ml	100 µg/ml	150 µg/ml	200 µg/ml	250 µg/ml	300 µg/ml	350 µg/ml	_
Average % of non-viable cells	6.9	8.5	9.4	22.8	60.3	72.9	81.1	3.2

Incubation with 50, 100 and 150 µg/ml of hygromycin had no significant effects on cell survival, since the average percentages of nonviable cells that were observed to be present in all of these wells was comparable to that of the control wells (representing 6.9 %, 8.5 % and 9.4 % of the total number of cells repectively, as opposed to 3.2% for the control wells; see table 3.4 above). Thus, these concentrations were assessed as insufficient to select for stably transfected cells containing the Hyg R gene within their chromosomes. In comparison with the control wells, the addition of 250, 300 and 350 µg/ml of hygromycin resulted in

extensive cell death, with the percentages of dead cells representing 60.3 %, 72.9 % and 81.1% of the total cell population in each well, respectively. Based on the fact that the addition of 200 µg/ml of hygromycin resulted in intermediate cell death (22.8 % of dead cells) and an easily observable difference in cell survival between cells that were contained in these wells and the control wells (see table 3.4 above), there was concluded that for stable transfectant cell selection the ideal concentration of hygromycin to be added into the culture medium is 200 µg/ml. Similar conclusions were drawn after the inspection of cells that were contained in each well. The observed number of floating nonviable cells was insignificant for concentrations of 50, 100 and 150 µg/ml and too high for concentrations of 250, 300 and 350 µg/ml of hygromycin. An intermediate cell death extent was recorded following exposure to 200 µg/ml of hygromycin.

3.3.3 TRANSFECTION OF CHO CELLS WITH p3'SSdimerClonEGFP AND pSV2-DHFR 8.32 PLASMIDS

CHO cells were seeded into the appropriate number of flasks as described in section 3.3.1 above and harvested as described in section 2.3.3.2 of Materials and Methods. Ca_2PO_4 double transfection was performed as described in section 2.6.2 of Materials and Methods. In order to optimise the transfection efficiency, $CaCl_2$-p3'SSdimerClonEGFP-pSV2-DHFR8.32, $CaCl_2$-p3'SSdimerClonEGFP, $CaCl_2$-pSV2-DHFR8.32 plasmid DNA and $CaCl_2$-dH_2O mixtures were incubated in TR buffer of varying pH levels (pH 6.94 - 7.11) prior to their addition to their corresponding flasks, as described in table 3.5 below. The $CaCl_2$-DNA and $CaCl_2$-dH_2O solutions were prepared as described in section 2.6.2 of Materials and Methods, whereas the TR buffer-$CaCl_2$-DNA and TR buffer-$CaCl_2$-dH_2O mixtures were prepared by mixing equal volumes of TR buffer at pH levels of 6.94, 7.05 and 7.11 with either $CaCl_2$- p3'SSdimerClonEGFP DNA and $CaCl_2$- pSV2-DHFR 8.32 DNA or $CaCl_2$-dH_2O, as shown in table 3.5 below.

Table 3.5 Calcium phosphate double transfection mixtures

Tube	TR buffer (0.5 ml)	CaCl$_2$ (0.5 ml) mixed with	ProCHO-AT selection medium	Complete F-12 HAM medium	Hygromycin	Flask
1 a	pH 6.94	p3'SSdimerClonEGFP plasmid DNA	+	-	+	1
1 b	pH 6.94	pSV2-DHFR 8.32 plasmid DNA				
2 a	pH 7.05	p3'SSdimerClonEGFP plasmid DNA	+	-	+	2
2 b	pH 7.05	pSV2-DHFR 8.32 plasmid DNA				
3 a	pH 7.11	p3'SSdimerClonEGFP plasmid DNA	+	-	+	3
3 b	pH 7.11	pSV2-DHFR 8.32 plasmid DNA				
4	pH 6.94	dH$_2$O	+	-	+	4
5	pH 7.05	dH$_2$O	+	-	+	5
6	pH 7.11	dH$_2$O	+	-	+	6
7	pH 7.05	p3'SSdimerClonEGFP plasmid DNA	-	+	+	7
8	pH 7.05	pSV2-DHFR 8.32 plasmid DNA	+	-	-	8
9	pH 7.05	dH$_2$O	+	-	+	9

Consistent with the observations that were recorded for single transfectants, the examination of cells under the microscope at high magnification one day following transfection revealed that the overall appearance of cells in flasks 1-9 had become darker and cells were observed to possess a profound 'peppery' appearance, characteristic of the integration of Ca$_2$PO$_4$ particles into their cytoplasm. These small black dots were absent from the cytoplasm of control cells in flask 10. Three days after the addition of ProCHO-AT medium with hygromycin to the flasks, cells present in flasks 1, 2 and 3 possessing both plasmids were observed to have a higher

cell density compared to cells present in flasks 4, 5, 6 and 9 where the $CaCl_2$-dH_2O mixtures had been added. Comparison of doubly transfected with both plasmids and $CaCl_2$-dH_2O transfected cells with control cells also confirmed this difference. The density and appearance of cells in flasks 7 and 8 were comparable to that of control flask 10, indicating that for these cells transfection had also been successful.

The observations mentioned above were maintained for the following six days, during which the first signs of colonies of stably transfected cells with either both p3'SSdimerClonEGFP and pSV2-DHFR 8.32 plasmids (in flasks 1-3) or only with p3'SSdimerClonEGFP plasmid (in flask 7) began to appear. These colonies were absent from flasks 4-6 in which only a few living and unhealthy cells were observed to be present. Cells in flask 8 transfected with pSV2-DHFR 8.32 plasmid were shown to decrease in density during this period of time. Eleven days after transfection, large and discrete colonies of cells had clearly become apparent in flasks 1-3. No such colonies could be observed in flasks 4, 5, 6 and 9 (transfected with $CaCl_2$-dH_2O) or control flask 10. Cells in flasks 4, 5, 6 and 9 were characterised by a significantly lower cell density compared to flasks 1-3 and by extensive cell death.

3.3.4 EXPANSION, SCREENING AND STORAGE OF CHINESE HAMSTER OVARY (CHO) CELL CLONES

Stable clones were isolated and expanded from single colonies as described in section 2.7 of Materials and Methods. Single and double transfectants were serially cloned and placed into LN_2 container for long-term storage, after having reached confluency in T25 flasks.

3.3.4.1 SINGLE TRANSFECTANTS

CHO cells were transfected with p3'SSdimerClonEGFP plasmid as described in section 2.6.1. Following the generation of 20 stably transfected clones, they were stored in liquid nitrogen (LN_2) container indefinitely. For each individual clone, the growth rate characteristics were recorded and are presented on table 3.6 below.

Table 3.6: Growth rate efficiency of each single transfected clone until long-term storage in LN$_2$ container

CHO-R clones	Days in selection	Duration of Bulking				Total culture duration	Growth rate characteristics	Total number of cells
	T75	96-WELL	24 –WELL	6-WELL	T25			
01	21	10	4	4	13	52	SLOW	1 x 10^6
02	21	10	4	4	4	43	FAST	6 x 10^5
03	21	10	4	4	27	66	SLOW	1 x 10^6
05	21	10	6	2	2	41	FAST	7 x 10^5
07	21	10	6	4	9	50	INTERMEDIATE	9 x 10^5
08	21	10	6	4	9	50	INTERMEDIATE	1.4 x 10^6
09	21	10	7	3	2	43	FAST	6 x 10^5
11	21	10	9	2	2	44	FAST	1.1 x 10^6
12	21	10	11	13	2	57	SLOW	9 x 10^5
13	21	14	7	11	14	67	SLOW	8 x 10^5
14	28	10	7	2	2	49	INTERMEDIATE	9 x 10^5
16	28	8	10	5	2	53	SLOW	9 x 10^5
17	28	10	6	3	3	50	INTERMEDIATE	1x 10^6
18	28	10	9	4	2	53	SLOW	1x10^6
19	28	10	9	4	3	54	SLOW	7 x 10^5
20	28	11	8	4	3	54	SLOW	8 x 10^5
21	28	10	9	6	8	61	SLOW	7 x 10^5
22	28	10	9	6	10	63	SLOW	1x 10^6
23	28	11	8	6	6	59	SLOW	1.3 x 10^6
24	28	13	6	6	9	62	SLOW	1 x 10^6

On table 3.6 shown above, the numbers of days in culture before isolation and during the different stages of serial cloning (96-well plate, 24-well plate, 6-well plate and T25 flask) are shown. Also presented is the final total number of cells for each clone before indefinite storage in LN$_2$ container.

3.3.4.2 DOUBLE TRANSFECTANTS

3.3.4.2.1 INITIAL SCREENING OF CLONES

Initial screening was performed as described in section 2.8 of Materials and
Methods. Following double transfection with p3'SSdimerClonEGFP and pSV2-
DHFR 8.32 plasmids, 167 clones were generated but only 68 of these clones were
frozen down in LN_2 container. The remaining clones either failed to be expanded, or
they were shown to be negative for EGFP expression following their screening on
Axiovert 200 M inverted fluorescence microscope. Screening observations were
recorded and are presented on table 3.7 below.

Table 3.7 Screening of doubly transfected CHO-R-O clones

CHO-R-O CLONE	SCREENING FOR EGFP EXPRESSION	FLUORESCENT SIGNAL / QUALITY OF TRANSFECTION
001	Positive	1-2 spots
002	Positive	2 expanded spots
003	Positive	2 intense spots
004	No	-
005	Negative	-
006	Positive	3 spots
007	Positive	2-3 spots
008	Positive	2-3 spots
009	Positive	Excellent
010	Positive	Good
011	Positive	1-2 spots-not too intense
012	Positive	1-2 discrete spots
013	Positive	2 intense spots
014	Positive	2 intense spots
015	Negative	-
016	Negative	-
017	Positive	2 intense spots
018	Positive	4 discrete spots
019	Positive	Excellent
020	Positive	2 expanded spots
021	Positive	2 expanded and intense spots
022	Positive	2 discrete spots
023	Positive	3 spots
024	Negative	-
025	Positive	2 discrete and intense spots
026	Positive	2 big spots
027	Negative	-
028	Negative	-
029	Positive	1 spot-not too intense
030	Positive	2 intense spots
031	Positive	4 big and discrete spots
032	Negative	-
033	Negative	-
034	Negative	-

CHO-R-O CLONE	SCREENING FOR EGFP EXPRESSION	FLUORESCENT SIGNAL / QUALITY OF TRANSFECTION
035	Negative	-
036	Positive	3-4 expanded and discrete spots
037	Negative	-
038	Positive	4 remarkably large spots
039	Positive	1 spot
040	Negative	-
041	Negative	-
042	Negative	-
043	Positive	2 large spots
044	Negative	-
045	Positive	1 intense spot
046	Positive	2 pairs of large and remarkably intense spots
047	Negative	-
048	Negative	-
049	Negative	-
050	Negative	-
051	Positive	1 moderately sized spot
052	Positive	1 moderately sized spot
053	Negative	-
054	Positive	3 spots
055	Negative	-
056	Negative	-
057	Positive	4 large and intense spots
058	Positive	2 large and intense spots
059	Positive	1 large spot
060	Negative	-
061	Positive	1 small spot
062	Negative	-
063	Negative	-
064	Negative	-
065	Negative	-
066	Positive	2 spots- 1 expanded
067	Negative	-
068	Negative	-
069	Negative	-
070	Negative	-
071	Negative	-
072	Negative	-
073	Positive	1 small but intense spot
074	Negative	-
075	Positive	1 small spot
076	Positive	1 large spot
077	Negative	-
078	Positive	4 expanded and intense spots
079	Positive	4 connected spots
080	Negative	-
081	Negative	-
082	Negative	-
083	Negative	-
084	Negative	-
085	Negative	-
086	Negative	-
087	Negative	-
088	Negative	-

CHO-R-O CLONE	SCREENING FOR EGFP EXPRESSION	FLUORESCENT SIGNAL / QUALITY OF TRANSFECTION
089	Negative	-
090	Negative	-
091	Negative	-
092	Negative	-
093	Negative	-
094	Negative	-
095	Negative	-
096	Negative	-
097	Negative	-
098	Negative	-
099	Negative	-
100	Negative	-
101	Negative	-
102	No. Cells present on coverslip-clone was kept	-
103	Negative	-
104	Negative	-
105	Negative	-
106	Negative	-
107	Negative	-
108	Positive	1 large spot of moderate intensity
109	Positive	1 tiny but intense spot
110	Negative	-
111	No	-
112	Positive	1 large spot
113	No	-
114	Negative	-
115	Positive	1 small but intense spot
116	Positive	5 small but intense spots
117	Negative	-
118	Negative	-
119	Negative	-
120	Positive	2 small, quite intense and interconnected spots
121	Positive	2 spots- 1 of these is expanded and intense
122	Positive	2 expanded and large spots
123	Negative	-
124	Negative	-
125	Negative	-
126	Negative	-
127	Negative	-
128	Negative	-
129	No	-
130	Negative	-
131	Positive	1 small but intense spot
132	Negative	-
133	Negative	-
134	Negative	-
135*	Positive	2 spots-1 of these is larger and more intense
136	Negative	-
137	Positive	1 remarkably large and intense spot
138	Negative	-

CHO-R-O CLONE	SCREENING FOR EGFP EXPRESSION	FLUORESCENT SIGNAL / QUALITY OF TRANSFECTION
139	Positive	3 small and discrete spots
140	Positive	2 discrete spots-1 of these is expanded
141	Positive	3 spots-2 of these are expanded and intense
142	Negative	-
143	Positive	2 discrete spots-1 of these is expanded and intense
144	Negative	-
145	Negative	-
146	Negative	-
147	Positive	1 expanded spot
148	Negative	-
149	Negative	-
150	Positive	3 intense spots-2 of these are expanded
151	Positive	2 quite large spots
152	Negative	-
153	Positive	1 expanded spot
154	Negative	-
155	Positive	1 spot
156	Negative	-
157	Negative	-
158	Positive	1 expanded spot
159	Negative	-
160	Negative	-
161	Negative	-
162	Negative	-
163	Negative	-
164*	Positive	15 intense spots-3 of these are remarkably large
165*	Positive	More than 20 expanded spots
166*	Positive	16 intense and expanded spots
167*	Positive	15 intense and expanded spots

Table 3.7 above provides information associated with the initial screening of the 167 double transfected clones. Only clones that were proved to be positive for EGFP expression were frozen in LN$_2$ container for long-term storage. Regarding the assessment of EGFP expression for each individual clone, the total number of fluorescent spots was recorded following examination of four random FOV (see section 2.8.2). It should be noted that * sign denotes screening of cells at 24-well plate stage of expansion.

Representative images of discrete and intense and expanded and intense spots within the nuclei of CHO-R-O-25, CHO-R-O-9 and CHO-R-O-167 cells are presented in figure 3.3 below, whereas in figure 3.4 the graph shown provides information associated with the % frequency of EGFP-expressing cells, in a number of different clones. Examination of these pictures reveals that the discrete and intense fluorescent spot of clone CHO-R-O-167 is larger compared to those of clones CHO-R-O-9 and CHO-R-O-25, while the expanded and intense spots of clones CHO-R-O-9 and CHO-R-O-167 (figures 3.3 e and f) are larger in comparison with that of clone CHO-R-O-25 (figure 3.3 d). This EGFP spot over-expression for clones CHO-R-O-9 and CHO-R-O-167 is possibly due to the fact that there was a lower ratio of lac O sequences within the nuclei of cells in conjunction with the fact that lac repressor-EGFP fusion proteins were present in excess (173, 238). This abnormal stoichiometry resulted in the non-specific binding of EGFP to random sequences of the genome, followed by the subsequent augmentation of the fluorescent signal observed within the nuclei of these cells.

CHO-R-O-25	CHO-R-O-9	CHO-R-O-167

(a)   (b)   (c)

(d)   (e)   (f)
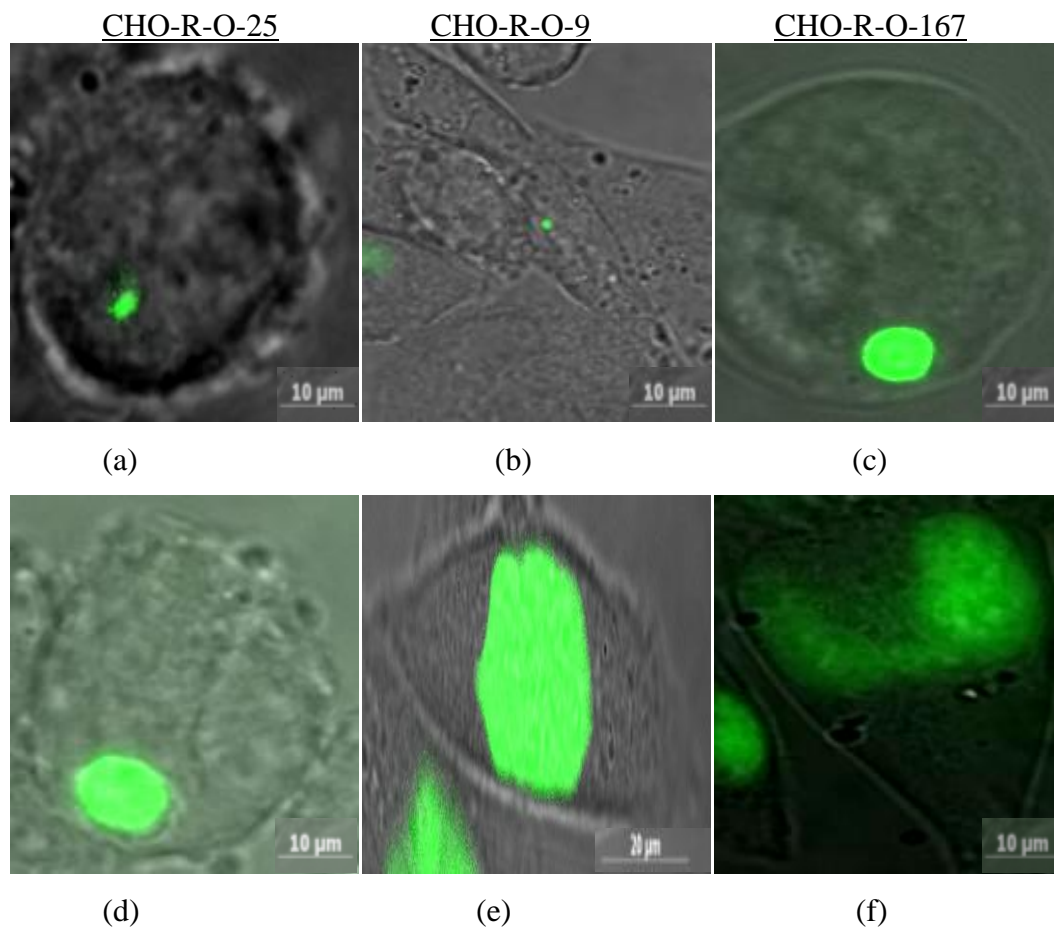
Figure 3.3 Representative examples of discrete and intense and expanded and intense fluorescent spots within the nuclei of CHO-R-O-25, CHO-R-O-9 and CHO-R-O-167 cells

a) **Discrete and intense fluorescent spot within the nucleus of a CHO-R-O-25 cell**
b) **Discrete and intense fluorescent spot within the nucleus of a CHO-R-O-9 cell**
c) **Discrete and intense fluorescent spot within the nucleus of a CHO-R-O-167 cell**
d) **Expanded and intense fluorescent spot within the nucleus of a CHO-R-O-25 cell**
e) **Expanded and intense fluorescent spot within the nucleus of a CHO-R-O-9 cell**
f) **Expanded and intense fluorescent spot within the nucleus of a CHO-R-O-167 cell**
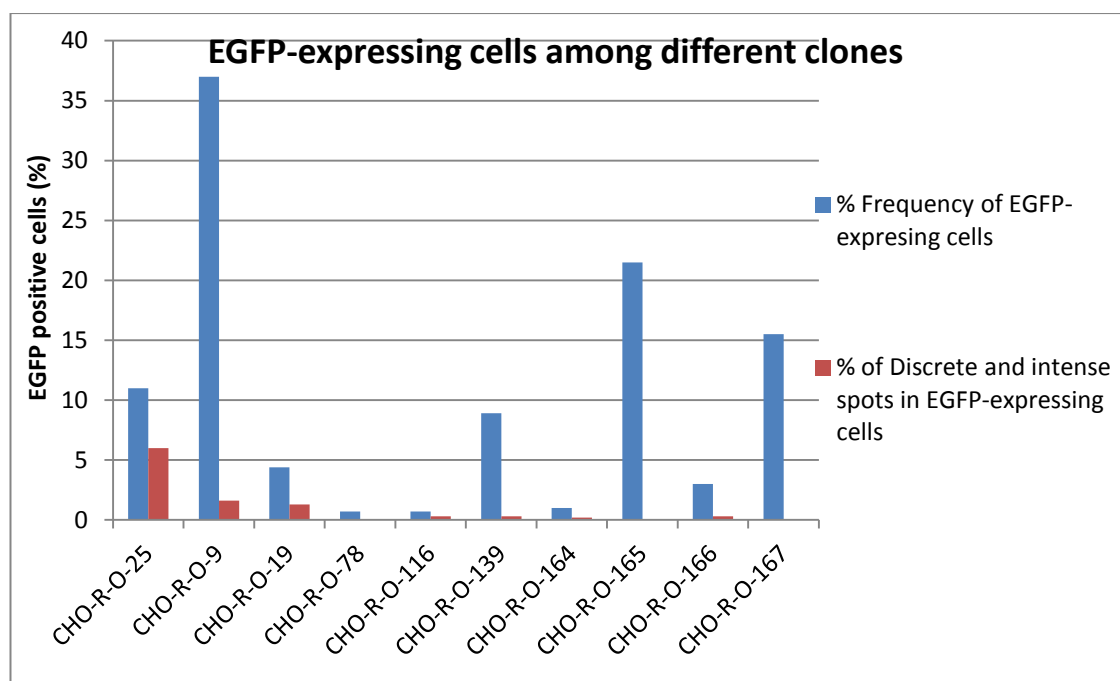
Figure 3.4 Percentages of EGFP-expressing cells and discrete and intense fluorescent spots within these cells, following the initial screening of clones CHO-R-O-25, CHO-R-O-9, CHO-R-O-19, CHO-R-O-78, CHO-R-O-116, CHO-R-O-139, CHO-R-O-164, CHO-R-O-165, CHO-R-O-166 and CHO-R-O-167

3.3.4.2.2 EGFP EXPRESSION STABILITY ASSESSMENT

In order to ensure that the level of EGFP expression is maintained in doubly transfected cells over time, cells growing on glass-bottom dishes were regularly screened on the Axiovert 200 M inverted fluorescence microscope using the Multidimensional Acquisition function of Axiovision 4.5 acquisition program. This screening also facilitated the selection of the clone of interest for subsequent time-lapse experiments. Ideally, the cells from the clone of interest would be characterised by a high frequency of cells containing discrete and intense fluorescent spots. There were two main reasons behind this preference. First in this way, chromatin regions within the nuclei of cells that were tagged by EGFP would be able to be compared with untagged chromatin regions in time-lapse experiments, following exposure of cells to chemicals or γ-irradiation. Second, alterations regarding the intensity, shape and expansion of fluorescent spots could be tracked more efficiently in discrete and intense compared to over expanded and diffuse fluorescent spots, within the nuclei of cells under investigation.

A number of clones termed as CHO-R-O-9, CHO-R-O-19, CHO-R-O-25, CHO-R-O-78, CHO-R-O-116, CHO-R-O-139, CHO-R-O-164, CHO-R-O-165,

CHO-R-O-166 and CHO-R-O-167 were screened for EGFP expression and the percentages of EGFP-positive cells and cells containing discrete and intense fluorescent spots within their nuclei were determined over seven consecutive passage numbers (see graphs in figures 3.5 and 3.6 below).
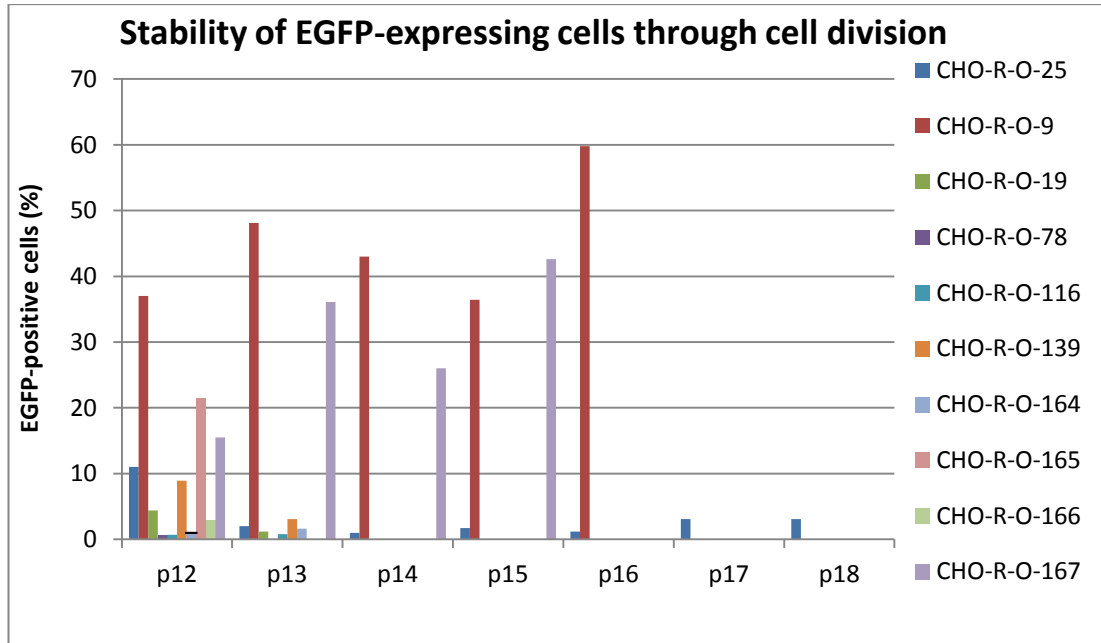
Figure 3.5 Graphic representation of the fraction of EGFP-expressing cells in clones CHO-R-O-25, CHO-R-O-9, CHO-R-O-19, CHO-R-O-78, CHO-R-O-116, CHO-R-O-139, CHO-R-O-164, CHO-R-O-165, CHO-R-O-166 and CHO-R-O-167 over seven consecutive passage numbers (p12 –p18).
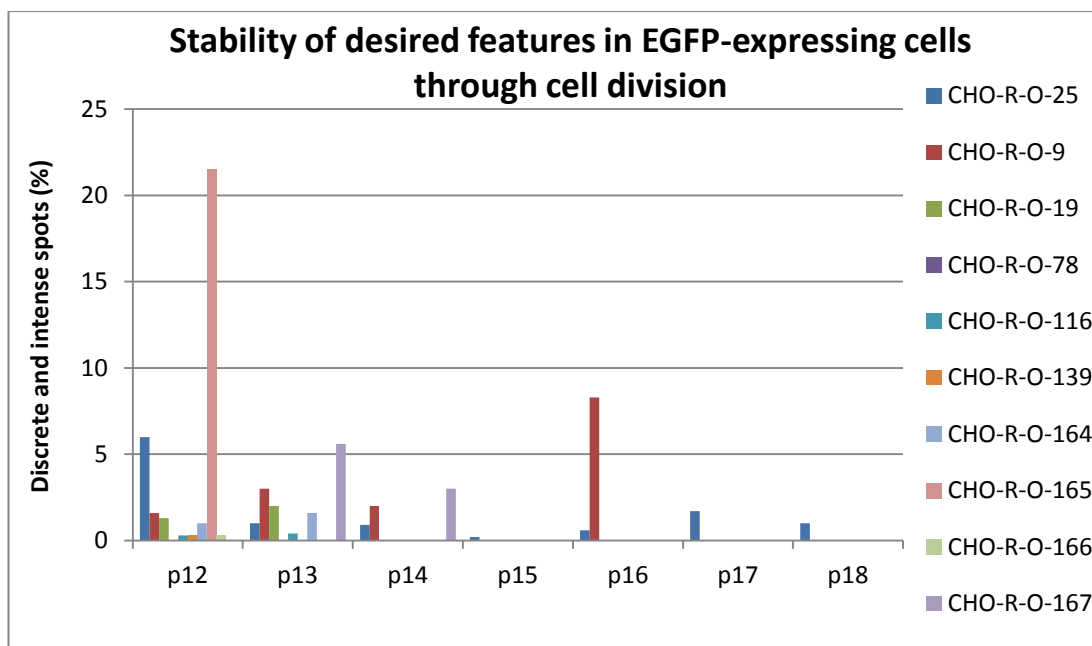
Figure 3.6 Percentage of discrete and intense fluorescent spots within EGFP-expressing cells of clones CHO-R-O-25, CHO-R-O-9, CHO-R-O-19, CHO-R-O-78, CHO-R-O-116, CHO-R-O-139, CHO-R-O-164, CHO-R-O-165, CHO-R-O-166 and CHO-R-O-167 over seven consecutive passage numbers (p12 –p18).

Initial screening observations had suggested that the overall frequency of EGFP – expressing cells within clone CHO-R-O-25 was 11 % with 6 % of these cells containing discrete and intense fluorescent spots. However, later screening observations suggested that the overall percentage of EGFP – expressing cells had been decreased to 1- 2 %, with <1 % of fluorescent spots being discrete and intense. In both of two subsequent screening observations of CHO-R-O-25 cells that were derived from a separate stock, the overall percentage of EGFP-expressing cells had been increased to 3.1 %, with cells containing discrete and intense fluorescent spots representing 1.7 % and 1 % of the total population, respectively (see table 3.8 below). In addition, observation of table 3.9 (a-i) below suggests that despite the fact that in other clones the overall percentage of fluorescent spot containing cells might have been higher than that of CHO-R-O-25, the latter was selected for further analysis, because the majority of EGFP-expressing cells were observed to display the desired features in the initial screening with 6 % of the total of EGFP-expressing cells containing a discrete and intense fluorescent spot within their nuclei.

Table 3.8 Presentation of EGFP-expression features for clone CHO-R-O-25

CLONE	% FREQUENCY	CELLS WITH DISCRETE AND INTENSE SPOTS (%)	CELLS WITH EXPANDED AND INTENSE SPOTS (%)	CELLS WITH EXPANDED AND DIFFUSE SPOTS (%)
CHO-R-O-25 (1st screening)	11	6	5	0
CHO-R-O-25 (2nd screening)	2	1	1	0
CHO-R-O-25 (3rd screening)	1	0.9	0.1	0
CHO-R-O-25 (4th screening)	1.7	0.2	0.5	1
CHO-R-O-25 (5th screening)	1.2	0.6	0	0.6
CHO-R-O-25 (6th screening)	3.1	1.7	0.8	0.5
CHO-R-O-25 (7th screening)	3.1	1	0.5	1.5
Average	3.3	1.6	1.1	0.5

Table 3.8 above shows the percentages of EGFP - expressing cells, the percentages of discrete and intense, expanded and intense and expanded and diffuse spots in clone CHO-R-O-25 following the performance of seven independent screening experiments on Axiovert 200 M inverted fluorescence microscope. Note the abrupt decrease in the percentage of EGFP-expressing cells and the proportion of these cells containing discrete and intense spots in screening observations 2-5 and the slight increase in observations 6 and 7

Table 3.9 Presentation of EGFP-expression features for the remaining screened clones

CLONE	FREQUENCY (%)	DISCRETE & INTENSE SPOTS (%)	EXPANDED & INTENSE SPOTS (%)	CELLS >1 SPOT (%)
CHO-R-O-9 (p10)	37	1.6	16.7	4.8
CHO-R-O-9 (p11)	48.1	3	28.8	6
CHO-R-O-9 (p12)	43	2	23	5.2
CHO-R-O-9 (p13)	36.4	0	22.3	7.3
CHO-R-O-9 (p14)	59.8	8.3	41.1	8.8
AVERAGE	44.9	3	26.4	6.4

a) Screening of clone CHO-R-O-9 over five consecutive passage numbers (p10 – p14)

CLONE	FREQUENCY (%)	DISCRETE & INTENSE SPOTS (%)	EXPANDED & INTENSE SPOTS (%)	CELLS >1 SPOT (%)
CHO-R-O-19 (p10)	4.4	1.3	0.21	0.3
CHO-R-O-19 (p11)	1.2	2	0.9	0.4
AVERAGE	2.8	1.6	0.6	0.35

b) Screening of clone CHO-R-O-19 over two consecutive passage numbers (p10 – p11)

CLONE	FREQUENCY (%)	DISCRETE & INTENSE SPOTS (%)	EXPANDED & INTENSE SPOTS (%)	CELLS >1 SPOT (%)
CHO-R-O-78 (p10)	0.7	0	0	0

c) Screening of clone CHO-R-O-78 at p10

CLONE	FREQUENCY (%)	DISCRETE & INTENSE SPOTS (%)	EXPANDED & INTENSE SPOTS (%)	CELLS >1 SPOT (%)
CHO-R-O-116 (p10)	0.7	0.3	0.3 (diffuse)	0
CHO-R-O-116 (p11)	0.8	0.4	0.4 (diffuse)	0
AVERAGE	0.8	0.4	0.4	0

d) Screening of clone CHO-R-O-116 over two consecutive passage numbers (p10 – p11)

CLONE	FREQUENCY (%)	DISCRETE & INTENSE SPOTS (%)	EXPANDED & INTENSE SPOTS (%)	CELLS >1 SPOT (%)
CHO-R-O-139 (p10)	8.9	0.3	2.5	0.3
CHO-R-O-139 (p11)	3.1	0	0.3	0.3
AVERAGE	6	0.1	1.4	0.3

e) Screening of clone CHO-R-O-139 over two consecutive passage numbers (p10 – p11)

CLONE	FREQUENCY (%)	DISCRETE & INTENSE SPOTS (%)	EXPANDED & INTENSE SPOTS (%)	CELLS >1 SPOT (%)
CHO-R-O-164 (p10)	1	0.2	0	0
CHO-R-O-164 (p11)	1.6	0	1.6 (diffuse)	0
AVERAGE	1.3	0.1	0.8	0

f) Screening of clone CHO-R-O-164 over two consecutive passage numbers (p10 – p11)

CLONE	FREQUENCY (%)	DISCRETE & INTENSE SPOTS (%)	EXPANDED & INTENSE SPOTS (%)	CELLS >1 SPOT (%)
CHO-R-O-165 (p10)	21.5	0	7.8	5.2

g) Screening of clone CHO-R-O-165 at p10

CLONE	FREQUENCY (%)	DISCRETE & INTENSE SPOTS (%)	EXPANDED & INTENSE SPOTS (%)	CELLS >1 SPOT (%)
CHO-R-O-166 (p10)	3	0.3	2.8	0

h) Screening of clone CHO-R-O-166 at p10

CLONE	FREQUENCY (%)	DISCRETE & INTENSE SPOTS (%)	EXPANDED & INTENSE SPOTS (%)	CELLS >1 SPOT (%)
CHO-R-O-167 (p10)	15.5	0	0.6	0.3
CHO-R-O-167 (p11)	36.1	5.6	11.4	4.6
CHO-R-O-167 (p13)	26	3	6	3.7
CHO-R-O-167 (p15)	42.6	0	18.4	2.1
AVERAGE	30.1	2.2	9.1	2.7

i) Screening of clone CHO-R-O-167 at p 10, p11, p13 and p15

Table 3.9 above shows the percentages of EGFP - expressing cells, discrete and intense and expanded and intense spots and the percentages of cells containing more than one spot within their nuclei following screening of clones CHO-R-O-9, CHO-R-O-19, CHO-R-O-78, CHO-R-O-116, CHO-R-O-139, CHO-R-O-164, CHO-R-O-165, CHO-R-O-166 and CHO-R-O-167 on Axiovert 200 M inverted fluorescence microscope

3.4 DISCUSSION

3.4.1 SELECTION AND CLONING OF STABLE TRANSFECTANTS

Morphological characteristics of transfected cells during screening revealed that the doubly transfected CHO-R-O-25 cells were, in the main, more rounded in comparison to CHO DG44 un-transfected cells which were spindle-shaped and more flattened (see figures 4.3 and 4.4 below). This finding was consistent with that of Belmont et al (1999), where transfected CHO cells were more rounded compared to un-transfected cells (177). Similarly, 13 and 11 days into selection after single and double transfection respectively, control un-transfected flasks were characterised by a high degree of cell death and remarkably low cell density in comparison with the transfected cells (sections 3.3.1 and 3.3.3). The replacement of hygromycin in the medium of the culture flasks during selection every 3 – 4 days was necessary due to the short half-life of this antibiotic (177). Further, it has been suggested that the level of GFP expression is lowered after growth of transfected cells in the absence of selection agent in the medium for one month (257). Studies in human cells transfected with plasmids containing viral origins of replication have shown that this is due to the loss of plasmids from the chromosomes of the transfected cells (258). More specifically, the interaction between the lac I-RFP-NLS fusion construct with the 264-copy lac O repeat in viral derived plasmid within HeLa cells has shown that this plasmid loss in the absence of selective pressure is due to the failure of the plasmids to be synthesized during DNA replication or abnormal segregation of chromosomes during mitosis (259).

In previous studies the cloning of stable transfectants with the p3'SSdimerClonEGFP plasmid led to satisfactory expression of the lac repressor-GFP fusion construct that could bind to the entirety of the lac operator sites (237). However, in some instances the nuclear background staining is high leading to poor S:N ratio (238). Therefore, it is important to identify optimal GFP transfectants at an early stage in the cloning process (238). Two approaches can be used. The first approach involves the culturing of cell colonies onto 12-mm glass coverslips that are present in small plastic Petri dishes. A different dilution of cells is applied onto each coverslip and once they have grown enough to be observable by light microscopy, they are transferred by aseptic techniques to 4 cm Petri dishes. After having located

colonies with optimal levels of lac repressor-GFP expression under the U.V. light microscope, the regions of the coverslips that possess colonies of interest are broken with the aid of a sterile diamond pen and cells trypsinized before being transferred and cloned into the wells of 96-well plates (238). This method is suitable for the quick, short-term detection of GFP fluorescence (177).

The second approach involves the isolation of numerous colonies of cells by either employing filter-tipped based trypsinization or by using micropipette tips to directly pick up separate colonies (177). This is followed by the cloning of cells into 96-well plates. Additional screening can be performed to ensure the purity of the identity of the clones (177). Great care has to be taken in order to avoid the mixing of transfectant cells derived from different clones, while attempting to pick up colonies of cells. This method is the easiest to follow and it results in the more efficient culturing of cells than the method described by Strukov et al (2005) (238). The main drawbacks of this method are that it is more expensive due to the high cost of the 96-well plates and that colony selection is influenced by the different rates of cell division of different clones (177).

The second method was employed for the cloning of single and double transfectants in this study, with colonies isolated with the aid of unplugged glass Pasteur pipettes (section 2.7.1). Most of the discrete colonies of cells were present at a small distance from each other and in order to prevent the risk of cross-contamination between different clones derived from different cell progenitors, only a few distinct colonies located at distant sites were picked up. These were then cloned as standard. All other colonies were isolated and cloned by additional serial dilution cloning into the wells of 96 – well plates (section 2.7.2). Colonies of single and double transfected cells were obtained from all three cell suspensions that contained 3.5, 35 and 350 cells, respectively (section 2.7.2). In total, 20 single transfected and 68 double transfected clones were isolated and frozen in LN_2 container (see tables 3.6 and 3.7, respectively).

3.4.2 GENERAL DISCUSSION ON LAC OPERON APPROACH

Undoubtedly, the lac operon approach has greatly facilitated the visualisation of specific chromatin sites in living cells throughout the cell cycle, without affecting the ultra structure of chromatin (173, 235, 238). In living budding yeast (211) and CHO cells (173), single copies of the integrated lac O repeats have been efficiently localised. In *Saccharomyces cerevisiae* budding yeast, the separation of sister chromatids during mitosis and chromosomal movements have been tracked (211). In addition, in the same organism information associated with mitotic spindle dynamics and chromosome and centromere separation during mitosis has been obtained through the employment of this system (260). In CHO cells, the structure of chromatin fibres has been studied in great detail (173, 235) and in other studies it has been followed through different stages of the cell cycle, unveiling a relationship between DNA replication, transcription and the alteration of chromatin fibre conformations (203, 241). Moreover, in living human cells the tracking of restricted chromatin movements has been permitted through the binding of the 126-copy lac O repeat to lac repressor – EGFP – NLS fusion protein (64).

In terms of the efficiency and stability of the insertion of lac O repeats to chromosomal sites of living cells, the disadvantage of the lac repressor-GFP/lac operator labelling approach is that in some occasions this is a quite difficult task to achieve (177) and that the large length of the lac operator insert is likely to perturb chromosomal structure and function. In addition, the DNA sequences under investigation cannot be always detected within specific chromosomal sites (235). Moreover, according to Belmont et al (1999), the stability of expression of the HSRs is reduced by the expression of lac repressor for long periods of time (177). The difficulties of the *in vitro* detection of lac operator repeats have led to the proposal that the visualisation of lac operator repeats may produce better results by performing indirect immunostaining of the repeats, instead of their direct visualisation in living cells (177).

3.4.3 EGFP EXPRESSION CHARACTERISTICS

Screening observations on Axiovert 200 M inverted fluorescence microscope suggested that the majority of the clones visualised were characterized by low percentages of EGFP-expressing cells (tables 3.8 and 3.9 in section 3.3.4.2.2). This is consistent with the findings of Belmont et al (1999), who observed only a minority of generated clones (≥ 5 %) to be characterised by high lac repressor –EGFP - NLS expression levels following the transfection of A03 CHO cell line with plasmids containing the lac O repeat and the lac repressor – EGFP – NLS fusion protein (177). Moreover, Strukov et al (2005) demonstrated that the binding of lac repressor – EGFP construct to the 256-copy lac operator repeat in the A03 clone of CHO cells (241) corresponded only to 10 % of the total amount of lac O repeats that were present within the chromosomes of these cells (238). The authors speculated that the efficiency of binding of lac repressor-EGFP to lac operator repeats is dependent on the integrated position of the repeats within the chromosomes (238). This is therefore a plausible explanation for the low frequency of EGFP-expressing cells in clone CHO-R-O-25 (3.3 %; table 3.8), taking into consideration the stringent cloning procedure employed (section 2.7), and which is further supported by the variable frequencies of cells containing EGFP expression in CHO-R-O-9, CHO-R-O-165 and CHO-R-O-167 clones (45 %, 22 % and 30 % respectively; see table 3.9 a, g and i).

It has been argued that temperature conditions during culturing affect GFP protein maturation and expression levels in *E. coli,* yeast (261) and mammalian cells (261-264). For example, chromogranin B – GFP fusion protein failed to mature in HeLa cells at 37 ^{o}C and thus exhibited no fluorescence, however, the decrease of temperature levels to 15 ^{o}C and 20 ^{o}C resulted in the detection of fluorescence (262). In another study that employed vertebrate and primary embryonic cells transfected with GFP cDNA it was shown that while incubation of cells at 37 ^{o}C resulted in the production of a very weak fluorescence signal, incubation at 30 ^{o}C resulted in the generation of intense fluorescence (263). In addition, following the fusion of GFP to human glucocorticoid receptor, the resulting fusion construct was functional in the activation of the mammary tumour virus promoter only at 30 ^{o}C and not at 37 ^{o}C (263). Consistent with this, Robinett et al (1996) found that the culturing of cells at 32°C for 2 days resulted in the considerable increase of GFP-expressing cells from an insignificant fraction to 20 - 50 % (173). Finally, similar conclusions have been drawn by Pines (1995) who had used cyclin-GFP fusion proteins in order to study

the activation of cyclin-dependent kinases (CDKs) and progression through the cell cycle in living COS-7, HeLa and NIH 3T3 cells. Their study demonstrated that incubation of cells at 33 ^{o}C results in the production of an improved fluorescence signal in comparison with incubation at 37 ^{o}C (264).

Heim et al (1995) induced a Serine 65 to Threonine (S65T) mutation in GFP, thereby generating the improved GFP (iGFP) protein. This iGFP version increased the maturation rate and intensity of fluorescence in this protein, especially after transient transfection. However, its disadvantage was that it was characterised by variations in fluorescence intensity within several days after stable transfection (265). For these reasons, Belmont et al (1999) employed the enhanced GFP (EGFP) protein, in order to fluorescently label chromatin in CHO cells. The difference of EGFP from the original GFP is that it contains two point mutations not found in GFP. The authors concluded that regarding transient transfection, the protein fluoresces ideally at 37 ^{o}C and in stable transfection studies its expression is not affected by temperature conditions during culturing (177). Based on this, it was reasonable to use the lac repressor-EGFP fusion construct in our investigation.

A number of studies have shown that plasmid copy number within the chromosomes is intimately associated with transgene expression levels within host cells (257, 266, 267). In transgenic mouse cells, Garrick et al (1998) demonstrated that the presence of transgene tandem repeats is responsible for gene silencing induction. By using lox/Cre mediated recombination it was shown that the decrease in the number of transgene copies was linked to a decrease in the methylation levels at the transgene expression site within the genome and the interlinked increase in transgene expression levels (266). Similar results were obtained from experiments on murine embryonal carcinoma stem cells, in which multi-copy plasmid insertions within chromosomes resulted in a lower expression level compared to single-copy plasmid integrations (267). The authors attributed this phenomenon to methylation events on the gene sequences of tandem repeats that in turn resulted in gene silencing (267). In a subsequent study, Derouazi et al (2006) demonstrated that the level of GFP expression in transfected CHO DG44 cells is inversely correlated with the plasmid copy number in the chromosomes of the clones. More specifically, it was shown that cells from a clone characterised by the highest level of GFP expression contained a low-copy plasmid number, whereas cells from a clone characterised by the lowest level of GFP expression contained a high-copy plasmid number (257).

Following the generation of stably transfected cells in this study, fluorescence microscopy screening revealed differences associated with the morphological features of fluorescent spots within the nuclei of different clones (section 3.3.4.2.1). While in cells of certain clones such as CHO-R-O-25 the majority of the fluorescent spots were discrete and intense (table 3.8), in other clones such as CHO-R-O-9 most of the fluorescent spots were expanded and intense (table 3.9 a). In addition, examples of EGFP over-expression were apparent in clones CHO-R-O-9 (figure 3.3 e) and CHO-R-O-167 (figure 3.3 f). In essence, the fluorescence signal that is produced from the random roaming of lac repressor proteins within the nuclear space has been shown to increase the nuclear background staining and confuse the observations (39). Given that a proportion of lac repressor-GFP construct is strongly bound to a nuclear substructure, fluorescence loss in photobleaching (FLIP) experiments can be performed in order to increase the S:N ratio and thus remove some of the background nuclear staining produced by these freely roaming GFP-tagged proteins, without affecting the fluorescence signal of the lac O - bound lac repressor - GFP proteins (268, 269).

Robinett et al (1996) have provided their own explanation for EGFP over-expression. The authors have argued that this phenomenon is due to a combination between the elevated expression levels of lac repressor - EGFP fusion protein in comparison to the copy number of lac O repeats that have been incorporated into the chromosomes and the level of nonspecific binding of the fusion proteins on random DNA sequences of the genome (173). In their work, the authors termed this over-expression as nuclear background staining (173). Strukov et al (2005) have further supported this notion by arguing that lac repressor-EGFP expression must be at appropriate levels to ensure the ideal binding of fusion protein to lac O repeats, while at the same time maintaining a low nuclear background level (238). The authors further argued that in cells characterised by low levels of EGFP fluorescence signal the visualisation efficiency was increased, because the S:N ratio was more favourable. Based on this, the employment of a plasmid expression vector such as p3'SS (237) which contains a weak promoter (F9-1 polyoma promoter) produced the most favourable results. However, it should be highlighted that Strukov et al (2005) aimed in the detection of a single copy of lac O repeat in the nuclei of CHO cells. In other studies that assessed chromatin movements during

interphase, such as the study of Chubb et al (2002), the presence of multiple lac O copies were required for the most ideal detection sensitivity (64). In our project, fluorescence microscopy screening observations revealed that the S:N ratio was not favourable in clones such as CHO-R-O-9 and CHO-R-O-167 (figure 3.3 e and f respectively), but favourable in clones such as CHO-R-O-25 (figure 3.3 a). Only those clones with optimal S:N EGFP expression were selected for further experimentation. Accordingly, the co-transfection of CHO cells using equimolar concentrations of p3'SSdimer ClonEGFP and pSV2-DHFR 8.32 plasmids was ideal in order to achieve both favourable binding of the lac repressor-EGFP fusion proteins to the lac O repeats and the generation of low levels of EGFP over-expression / nuclear EGFP background.

3.4.4   SUMMARY OF FINDINGS

In conclusion, it has been shown that following the co-transfection of CHO DG44 cells with p3'SSdimer ClonEGFP and pSV2-DHFR 8.32 plasmids, numerous stably transfected clones can be generated. Following the isolation and screening of 167 clones, 68 clones that were shown to be positive for EGFP expression were stored in liquid nitrogen container. From these stable transfectants, CHO-R-O-25 cells were used for further experimentation. Screening revealed that these cells contained discrete and intense fluorescent spots, the physical alterations of which could be most ideally tracked. Although the percentage of EGFP-expressing CHO-R-O-25 cells was low (3.3 %; table 3.8), the fact that the vast majority of fluorescent spots within the nuclei of these cells exhibited the desired features (discrete and intense fluorescent spots), suggested that clone CHO-R-O-25 would be well-suited for use in subsequent time-lapse experiments. In contrast, in other clones (CHO-R-O-9 and CHO-R-O-167) the majority of cells contained fluorescent spots unfavourable for future experiments (expanded; table 3.9a and 3.9 i).

CHAPTER 4: ASSESSMENT OF CLONE CHO-R-O-25 CHARACTERISTICS

The observation of CHO-R-O-25 cells by light microscopy and their screening on Axiovert 200 M inverted fluorescence microscope had revealed that these cells were smaller compared to control CHO DG44 cells. In order to gain further insight into CHO-R-O-25 clone morphological and physiological characteristics, various experiments were performed. These included cell counts to determine growth rates, cytoplasmic, nuclear and dual (cytoplasmic and nuclear) staining to confirm that the EGFP spots are present within the nuclei of cells, PCNA staining to determine the fractions of replicating cells and fluorescence *in situ* hybridisation (FISH) to identify the chromosome containing the lac O incorporation. All experiments with the exception of FISH were also performed on CHO DG44 cells, in order to be able to identify any differences with the parental cell line.

4.1 GROWTH CHARACTERISTICS

The determination of growth characteristics was achieved using cell counts from cells grown in 6-well plates and T75 flasks as described in sections 4.1.1.1 and 4.1.1.2 below, respectively. It aimed to compare the durations of lag, exponential growth (log) and plateau phases of growth between CHO-R-O-25 and CHO DG44 control cells. Information associated with cell division times was obtained from population doubling time calculations (as described in section 4.1.1 below) corresponding to short-term (6-well plate) and long-term (T75 cumulative counts) growth rates.

4.1.1 GROWTH CURVES

Cell counts from CHO-R-O-25 and CHO DG44 cells growing in 6-well plates and T75 flasks were recorded in triplicate in order to determine the short-term and long-term growth characteristics of the transfected and control cells, respectively. The doubling time of cells was calculated using the following formula: Doubling Time = $(t_2 - t_1)$ * [log final total number of cells / log (final total number of cells / initial total number of cells)], where t_2 = final time point of exponential growth phase and t_1 = initial time point. The final total number of cells was reflected by the total number of cells at the last time point of exponential growth phase, whereas the initial total

number of cells corresponded to the total number of cells at the beginning of log phase.

4.1.1.1 SHORT-TERM GROWTH CURVES

CHO cells were maintained and passaged as described in section 2.3.3.2 of Materials and Methods. 1.6×10^5 of CHO-R-O-25 and control CHO DG44 cells was reseeded into 6-well plates in a total of 3 ml of medium. At 24, 48, 72, 96, 120 and 144 hours from reseeding cells were passaged and the total number of cells in each well determined. The results were pooled and plotted as shown on the graph of figure 4.1 below.
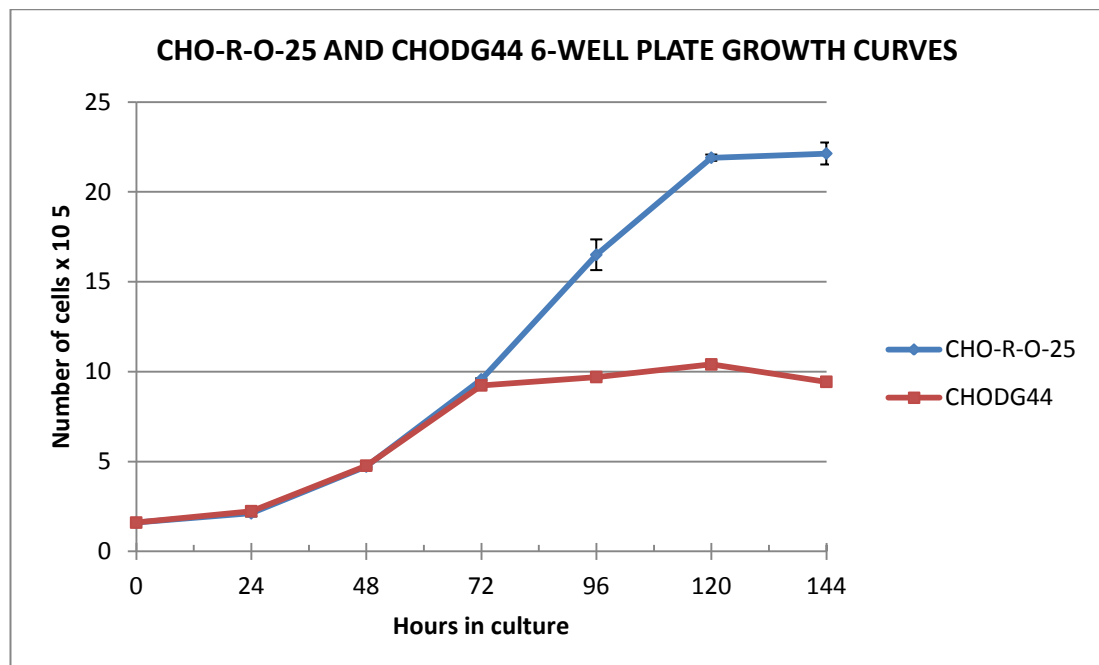
Figure 4.1 Short-term growth curves for CHO-R-O-25 and CHO DG44 cells. The cell counts for CHO-R-O-25 cells are present on the markers of the blue graph whereas the corresponding counts for CHO DG44 cells are represented by the markers of the red graph. Error bars represent S.D.

The doubling times of CHO-R-O-25 and CHO DG44 control cells were found to be equal to 22.4 hours and 23.8 hours, respectively. Therefore, based on these calculations the growth rates of these two populations are comparable, with CHO-R-O-25 cells doubling only ~1 hour and 30 minutes faster than CHO DG44 control cells. This finding indicates that the plasmid integrations within the chromosomes of

CHO-R-O-25 cells do not result in interferences or delays in cell division compared to the parent cell type. The exponential growth (log) phase of control CHO DG44 cells is represented by the time interval of 24 – 72 hours (figure 4.1). However, past this time point and until the last time point of cell count (144 hours), CHO DG44 cells reached the plateau phase. On the other hand, the log phase of CHO-R-O-25 cells lasted significantly longer, as it was shown to cover the 24 – 120 hour time interval. Unlike CHO DG44 cells, CHO-R-O-25 cells were observed to plateau during the last 24 hours (time interval of 120 – 144 hours).

4.1.1.2 LONG-TERM GROWTH CURVES

In order to illustrate the long-term growth characteristics of clone CHO-R-O-25 and control CHO DG44 cells, cumulative cell counts were performed for each cell type at each time point. 1.25×10^6 of CHO-R-O-25 and control CHO DG44 cells was reseeded in two T75 flasks. Upon confluency (~120 hours later), the total number of cells in each flask was determined and 1.25×10^6 cells reseeded in another T75 flask. The same procedure was followed for 6 consecutive passage numbers. The results were used to construct graphs of CHO-R-O-25 and control CHO DG44 long-term growth rates over a period of ~900 hours, using the following formula: cumulative total number of cells = (total number of cells at present harvest x total number of cells at previous harvest) / seeding density. The cumulative total number of cells for the remaining time points was determined likewise. Following the calculation of the total number of cells for each cell type at each time point, the cumulative total number of cells at the time points of passage were determined (see table 4.1 and figure 4.2 below).

Table 4.1 Cumulative growth rates of CHO-R-O-25 and CHO DG44 cells cultured over a period of ~ 38 days

CHO-R-O-25		CHO DG44	
Hours in culture	Average total number of cells (x 10^6)	Hours in culture	Average total number of cells (x 10^6)
0	1.25	0	1.25
98	7.95	102	7.45
215	56.948	212	51.112
321	413.6942	324	351.935
407	2728.461	406	2559.535
539	18014.84	541	15866.46
671	129134. 7	676	122482.3
775	475032.1	790	813013.5
897	6266170	903	5772166
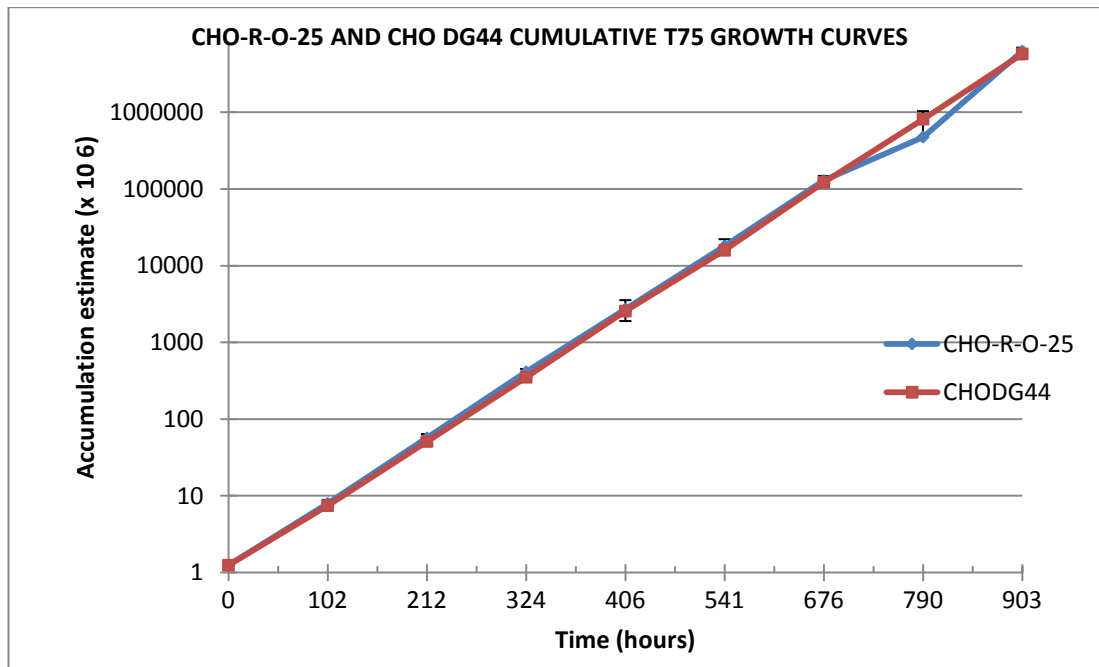
Figure 4.2 Long –term growth curves for CHO-R-O-25 and CHO DG44 cells. The cumulative cell counts for CHO-R-O-25 cells are present on the markers of the blue graph whereas the corresponding cumulative cell counts for CHO DG44 cells are found on the markers of the red graph.

Both CHO-R-O-25 and CHO DG44 cell lines are characterised by comparable rates of long-term growth, as evidenced by the fact that the two graphs are almost superimposable (figure 4.2). Further, the cell population doubling time for CHO-R-O-25 cells was found to be equal to 37.3 hours, whereas the corresponding time for CHO DG44 cells was 40.7 hours. This however is not consistent with the short-term growth rates for CHO-R-O-25 and CHO DG44 cells (22.42 and 23.84 hours respectively; section 4.1.1.1). This difference is likely a consequence of the long-term growth curves essentially flattening the exponential phase, through the inclusion of the lag period in the slope. Overall though, no differences in growth rate were observed between these cell lines, supporting the previous argument that plasmid incorporations within the chromosomes of CHO-R-O-25 cells do not delay the cell division times of these cells. Representative Phase images of CHO DG44 and CHO-R-O-25 cells are shown in figures 4.3 and 4.4 below.
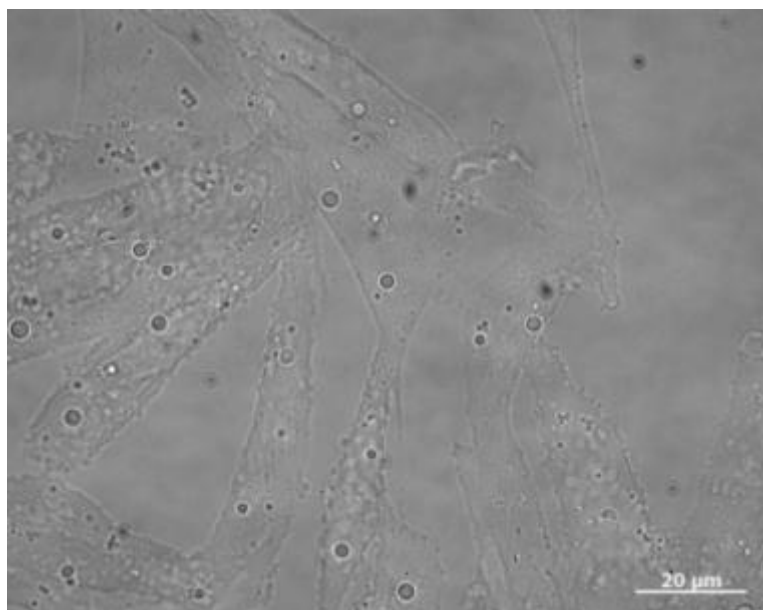
Figure 4.3 Phase picture showing the morphology of CHO DG44 control cells.
This image was acquired on Axiovert 200 M inverted fluorescence microscope using the 63 x objective lens (Scale bar = 20 µm)
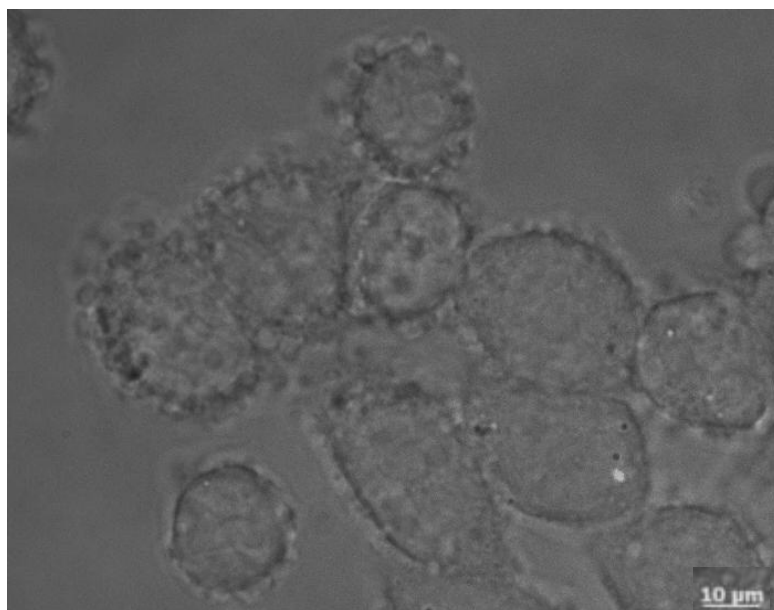
Figure 4.4 Phase picture showing the morphology of CHO-R-O-25 clone cells.
This image was also acquired on Axiovert 200 M inverted fluorescence microscope
using the 63 x objective lens (Scale bar = 10 μm)

4.2 CONFIRMATION OF NUCLEAR LOCALISATION OF EGFP SPOTS

In order to confirm that the fluorescent spots that were observed on the initial screening (section 3.3.4.2.1) were present within the nuclei of cells, cytoplasmic and nuclear staining was performed on CHO-R-O-25 doubly transfected cells and control CHO DG44 cells using DiOC6(3) and Hoechst 33342 dye, respectively. Staining confirmed the presence of fluorescent spots within the nuclei of CHO-R-O-25 cells in conjunction with the absence of fluorescent spots from the nuclei of control CHO DG44 cells (see figures 4.5 and 4.6 below). DiOC6(3) (green) is a mitochondrial stain which has stained the cytoplasm of the cells (figures 4.5a and 4.6a), whereas Hoechst 33342 dye (blue) is a nucleic acid stain delineating the nuclei of cells (figures 4.5b and 4.6b). Dual staining of both of the cytoplasm and nuclei of cells is shown in figures 4.5c and 4.6c.

EGFP spot   EGFP spot   EGFP spot

a)   b)   c)
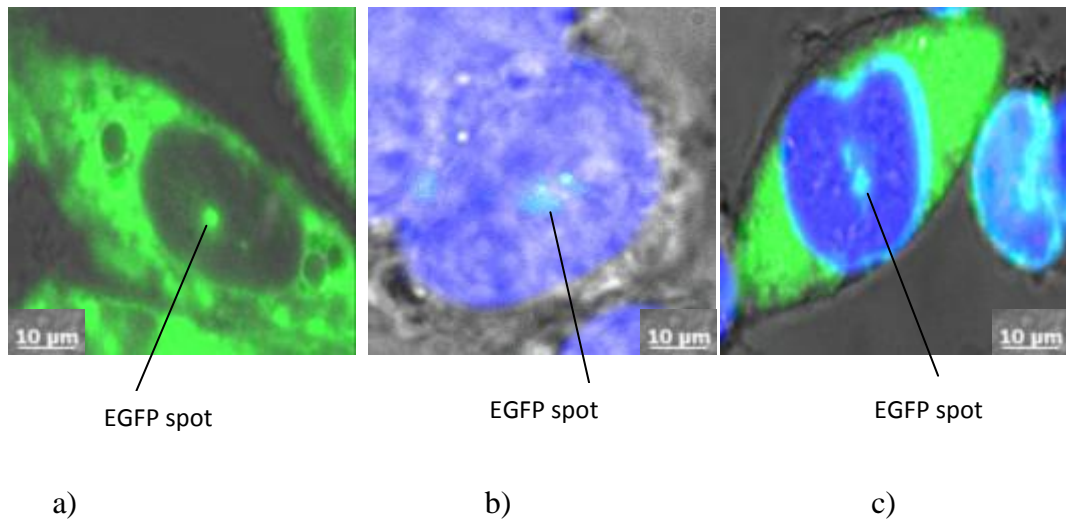
Figure 4.5 Cytoplasmic and nuclear staining of CHO-R-O-25 cells. For each individual image, the EGFP spots within the nuclei of cells are depicted (Scale bar = 10 µm)

a) **DiOC6(3) cytoplasmic staining**
b) **Hoechst 33342 dye nuclear staining**
c) **DiOC6(3) and Hoechst 33342 dye dual cytoplasmic and nuclear staining**

a)   b)   c)
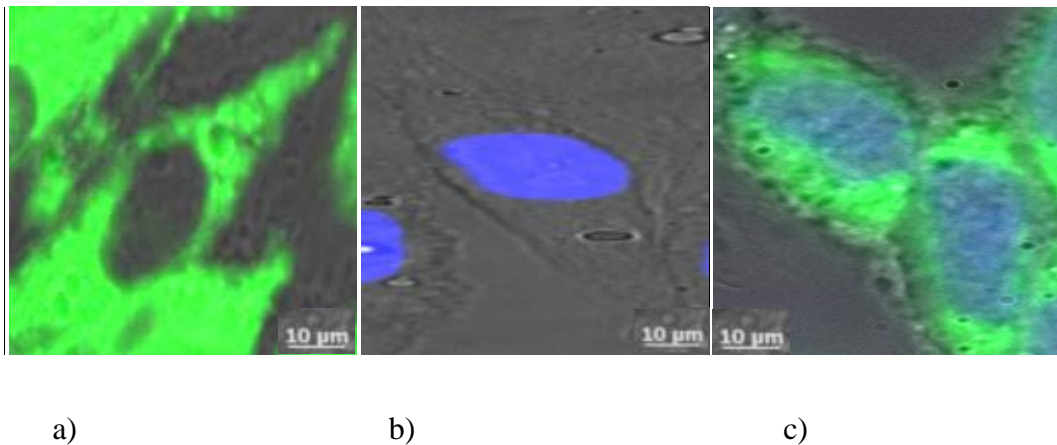
Figure 4.6 Cytoplasmic and nuclear staining of CHO DG44 control cells. Note the absence of EGFP spots from the nuclei of un-transfected CHO DG44 cells (Scale bar = 10 µm)

a) **DiOC6(3) cytoplasmic staining**
b) **Hoechst 33342 dye nuclear staining**
c) **DiOC6(3) and Hoechst 33342 dye dual cytoplasmic and nuclear staining**

4.3 DNA REPLICATION IN CHO-R-O-25 CELLS

4.3.1 PCNA STAINING

PCNA is involved in the DNA replication process that occurs during S phase and therefore stains positively cells that are present in that phase of the cell cycle. The PCNA staining procedure was followed in order to determine the fractions of CHO DG44 and CHO-R-O-25 cells undergoing DNA replication, as described in section 2.10.1 of Materials and Methods. At 72 hours after reseeding, CHO DG44 and CHO-R-O-25 cells were fixed and stained. The average percentage of CHO DG44 control cells in S phase was 25.4 % (± 4.4 %), while the corresponding average percentage of CHO-R-O-25 cells was 36.1 % (± 8.3 %; see graph on figure 4.9 below). Although a greater fraction of CHO-R-O-25 cells were in S phase of the cell cycle at 72 hours following reseeding in all three independent experiments compared to parent cells, this difference was not statistically significant ($p = 0.144$; figure 4.9). Representative images of PCNA positive CHO DG44 and CHO-R-O-25 nuclei are shown in figures 4.7 and 4.8, respectively.
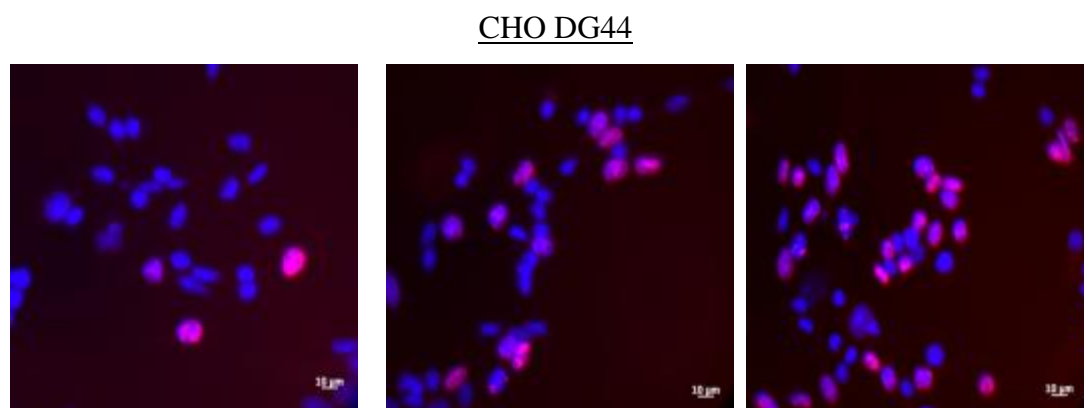
<u>CHO DG44</u>

Figure 4.7 PCNA + CHO DG44 nuclei. The stained nuclei (red) are undergoing DNA replication, whereas the unstained nuclei (blue) are in different phases of the cell cycle. Scale bar = 10 μm
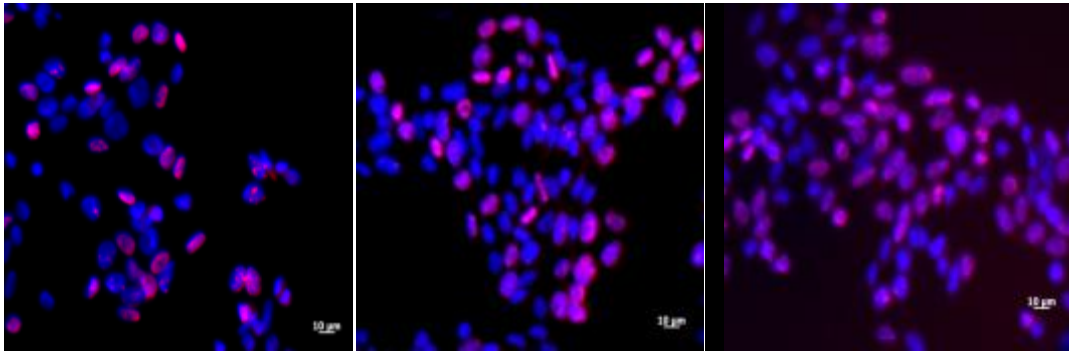
Figure 4.8 PCNA + CHO-R-O-25 nuclei. The stained nuclei (red) are undergoing DNA replication, whereas the unstained nuclei (blue) are in different phases of the cell cycle. Scale bar = 10 μm
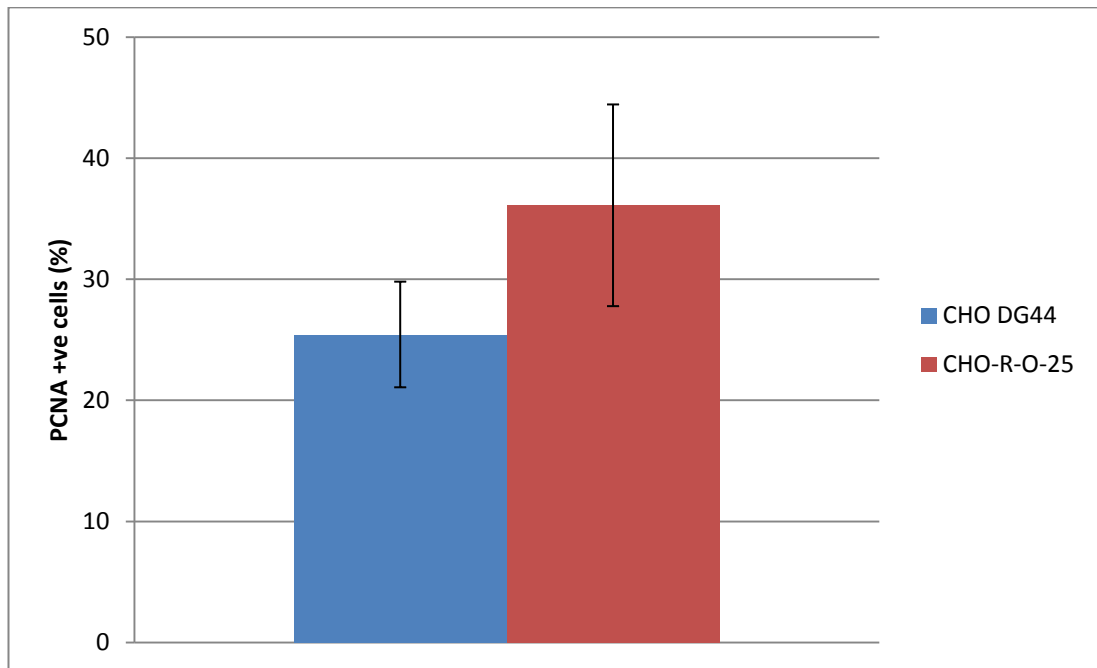
Figure 4.9 Graphic representation of the pooled % fraction of PCNA + CHO DG44 and CHO-R-O-25 nuclei. Error bars represent S.D.

4.4 DETERMINATION OF STABLE INTEGRATION OF pSV2-DHFR 8.32 PLASMID BY FLUORESCENCE IN SITU HYBRIDISATION (FISH)

4.4.1 METAPHASE CHROMOSOME PREPARATION

Metaphase chromosomes were harvested as described in section 2.11.1 of Materials and Methods. Following the seeding of 1.25×10^4 cells / cm^2 in each flask, cells were incubated at 37 ^{o}C for ~72 hours. Four independent experiments were performed in which different colcemid exposure time intervals and different volumes of 0.075 M KCl and 3:1 M:AA were applied. In addition, cells were harvested at different confluency percentages with the aim to identify the ideal confluency that results in potentially the highest number of cells arrested in metaphase stage of the cell cycle, after harvest. In an initial attempt to optimise the colcemid exposure time for cultured cells, 3.7 - 15.5 hour exposure times were applied for preps CHO-R-O-25 A, B and C. The results indicated that the highest number of nuclei arrested at the metaphase stage of the cell cycle corresponded to 3.7 and 4.3 hour exposure times (preps CHO-R-O-25 B and CHO-R-O-25 C; see table 4.2 below), therefore a decision was made to incubate preps CHO-R-O-25 R, S and T with colcemid for a time period range of 2.5 – 4.5 hours in the subsequent experiment. Having completed this experiment, the ideal colcemid exposure time was determined to be 3.5 hours (prep CHO-R-O-25 S; see table 4.2 below). Following slide dropping, the quality of each chromosome preparation was assessed through determination of the mitotic index (M.I.) and the percentage of encapsulated chromosomes within nuclei. Information associated with the quality of the preps and times and variables, is presented on table 4.2 below.

Table 4.2 Summary of CHO-R-O-25 metaphase qualities

Experiment	Sample (CHO-R-O)	Colcemid (5 μl/ml) exposure (hours)	0.075 M KCl incubation (minutes)	Culture duration (hours)	Average M.I. (%)	Quality of prep
1	25 A (p15)	15.5	8	69	0.3	Clumped chromosomes
1	25 B (p15)	4.3	8	70	1.1	Clumped chromosomes
1	25 C (p15)	3.7	8	72	1.2	Clumped chromosomes
2	25 (i) (p16)	2.5	7	70.5	0	Clumped chromosomes
2	25 (ii) (p16)	3.5	8	71.5		Clumped chromosomes
2	25(iii) (p16)	4.5	7	72.5		Clumped chromosomes
3	25 R (p21)	2.5	8	66	2.5	Clumped chromosomes
3	25 S (p21)	3.5	8	67	5.9	Well spread and easily distinguishable chromosomes
3	25 T (p21)	4.5	8	68	2.6	Clumped chromosomes
4	25D (p12)	3.5	8	77	4.4	Clumped chromosomes
4	25E (p12)	3.5	9	77	0	Clumped chromosomes
4	25F (p12)	3.5	8	78	4.3	Clumped chromosomes

Optimal slides of metaphase chromosome spreads were obtained from harvest sample CHO-R-O-25 S (p21), using the method described in section 2.11.2 of Materials and Methods. The majority of metaphase cells were burst open and the chromosomes well spread. Moreover, in the vast majority of spreads, all 20 chromosomes could be easily distinguished from each other and on each individual chromosome the centromeres and sister chromatids could also be clearly observed. 16 slides were dropped and stored fresh in the freezer at -20 ^{o}C. For two slides, the M.I. was determined as described in section 2.11.3, by using the following formula:

M.I. = Total # of mitoses / (Total # of mitoses + Total # of nuclei in the FOV) x 100.

Using the formula above, the average M.I. was calculated to be 5.9 % (see table 4.2). Therefore, based on the fact that this chromosome preparation was characterised by the highest quality, dropped slides were used for the subsequent performance of FISH experiments.

4.4.2 PREPARATION OF LAC O PROBE DNA

25 µg of pSV2-DHFR 8.32 plasmid DNA was digested with restriction enzymes Xho 1 and Sal 1, as described in section 2.5.1 of Materials and Methods. After digestion, 5 µg of digested and 1 µg of undigested pSV2-DHFR 8.32 plasmid DNA sample was loaded in each one of 6 wells of a 1% agarose gel and electrophoresed for 7 hours at 50 Volts. Bands corresponding to the lac O DNA sequences (see figure 4.10) were excised from the gel, weighed and placed into 5 sterile eppendorf tubes, as described below.
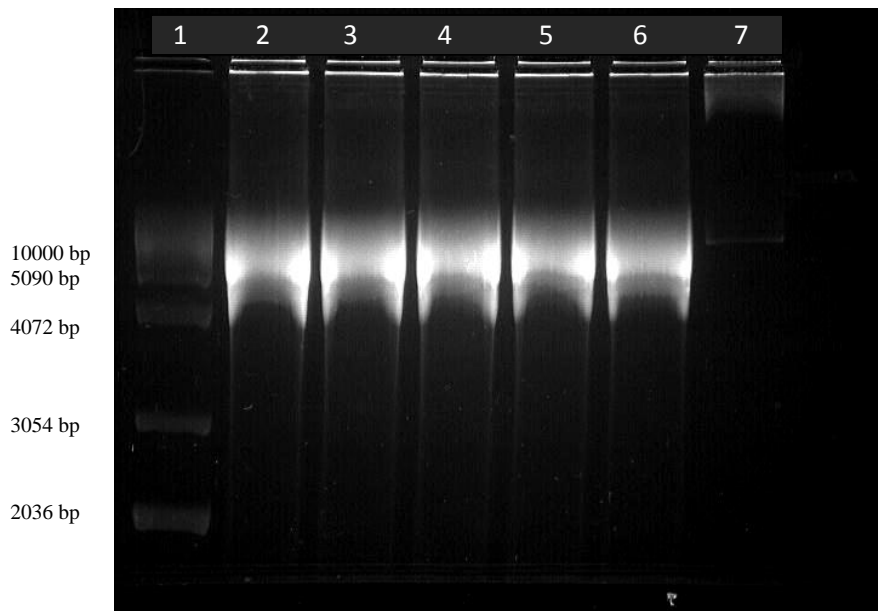
Figure 4.10 Restriction digestion of 25 µg of pSV2-DHFR 8.32 plasmid DNA. In each one of wells 2 – 6, 5 µg of digested plasmid DNA was loaded. The uppermost bands that correspond to the 10 kb lac O repeat were excised from the gel and purified. In well 7, 1 µg of undigested pSV2-DHFR 8.32 plasmid DNA was loaded.

The weights of the 5 gel slices were 244.5 mg, 276.1 mg, 352.9 mg, 282.7 mg and 256.6 mg, respectively. The gel slices were subsequently purified using the MinElute Gel Extraction kit by following the procedure described in section 2.4.2.4 and pooled into one sterile eppendorf that was stored in the freezer at -20 $^{\circ}$C. The lac O probe DNA concentration was found to be 0.0571 µg / µl by Nanodrop ND-1000 and thus the total amount of DNA was calculated as 5.54 µg. Despite the fact that the total amount of DNA that was obtained after digestion and purification of the gel slices was less than expected, suggesting that DNA was lost during these processing steps, it was sufficient to proceed.

Nick translation was performed by following the procedure described in section 2.11.4. In order to check whether DNA fragments of the desired sizes had been generated, a small amount of the mixture corresponding to ~50 ng of lac O probe DNA was loaded on a 2 % gel and agarose gel electrophoresis performed. After the end of electrophoresis, examination of the picture of the gel suggested that DNA fragments possessing a size of ~100 – 800 bp had been efficiently produced, as a smear of DNA that extended from the 134 bp marker to immediately below the 1018 bp marker could be observed on lane 3, where the nick translated lac O DNA sample had been loaded (see figure 4.11 below). Based on the intensity of the smear of DNA that was higher on the area of the gel between the 201bp and 506 bp markers, it was shown that most DNA fragments had a size of 200 – 500 bp. Therefore, short DNA fragments were generated that had the potential to efficiently hybridise to chromosomal DNA.
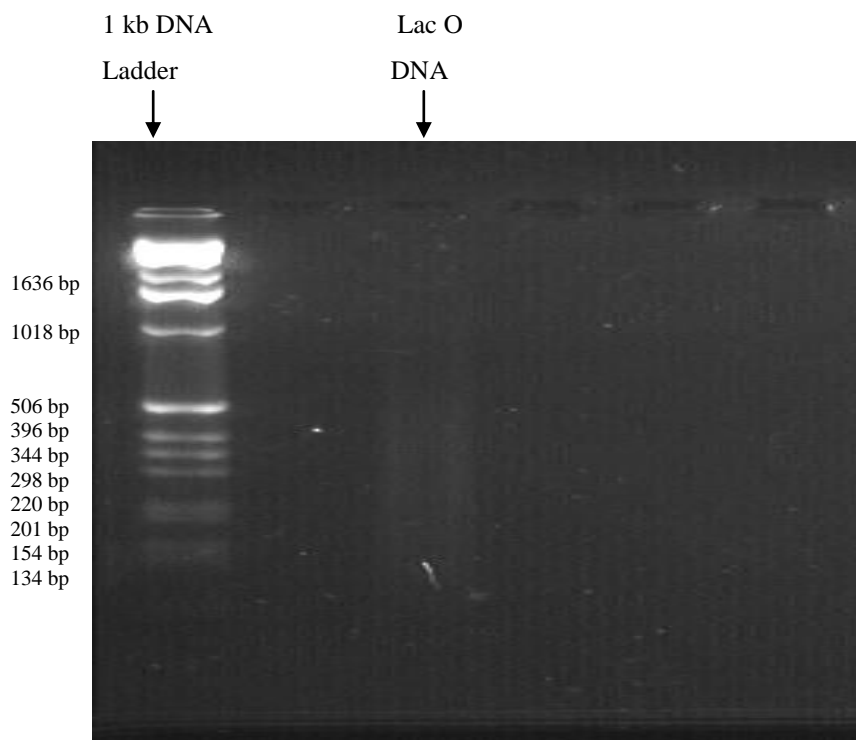
Figure 4.11 Agarose gel electrophoresis of ~50 ng of nick translated lac O probe DNA

4.4.3 COT-1 DNA ISOLATION FROM CHO CELLS

Cot-1 DNA was extracted from approximately 1×10^8 CHO DG44 cells, as described in section 2.11.5 of Materials and Methods. In the initial attempt to identify the ideal duration and number of sonication pulses, in addition to the volume and amount of DNA sample that would result in the production of DNA fragments of the desired size, sonication tests were carried out using variable values for each one of the aforementioned parameters. Samples containing 1-10 µg of DNA in a volume of 100 µl were exposed to $3 - 30$ sonication pulses for durations of 20 seconds and 30 seconds each. In addition, 6 pulses for a total duration of 20 seconds each were induced to samples containing 5 µg of DNA in volumes of 200 - 500 µl, samples containing 10 µg of DNA in volumes of 200 µl - 1 ml and samples containing 20µg of DNA in a volume of 1 ml.

Following ultrasound DNA fragmentation and ethanol precipitation (described in sections 2.11.5.4 and 2.11.5.5, respectively), 2 µg of the dissolved DNA sample was loaded on a 1 % gel in order to check whether DNA fragments of the desired size had been produced after sonication. After the end of electrophoresis, examination of the gel suggested that DNA fragments of a size of ~298 – 1018 bp had been efficiently generated by sonication (see figure 4.12 below). The vast majority of the DNA fragments were estimated to possess a size of 500 – 750 bp, as judged by the fact that the intensity of the smear of DNA was higher in the region of the gel between the 506 bp and 1018 bp markers. These results suggested that 24 – 30 sonication pulses for 30 seconds each were enough to generate ~500 bp DNA fragments.

1 kb DNA
Ladder

Sonicated
DNA sample
(Tube 8: 24-30 pulses
for 30 seconds each)

1636 bp

1018 bp

506 bp

396 bp
344 bp
298 bp
220 bp
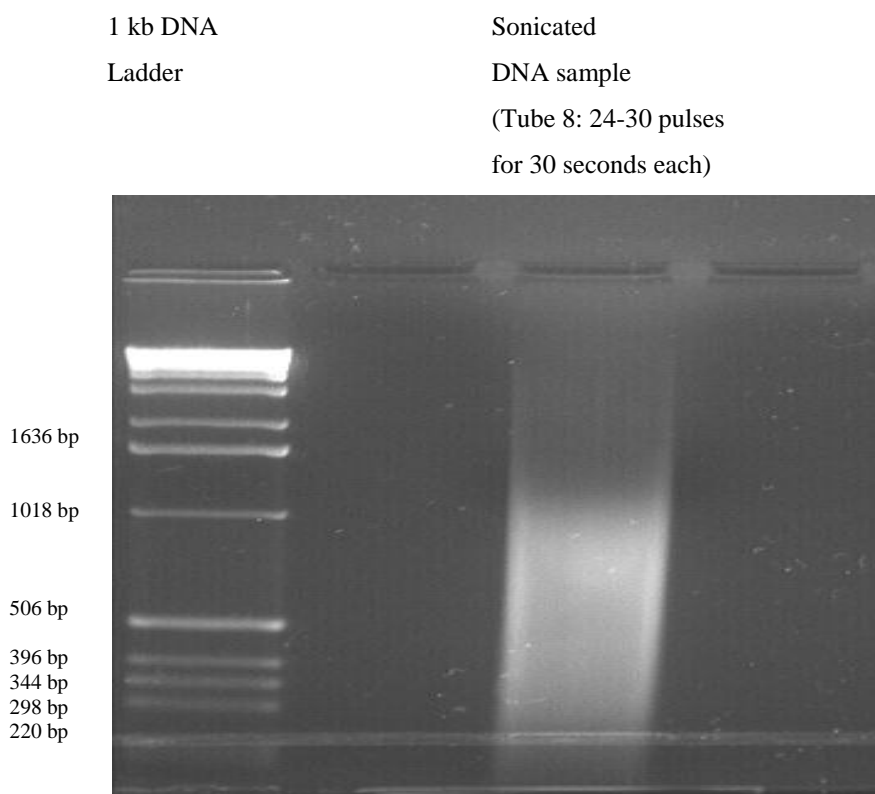
Figure 4.12 Agarose gel electrophoresis of 2 μg of sonicated CHO DG44 DNA sample

Following DNA re-annealing and S1-nuclease hydrolysis of the already sonicated CHO DG44 DNA sample (described in sections 2.11.5.6 and 2.11.5.7, respectively), DNA was purified and the DNA concentration was determined by spectrophotometry as described in section 2.1.4.1. The concentration of DNA was 0.10497 μg / μl and the total amount of DNA 103.8 μg. In addition, the quality of DNA was shown to be satisfactorily high, as the A_{260}/A_{280} and A_{260}/A_{230} ratios were found to be equal to 1.93 and 2.22, respectively.

4.4.4 LAC O HYBRIDISATION IN CHO-R-O-25 CELLS

Four independent FISH experiments were performed using CHO-R-O-25 chromosome preparation slides that had been dropped as described in section 2.11.2 of Materials and Methods. With regard to experiments 1 and 2 acquisition was performed as described in section 2.11.6.5, using the Smart Capture 2 and MetaSystems capture software systems, respectively. For all four experiments observations indicated that the chromosomes had been successfully denatured, based on their swelled and fuzzier appearance. In the first experiment, the blocking

solution was prepared using B.S.A. resulting in the acquisition of images with high background. This impacted on the ability to accurately identify the lac O FISH signals. In order to optimise the procedure and remove as much background as possible from the slides, Marvel milk powder was used as a blocking agent. This resulted in the significant removal of background. Representative examples of metaphases blocked with B.S.A. and Marvel-containing blocking solutions are shown in figures 4.13 (a) and (b), respectively. In addition, the effect of hamster Cot-1 DNA on the hybridisation procedure was assessed. This was carried out in order to exclude the possibility that signal observed on the chromosomes was due to the binding of the repetitive sequences of the probe DNA to random repetitive sequences of the genome. The results suggested that there were no significant differences between the + Cot-1 DNA and − Cot-1 DNA fields of view regarding the presence or absence of signal on chromosomes, indicating that Cot-1 DNA has no significant effect on the hybridisation procedure [see figure 4.13 (b) below].
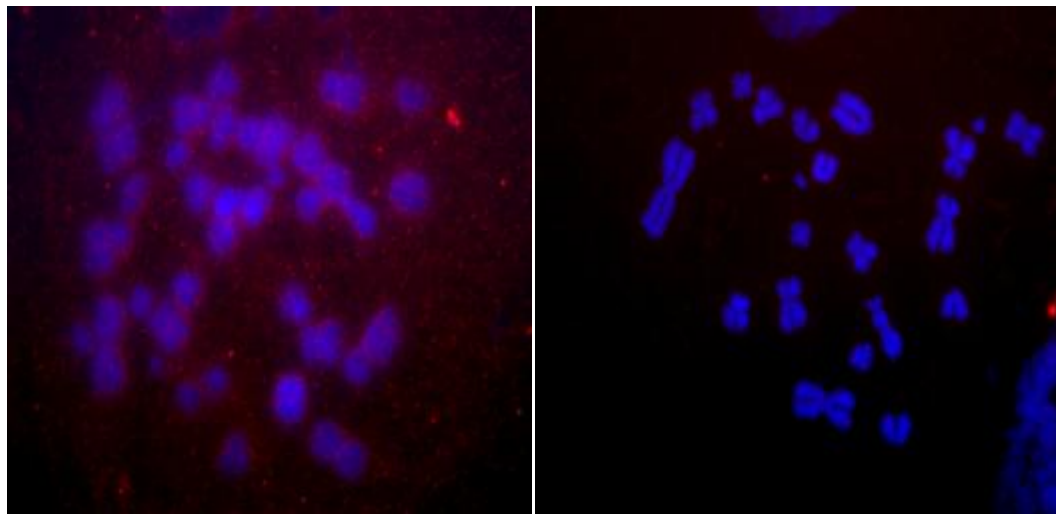
a)   b)

Figure 4.13 Metaphase spreads with (a) high background (b) no background. In (b) hybridisation was performed in the presence and absence of Cot-1 DNA, suggesting that Cot-1 DNA plays no part in the hybridisation procedure.

A total number of 538 and 167 interphase nuclei and metaphases were scored for two independent experiments, respectively. A positive TR signal, consistent with efficient lac O probe hybridisation was detected in 1.2 % and 2.6 % of the total number of interphase nuclei and metaphases, respectively. The TR + signal was observed to be present on a small metacentric chromosome [figure 4.14 (a) and (b)].

The majority of these TR + metaphases were composed of 20 chromosomes, but three metaphases were aneuploid [2 metaphases consisted of 21 chromosomes (figure 4.14) and 1 metaphase contained only 18 chromosomes].

a)
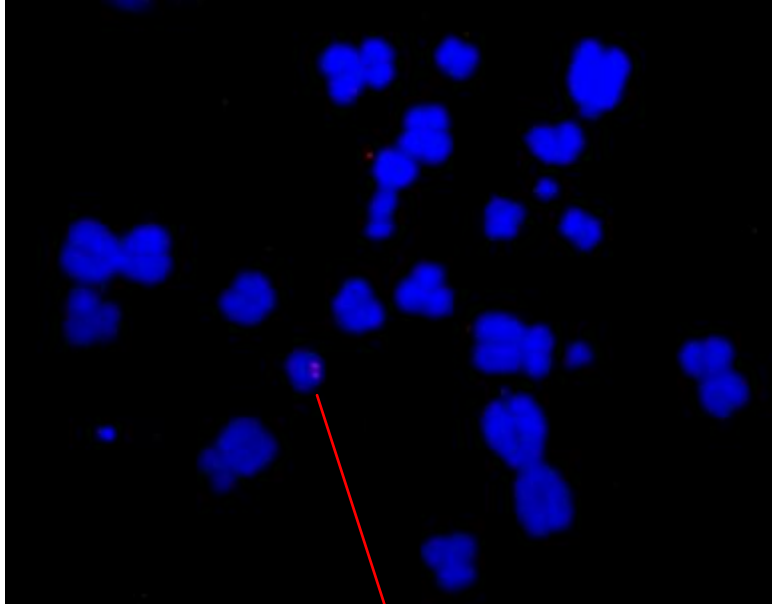
Small metacentric chromosome harbouring plasmid integration
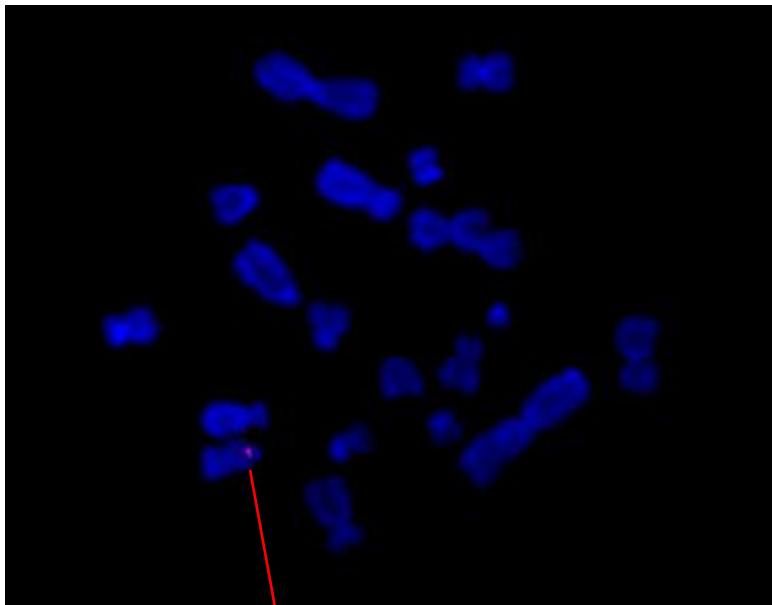
b)

Signal present on a small metacentric chromosome

Figure 4.14 Representative examples of TR + metaphases with small metacentric chromosome harbouring the signal (depicted with red arrows)

4.4.5 IDENTIFICATION OF CHROMOSOME CONTAINING LAC O INTEGRATION

Following the determination of the chromosome harbouring the pSV2-DHFR 8.32 plasmid integration as a small metacentric chromosome, the next step was to assess the identity of that chromosome. Based on the karyotype of CHO DG44 cell line performed by Derouazi et al (2006), the normal diploid number is 20 chromosomes (257). Seven of these chromosomes are normal, namely chromosomes 1 (copy 1), 1 (copy 2), 2, 4, 5, 8 and 9. Seven of them are derivative chromosomes [der (4), der (5), der (6), der (7), der (8), der (10) and der (X)], four belong to the Z group (Z1, Z4, Z8 and Z13), whereas two are the marker chromosomes (mar 1 and mar 2; figure 4.15 b). The derivative chromosomes have arisen as a consequence of chromosomal exchanges and translocations in the parental cell line (257). The marker chromosomes are completely different regarding their structure compared to the chromosomes of the parental cell line (257), whereas the Z group chromosomes have been described in (270).

In order to identify the chromosome harbouring the plasmid integration, the chromosomes were arranged in order according to their size. They were then compared to the sizes of the chromosomes from Giemsa staining (G-banding) of CHO DG44 cells carried out by Derouazi et al (2005), that is shown in figure 4.15 (b) below. In addition, based on the fact that the centromeric position also plays a role in the determination of chromosomal identity, an attempt was made to compare the position of the centromere of each chromosome on figure 4.15 (a) to the Giemsa stained chromosomes. Based on this, it is suggested that the chromosome carrying the plasmid incorporation is likely to be normal chromosome 9 [compare figures 4.15 (a) and (b) below]. To confirm this, hybridisation with a whole chromosome probe for chromosome 9 needs to be performed.

a)

Chromosome 9 (normal) suspected of harbouring plasmid incorporation according to its size

Chromosome 9 (normal) suspected of harbouring plasmid integration according to its size
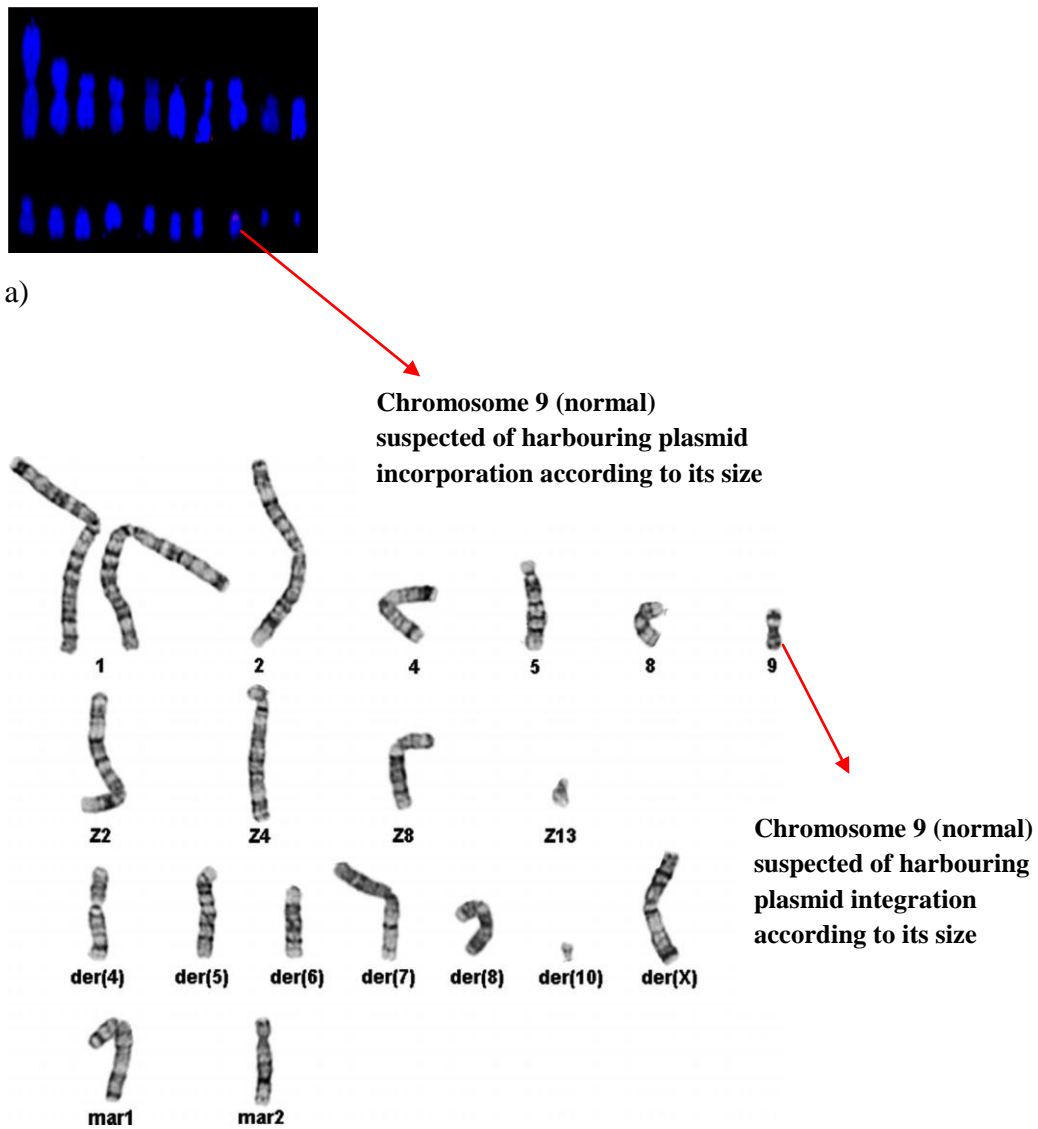
Derouazi et al 2005

b)

Figure 4.15 Identification of chromosome harbouring the plasmid incorporation in CHO-R-O-25 cells

a) Arrangement of CHO-R-O-25 chromosomes in order according to their sizes (from largest to smallest). Note the chromosome of plasmid integration that is depicted with an arrow

b) Karyotyping of CHO DG44 chromosomes following Giemsa staining (G-banding) performed by Derouazi et al (2005). The normal chromosomes 1 (copy 1), 1 (copy 2), 2, 4, 5, 8 and 9 are present on the uppermost row, Z2, Z4, Z8 and Z13 Z group chromosomes are located underneath and below them are the der (4), der (5), der (6), der (7), der (8), der (10) and der (X) derivative chromosomes. At the bottom row, the marker chromosomes mar 1 and mar 2 are present. The candidate chromosome containing the plasmid incorporation, namely chromosome 9, is shown with an arrow.

4.5 DISCUSSION

4.5.1 Chinese Hamster Ovary (CHO) DG44 CELLS

CHO DG44 cells were derived from CHO-K1 cell line following the deletion of the endogenous dihydrofolate reductase (DHFR) locus either by γ-irradiation (244, 271, 272) or by ethyl methanesulfonate [EtMes; (271)]. Following this deletion, cells were selected with tritiated deoxyuridine (^{3}HdUrd) in order to identify the generated mutants. Initially, mutants in which the DHFR locus was half-functional were isolated using a combination of methotrexate (MTX) and ^{3}HdUrd as selective agents. Mutants completely deficient in DHFR activity were isolated by their inability to grow in medium lacking the amino acids purine, thymidine and glycine (244, 271, 272). We obtained CHO DG44 cells that were generated as described above from Invitrogen. These cells were well-suited for recombinant protein expression.

4.5.2 GROWTH CHARACTERISTICS OF CHO DG44 AND CHO-R-O-25 CELLS

Based on the determination of short and long-term doubling times in this study, it was shown that the population doubling time of CHO DG44 cells was 23.8 – 40.7 hours, whereas the doubling time of CHO-R-O-25 cells was 22.4 – 37.3 hours. The cell cycle duration of CHO DG44 cells is 24 hours (241) and information from the data sheet of these cells would be consistent with a population doubling time of 16 – 22 hours (Invitrogen). Our data however suggest that only the short-term (23.8 and 22.4 hours for CHO DG44 and CHO-R-O-25 cells, respectively) and not the long-term doubling times (40.7 and 37.3 hours for CHO DG44 and CHO-R-O-25 cells, respectively) are consistent with these expectations. These differences are most likely attributed to the different slopes between the long-term and short-term growth curves. In the long-term growth curves the apparent population doubling times are longer because they include the lag phases as part of the graphs, although these cannot be observed on the graphs (figure 4.2). Therefore, the short-term growth curves represent a more accurate estimation of the growth rates and population doubling times in CHO DG44 control and CHO-R-O-25 cells. The short-term growth curves for CHO DG44 and CHO-R-O-25 cells (figure 4.1) revealed that the

lag phase occurred for both cell types during the first 24 hours after reseeding, with the exponential growth phase occurring over the time period of 24 – 72 hours for CHO DG44 and between 24 and120 hours for CHO-R-O-25 cells. No obvious differences in the rate of growth were observed between the transfected (CHO-R-O-25) and un-transfected (CHO DG44 cells).

4.5.3 DNA REPLICATION IN CHO DG44 AND CHO-R-O-25 CELLS

PCNA staining indicated that the fractions of CHO DG44 and CHO-R-O-25 cells undergoing DNA replication were comparable (figure 4.9). The percentage of PCNA positive CHO-R-O-25 cells was 36.1 % ($\pm$ 8.3 %), whereas that of control CHO DG44 cells was 25.4 % ($\pm$ 4.4 %). Despite the fact that the percentage of CHO-R-O-25 cells in S phase was higher than that of CHO DG44 cells, the difference between these two cell types was not statistically significant, according to the results of the student t-test (p = 0.144). Therefore, roughly one third of the total CHO-R-O-25 and CHO DG44 cell populations were shown to be in S phase. For CHO DG44 control cells, the fact that the S phase duration is approximately 8 – 9 hours and that the total duration of cell cycle in these cells is equal to 24 hours (241), with a population doubling time of 23.8 – 40.7 hours, suggests that these results are consistent with the expectations. In addition, these data demonstrate that the plasmid incorporations within the chromosomes of CHO-R-O-25 cells do not account for any discrepancies or delays in cell cycle progression. Similarly, flow cytometric analysis of fixed CHO DG44 cells stained with propidium iodide has shown that the percentage of S phase cells is approximately equal to 10 % (273). The higher percentages of PCNA-positive cells in our study can be attributed to the fact that unlike propidium iodide staining followed by flow cytometry, PCNA staining also labels cells present in G_1 phase of the cell cycle.

4.5.4 DETERMINATION OF PLASMID INTEGRATION CHROMOSOMAL SITE BY FISH

Observation of the TR+ metaphases on figure 4.14 shows lac O probe hybridisation to correspond to two small dots being present on the two sister chromatids of (apparently) the same metacentric chromosome. Taking into consideration the fact that the size of the lac O is only 10 kb, signal size is consistent with the expectations. The performance of FISH allowed the determination of the number of different plasmid integration sites throughout the genome of fixed CHO-R-O-25 cells. For instance, the possibility that there are two sites of plasmid integration would be illustrated by the presence of signal on two (or more) different chromosomes of the same metaphase. If multiple sites were transcriptionally active, then multiple fluorescent spots would be expected to be present within the nuclei of EGFP-expressing cells. However, as it has already been determined following screening, the vast majority of the CHO-R-O-25 EGFP-expressing cells were shown to contain only a single fluorescent spot within their nuclei, regardless of whether that was discrete and intense or expanded and diffuse. Therefore, it is concluded that there is only a single plasmid integration site within the chromosomes of CHO-R-O-25 cells. This finding is consistent with the results of Derouazi et al (2006), who have shown that in all but one of the sixteen clones that were created after transfection a single plasmid integration site within the chromosomes could be identified (257).

In order to identify the chromosomal sites of plasmid incorporations in the generated clones, Derouazi et al (2006) compared the inverted FISH images to the karyotype provided by the G-banding. Crucially, it was demonstrated that in the majority of the transfected cell lines (63 %), the karyotype was different from that of CHO DG44 cells. A number of chromosomes in the transfected cells were characterised by several chromosomal aberrations (257). In this study, the small metacentric chromosome containing the lac O signal was similarly compared with CHO DG44 karyotype, revealing similarities with chromosome 9. However, in the absence of chromosome 9 whole chromosome painting, we cannot rule out that the chromosome carrying the plasmid integration is a novel chromosome generated by chromosomal exchanges.

4.5.5 SUMMARY OF FINDINGS

Cytoplasmic and nuclear staining confirmed the presence of EGFP spots within the nuclei of transfected CHO-R-O-25 cells and the absence of fluorescent spots from the nuclei of control CHO DG44 cells (figures 4.5 and 4.6). Furthermore, the population doubling times for CHO DG44 and CHO-R-O-25 cells were comparable (23.8 – 40.7 and 22.4 – 37.3 hours, respectively), despite the fact that according to the short-term growth rate determination, the log phase in CHO-R-O-25 cells was 48 hours longer than that of control CHO DG44 cells (figure 4.1). No statistically significant differences were observed for the fractions of replicating CHO-R-O-25 and CHO DG44 cells (figure 4.9). These findings demonstrated that plasmid integrations within the chromosomes have not interfered with the cellular growth process. Finally, FISH revealed that the lac O incorporation has occurred within a small metacentric chromosome, which according to its size is possibly a normal chromosome 9.

CHAPTER 5: DNA DAMAGE EVENTS AND REPAIR PROCESSES REVEALED BY TIME-LAPSE MICROSCOPY

In order to investigate the relationship between alterations in chromatin physical properties and repair events following exposure to DNA damaging agents, time-lapse microscopy was performed in CHO-R-O-25 cells. Following the determination of the appropriate BLM and H_2O_2 doses that result in damage induction while maintaining cell viability, selected cells containing discrete and intense fluorescent spots were exposed to BLM, H_2O_2 and γ-irradiation. Individual time-lapse series were then analysed on image J in order to compare the trends of mean intensity, area and total intensity alterations between treated and untreated cells. In addition, DNA DSBs were detected with the aid of foci script analysis (in collaboration with Andrew McVean, Brunel University), following staining for γ-H2AX phosphorylated histone variant. The percentages of γ-H2AX positive nuclei, the total number of foci and the mean number of foci per nucleus were determined in treated and untreated cells.

5.1 OPTIMISATION OF BLM AND H_2O_2 DOSE CONCENTRATIONS

The aim of this experiment was to determine the appropriate BLM and H_2O_2 concentrations that result in the production of DSBs within the genome of cells, while retaining cell viability. The experiments were performed in duplicate. 1.6×10^5 CHO DG44 and CHO-R-O-25 cells were reseeded in each well of two 6-well plates, incubated at 37 ^{o}C for ~72 hours before addition of 0, 10, 15 and 20 µg/ml of BLM or 0, 100, 200, 300, 350 and 400 µM of H_2O_2. BLM and H_2O_2 exposed cells were then further incubated at 37 ^{o}C for 30 minutes and 3 hours respectively, as described in section 2.12.1.1. The number of dead cells from each well was assessed by trypan blue exclusion dye as described in section 2.3.5. In summary, it was shown that exposure up to concentrations of 20 µg/ml of BLM and 400 µM of H_2O_2 is tolerated by the vast majority of CHO-R-O-25 and CHO DG44 cells.

Following exposure to BLM, the fraction of nonviable CHO-R-O-25 and CHO DG44 cells that have incorporated trypan blue is higher for the concentration

range of 10 – 20 μg/ml compared to the unexposed cells (p < 0.05; figure 5.1). The range of nonviable CHO-R-O-25 and CHO DG44 cells at this concentration range was 5.9 – 7.6 % and 6.1 – 8 % respectively, as opposed to 2.7 % and 3.5 % of unexposed CHO-R-O-25 and CHO DG44 nonviable cells, respectively (figure 5.1).
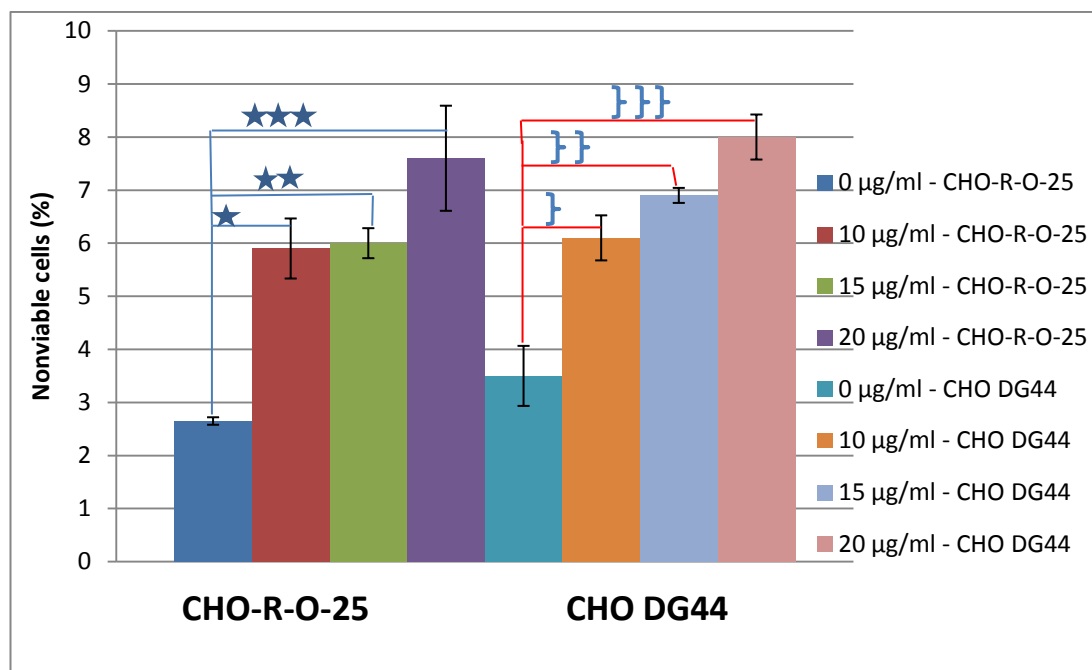
Figure 5.1 Fractions of nonviable CHO-R-O-25 and CHODG44 cells after exposure to 0 - 20 μg/ml of BLM. Error bars represent S.D.
(* p = 0.015, ** p = 0.0038, *** p = 0.0195; } p = 0.035, }} p = 0.014, }}} p = 0.012)

For both CHO-R-O-25 and CHO DG44 cells exposed to H_2O_2, the fraction of nonviable cells increases with the increasing concentration of H_2O_2 (figure 5.2). The percentage of nonviable unexposed CHO-R-O-25 cells is 2.2 % compared to 3.7 % for cells treated with 100 μM of H_2O_2 (p = 0.036), while the corresponding percentage of unexposed CHO DG44 cells is 1.6 % as opposed to 4.5 % for cells exposed to 100 μM of H_2O_2 (p = 0.0196; figure 5.2). The difference between the percentage of nonviable cells after exposure to 100 μM and 200 μM of H_2O_2 was statistically significant only in CHO-R-O-25 cells (3.7 % versus 5.5 % of dead cells, respectively; p = 0.035) and not in CHO DG44 cells (4.5 % as opposed to 5 % of dead cells, respectively; p=0.38). There was no apparent difference in nonviability for the dose range of 200 – 350 μM of H_2O_2 in both cell types (p > 0.05). However, in both cell types a significant difference was recorded between cells exposed to 400 μM and 0 – 350 μM of H_2O_2 (p< 0.05). Specifically, the range of nonviability after exposure to 400 μM of H_2O_2 was 7.7 – 8.5 % (p = 0.29), as opposed to 1.6 – 2.2 %

($p = 0.039$) and 5.1 – 6.1 % ($p = 0.12$) of nonviable untreated and 350 µM H_2O_2 -exposed CHO DG44 and CHO-R-O-25 cells, respectively.
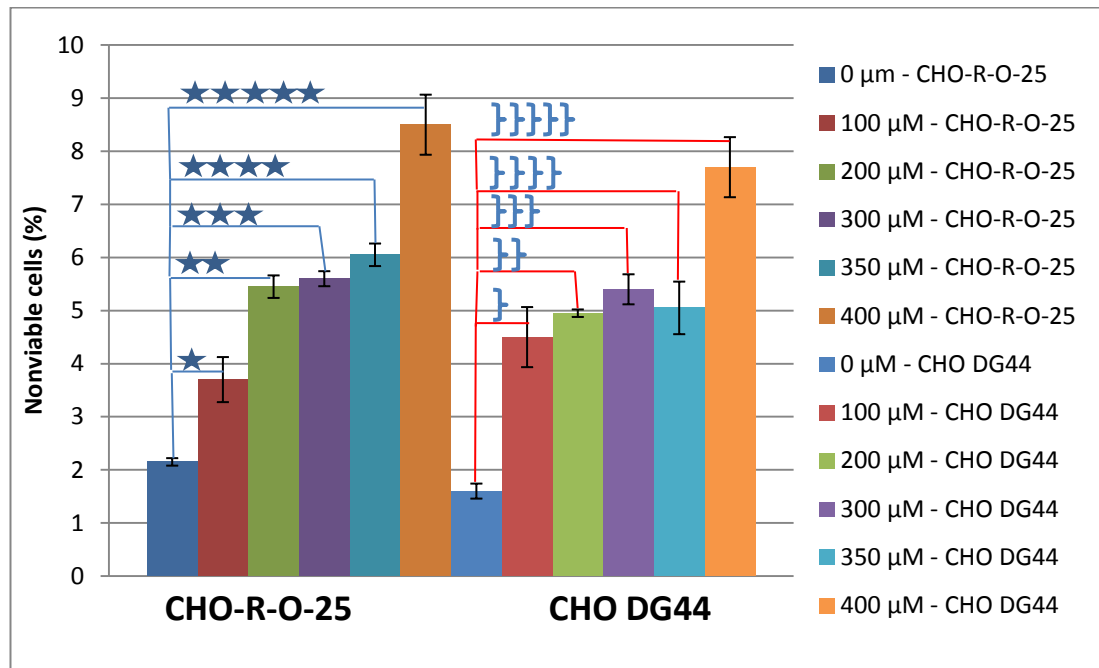
Figure 5.2 Fractions of nonviable CHO-R-O-25 and CHO DG44 cells following exposure to 0 - 400 µM of H_2O_2. Error bars represent S.D.
(* p = 0.036, ** p = 0.002, *** p = 0.001, **** p = 0.016, ***** p = 0.004; } p = 0.0196, }} p = 0.001, }}} p = 0.003, }}}} p = 0.01, }}}}} p = 0.0045)

No significant differences were observed between the average percentages of nonviable CHO-R-O-25 and CHO DG44 cells after exposure to 400 µM of H_2O_2 (8.5 % versus 7.7 % nonviable cells, respectively; $p = 0.29$; figure 5.3) and 20 µg/ml of BLM (7.6 % versus 8 % nonviable cells, respectively; $p = 0.652$; figure 5.3). Similarly, the differences between the percentages of CHO-R-O-25 and CHO DG44 cells exposed to 400 µM of H_2O_2 in comparison to those of CHO-R-O-25 and CHO DG44 cells exposed to 20 µg/ml of BLM are not considered as statistically significant, as $p > 0.05$ (figure 5.3).
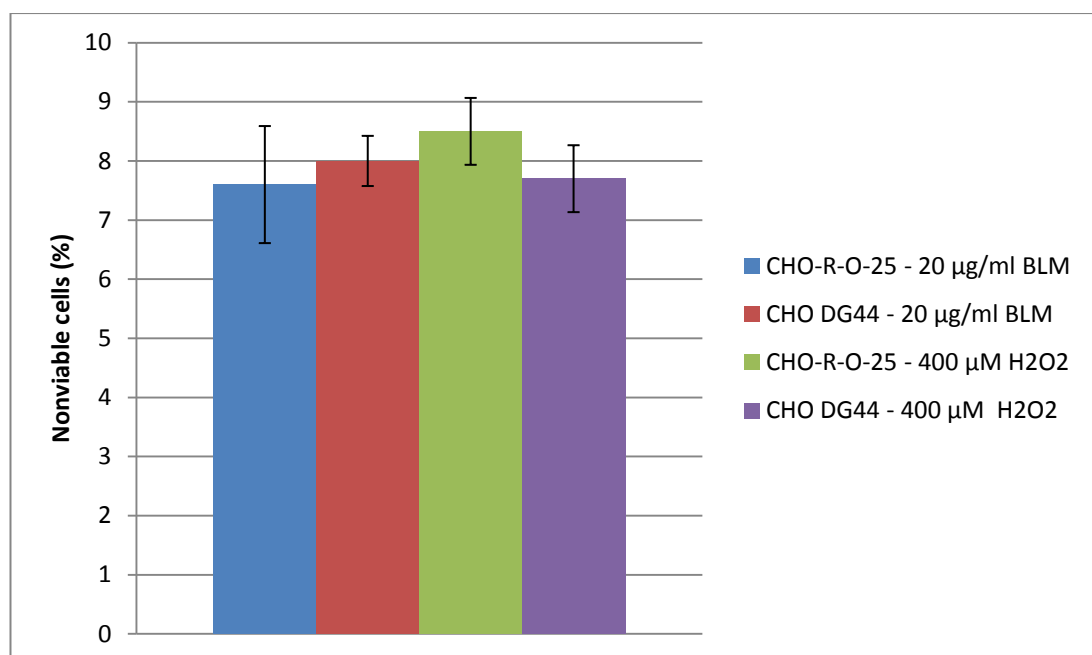
Figure 5.3 Comparison between the proportions of CHO-R-O-25 and CHO DG44 nonviable cells after exposure to 20 µg / ml of BLM and 400 µM of H$_2$O$_2$. Error bars represent S.D.

The maintenance of cell viability over a 2 hour period was crucial for the purpose of time-lapse acquisition, where alterations in the intensity and area of the fluorescent spots within the cells of interest could be correlated to DNA damage events over this experimental time-frame. Based on the finding that exposure of CHO-R-O-25 and CHO DG44 cells to concentrations of 20 µg/ml of BLM and 400 µM of H$_2$O$_2$ was lethal to only 7.6 – 8.5 % of cells, these concentrations were desirable. To assess the induction frequency of DNA DSBs at these concentrations, cells were exposed to BLM and H$_2$O$_2$ and stained by immunofluorescence for the phosphorylated histone variant γ-H2AX, that is involved in the DNA damage repair process (section 5.2).

5.2 STAINING FOR γ-H2AX FOR DETECTION OF DNA DSBs

The induction of DNA DSBs in 1 HD human fibroblasts and CHO-R-O-25 cells after exposure to selected damaging agents (20 µg / ml BLM, 400 µM H$_2$O$_2$, 1 Gy and 4 Gy γ-irradiation) was quantified by immunofluorescence detection of γ-H2AX, by following the procedure that is described in section 2.10.2. The aim was to determine the fractions of nuclei that contained DSBs within their genome and also to determine the average number of foci in each nucleus. For each individual experiment an unexposed (sham) slide was also included for comparison. 1 HD cells were included as a cell type comparison and to act as a positive control for human γ-

H2AX antibody in CHO cells. 5×10^5 1 HD cells and 4×10^5 CHO-R-O-25 cells were reseeded on slides and cells were incubated at 37 ^{o}C for 72 hours, before treating each slide with the appropriate DNA damaging agent. Cells treated with 20 μg / ml of BLM and 400 μM of H_2O_2 were exposed to the aforementioned concentrations for 30 minutes and then immediately fixed and stained, whereas cells exposed to γ-IR were incubated for 30 minutes at 37°C after the end of irradiation, before being fixed.

5.2.1 OBSERVATIONS FOLLOWING THE ACQUISITION OF IMAGES

Immunostaining was assessed as successful for all slides, demonstrating the broad cross-reactivity of anti-phospho-histone H2AX antibody in human and hamster species. This was expected, based on the high degree of conservation among the DNA sequences of different species. Numerous pictures were captured as described in section 2.10.3. Marked differences were observed regarding the appearance of sham and treated nuclei, with most of the treated nuclei containing numerous discrete foci, that were in turn absent from the majority of sham nuclei (figure 5.4).
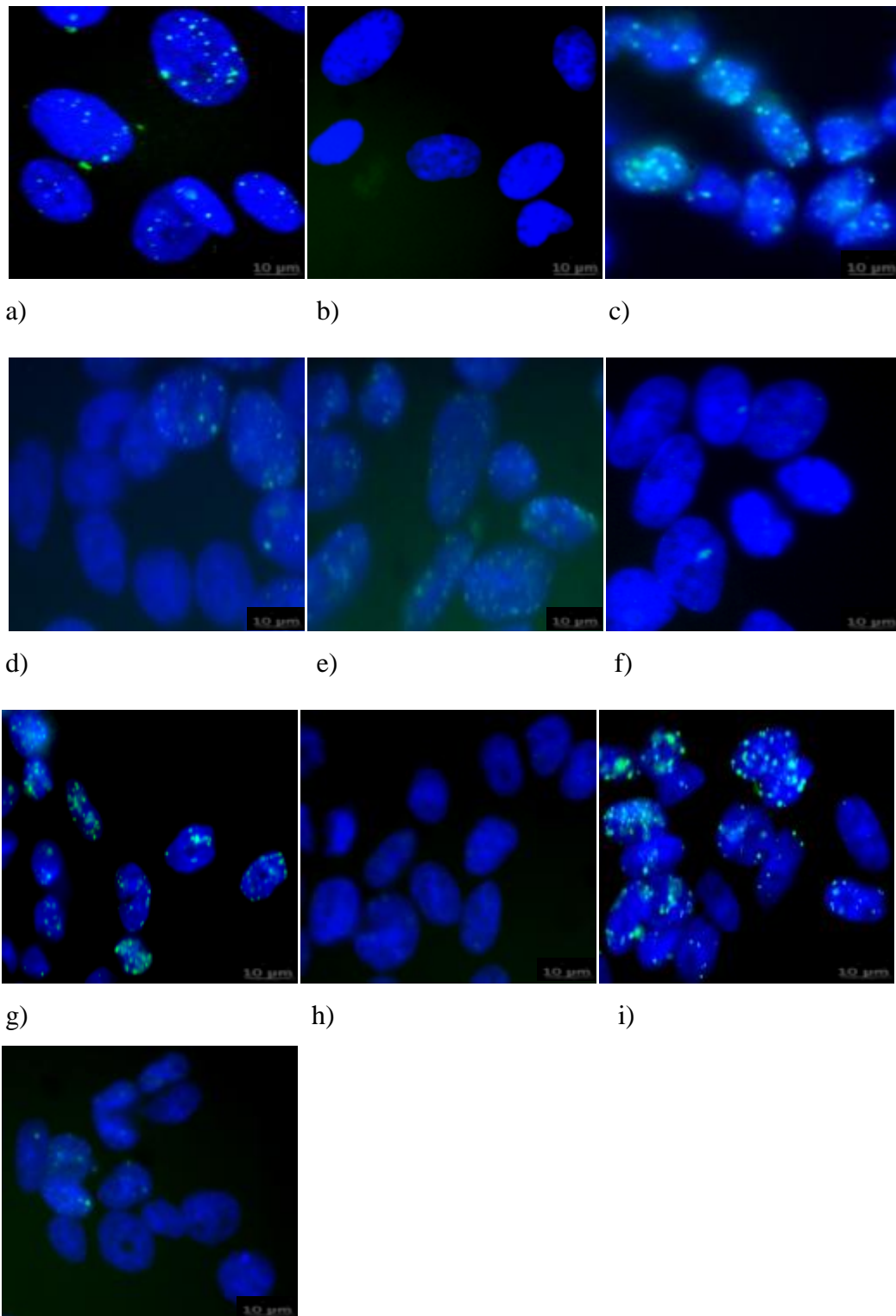
Figure 5.4 Representative images of 1HD and CHO-R-O-25 cells stained with antibody against γ-H2AX

a) 1 HD human fibroblasts exposed to 1 Gy γ-IR;   b) 1 HD human fibroblasts sham
c) CHO-R-O-25 cells exposed to 1 Gy γ-IR;   d) CHO-R-O-25 cells sham
e) CHO-R-O-25 cells exposed to 4 Gy γ-IR;   f) CHO-R-O-25 cells sham
g) CHO-R-O-25 cells exposed to 400 μM H_2O_2 h) CHO-R-O-25 cells sham
i) CHO-R-O-25 cells exposed to 20 μg / ml BLM;   j) CHO-R-O-25 cells sham

5.2.2 γ-H2AX FOCI SCRIPT ANALYSIS

Images of >100 well-separated nuclei were captured as described in section 2.10.3. The images were then analysed by the script (developed in-house, McVean et al manuscript in progress), in order to determine the percentages of positive nuclei for phosphorylated H2AX, the total number of foci and the mean number of foci / nucleus.

The results from the script foci analysis revealed that as expected, the total number of CHO-R-O-25 nuclei containing at least one γ-H2AX focus was higher in the nuclei exposed to BLM, H_2O_2, 1 Gy γ-IR and 4 Gy γ-IR compared to the untreated nuclei ($p< 0.05$; figure 5.5 and table 5.1). In addition, it was shown that the total number of 1 HD nuclei containing at least one focus was higher for 1 Gy γ-IR treatment compared to the sham (figure 5.5 and table 5.1). More specifically, the average percentage of positive nuclei for γ-H2AX in H_2O_2 treated cells was 86 % compared to 16 % ($p = 0.001$) for the untreated cells and in BLM treated cells it was 80 % compared to 13 % ($p = 0.002$) for sham. Consistent with the expectations, the fraction of γ-H2AX positive CHO-R-O-25 nuclei exposed to 4 Gy γ-IR (96%) was higher than that of CHO-R-O-25 (77%; $p= 0.005$) and 1 HD nuclei (89%; $p = 0.041$) exposed to 1 Gy γ-IR (figure 5.5 and table 5.1).
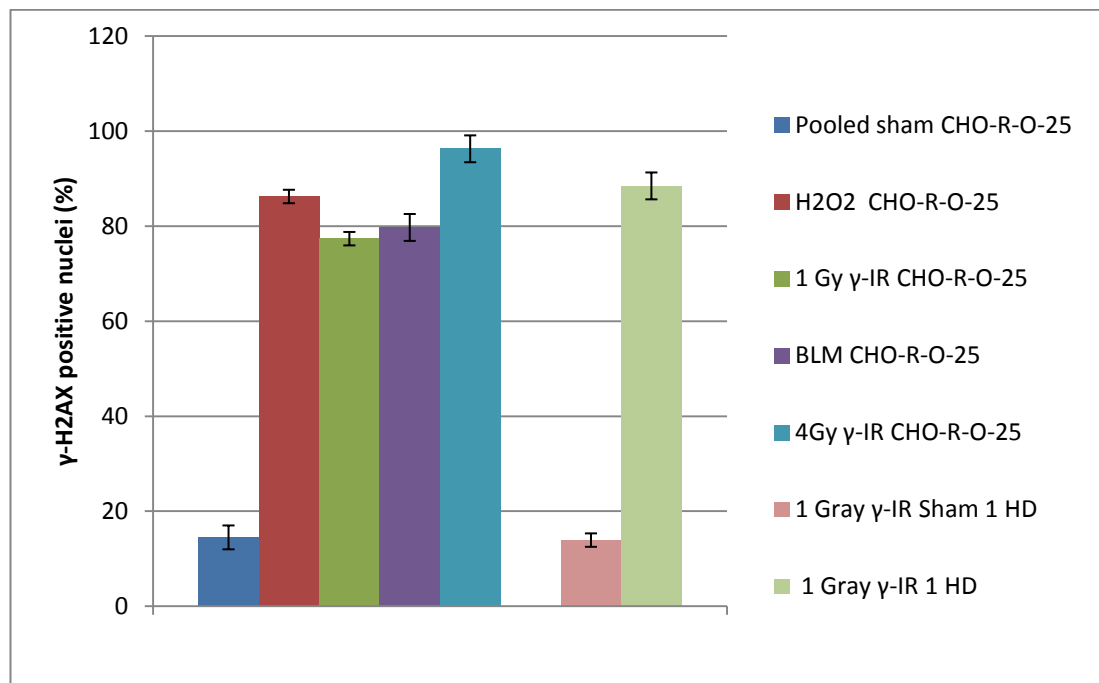
Figure 5.5 Percentages of γ-H2AX positive CHO-R-O-25 nuclei following treatment with BLM, H_2O_2, 1 Gy γ-IR and 4 Gy γ-IR and percentage of γ-H2AX positive 1 HD nuclei after exposure to 1 Gy γ-IR. Error bars represent S.D.

Table 5.1 Effect of various treatments on γ-H2AX foci induction in CHO-R-O-25 and 1 HD cells

Cell type	CHO-R-O-25					1 HD	
Treatment	sham pooled	H_2O_2	BLM	1 Gy γ-IR	4 Gy γ-IR	1 Gy γ-IR	1 Gy γ-IR sham
Total number of positive nuclei	21	119	114	123	129	138	22
Total number of nuclei	146	138	143	159	134	156	158
% of positive nuclei	15	86	80	77	96	89	14
Total number of foci	113	1744	2754	1891	8466	1506	77
Mean number of foci / nucleus	1	13	19	12	63	10	1

The mean number of foci per nucleus was determined for each test. The threshold above which a focus was being identified by the script was 3 pixels. Consistent with expectations, for CHO-R-O-25 nuclei treated with H_2O_2, BLM, 1 Gy γ-IR and 4 Gy γ-IR and 1 HD nuclei exposed to 1 Gy γ-IR, the mean number of foci per nucleus was significantly higher compared to the untreated (sham) cells ($p < 0.05$; figure 5.6 and table 5.1). The mean number of foci / nucleus for H_2O_2, BLM, 1 Gy γ-IR and 4 Gy γ-IR treated CHO-R-O-25 nuclei was 13 [11 – 15], 19 [18 – 20], 12 [11 - 13] and 63 [60 – 66], respectively, as opposed to 1 for sham nuclei of the corresponding experiments (table 5.1 and figure 5.6). Moreover, the mean number of foci / nucleus for 1 HD γ-irradiated nuclei was 10 [9 - 11] compared to 1 for sham nuclei. Consistent with expectations, the highest mean number of foci / nucleus was recorded for CHO-R-O-25 nuclei exposed to 4 Gy γ-IR (63 foci / nucleus). This value was approximately 5-fold and 6-fold higher than those of CHO-R-O-25 and 1 HD nuclei exposed to 1 Gy γ-IR (12 and 10 foci per nucleus, respectively).
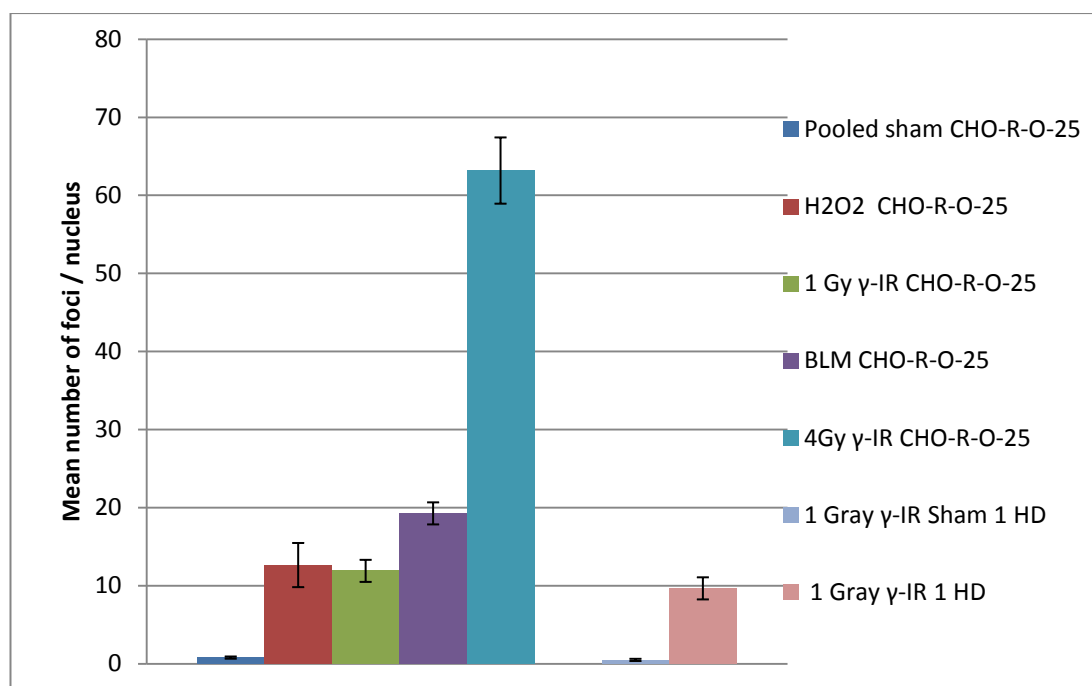
Figure 5.6 Mean number of γ-H2AX foci / nucleus for CHO-R-O-25 cells exposed to BLM, H₂O₂, 1 Gy γ-IR and 4 Gy γ-IR and 1 HD cells exposed to 1 Gy γ-IR

5.3 TIME-LAPSE MICROSCOPY

2×10^5 CHO-R-O-25 cells were seeded onto glass-bottom dishes and incubated at 37 ^{o}C for ~48 hours. The medium was then removed and 30 mM HEPES buffer (pH 7.3) added, before transportation to Axiovert 200 M inverted fluorescence microscope (section 2.8.3). The total duration of each time-lapse series was 2 hours, with one image acquired every 2 minutes. For BLM and H₂O₂ series1, 2 and 3, acquisition was commenced immediately following the addition of the drug, while in series 4 drugs were added at 14 minutes and 10 minutes into acquisition respectively, with the aim of assessing immediate effects on the physical properties (i.e. area and intensity) of the lac I-EGFP signal, after exposure to damaging agents. Regarding γ-ray exposures, in series 1, 2 and 3 cells were exposed to a dose of 1 Gy at RT with acquisition following 20, 24 and 22 minutes after irradiation, respectively. For series 4, cells were exposed to 1 Gy γ-IR on ice until the beginning of acquisition, in order to delay the initiation of DNA repair. Regarding cells exposed to 4 Gy and 6 Gy of γ-IR, acquisition was commenced 22 and 26 minutes after the end of exposures, respectively. In the discussion associated with the qualitative observations of EGFP

spots in sections 5.3.2 - 5.3.5 below, spot diffusion is defined as the decrease in the spot intensity that is often (but not necessarily) accompanied by its size expansion.

5.3.1 BACKGROUND CORRECTIONS ON IMARIS 572 PROGRAM

Background corrections were performed by following the procedure described in section 2.13.5. This image enhancement procedure resulted in the removal of FITC channel background using a filter background subtraction, which was accompanied by associated slight decreases in fluorescent spot size and increases in intensity within the cells of interest (see figures 5.7 – 5.24). Based on the fact that the majority of DNA damage repair processes take place during the first 60 minutes (126-129, 133, 134) after exposure to the damaging agent, the presented pictures in sections 5.3.3 – 5.3.5 correspond to the first 60 minutes after exposure in H_2O_2, BLM and γ-IR treated cells. Note that the entire 2 hour acquisition period for each time-lapse series is provided in the supplementary material as a CD.

5.3.2 QUALITATIVE OBSERVATIONS OF EGFP SPOTS IN UNTREATED CELLS

In series1, the cell selected for time-lapse tracking was spindle-shaped and elongated containing an intense and discrete EGFP spot at the edge of its nucleus (figure 5.7). The first expansion of the spot was recorded 24 – 30 minutes into acquisition and it progressively became more diffuse from 30 minutes until the end of visualisation (2 hours). The area of the spot remained relatively stable for the duration of acquisition, with slight expansions recorded at 30, 60 and 120 minutes.

Control time-lapse series 1

0 minutes	2 minutes	4 minutes	6 minutes
8 minutes	10 minutes	12 minutes	14 minutes
16 minutes	18 minutes	20 minutes	22minutes
24 minutes	26 minutes	28 minutes	30 minutes
32 minutes	34 minutes	36 minutes	38 minutes
40 minutes	42 minutes	44 minutes	46 minutes
48 minutes	50 minutes	52 minutes	54 minutes
56 minutes	58 minutes	60 minutes	
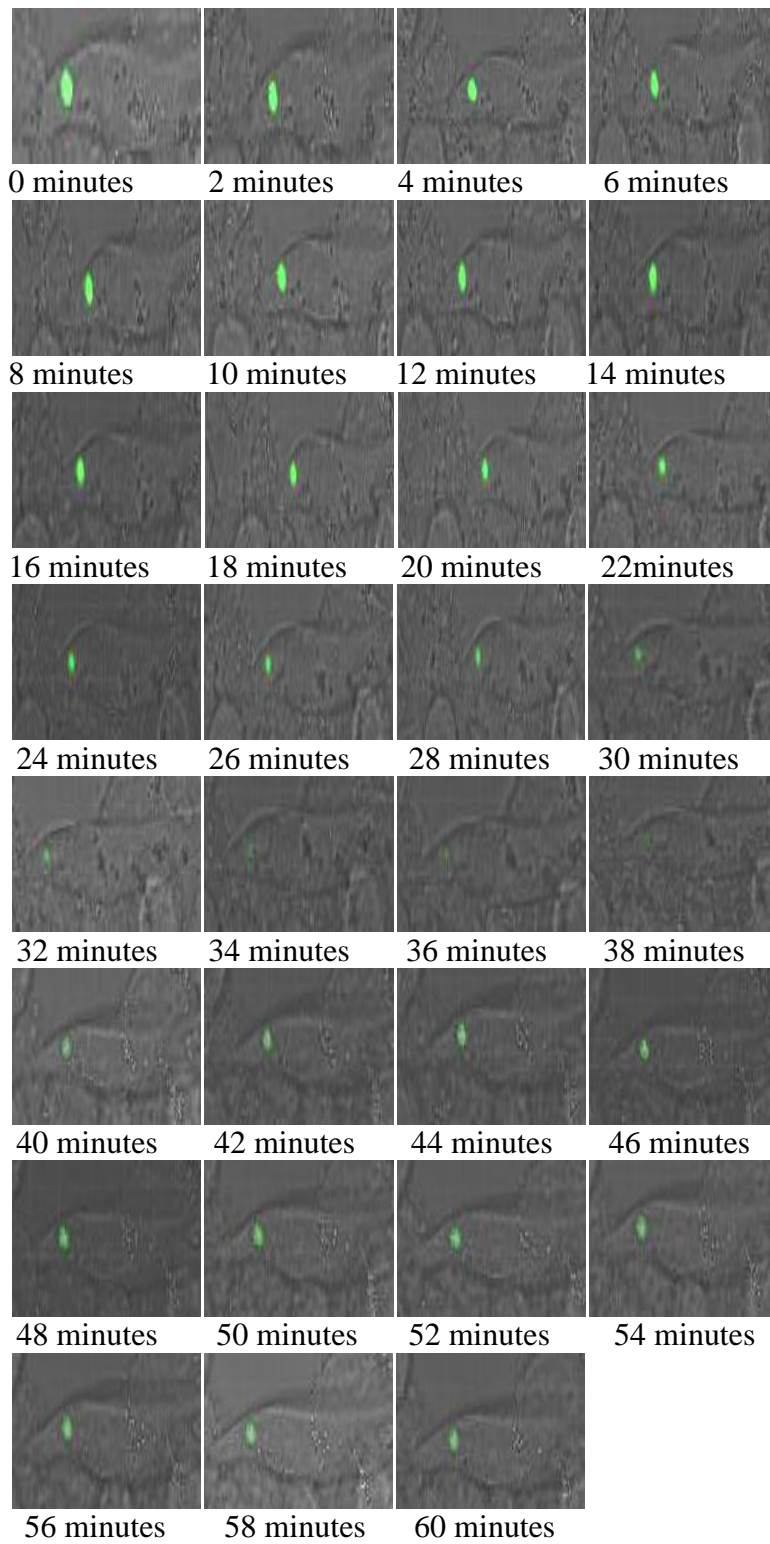
Figure 5.7 Time-lapse images corresponding to untreated series 1, showing LacI - EGFP expression during the first 60 minutes into acquisition

In series 2, the selected cell was small, rounded and relatively isolated, containing a discrete and intense fluorescent spot at the edge of its nucleus (figure 5.8). Slight expansions of the spot were observed during 22 – 30 minutes and at 38, 46 and 50 minutes.

Control time-lapse series 2

0 minutes   2 minutes   4 minutes   6 minutes   8 minutes

10 minutes   12 minutes   14 minutes   16 minutes   18 minutes

20 minutes   22 minutes   24 minutes   26 minutes   28 minutes

30 minutes   32 minutes   34 minutes   36 minutes   38 minutes

40 minutes   42 minutes   44 minutes   46 minutes   48 minutes

50 minutes   52 minutes   54 minutes   56 minutes   58 minutes
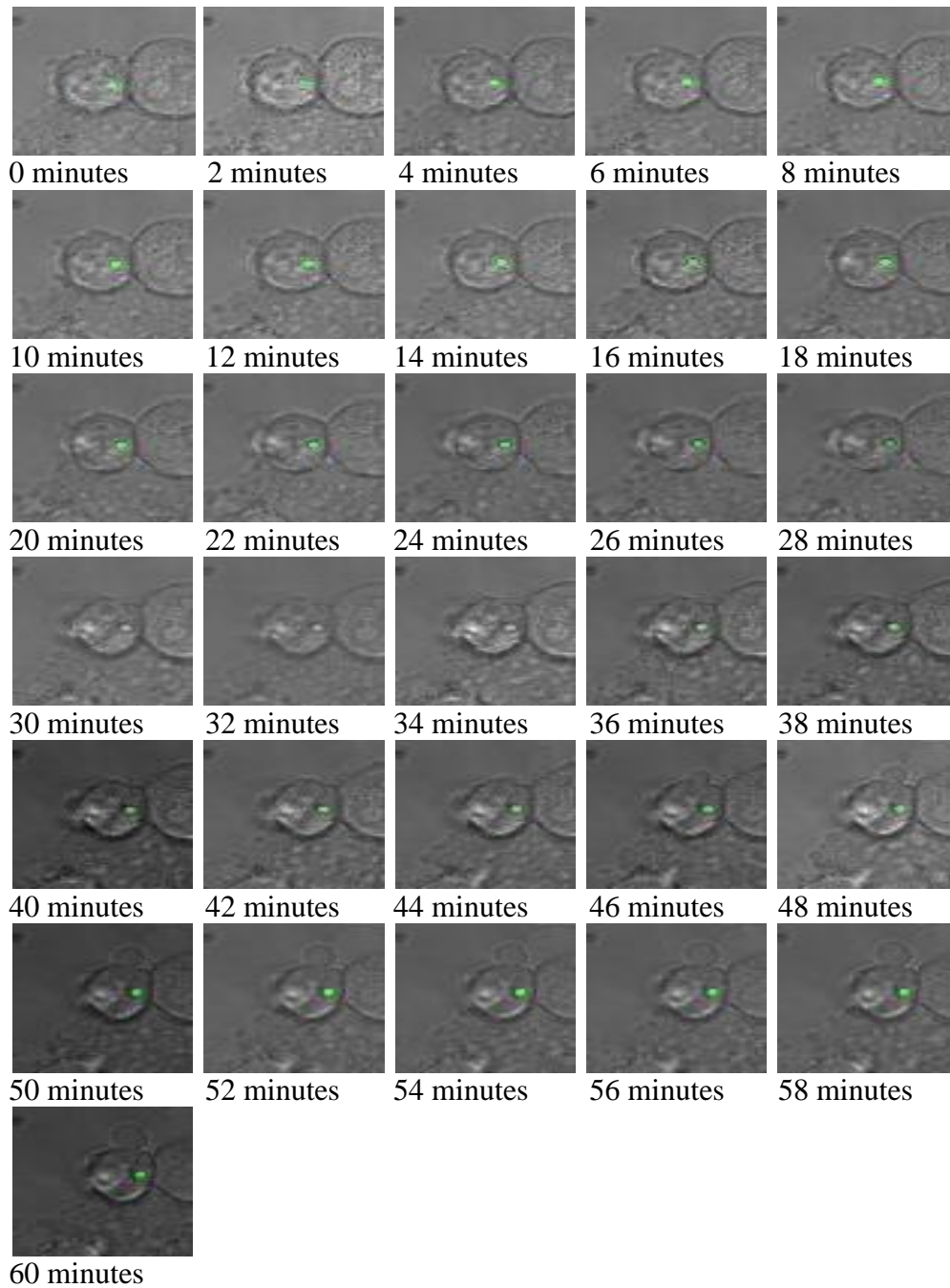
60 minutes

Figure 5.8 Time-lapse images corresponding to untreated series 2, showing LacI - EGFP expression during the first 60 minutes into acquisition

Similarly, in series 3 the area of the fluorescent spot was observed to remain unaltered during the course of acquisition. Slight expansions and diffusions of the spot were observed during 42 – 54 minutes and at 108 minutes (figure 5.9).

Control time-lapse series 3

0 minutes	2 minutes	4 minutes	6 minutes	8 minutes
10 minutes	12 minutes	14 minutes	16 minutes	18 minutes
20 minutes	22 minutes	24 minutes	26 minutes	28 minutes
30 minutes	32 minutes	34 minutes	36 minutes	38 minutes
40 minutes	42 minutes	44 minutes	46 minutes	48 minutes
50 minutes	52 minutes	54 minutes	56 minutes	58 minutes
60 minutes				
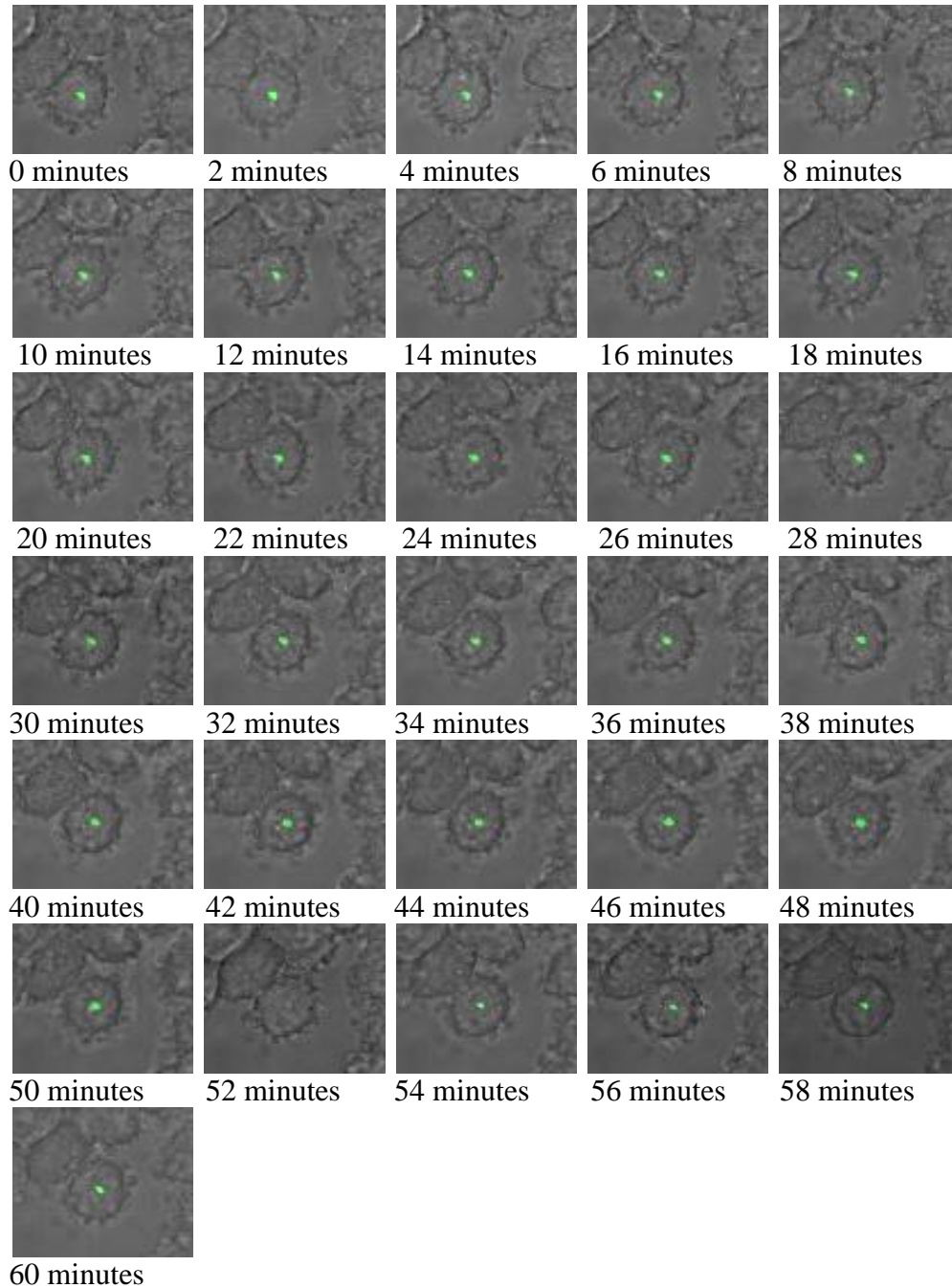
Figure 5.9 Time-lapse images corresponding to untreated series 3, showing LacI - EGFP expression during the first 60 minutes into acquisition

5.3.3 QUALITATIVE OBSERVATIONS OF EGFP SPOTS IN CELLS EXPOSED TO H_2O_2

In series1, the cell of interest appeared to be small and round, containing an intense fluorescent spot of intermediate size at the edge of its nucleus (figure 5.10). Fluctuations in intensity and apparent diffusion of the spot were observed within the first 30 minutes, before an obvious diffusion of the spot accompanied by a size reduction during 32 - 36 minutes. These fluctuations in the intensity and changes in the shape of the spot continued and its intensity was further decreased during 82 - 118 minutes. It should be noted that some cells in the FOV were blebbed, but this had no apparent effect on EGFP spot signal within the cell under examination.

H$_2$O$_2$ time-lapse series 1
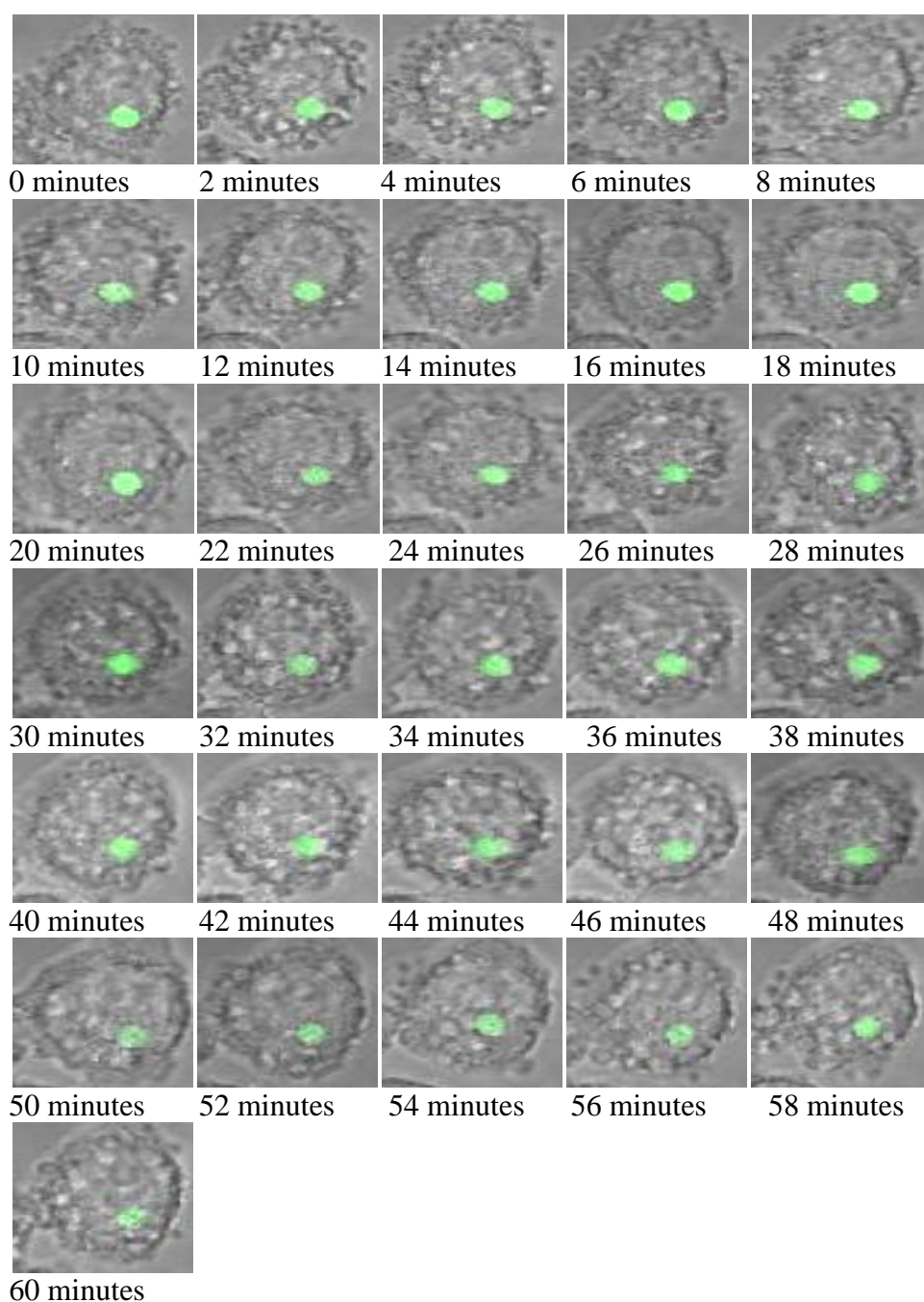
Figure 5.10 Time-lapse images corresponding to H$_2$O$_2$ series 1, showing LacI - EGFP expression during the first 60 minutes into acquisition

In series 2, the cell selected for tracking was oval and intermediate in size, containing an expanded but not too intense spot within its nucleus (figure 5.11). During the first 30 minutes there were slight alterations in spot area and apparent intensity, whereas during 38 – 50 minutes, the spot became progressively more diffuse, slightly more expanded and assumed irregular shapes. This was not

215

associated with the subsequent refocusing at 52 minutes, after which the spot became only slightly more discrete and intense.

H$_2$O$_2$ time-lapse series 2

0 minutes	2 minutes	4 minutes	6 minutes	8 minutes
10 minutes	12 minutes	14 minutes	16 minutes	18 minutes
20 minutes	22 minutes	24 minutes	26 minutes	28 minutes
30 minutes	32 minutes	34 minutes	36 minutes	38 minutes
40 minutes	42 minutes	44 minutes	46 minutes	48 minutes
50 minutes	52 minutes	54 minutes	56 minutes	58 minutes
60 minutes				
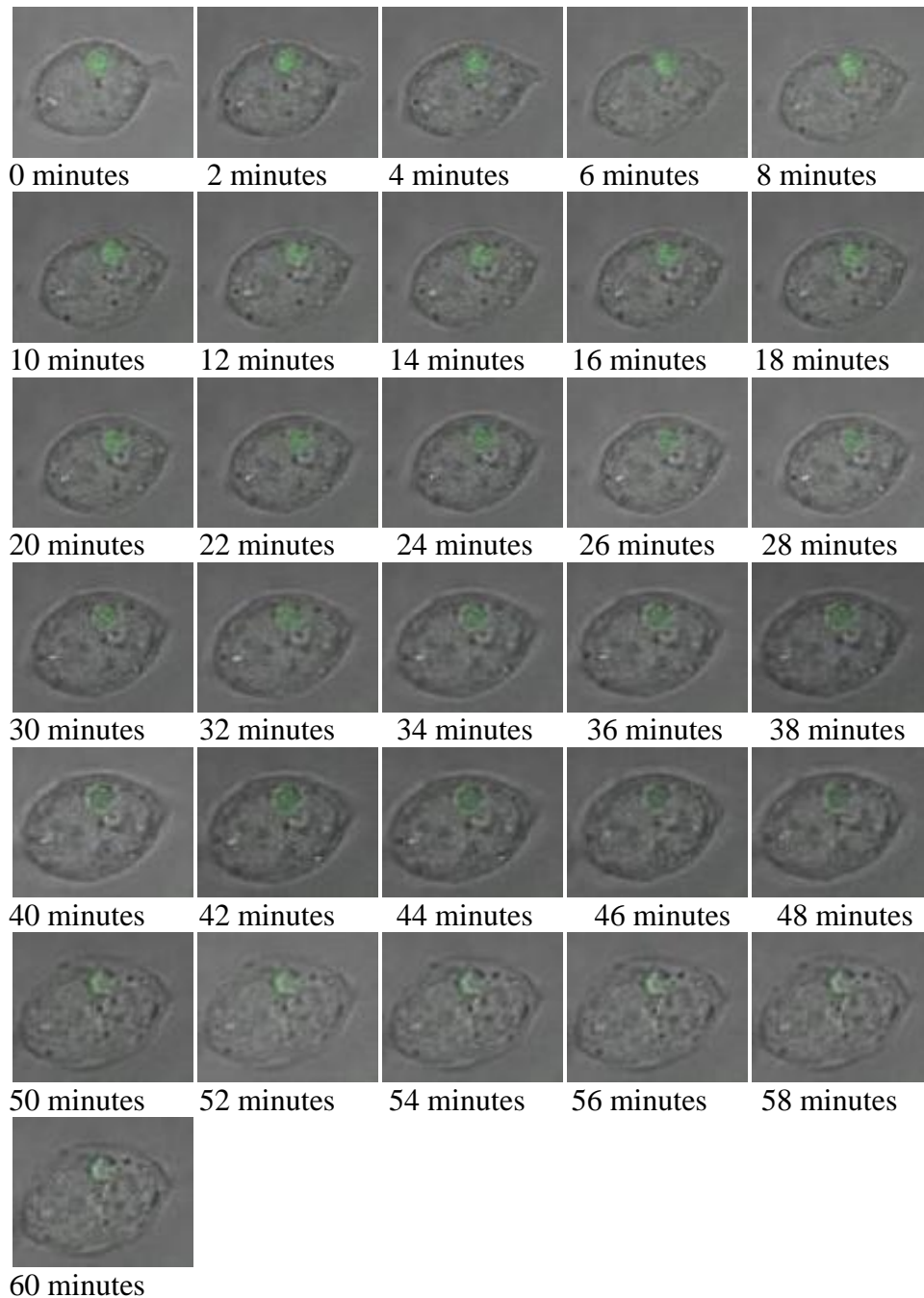
Figure 5.11 Time-lapse images corresponding to H$_2$O$_2$ series 2, showing LacI - EGFP expression during the first 60 minutes into acquisition

In series 3, the cell of interest was small and rounded containing a discrete and intense spot at the edge of its nucleus (figure 5.12). During the first 20 minutes, the spot became progressively more diffuse, but during 22 – 32 minutes its apparent

216

intensity level was elevated. During 34 - 60 minutes it progressively became more diffuse and also reduced in size, but interestingly this changed between 62 - 76 minutes, when the spot became more diffuse and expanded in size. This was not a consequence of the spot becoming out of focus, because after refocusing at 80 minutes the spot only became slightly more discrete.

<u>H_2O_2 time-lapse series 3</u>

0 minutes	2 minutes	4 minutes	6 minutes	8 minutes
10 minutes	12 minutes	14 minutes	16 minutes	18 minutes
20 minutes	22 minutes	24 minutes	26 minutes	28 minutes
30 minutes	32 minutes	34 minutes	36 minutes	38 minutes
40 minutes	42 minutes	44 minutes	46 minutes	48 minutes
50 minutes	52 minutes	54 minutes	56 minutes	58 minutes
60 minutes				
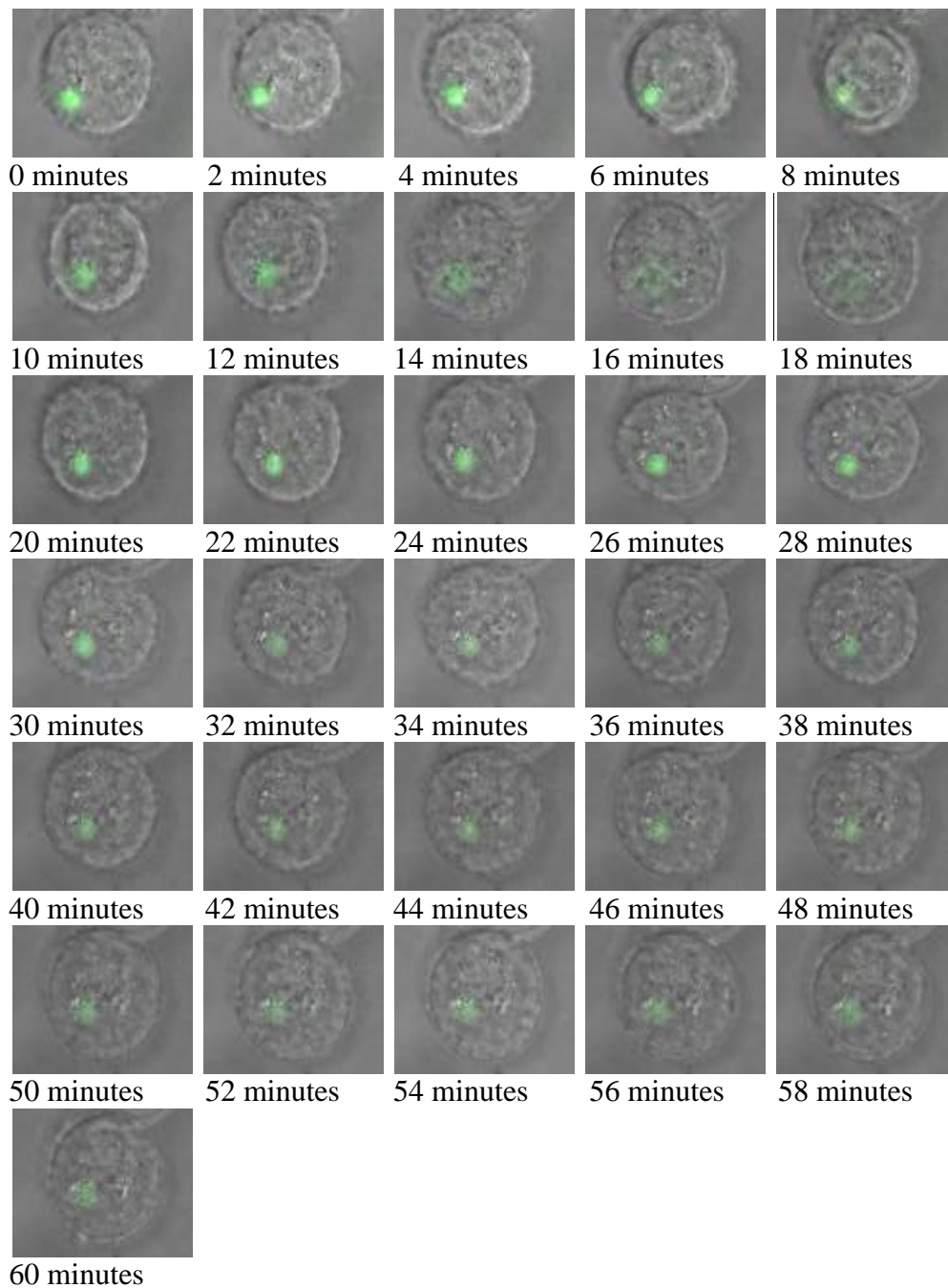
Figure 5.12 Time-lapse images corresponding to H_2O_2 series 3, showing LacI - EGFP expression during the first 60 minutes into acquisition

In series 4, the cell of interest was spindle-shaped and elongated containing an intense fluorescent spot within its nucleus (figure 5.13). H_2O_2 was added after 10 minutes into acquisition. During the first 10 minutes after H_2O_2 addition, the spot became fuzzier and more diffuse, but its appearance reverted to become more intense 25 minutes after agent addition. Additionally, the size of the cell decreased over 15-30 minutes after H_2O_2 addition.

H_2O_2 time-lapse series 4

| 0 minutes | 2 minutes | 4 minutes | 6 minutes | 8 minutes |

| 12 minutes | 14 minutes | 16 minutes | 18 minutes | 20 minutes |

| 22 minutes | 24 minutes | 26 minutes | 28 minutes | 30 minutes |

| 32 minutes | 34 minutes | 36 minutes | 38 minutes | 40 minutes |

| 42 minutes | 44 minutes | 46 minutes | 48 minutes | 50 minutes |

| 52 minutes | 54 minutes | 56 minutes | 58 minutes | 60 minutes |
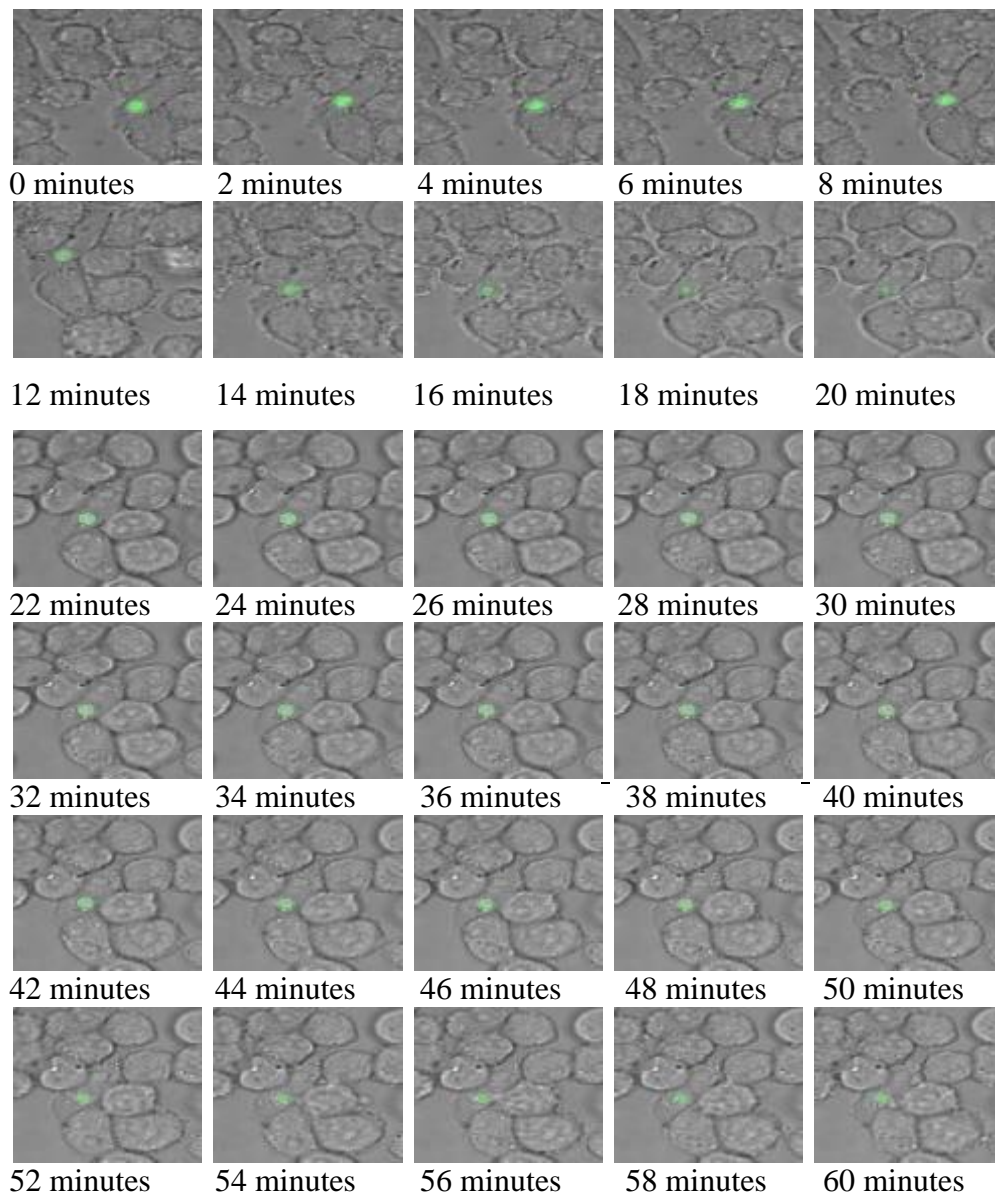
Figure 5.13 Time-lapse images corresponding to H_2O_2 series 4, showing LacI - EGFP expression during the first 60 minutes into acquisition. It should be noted that due to H_2O_2 addition, the image at 10 minutes was failed to be captured.

5.3.4 QUALITATIVE OBSERVATIONS OF EGFP SPOTS IN CELLS EXPOSED TO BLM

In series 1, the cell of interest was small and round containing an intense and slightly expanded fluorescent spot at the edge of its nucleus (figure 5.14). During the first 10 minutes after exposure, irregular shapes were observed with size and intensity slightly altered and the spot then became progressively more diffuse and expanded. After refocusing of the cell at 36 minutes, the spot appeared to be slightly more intense and slightly reduced in size, whereas during 72 – 86 minutes it assumed different irregular shapes and appeared to be slightly fragmented at 86 and 96 minutes. Following refocusing at 110 minutes, it became slightly more intense and larger, but during 110 - 120 minutes it became smaller and appeared to be slightly fragmented at 110 and 114 minutes. These fragmentations were independent of defocusing, as revealed by refocusing at 110 minutes.

BLM time-lapse series 1

0 minutes	2 minutes	4 minutes	6 minutes	8 minutes
10 minutes	12 minutes	14 minutes	16 minutes	18 minutes
20 minutes	22 minutes	24 minutes	26 minutes	28 minutes
30 minutes	32 minutes	34 minutes	36 minutes	38 minutes
40 minutes	42 minutes	44 minutes	46 minutes	48 minutes
50 minutes	52 minutes	54 minutes	56 minutes	58 minutes
60 minutes	86 minutes	96 minutes	110 minutes	114 minutes

**Figure 5.14 Time-lapse images corresponding to BLM series 1, showing LacI - EGFP expression during the first 60 minutes into acquisition and selected images during 86 - 114 minutes, showing slight fragmentation of the spot (see text)**

In series 2, the cell of interest was large and spindle-shaped, containing a discrete and quite intense fluorescent spot at the edge of its nucleus (figure 5.15). During the first 20 minutes, the spot periodically appeared to be slightly fragmented and assumed irregular shapes. At 22 and 24 minutes it expanded, before becoming slightly smaller and assuming irregular shapes during 28 - 30 minutes. Between 32 and 58 minutes, there were fluctuations in the intensity and size of the spot and it appeared to be fragmented in certain pictures. From 64 minutes onwards, EGFP expression was abolished, with apparent cell death during 76 – 128 minutes. Presumably, the mode of cell death was necrosis, as the cell was observed to burst, releasing its constituents into the medium. The observation that during 70 - 120 minutes all of the cells in the same FOV as the cell of interest had also died off in the same manner suggested that a common pathway was responsible for induction of cell death in this dish (for related evidence see CD at the back of this thesis).

BLM time-lapse series 2

0 minutes   2 minutes   4 minutes   6 minutes   8 minutes

10 minutes   12 minutes   14 minutes   16 minutes   18 minutes

20 minutes   22 minutes   24 minutes   26 minutes   28 minutes

30 minutes   32 minutes   34 minutes   36 minutes   38 minutes

40 minutes   42 minutes   44 minutes   46 minutes   48 minutes

50 minutes   52 minutes   54 minutes   56 minutes   58 minutes
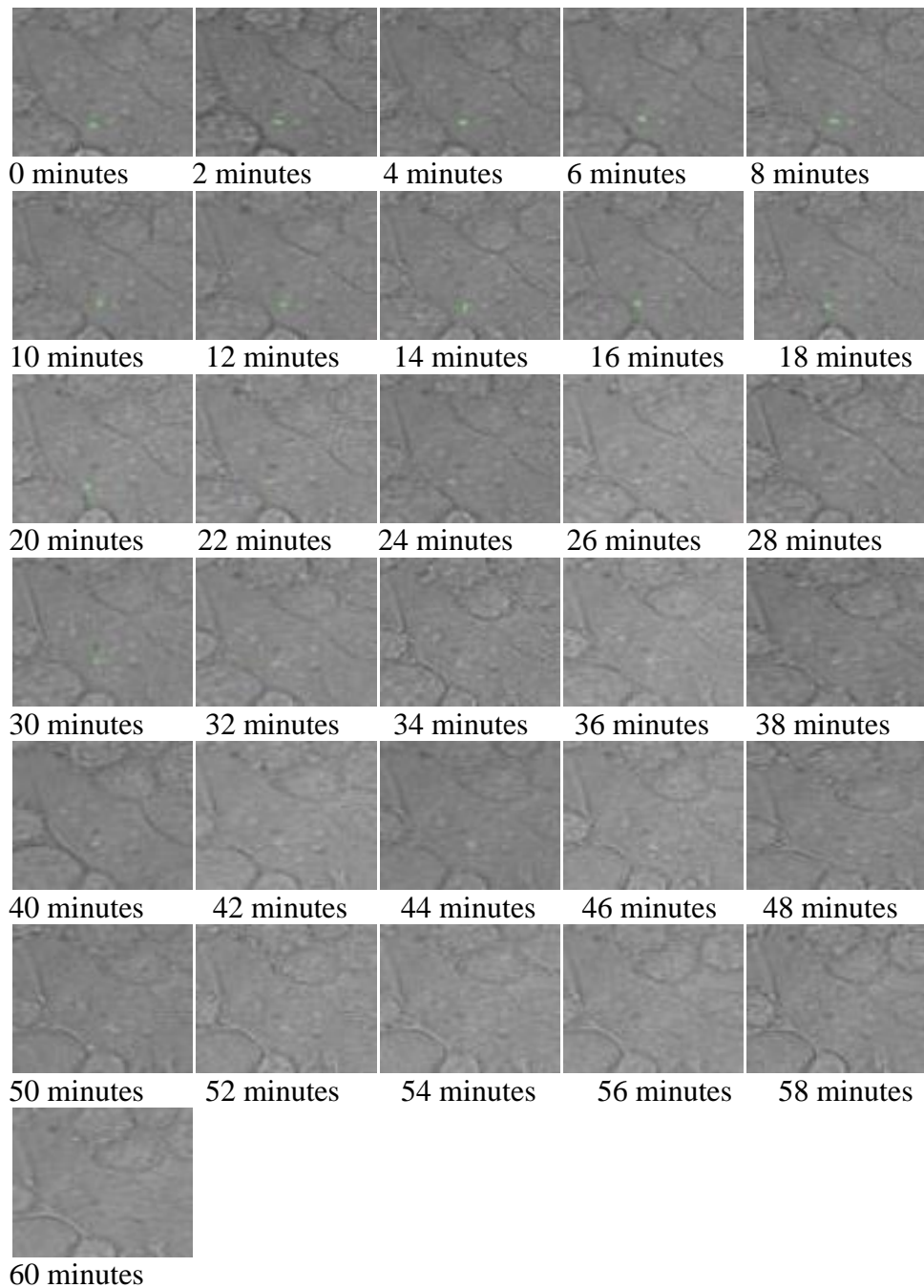
60 minutes

Figure 5.15 Time-lapse images corresponding to BLM series 2, showing LacI - EGFP expression during the first 60 minutes into acquisition

In series 3, the cell of interest was large and oval-shaped, containing an intense and quite large fluorescent spot at the edge of its nucleus (figure 5.16). During the first 6 minutes it changed in shape and was fragmented, whereas during 8 – 30 minutes it became more diffuse, assumed different irregular shapes and appeared to be occasionally fragmented. After refocusing at 36 minutes, it appeared to be larger and

fragmented, whereas between 38 - 90 minutes the spot was smaller, more diffuse, slightly fragmented and assumed different irregular shapes. Following refocusing at 94 minutes, it became slightly more discrete and intense, whereas during 96-120 minutes its appearance was reverted to more diffuse and changed in shape.

BLM time-lapse series 3
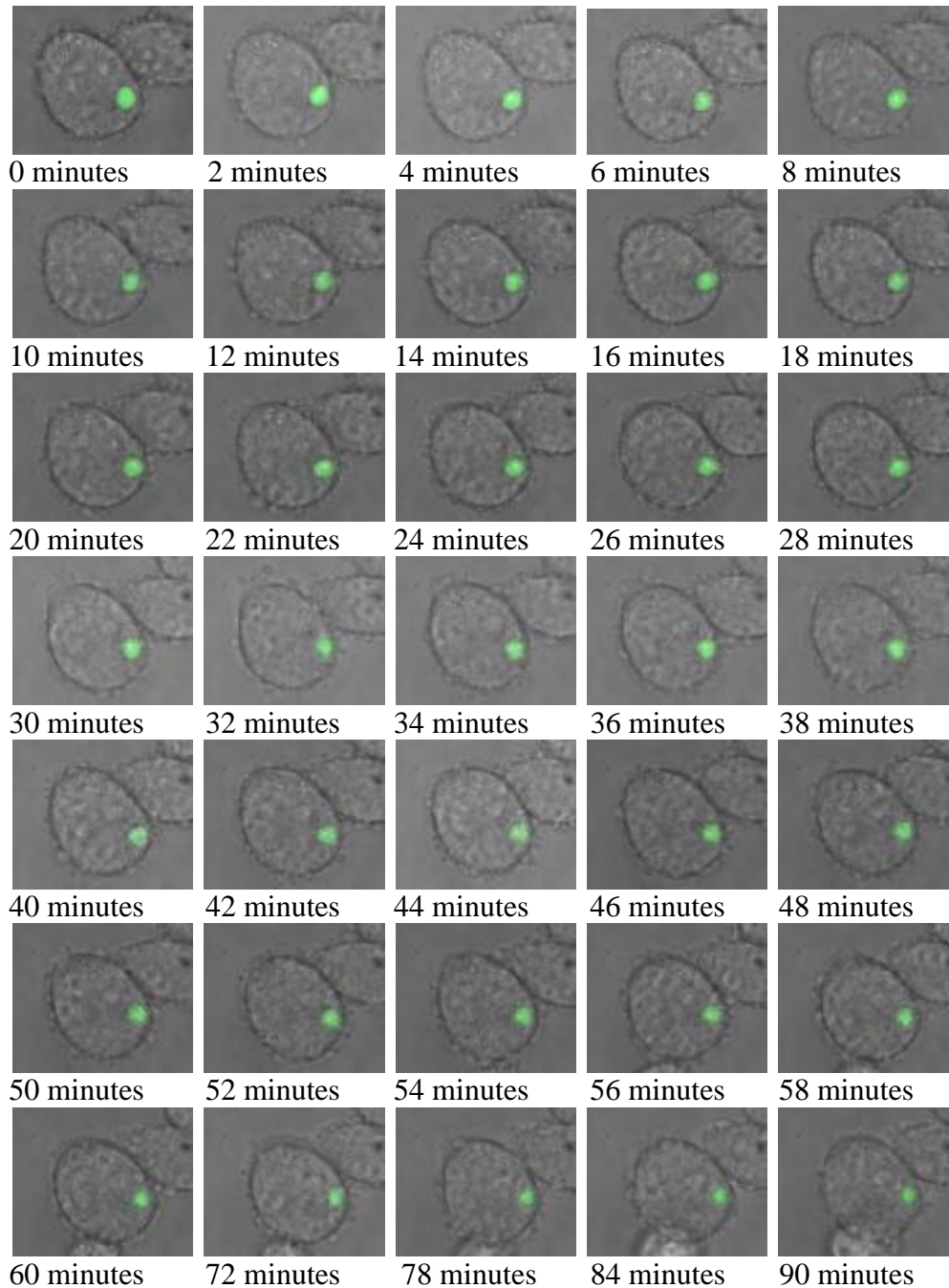
Figure 5.16 Time-lapse images corresponding to BLM series 3, presenting LacI - EGFP expression during the first 60 minutes into acquisition and selected images during 72 – 90 minutes, showing slight fragmentation of the spot (see text)

In series 4, the cell of interest was small and oval-shaped containing a discrete and intense spot near the edge of its nucleus (figure 5.17). BLM was added into the dish after 14 minutes into acquisition. Before BLM addition, no changes in shape or size of the spot were recorded, whereas as early as 8 minutes after BLM addition (22 minutes into acquisition), it appeared to be slightly more expanded, more intense and altered in shape. Between 18 and 30 minutes, the spot became slightly fragmented and altered in shape, but the EGFP fluorescence remained intense. Irregular slightly expanded shapes remained a feature for the remainder of the time-lapse acquisition.

BLM time-lapse series 4

|				
0 minutes	2 minutes	4 minutes	6 minutes	8 minutes
10 minutes	12 minutes	14 minutes	16 minutes	18 minutes
20 minutes	22 minutes	24 minutes	26 minutes	28 minutes
30 minutes	32 minutes	34 minutes	36 minutes	38 minutes
40 minutes	42 minutes	44 minutes	46 minutes	48 minutes
50 minutes	52 minutes	54 minutes	56 minutes	58 minutes
60 minutes				
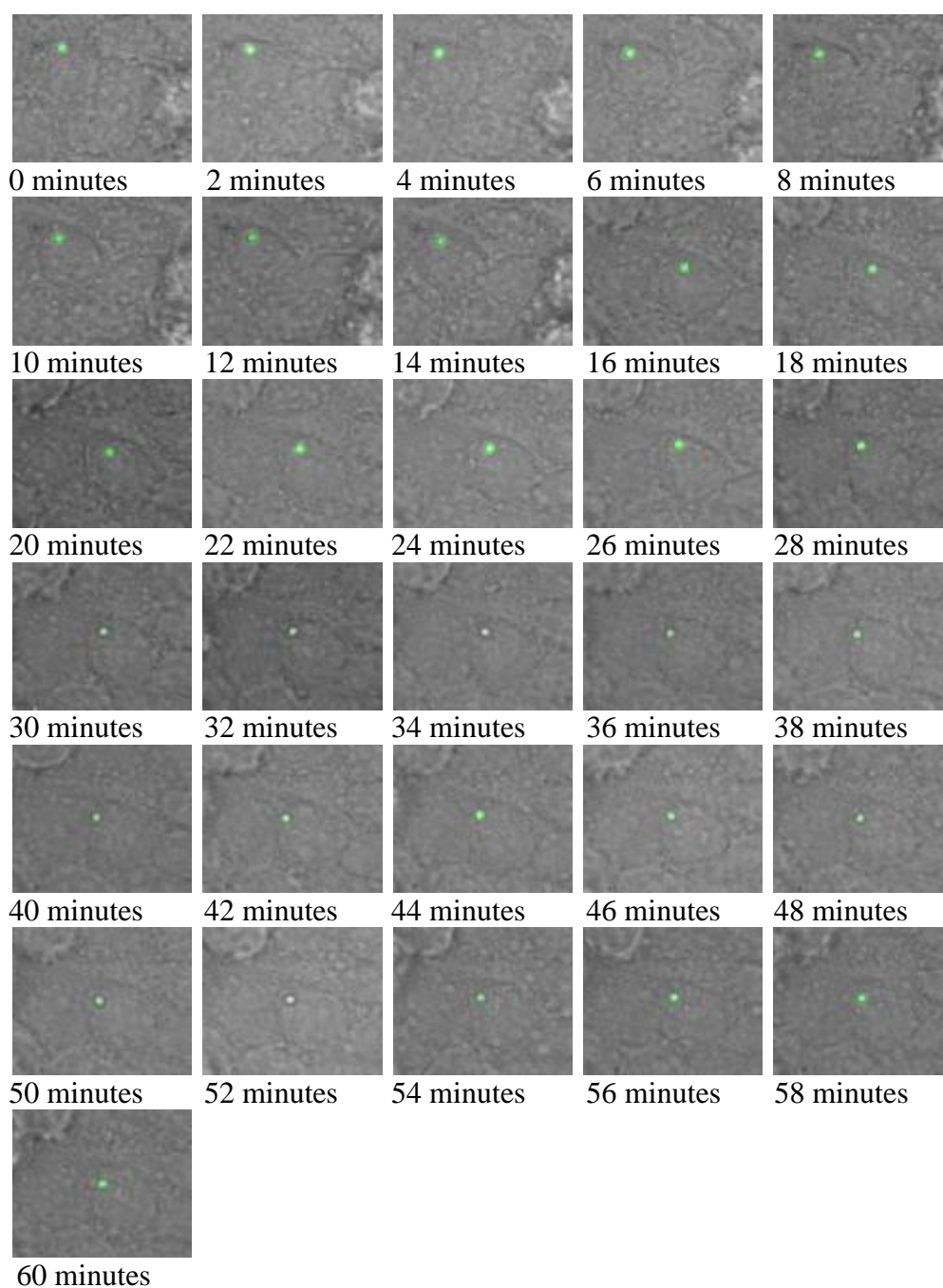
Figure 5.17 Time-lapse images corresponding to BLM series 4, presenting LacI - EGFP expression during the first 60 minutes into acquisition. In this series, BLM was added after 14 minutes into acquisition

Similar to the time-lapse series in which cells were exposed to H_2O_2, cells exposed to 20 µg/ml of BLM in series 1, 3 and 4 remained viable during the 2 hour period of acquisition, confirming that this dose can be tolerated by the majority of CHO-R-O-

25 cells. In series 2 however, cell death was recorded for all of the cells present in the same FOV between 70 -120 minutes (see CD supplementary material). This may be accounted for by BLM-induced cell death and could correspond to the frequency of CHO-R-O-25 cell death previously measured at this BLM dose (7.6% nonviability after incubation for 30 minutes at 37 $^{\circ}$C; figure 5.1).

5.3.5 QUALITATIVE OBSERVATIONS OF EGFP SPOTS IN CELLS EXPOSED TO γ-IRRADIATION

In time-lapse series 1, the cell of interest was oval and intermediate in size, containing an intense and quite expanded fluorescent spot within its nucleus (figure 5.18). The first image in the course of acquisition was captured 20 minutes after exposure to γ-IR. During the first 26 minutes into acquisition (20 - 46 minutes after irradiation), the spot appeared to be fragmented and became more diffuse. Between 32 and 60 minutes, the spot assumed irregular shapes and was occasionally expanded, whereas during 62 – 74 minutes, it became larger and more diffuse. During 76 - 88 minutes it remained diffuse, but it was no longer observed to be fragmented. Despite the fact that the majority of cells in the FOV were blebbed, EGFP spot expression remained unaffected during the course of time-lapse acquisition.

1 Gy γ-irradiation time-lapse series 1
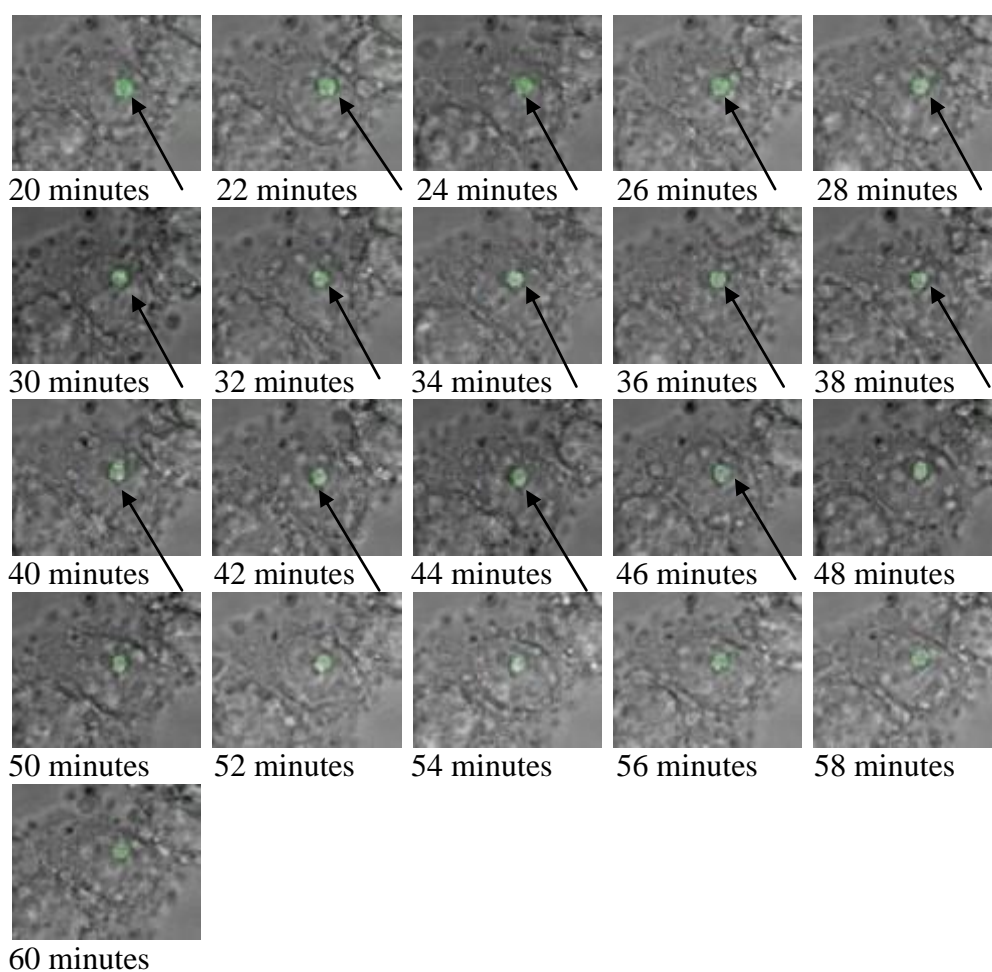
Figure 5.18 Time-lapse images corresponding to 1 Gy γ-irradiation series 1, presenting LacI - EGFP expression during the first 60 minutes after exposure. The first image in the series was captured 20 minutes after the end of exposure. Black arrows point to fluorescent spots that appeared to be fragmented during the first 26 minutes into acquisition (20 – 46 minutes after the end of irradiation).

In series 2, the cell of interest was quite large and spindle-shaped, containing a discrete and intense spot within its nucleus (figure 5.19). The first image in the course of acquisition was captured 24 minutes after exposure to γ-IR. During the first 22 minutes into acquisition (24 – 46 minutes after irradiation), the spot changed in shape, slightly expanded and became progressively more diffuse. Between 24 and 30 minutes into acquisition, the spot became fuzzier, slightly expanded and fragmented, before becoming progressively more diffuse and decreasing in size. At 78 minutes, the location of the spot was slightly changed, before finally appearing as small and intense.

1 Gy γ-irradiation time-lapse series 2

24 minutes	26 minutes	28 minutes	30 minutes	32 minutes
34 minutes	36 minutes	38 minutes	40 minutes	42 minutes
44 minutes	46 minutes	48 minutes	50 minutes	52 minutes
54minutes	56 minutes	58 minutes	60 minutes	78 minutes
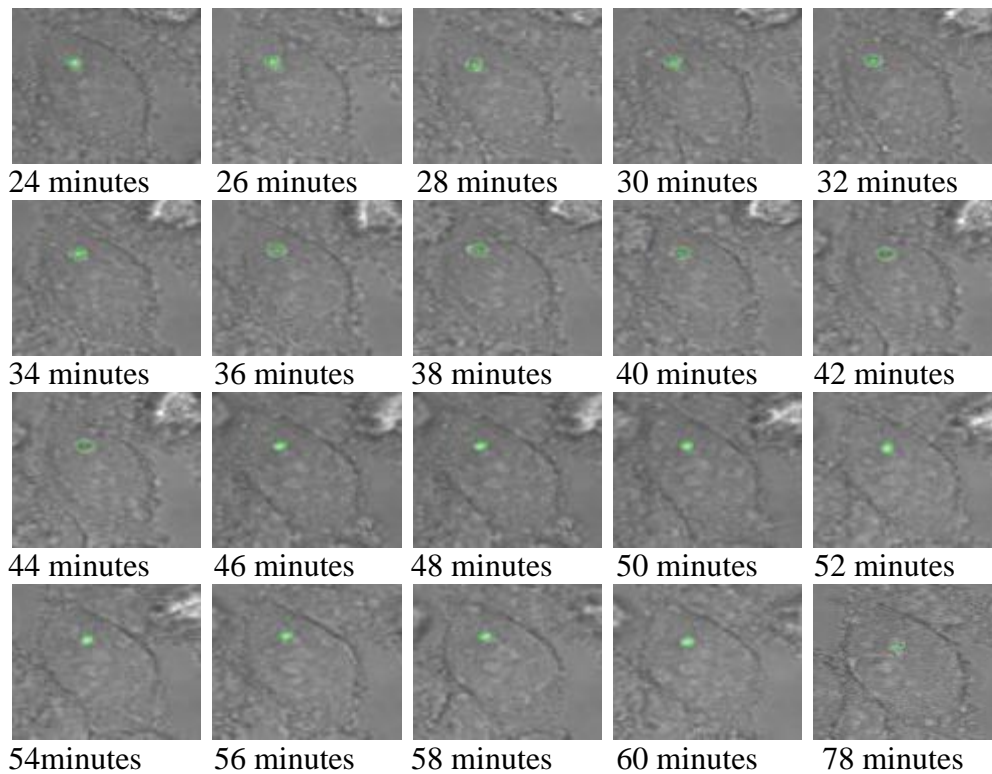
Figure 5.19 Time-lapse images corresponding to 1 Gy γ-irradiation series 2, presenting LacI - EGFP expression during the first 60 minutes after exposure. The first image in the series was captured 24 minutes after the end of exposure. Note the slight change in the location of the spot at 78 minutes.

In series 3, the cell selected for tracking was oval-shaped and contained a discrete spot at the edge of its nucleus (figure 5.20). The first image in the series was acquired 22 minutes after exposure to γ-IR. During the first 14 minutes into acquisition (22 – 36 minutes after exposure), the spot appeared to be more diffuse, slightly more expanded and occasionally fragmented. The spot remained diffuse until 60 minutes into acquisition and it was observed to change in shape, progressively becoming more diffuse and expanded.

1 Gy γ-irradiation time-lapse series 3

22 minutes	24 minutes	26 minutes	28 minutes	30 minutes
32 minutes	34 minutes	36 minutes	38minutes	40 minutes
42 minutes	44 minutes	46 minutes	48 minutes	50 minutes
52minutes	54 minutes	56 minutes	58 minutes	60 minutes
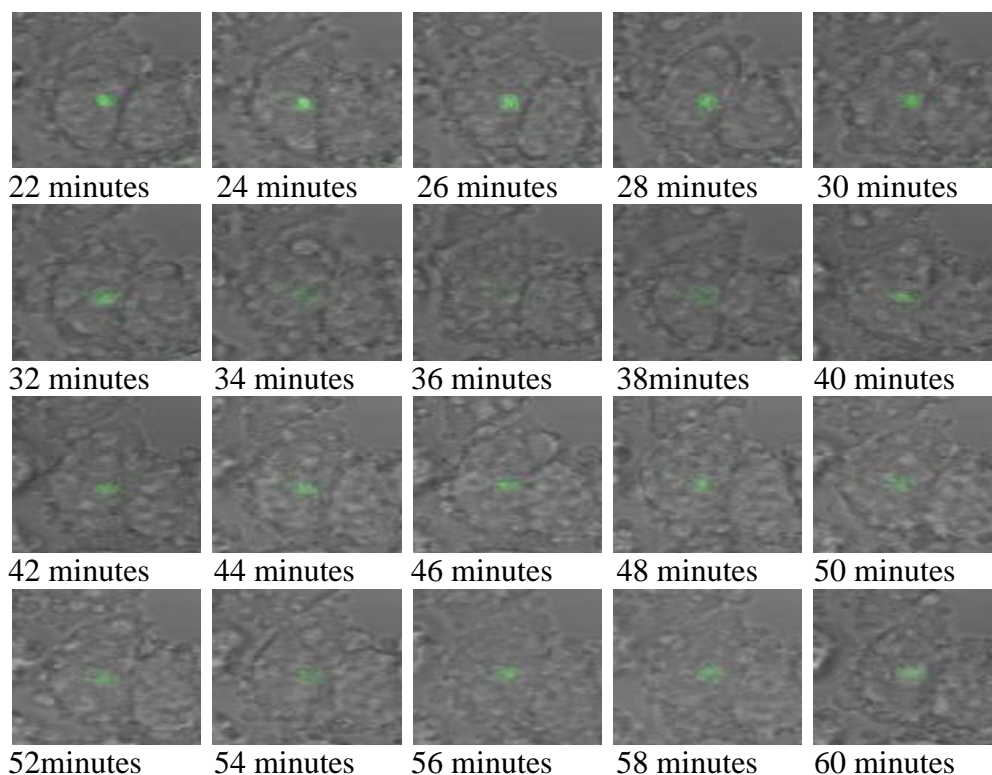
Figure 5.20 Time-lapse images corresponding to 1 Gy γ-irradiation series 3, presenting LacI -EGFP expression during the first 60 minutes after exposure. The first image in the series was captured 22 minutes after the end of exposure.

In time-lapse series 4, the cell of interest was spindle-shaped and elongated containing an expanded spot within its nucleus (figure 5.21). The cells were incubated on ice during exposure to γ-irradiation and until acquisition of the first image. During the first 30 minutes, the spot appeared to be fragmented, but its intensity level was not altered. However, its shape altered, becoming more oval-shaped and subsequently progressively more expanded, with fluctuations in apparent intensity levels.

1 Gy γ-irradiation time-lapse series 4

0 minutes   2 minutes   4 minutes   6 minutes   8 minutes

10 minutes   12 minutes   14 minutes   16 minutes   18 minutes

20 minutes   22 minutes   24 minutes   26 minutes   28 minutes

30 minutes   32 minutes   34 minutes   36 minutes   38 minutes

40 minutes   42 minutes   44 minutes   46 minutes   48 minutes

50 minutes   52 minutes   54 minutes   56 minutes   58 minutes
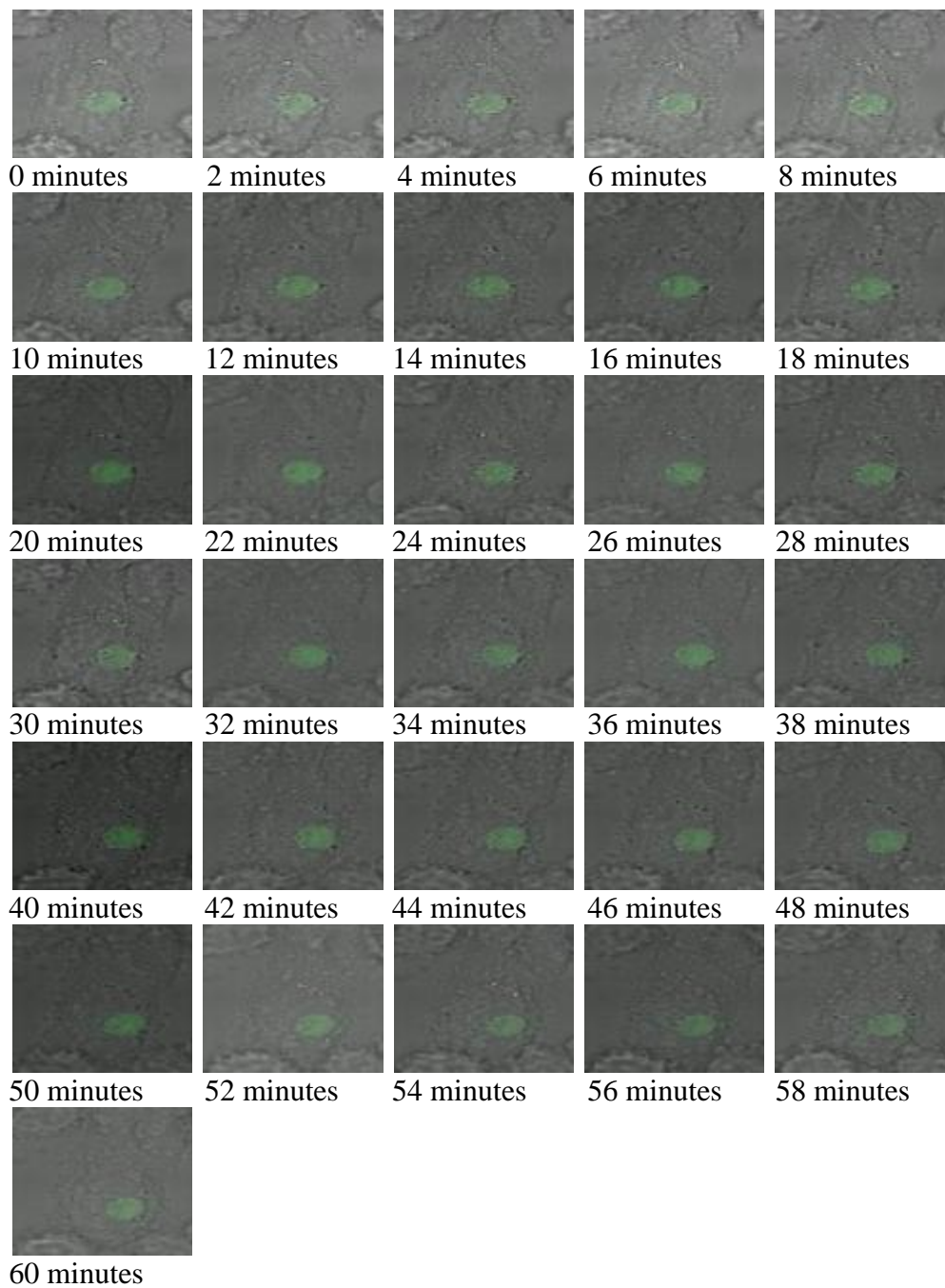
60 minutes

Figure 5.21 Time-lapse images corresponding to 1 Gy γ-irradiation series 4, presenting LacI - EGFP expression during the first 60 minutes after exposure. It should be mentioned that during exposure and until acquisition of the first image, cells were incubated on ice in order to delay the initiation of DNA damage repair. Note the different morphology of EGFP spot in comparison to time-lapse images corresponding to other treatments.

Based on the fact that the majority of DNA damage repair processes occur during the first 30 - 60 minutes after induction of damage, the first 30 minutes into acquisition in series 1 – 3 and the first 60 minutes in series 4 were expected to be characterised by the most significant changes in the appearance of the spots. In the four experiments described above, spots were observed to become more diffuse and expanded in size and also became quite fragmented, with their shapes altered more considerably during the first 30 minutes compared to the remaining time intervals of acquisition. Whether these alterations in chromatin physical properties were associated with DNA damage within the vicinity of the EGFP spots remains to be tested.

The cell selected for time-lapse microscopy after exposure to 4 Gy γ-IR was small and round, containing an expanded and quite diffuse fluorescent spot within its nucleus. The first image in the series was acquired 22 minutes after the end of irradiation (figure 5.22). During the first 30 minutes into acquisition (22 – 52 minutes after the end of exposure), the spot appeared to be fragmented, assumed irregular shapes and its size was decreased. The shape of the EGFP spot was altered and became more expanded and occasionally fuzzier during the second 30 minutes of acquisition, appearing less fragmented compared to the first 30 minutes. Between 62 and 120 minutes, the area that the spot occupied decreased, becoming quite irregular in shape.

4 Gy γ-irradiation time-lapse series 2

|				
22 minutes	24 minutes	26 minutes	28 minutes	30 minutes
32 minutes	34 minutes	36 minutes	38 minutes	40 minutes
42 minutes	44 minutes	46 minutes	48 minutes	50 minutes
52 minutes	54 minutes	56 minutes	58 minutes	60 minutes
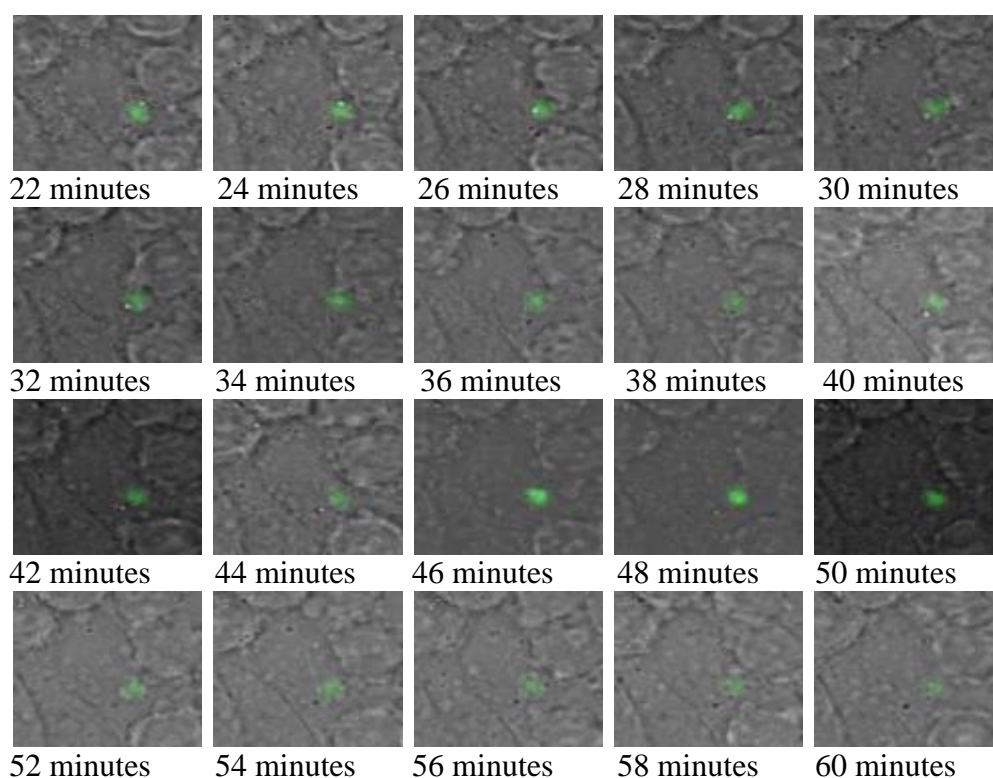
Figure 5.22 Time-lapse images corresponding to 4 Gy γ-irradiation series 2, presenting LacI - EGFP expression during the first 60 minutes after exposure. The first image in the series was captured 22 minutes after the end of exposure.

After exposure to 6 Gy γ-IR, the cell selected was round, containing a discrete and intense spot at the edge of its nucleus (figure 5.23). The first image in the series was acquired 26 minutes after exposure to irradiation. 30 minutes into acquisition (26 – 56 minutes after irradiation), the spot was observed to change in shape, became more expanded and occasionally appeared fragmented. Between 32 and 56 minutes into acquisition, it changed in shape becoming more rounded, more diffuse and smaller.

6 Gy γ-irradiation time-lapse series

| 26 minutes | 28 minutes | 30 minutes | 32 minutes | 34 minutes |
36 minutes	38 minutes	40 minutes	42 minutes	44 minutes
46minutes	48 minutes	50 minutes	52 minutes	54 minutes
56minutes	58 minutes	60 minutes		
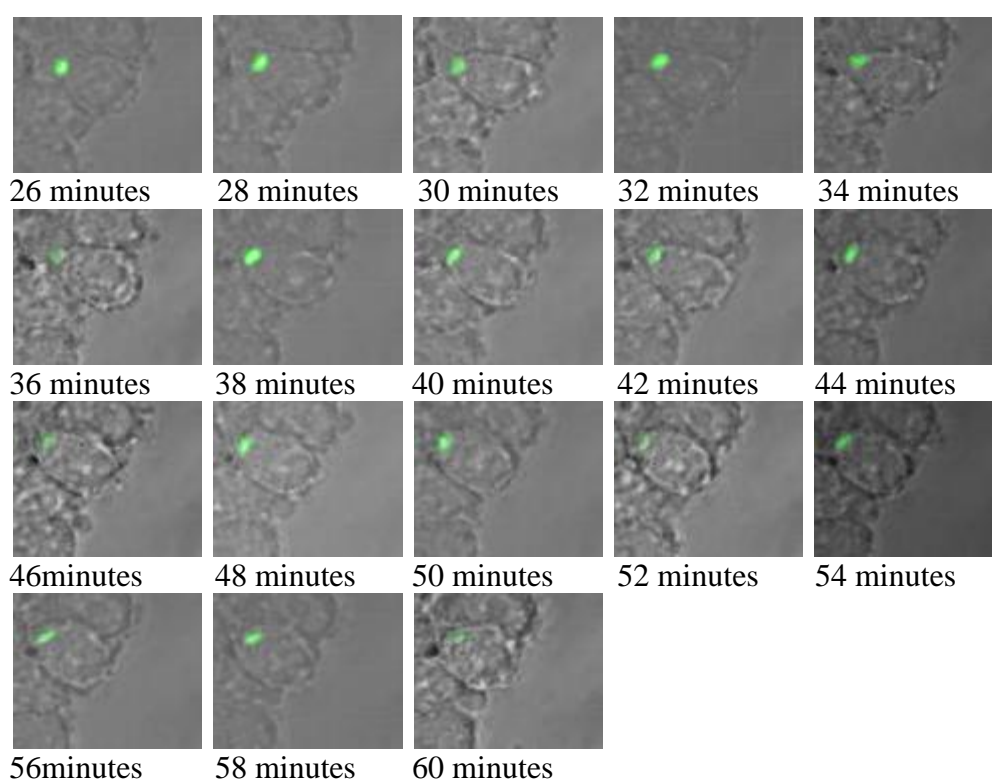
Figure 5.23 Time-lapse images corresponding to 6 Gy γ-irradiation series, presenting LacI - EGFP expression during the first 60 minutes after exposure. The first image in the series was captured 26 minutes after the end of exposure.

The observation that the spots appeared fragmented, altered in shape and expanded, especially during the first 30 minutes, is consistent with the timescales of DNA damage repair processing (126-129, 133, 134).

An apparent increase in the area of EGFP spots within the cells was observed after exposure to 4 Gy γ-IR in time-lapse series 1 and 3 (see figure 5.24 below). Within the nuclei of these cells, expanded and diffuse fluorescent spots that cover large nuclear areas are observed to be present at the beginning of acquisition. As mentioned in section 3.3.4.2.1 above, this endogenous EGFP expression is possibly the consequence of the existence of an excess of lac repressor-EGFP fusion proteins that has resulted in the oversaturation of lac O DNA sequences. As a result of this phenomenon, excess lac repressor-EGFP fusion proteins bind to non-specific DNA sequences of the genome (173, 238). Based on their aforementioned unfavourable features (figure 5.24), 4 Gy γ-IR series 1 and 3 were not analysed quantitatively on image J program. The main motive behind this decision was the morphology of the

spots that would not allow the determination of differences in their appearance over the course of time-lapse acquisitions.

a)   b)
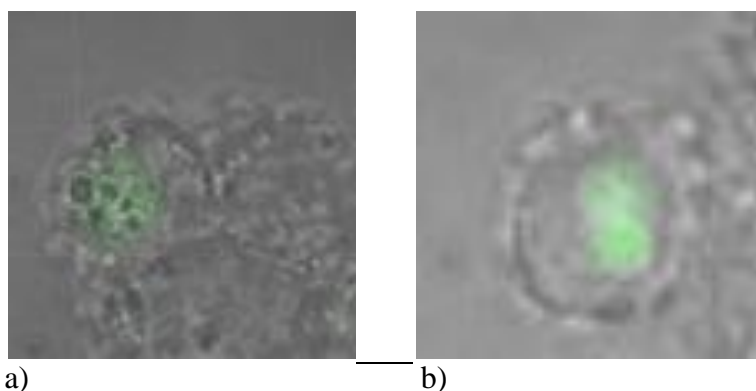
Figure 5.24 Time-lapse images of 4 Gy γ- irradiation series 1 (shown in a) and 3 (shown in b) at 0 minutes. Based on the observed over expression of EGFP spots within the nuclei of cells, a decision was made to omit quantitative image J analysis for these series (see text).

5.3.6 INFLUENCE OF FOCAL PLANE ON EGFP SPOT APPEARANCE

To establish whether changes associated with the diffusion of fluorescent spots in the time-lapse series were valid or artefacts owed to the defocusing of the cells during the course of acquisition, images were acquired at different focus positions in the multidimensional acquisition and z-stack modes on Axiovert 200 M inverted fluorescence microscope. Alterations in the characteristics (appearance, intensity and size) of the spots were then correlated to adjustments in the focus positions during acquisition (tables 5.2 – 5.3 and figures 5.25 - 5.28). On the graphs, value changes of 1 (e.g: 1.5 – 2.5 for intensity and 2 - 1 for size; see table 5.2), were assigned to remarkable alterations in spot intensity and size. On the other hand, slight alterations were represented by value changes of 0.5 (e.g.: 2.5 – 3 for intensity and 2.5 – 2 for size; see table 5.2).

Table 5.2 Effect of defocusing on EGFP spot characteristics after multidimensional acquisition (cells 1 and 2)

FOCUS POSITION (μm)	FLUORESCENT SPOT APPEARANCE	GRADIENT OF INTENSITY CHANGE	GRADIENT OF SIZE CHANGE
CELL 1			
32.15	Not visible	0	0
36.825	Not visible	0	0
39.525	Not visible	0	0
40.975	Barely visible, diffuse and expanded	0.5	2.5
42.325	More intense and slightly sharper	1.5	2
43.325	More intense and sharper	2.5	1
45.2 (in focus)	Slightly more intense and sharper	3	0
46.8	More diffuse and less sharp	2	1
46.85	Slightly more diffuse and slightly less sharp	1.5	1.5
47.7	Slightly more diffuse and sharper	1	2.5
51	Not visible	0	0
53.875	Not visible	0	0
56.7	Not visible	0	0
CELL 2			
25.85	Not visible	0	0
29.05	Not visible	0	0
30.925	Not visible	0	0
32.175	Not visible	0	0
33.625	Visible, diffuse and expanded	1	2.5
34.3	Slightly more intense and slightly sharper	1.5	2
34.775	Slightly more intense and sharper	2	1
36.4 (in focus)	More intense sharper	3	0
37.225	Less intense and less sharp	2	1
39.375	Less intense and less sharp	1	2
41.3	Not visible	0	0
44.775	Not visible	0	0
47.825	Not visible	0	0

Table 5.3 Effect of defocusing on EGFP spot characteristics after z-stack acquisition (cells 1 and 2)

FOCUS POSITION (μm)	FLUORESCENT SPOT APPEARANCE	GRADIENT OF INTENSITY CHANGE	GRADIENT OF SIZE CHANGE
CELL 1			
37	Not visible	0	0
38	Not visible	0	0
39	Diffuse and expanded	1	4
40	More intense and sharper	2	3
41	More intense and sharper	3	2
42	More intense and sharper	4	1
43	More intense and sharper	5	0
44	More diffuse and less sharp	4	1
45	More diffuse and less sharp	3	2
46	More diffuse and less sharp	2	3
47	More diffuse and less sharp	1	4
48	Not visible	0	0
49	Not visible	0	0
50	Not visible	0	0
CELL 2			
37	Not visible	0	0
38	Diffuse and expanded	1	4
39	More intense and sharper	2	3
40	More intense and sharper	3	2
41	More intense and sharper	4	1
42	More intense and sharper	5	0
43	Not visible	0	0
44	Not visible	0	0
45	Not visible	0	0
46	Not visible	0	0
47	Not visible	0	0
48	Not visible	0	0
49	Not visible	0	0
50	Not visible	0	0

Images were acquired at a nuclear depth distance of 1 μm from each other.

The results from the multidimensional (table 5.2; figures 5.25 and 5.26) and z-stack (table 5.3; figures 5.27 and 5.28) acquisitions were reproducible for both cells under examination. It was clear that the greater the distance between the focus positions,

the more pronounced the alterations in the intensity and size of the fluorescent spots under investigation. Therefore, these acquisitions revealed that defocusing is associated with increases in the area and decreases in the fluorescence intensity of EGFP spots (figures 5.25 – 5.28), suggesting that the cell of interest in each time-lapse series should be refocused regularly. These findings provide an explanation for the observed diffusion and decreases in mean intensity and calculated total intensity of the fluorescent spots in time-lapse sequences 1 – 3 in untreated cells, where no refocusing adjustments were made during the course of acquisition (figures 5.7 – 5.9 in section 5.3.2). In addition, it was established that a greater degree of defocusing can result in the disappearance of the fluorescent spots from the nuclei of cells.
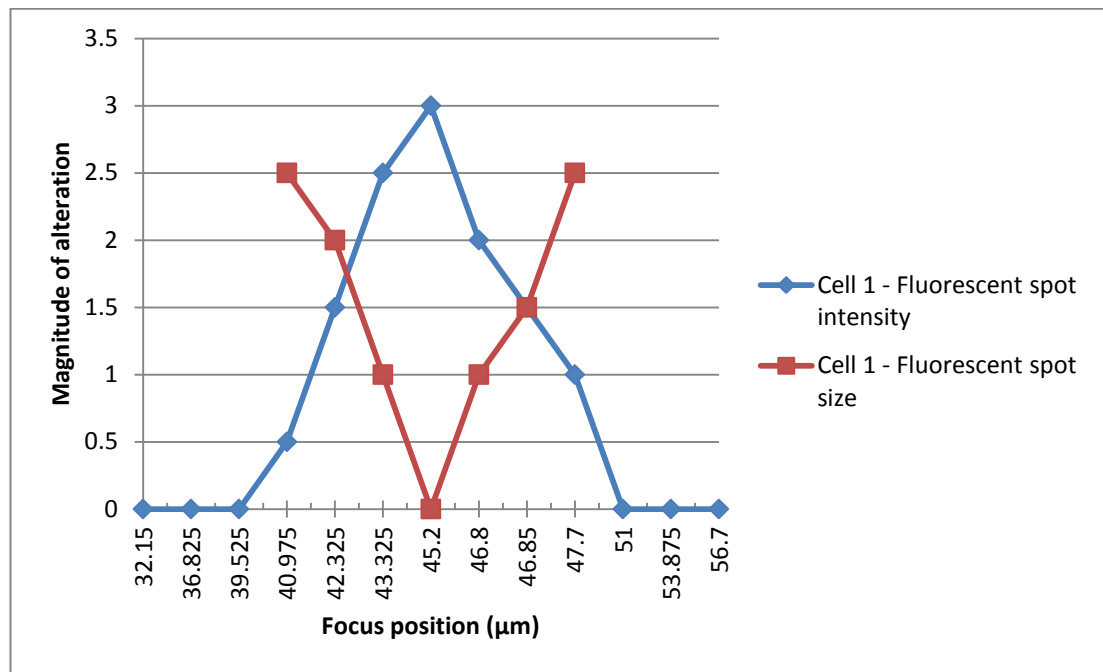
Figure 5.25 Graph correlating the different focus positions with alterations in fluorescent spot intensity and size, in multidimensional acquisition mode. Note the interdependence between the decrease in intensity and increase in the size of the spot due to defocusing
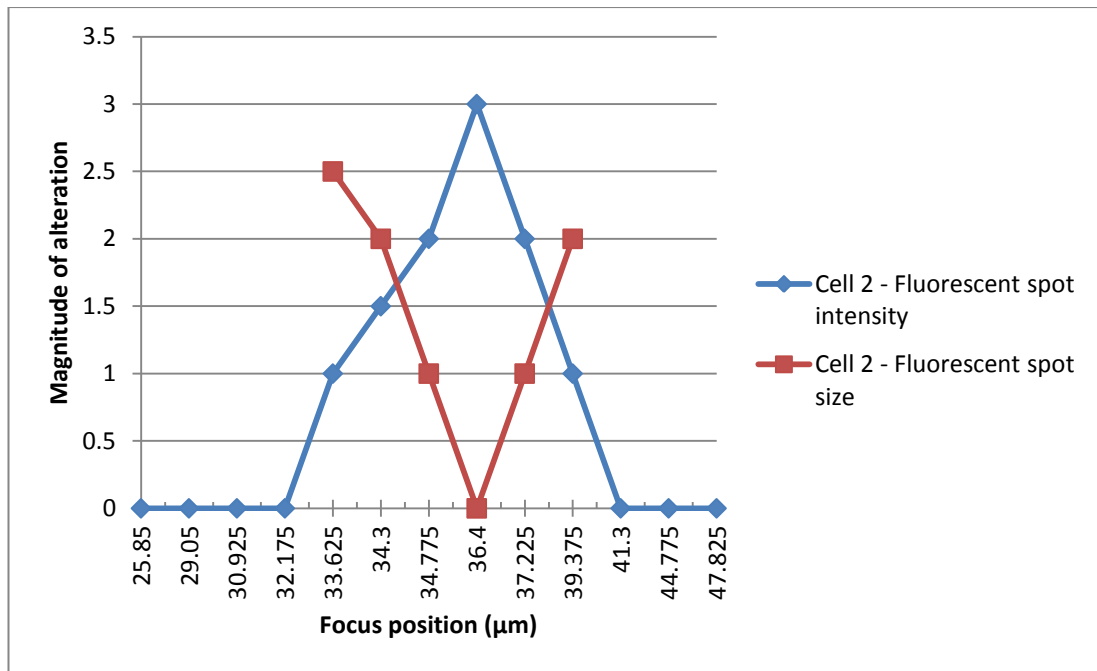
Figure 5.26 Correlation between the different focus positions and alterations in fluorescent spot intensity and size, in multidimensional acquisition mode
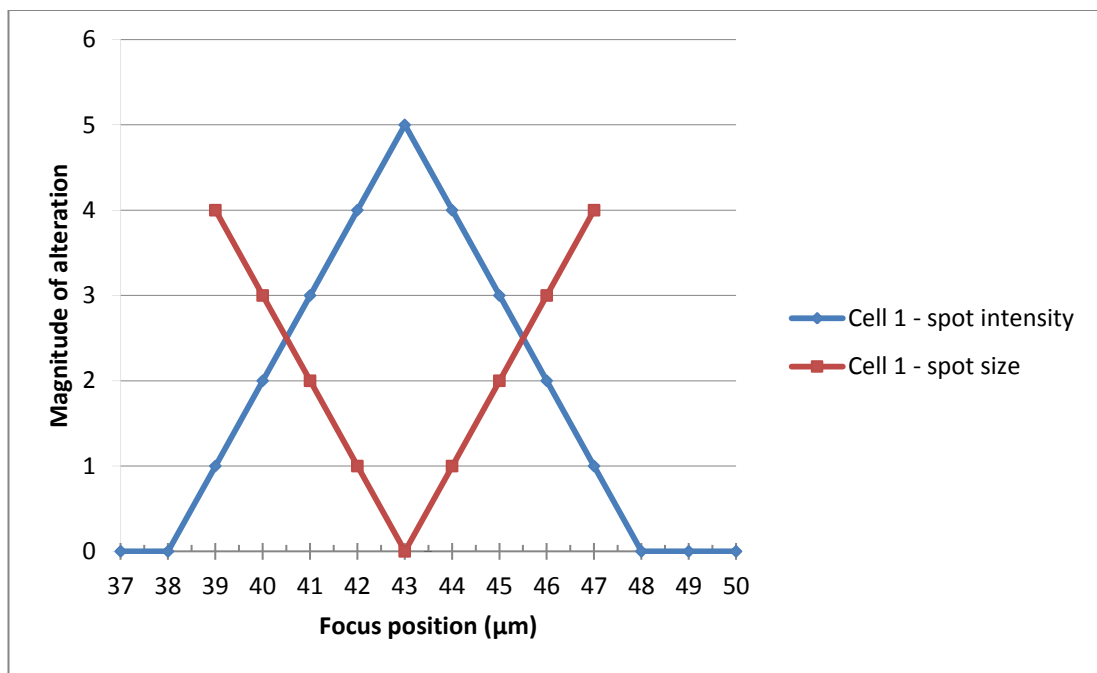
Figure 5.27 Interdependence between fluorescent spot intensity decrease and size increase. Z – stack acquisition was performed, with images acquired at a distance of 1 µm from each other
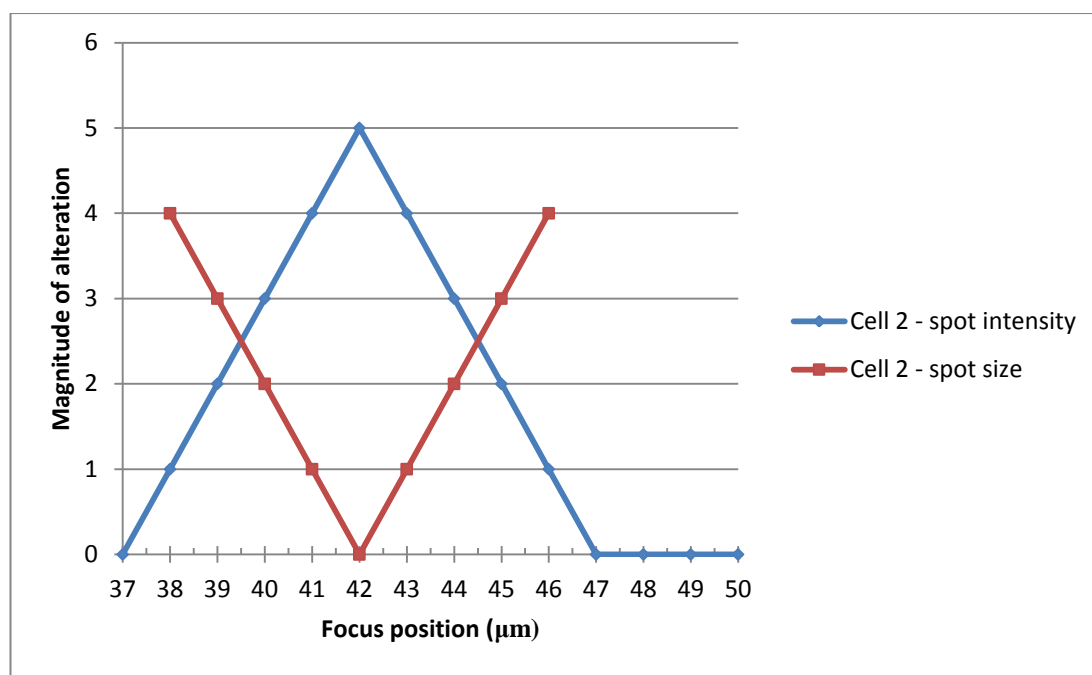
Figure 5.28 Interdependence between fluorescent spot intensity decrease and size increase. Z – stack acquisition was performed, with images acquired at a distance of 1 μm from each other.

5.4 ANALYSIS OF CHROMATIN PHYSICAL PROPERTIES IN TIME-LAPSE SERIES

In order to gain insight into the relationship between exposure of cells to DNA damaging agents and alterations in the physical properties of chromatin structure, quantitative analysis of each time-lapse series was performed on image J program (section 5.5). In control cells, the gradual diffusion of the EGFP spots over time would be expected to be due to photobleaching, defocusing (as no refocusing adjustments were performed in these experiments), or U.V. light-induced DNA damage during the period of image capturing. By contrast, for a given time-lapse series in which cells were exposed to a DNA damaging agent, diffusion of the fluorescent spot evidenced by the reduction in its mean intensity in conjunction with a simultaneous increase in its area, may imply chromatin relaxation consistent with DNA damage (139, 146-148). This relaxation may be relevant to the recruitment of DNA damage repair proteins to the damaged sites (139, 146-148). Following the completion of repair, an interdependent increase in the mean intensity and decrease in the area of the spot back to its initial values may imply restoration of chromatin

original structure, resulting in chromatin re-condensation and removal of repair proteins from the damaged sites [(149-151) and reviewed in (311-313)].

However, these are not the only events that could be associated with the alteration of chromatin physical properties. Another explanation includes spot diffusion and its subsequent disappearance due to the inhibition of EGFP transcription in the cell of interest, that is in turn owed to the abolishment of lacI – EGFP protein interaction with the lac O DNA sequences integrated into the genome. Furthermore, the cell cycle stage (chromatin becomes more relaxed and assumes a more open configuration during DNA replication) and defocusing are two other factors that may influence this phenomenon. Finally, it is likely that random acetylation events in the vicinity of the EGFP spots that are independent of any DNA damage responses, may account for the diffusion of the spots.

In order to account for misinterpretation based on loss of focus, the focal plane influence on EGFP spot appearance was assessed (section 5.3.6). In addition, all data were compared with control time-lapse series, in order to reveal whether any of the aforementioned factors are responsible for loss in signal intensity and change in shape of the EGFP spots. Consequently, having excluded these possibilities for time-lapse experiments in which cells were exposed to BLM, H_2O_2 or γ-irradiation, it would be reasonable to speculate that reductions in EGFP spot intensity and the associated increases in spot area may have been due to DNA damage – induced relaxation of chromatin in the vicinity of the fluorescent spots.

5.4.1 NORMALISATION OF VALUES

Following image J analysis, fluorescent spot mean intensity and area values were obtained and graphs associated with the alteration of these parameters over the course of the time - lapse experiments were constructed. In image J, the mean intensity corresponds to the mean pixel value within the pixel range assigned to the intensity of a given fluorescent object, whereas the area corresponds to its size that is counted in pixels^2. In order to avoid confusion associated with artefactual decreases in mean intensity accompanied by increases in area or decreases in total intensity values (see section 5.3.6 above), the time points of refocusing were also indicated on the graphs with arrows.

Based on the fact that the starting mean intensity and area values of the fluorescent spots within the cells of interest for each time-lapse series were variable,

an attempt was made to normalise the results. In order to achieve that, the relative changes in area and mean intensity values were normalised to the initial corresponding values for each time point. In this way, the changes in fluorescent spot area and mean intensity values relative to the corresponding initial values were determined, thus identifying any changes in spot characteristics (size and intensity). For all exposures, alterations in EGFP spot characteristics are presented as changes in total intensity. These values represent the products of the multiplication between the spot area and mean intensity values for each individual time point.

5.4.2 RELATIONSHIP BETWEEN CHROMATIN PHYSICAL PROPERTIES AND CELL VIABILITY IN TIME-LAPSE SERIES

The fact that the cells under examination and the majority of neighbouring cells in glass-bottom dishes in all but BLM 2 time-lapse series remained viable until the end of acquisition at 120 minutes, revealed that concentrations of 400 μM H_2O_2, 20 μg/ml BLM and doses of 1 Gy, 4 Gy and 6 Gy γ-irradiation were tolerable, to varying degrees by the cells selected for examination. In addition, the finding that the decreases in normalised mean intensity and the increases in normalised area values, relative to control, were correlated and independent of defocusing supports the prediction that these concentrations and doses were sufficient in order to produce an observable and meaningful effect on chromatin regions in the vicinity of the spots. This is further supported by the assessment of DSB induction following staining for γ-H2AX (section 5.2). Commenting on BLM series 2, EGFP expression abolishment was recorded at 64 minutes and cell death (presumably through necrosis) subsequently took place (see CD supplementary material at the back of this thesis). It is suggested that in this series the abolishment of EGFP expression was an indicator of subsequent cell death.

5.5 DETERMINATION OF POOLED TOTAL INTENSITY

Individual series of the same type of treatment were pooled into a single representative graph, showing the change in normalised total intensity of EGFP spot (see section 8.1 in appendix for statistical evidence suggesting that experiments can be pooled). This enabled the comparison between declining trends of normalised total intensity from different types of treatment.

5.5.1 TIME-LAPSE SERIES OF UNTREATED CELLS

For pooled untreated series 1 – 3, there was a negligible overall decline in normalised total intensity by 15.7 % between 0 and 120 minutes into acquisition, which is consistent with either photobleaching, or U.V. light-induced DNA damage. It could also be attributed to defocusing, as no refocusing adjustments were made for these untreated time-lapse series. This decrease constituted the background for comparison between normalised total intensity changes in the various treatments.
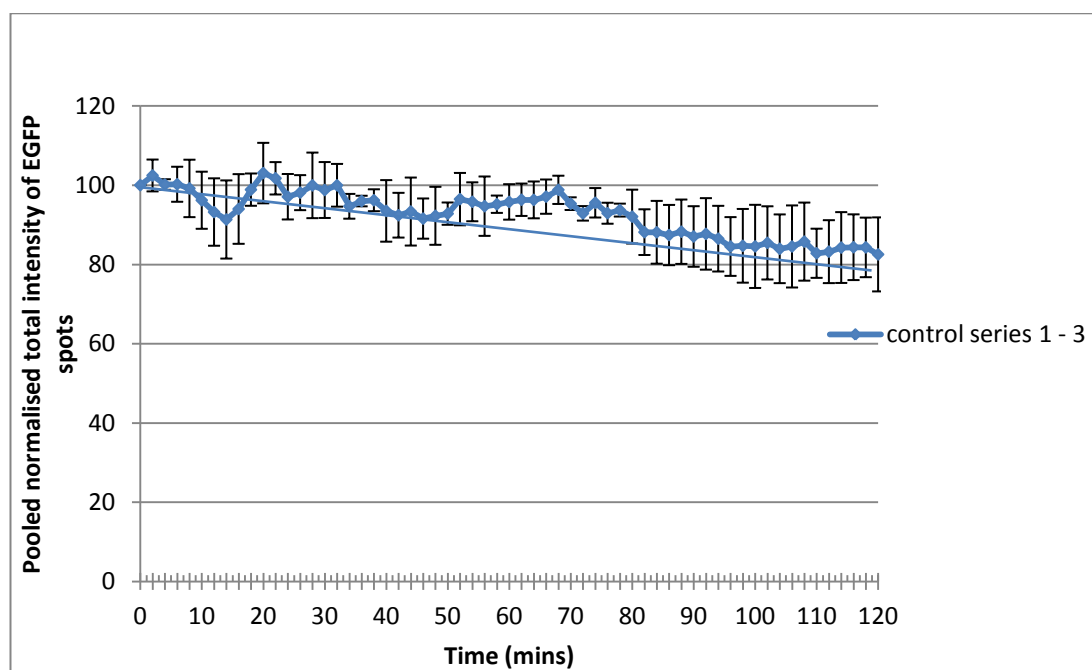
Figure 5.29 Pooled normalised change in total intensity of EGFP spots in untreated CHO-R-O-25 cells (series 1 – 3). Error bars represent S.D.

5.5.2 TIME-LAPSE SERIES OF CELLS EXPOSED TO H$_2$O$_2$

For pooled H$_2$O$_2$ series 1 – 4, during the first 10 minutes into acquisition there was an abrupt decrease in normalised spot total intensity by 35 % compared to its initial value (figure 5.30). This was followed by an even more considerable decrease during 20 - 38 minutes, when the normalised spot total intensity value was decreased by 52 % in comparison to its initial value. No such decreases were recorded on the graph reflecting the pooled normalised total intensity change in untreated series 1 – 3 (figure 5.29). During 72 – 120 minutes, there was a decrease in normalised spot total intensity that is attributed to photobleaching.
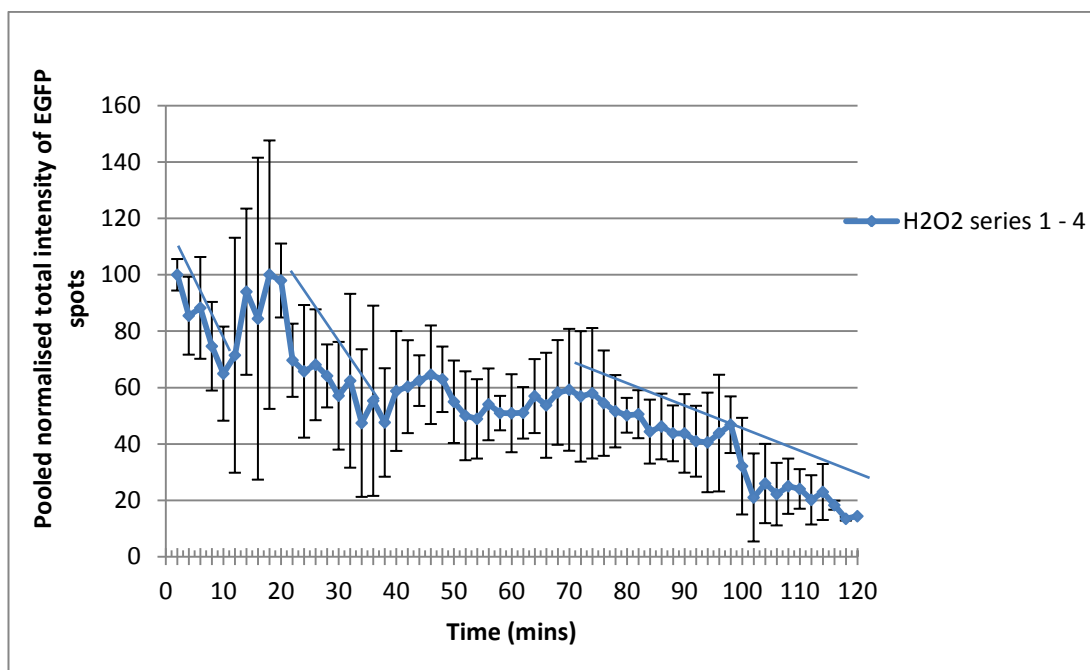
Figure 5.30 Pooled normalised change in total intensity of EGFP spots in CHO-R-O-25 cells exposed to H_2O_2 (series 1 – 4). Error bars represent S.D.

Observation of figure 5.30 above suggests that the error bars are large around 10 – 20 minutes into acquisition. This is due to the fact that during this time interval the trend of normalised total intensity alteration differed dramatically in time-lapse series 3, in comparison to the other three series (figure 5.31). In H_2O_2 series 1 and 4 the normalised total intensity was observed to decline during this period of time, while in series 2 it remained relatively stable (figure 5.31). In series 3 however, despite the substantial and abrupt decline during the first 10 minutes after H_2O_2 addition (by 47 % compared to its initial value), there was a steeper and more considerable increase during 10 – 18 minutes that resulted in the increase of spot normalised total intensity by ~ 80 % compared to its initial value (figure 5.32). During 18 - 38 minutes, there was an even more abrupt decline in normalised spot total intensity compared to the first 10 minutes and as a consequence of that decline, the normalised spot total intensity value at 38 minutes was dropped by 87 % compared to its initial value. This was the highest decrease in all four time-lapse series and was independent of defocusing. Between 40 and 60 minutes, the normalised total intensity values were slightly increased but remained below 50 % compared to the initial. During 78 - 120 minutes, there was a decrease in normalised total intensity possibly due to photobleaching.
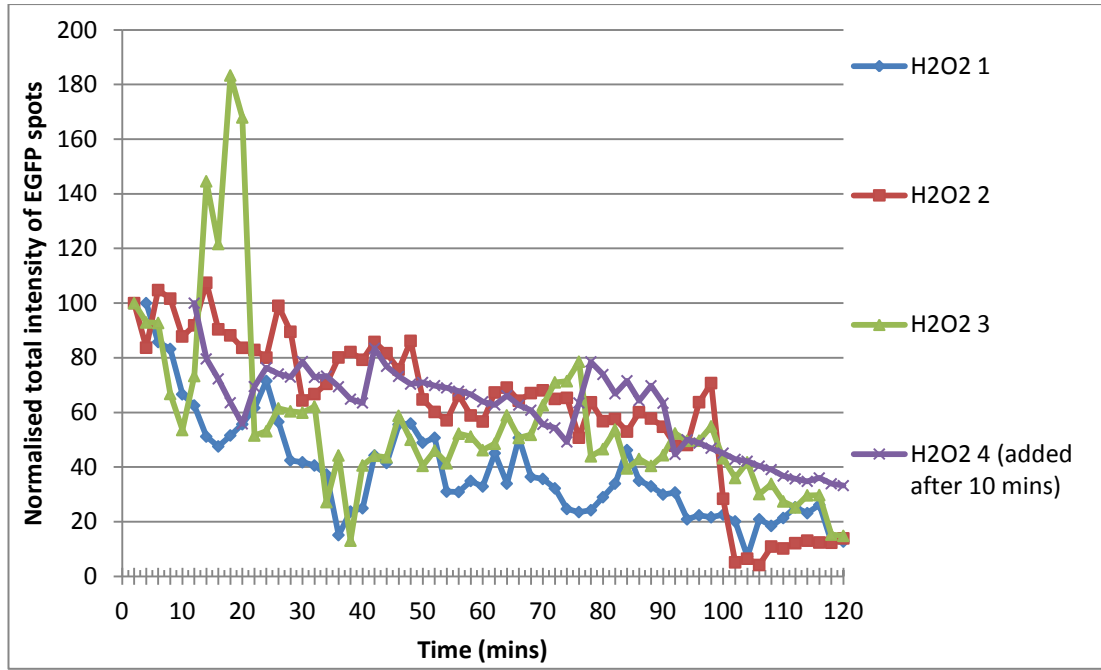
Figure 5.31 Normalised change in total intensity of EGFP spots in CHO-R-O-25 cells exposed to H_2O_2
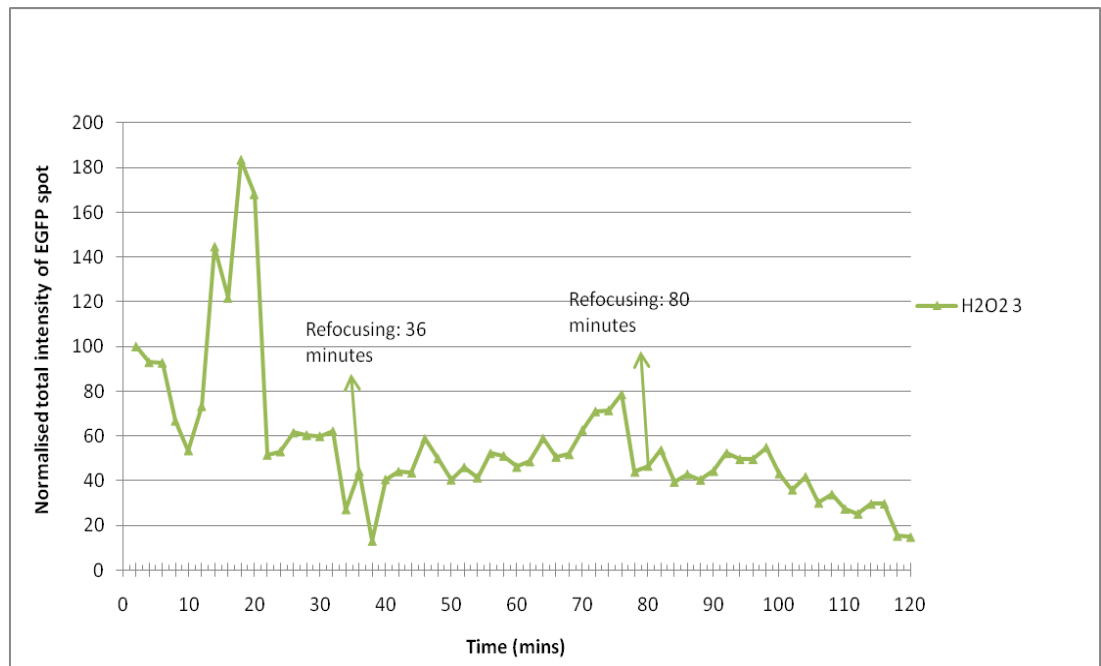
Figure 5.32 Normalised change in EGFP spot total intensity highlighting re-focusing time points in time-lapse series 3, after exposure to H_2O_2

In H_2O_2 series 3, the steep and considerable increase during 10 – 18 minutes reflected the higher magnitude of increase in normalised area values (figure 5.33) compared to the magnitude of decrease in normalised mean intensity values during this time interval (figure 5.34), rather than a real increase in spot total intensity values (figure 5.31). There were two expansions in spot area (figure 5.33). The first took place during 10 - 20 minutes following addition of H_2O_2 and the second occurred between 40 and 78 minutes. These expansions were observed to be accompanied by the diffusion of the fluorescent spot during these time intervals (figure 5.34).
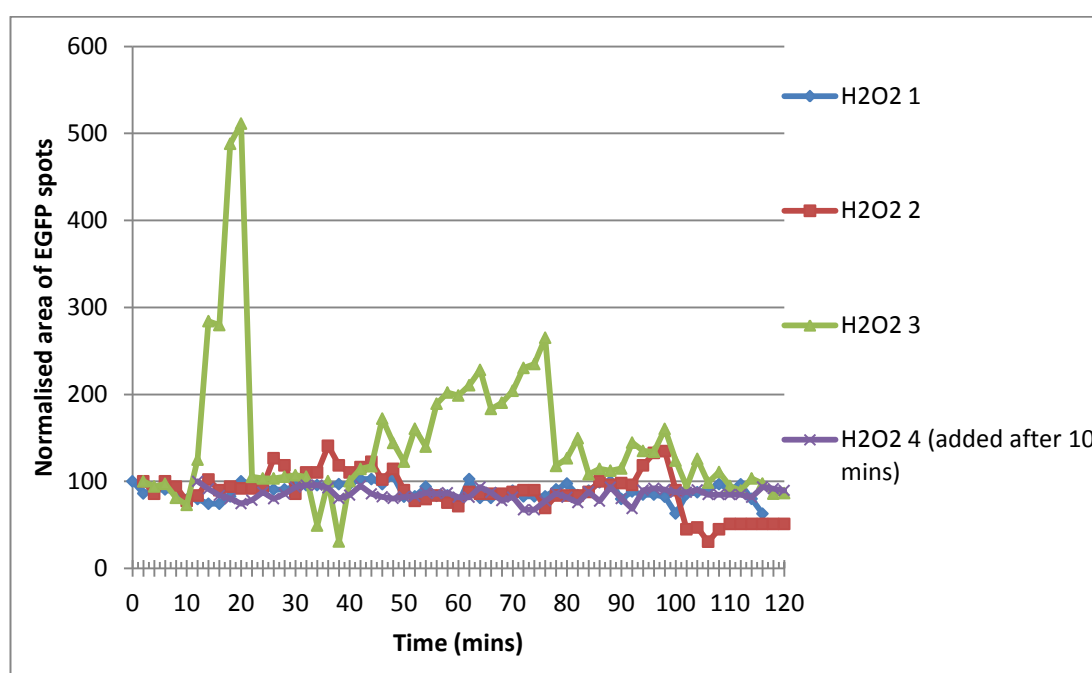
Figure 5.33 Normalised change in area of EGFP spots in CHO-R-O-25 cells treated with H_2O_2

The considerable decrease in normalised spot mean intensity during the first 20 minutes (figure 5.34) was concomitant with the increase in normalised spot area during 12 - 20 minutes (figure 5.33). These events were absent from control 1 – 3 series (figures 5.35 and 5.44) and were irrelevant of technical or artefactual factors such as defocusing, thereby indicating that they reflected the consequence of exposure to H_2O_2. It should be mentioned that this decline was more notable and abrupt compared to the corresponding declines in H_2O_2 series 1, 2 and 4. A second decrease in normalised mean intensity values occurred between 42 and 58 minutes.

Here, defocusing cannot be regarded as the cause of these changes, as refocusing at 80 minutes did not result in any significant increases in normalised mean intensity values.
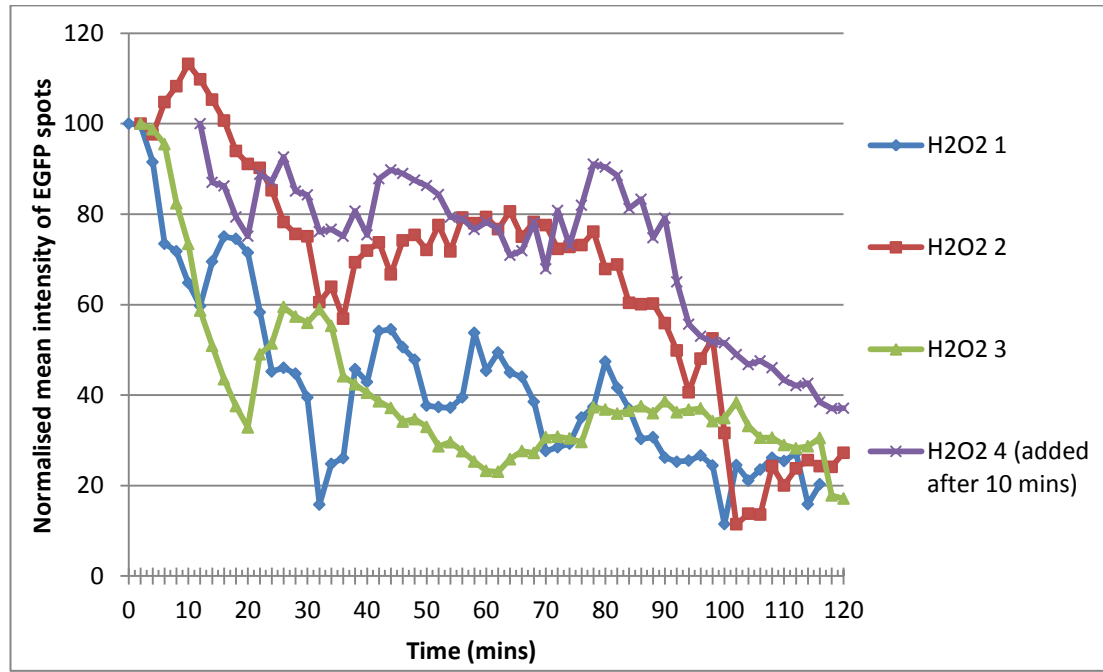
Figure 5.34 Normalised change in mean intensity of EGFP spots in CHO-R-O-25 cells exposed to H_2O_2
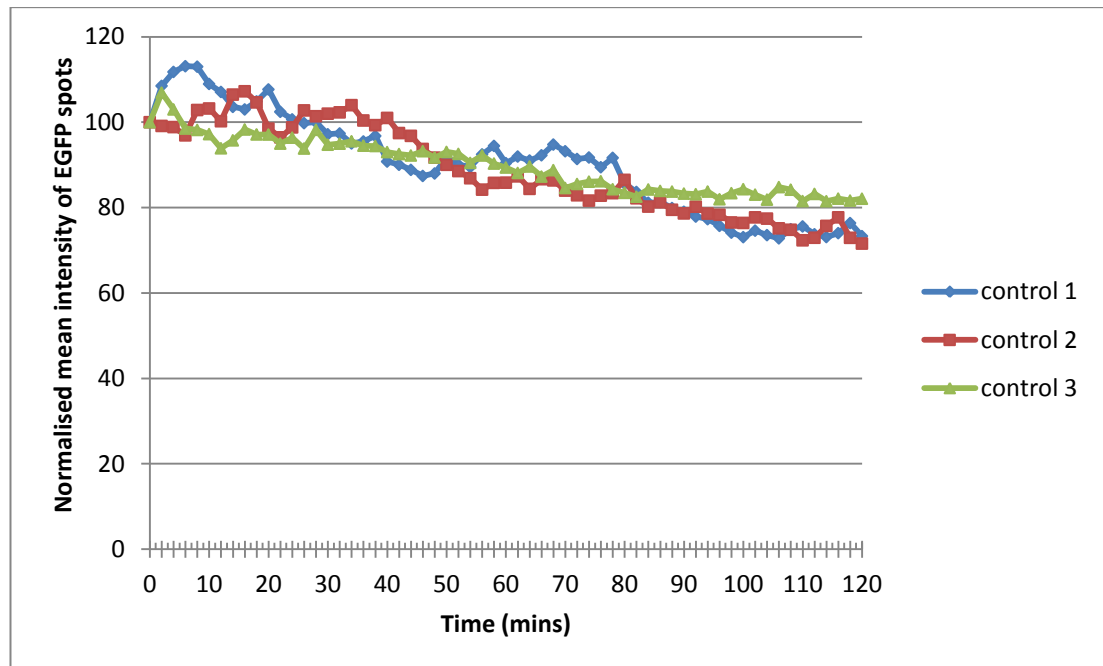
Figure 5.35 Normalised change in mean intensity of EGFP spots in untreated CHO-R-O-25 cells

5.5.3 TIME-LAPSE SERIES OF CELLS EXPOSED TO BLM

For pooled BLM series $1 - 4$, there was a substantial and abrupt decrease in normalised total intensity between 12 and 52 minutes into acquisition (figure 5.36). This decrease was more considerable in comparison to those of untreated (figure 5.29) and H_2O_2 (figure 5.30) pooled series, as it resulted in the drop of normalised total intensity value by 67 % in comparison to its initial value. During $62 - 120$ minutes, there was a gradual decrease that resulted in the drop of pooled normalised total intensity value by ~14 % compared to the value it possessed at 60 minutes (42.9 %). This decrease could be attributed to photobleaching.

The overall decline in pooled normalised total intensity after exposure to BLM was steeper compared to that of pooled untreated series $1 - 3$ (figure 5.29). In comparison with the H_2O_2 pooled series (figure 5.30), the decline corresponding to BLM pooled series was very similar, but steeper between 12 and 52 minutes into acquisition. This is largely owed to the abrupt and considerable normalised total intensity increase in H_2O_2 series 3 during $10 - 18$ minutes (figure 5.32), that contributed to the increase in pooled normalised total intensity around $10 - 20$ minutes back to its initial values. It would be expected that removal of series 3 from the H_2O_2 pooled series would result in almost identical declines in H_2O_2 and BLM pooled sets of series. Therefore, it is obvious that H_2O_2 series 3 shows a trend of total intensity alteration that is substantially different from those of H_2O_2 series 1, 2 and 4 and BLM series $1 - 4$. This could be due to a different extent of DNA damage in this series resulting in different repair processing compared to H_2O_2 series 1, 2 and 4 and BLM series $1 - 4$.

Finally, it should be mentioned that the normalised total intensity pixel decline for pooled BLM series $1 - 4$ is regarded as biphasic, as it could be represented by two slopes (figure 5.36). The first corresponds to the abrupt decline between 12 and 52 minutes, whereas the second reflects the more gradual decline during 56 - 120 minutes. In contrast, for pooled untreated and H_2O_2 series, the declines in normalised total intensity during the course of acquisition could be represented by a single and three slopes, respectively (figures 5.29 and 5.30, respectively).
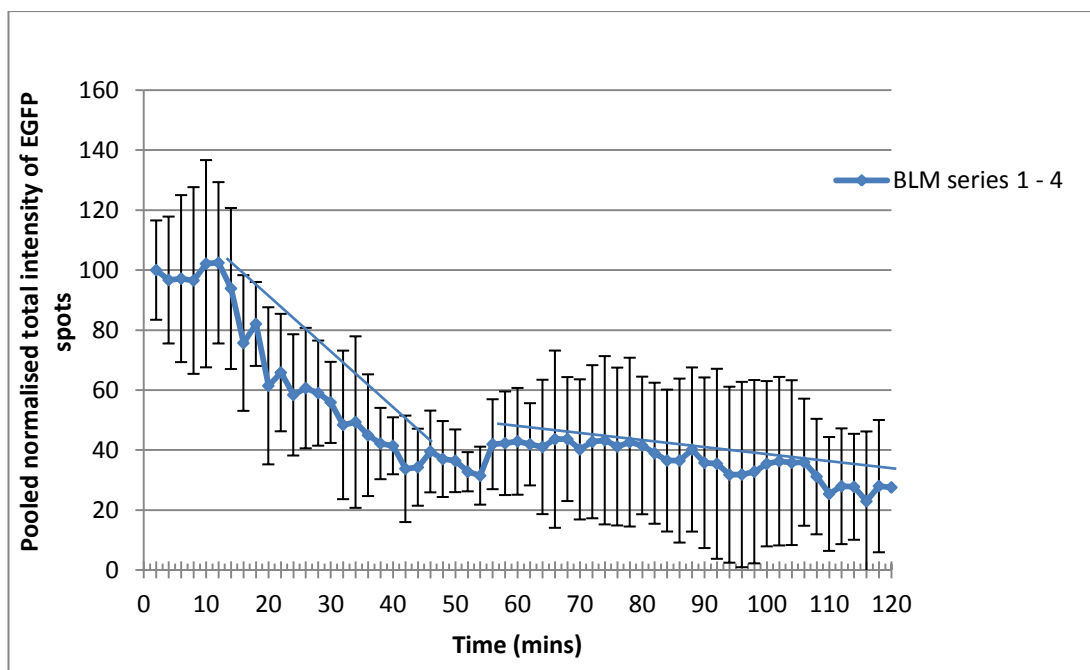
Figure 5.36 Pooled normalised change in total intensity of EGFP spots in CHO-R-O-25 cells exposed to BLM (series 1 – 4). Error bars represent S.D.

5.5.4 TIME-LAPSE SERIES OF CELLS EXPOSED TO 1 Gy γ-IRRADIATION

In this pooled set of time-lapse series, despite the increase in normalised total intensity values during 20 – 32 minutes after irradiation (first 12 minutes into acquisition), there was a steep decline between 32 and 52 minutes after exposure (12 – 32 minutes into acquisition; figure 5.37). This resulted in the decrease of normalised total intensity value by 37 % compared to its initial value. Despite the fact that this decrease was not as considerable as those recorded in pooled H_2O_2 and BLM series during 20 – 38 and 12 – 52 minutes into acquisition respectively (figures 5.30 and 5.36), it was more remarkable compared to the decline in pooled untreated series during the first 60 minutes into acquisition (figure 5.29). Moreover, it was comparable to the decrease in normalised total intensity in pooled H_2O_2 series during the first 10 minutes into acquisition (figure 5.30). The overall decrease of normalised total intensity in this pooled set of series was steeper in comparison to that of pooled untreated series. In relation to the overall declines corresponding to H_2O_2 and BLM pooled series, the decline recorded for this pooled set of series was slightly less pronounced.

The normalised total intensity pixel change for 1 Gy γ-IR pooled series is triphasic, as it could be represented by three slopes (figure 5.37). The first corresponds to the increase in pooled normalised total intensity during 20 – 32 minutes after irradiation, the second represents the abrupt decrease during 32 – 52 minutes after exposure and the third reflects the more gradual decline between 68 and 120 minutes after irradiation. The early increase is due to the higher magnitude of normalised area increases compared to mean intensity decreases during 20 – 32 minutes after exposure in individual series (compare figures 5.43 and 5.45). This resulted in the emergence of elevated normalised total intensity values in individual series (figure 5.38) during this period of time (see section 5.5.4.1 below). Biologically, the considerable increase in the area of the spot between 20 and 32 minutes after irradiation could indicate that repair processing was already in progress during that period of time and possibly during the first 20 minutes that intervened between the end of irradiation and acquisition of the first image. While the first abrupt decrease during 32 – 52 minutes after exposure might be due to the damaging effect of irradiation in the vicinity of the EGFP spot, the second more gradual decline during 68 – 120 minutes after irradiation could be attributed to photobleaching.
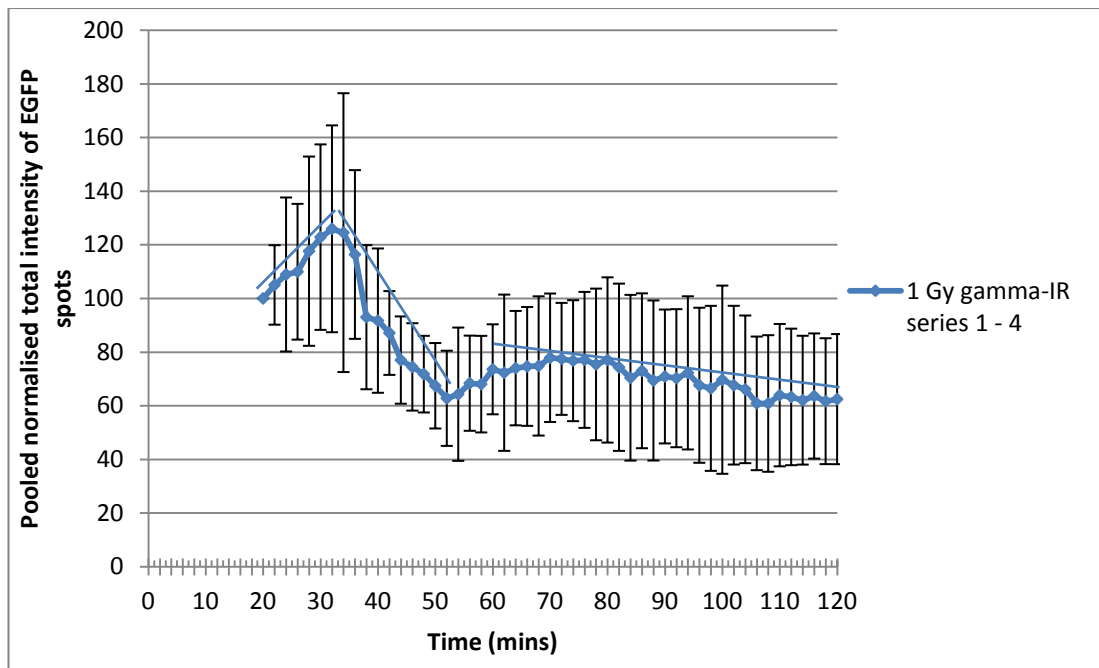
**Figure 5.37 Pooled normalised change in total intensity of EGFP spots in CHO-R-O-25 cells exposed to 1 Gy γ-irradiation (series 1 – 4). Error bars represent S.D.**

5.5.4.1 INDIVIDUAL TIME-LAPSE SERIES OF CELLS EXPOSED TO 1 Gy γ-IRRADIATION

Regarding 1 Gy γ-IR series 1, 2 and 3 the first images were acquired at 20, 24 and 22 minutes after the end of exposure to γ-irradiation, respectively. This resulted in the shifting of the values corresponding to the change and normalised change of total intensity on the graphs to the right (figure 5.38). On the other hand, in series 4 cells were incubated on ice during exposure and until acquisition of the first image. In this sequence therefore, the initial total intensity value on the graph corresponds to time point 0.

Regarding series 1, 2 and 3 the effect of γ-irradiation on DNA, evident by the decreases in normalised total intensity becomes apparent by the declining trends on the graphs during the first 60 minutes following the end of irradiation (40, 36 and 38 minutes into acquisition for series 1, 2 and 3, respectively; figure 5.38). These declines were more considerable compared to those of control series 1, 2 and 3 (figure 5.39), during the same period of time. On the other hand, only a small decrease followed by a considerable increase in normalised spot total intensity values was observed in series 4. Based on the fact that in series $1 - 4$ the normalised area values were shown to increase more notably (figure 5.43) in relation to the normalised mean intensity decreases (figure 5.45) during the first 60 minutes into acquisition, it is obvious that the increases in normalised total intensity (during $0 - 4$, $24 - 34$, $0 - 10$ and 16 - 18 minutes into acquisition for series 1, 2, 3 and 4, respectively) are owed to the high area values at these time points. Crucially, in all four time-lapse series the alterations in normalised total intensity values were independent of defocusing during the entire course of acquisition.
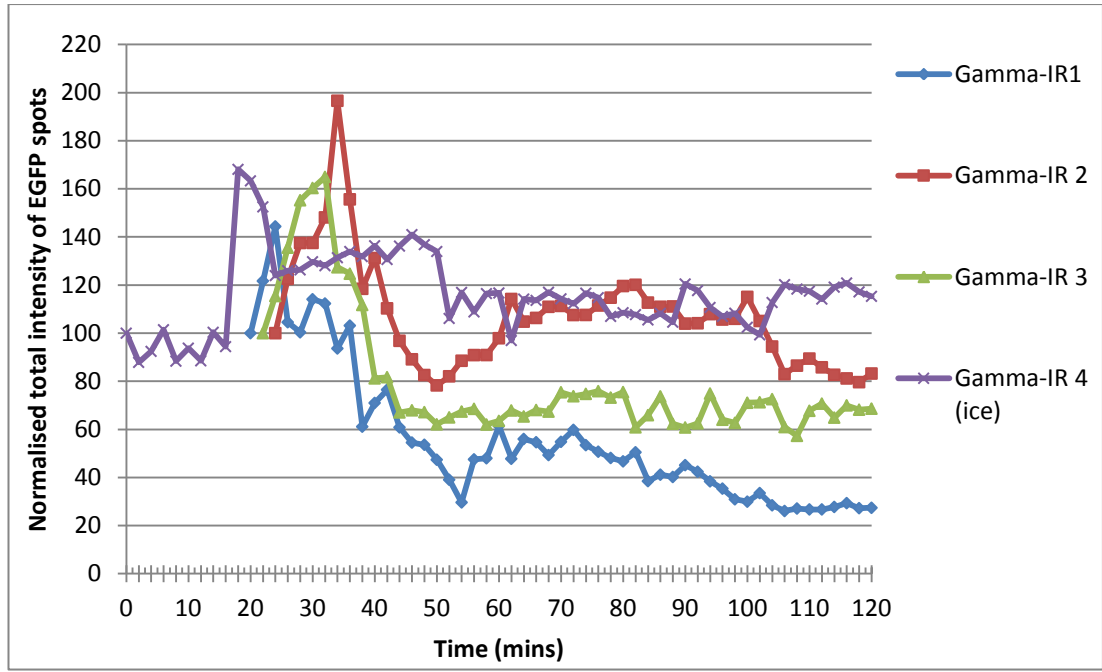
Figure 5.38 Normalised change in total intensity of EGFP spots in CHO-R-O-25 cells exposed to 1 Gy γ-irradiation
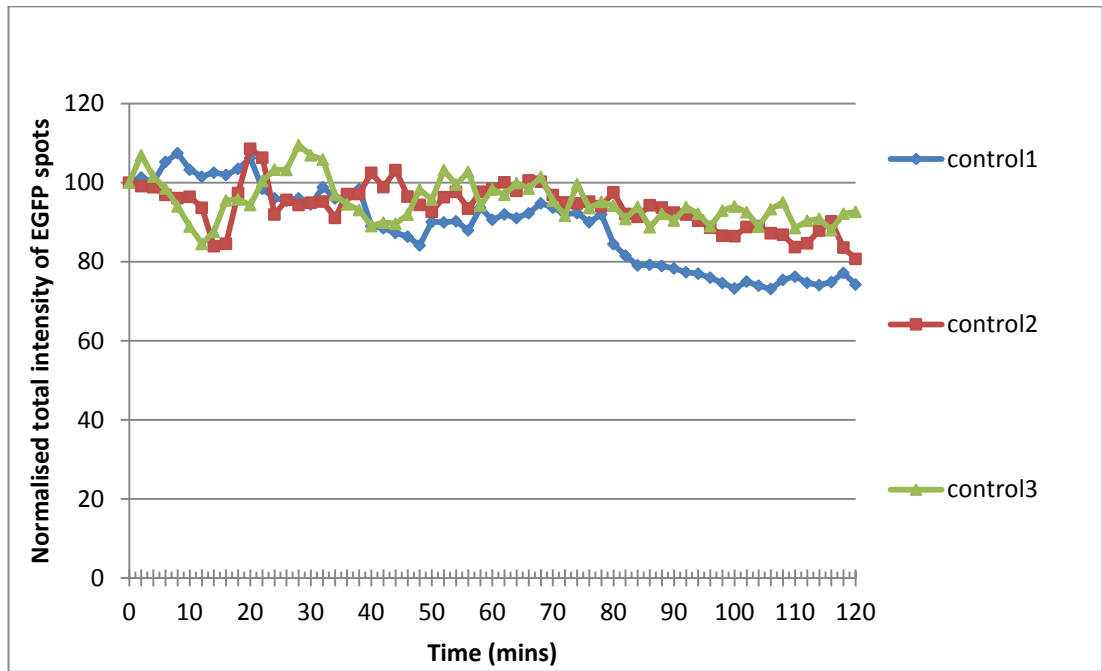
Figure 5.39 Normalised change in total intensity of EGFP spots in untreated CHO-R-O-25 cells

In 1 Gy γ-IR time-lapse series 1, there was a steep and substantial decline during 24 – 54 minutes after the end of exposure (4 – 34 minutes into acquisition), that resulted in the decrease of normalised spot total intensity value by 70 % compared to its initial value at 20 minutes (figure 5.40). During 54 – 60 minutes after the end of

exposure, there was an increase, resulting in the elevation of normalised spot total intensity value at 60 minutes by 32 %. Between 62 and 82 minutes after exposure the normalised total intensity remained stable, whereas during 84 – 120 minutes there was a decrease that could be attributed to photobleaching. For series 2, between 34 and 50 minutes after exposure there was an abrupt decline that resulted in the drop of normalised total intensity value at 44 minutes by 22 % compared to its initial value, which was still more pronounced than the highest decrease in normalised total intensity of untreated series 1 - 3 that was 16 % and corresponded to series 3, during the first 60 minutes into acquisition (figure 5.39). This decrease was followed by an increase until 82 minutes. During 82 – 120 minutes there was a decrease in normalised spot total intensity, which however was not as considerable as the one that occurred during 34 – 50 minutes. As a consequence of this decrease, the normalised total intensity value at 120 minutes was dropped by 17 % compared to its initial value. This decrease could be attributed to photobleaching.
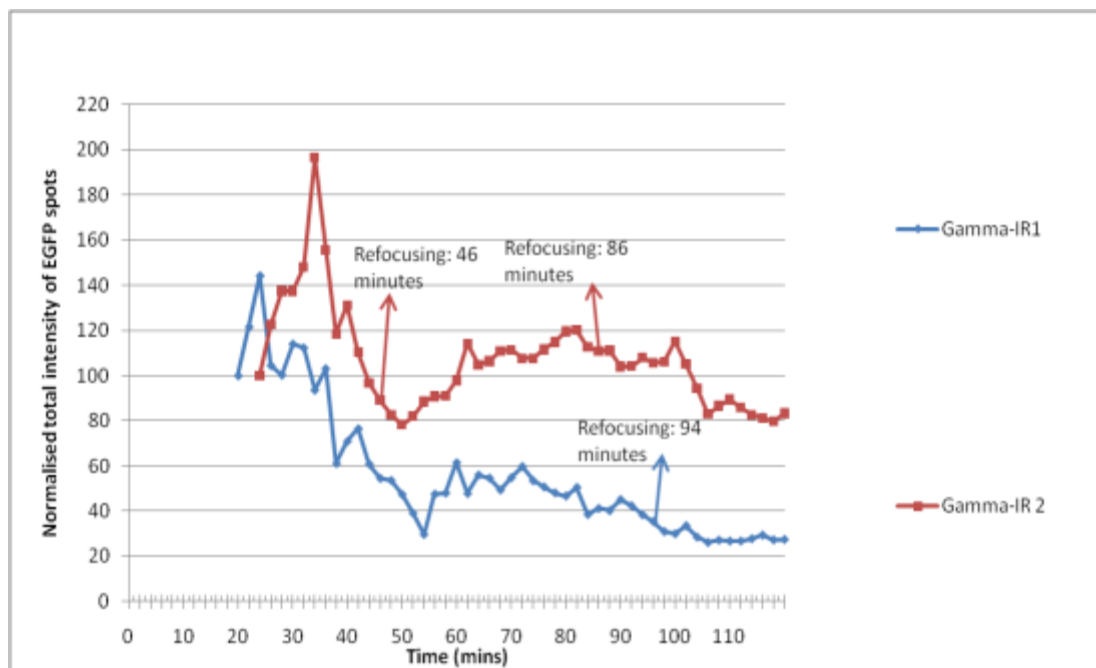
Figure 5.40 Normalised change in EGFP spot total intensity, highlighting re-focusing time points in time-lapse series 1 and 2, after exposure to 1 Gy γ-irradiation

In series 3, there was an equally considerable and abrupt decline in normalised spot total intensity during 32 – 44 minutes after exposure (first 10 - 22 minutes into acquisition), that resulted in the drop of normalised total intensity value by 33 % compared to its initial value at 22 minutes (figure 5.41). At 50 minutes after exposure, the value was lowered even further by 38 % compared to the beginning of

acquisition. The trend of the graph remained at the same declined level between 50 and 60 minutes. During 62 – 120 minutes the normalised total intensity value remained at the same declined level that it possessed between 32 and 60 minutes, when the γ-irradiation induced diffusion of the fluorescent spot had become prominent.
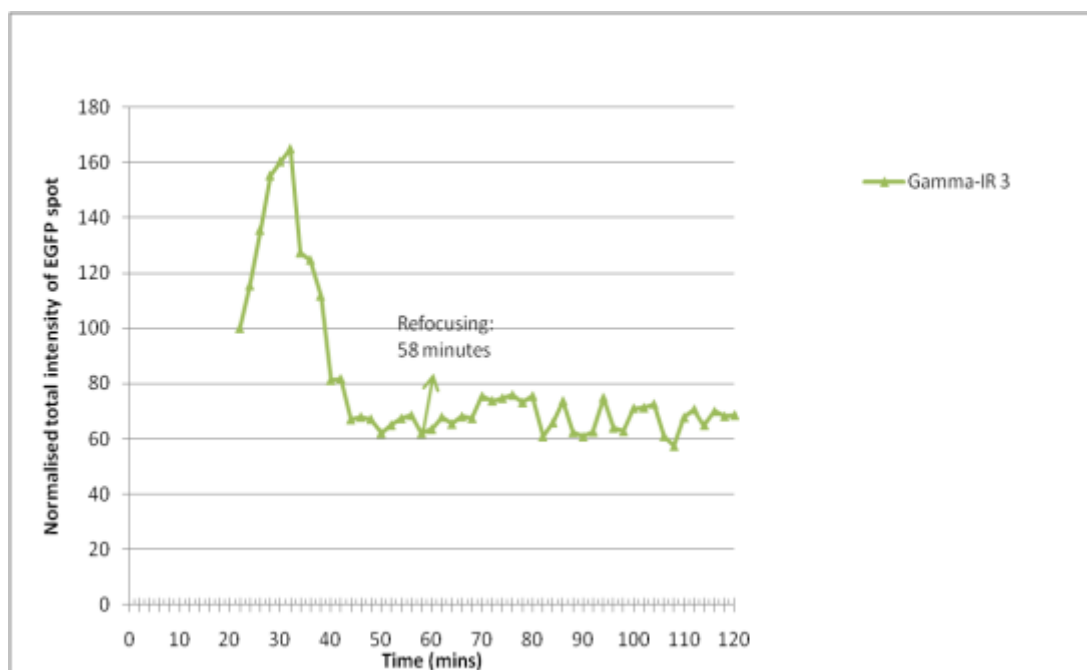
Figure 5.41 Normalised change in EGFP spot total intensity, highlighting the re-focusing time point in time-lapse series 3, after exposure to 1 Gy γ-irradiation

Overall, in series 1 – 3, the decreases in normalised total intensity strengthen the possibility that relaxation of chromatin at sites surrounding DSBs might have occurred, in response to DNA damage. In contrast, no such correlations could be drawn for time-lapse series 4, in which there was an abrupt and considerable increase in normalised total intensity between 18 and 48 minutes into acquisition (figure 5.42). During 50 – 60 minutes, the normalised spot total intensity values were dropped near the basal levels, but were still higher than the initial value. However, as mentioned above, this finding was due to the fact that the magnitude of increase in normalised spot area values (figure 5.43) was higher than that of the decrease in normalised mean intensity values (figure 5.45), thereby neutralizing the normalised total intensity decline during the course of acquisition. Between 62 and 120 minutes there was an overall increase in normalised spot total intensity, despite the various fluctuations.

Interestingly, among all treatments, initial increases in normalised spot total intensity are observed only in the four time-lapse series corresponding to cells exposed to 1 Gy γ-irradiation. It is likely that for all these series (and particularly for series 4 in which cells were incubated on ice until acquisition of the first image), these increases reflect a lag period that lasts until the cells are adapted to the permissive for repair temperature conditions in the stage of the microscope. Possibly, changes in chromatin conformation reflected by decreases in normalised spot total intensity occur after the end of this lag period. These changes are absent from control series and would be expected to be different from corresponding changes in series where cells were treated with other DNA damaging agents.
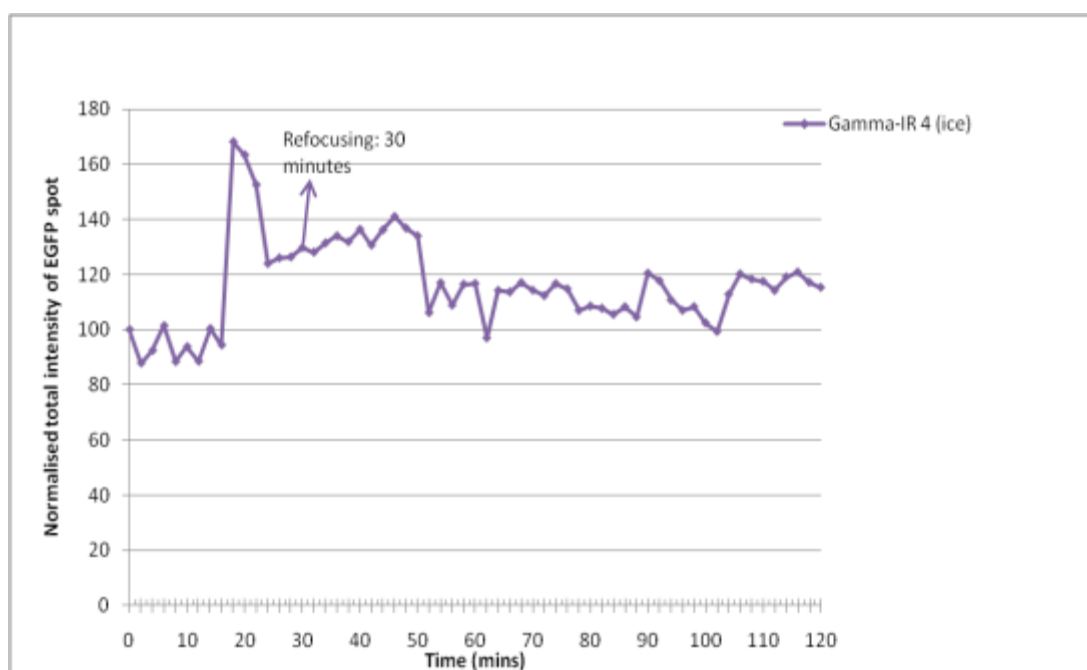
Figure 5.42 Normalised change in EGFP spot total intensity, highlighting the re-focusing time point in time-lapse series 4, after exposure to 1 Gy γ-irradiation

5.5.4.2 CHANGES IN PHYSICAL PROPERTIES OF EGFP-LABELLED CHROMATIN IN CELLS EXPOSED TO 1 Gy γ-IR

The normalised change in spot area shows increases during the first 20 minutes in all four time-lapse series (figure 5.43). These increases were absent from control series 1 – 3 (figure 5.44). The time intervals during which these changes took place correspond to 20 – 36, 24 – 36, 22 – 36 and 0 – 18 minutes after exposure to 1Gy γ-irradiation for series 1, 2, 3 and 4, respectively (figure 5.43). Around the same time intervals, decreases in normalised mean intensity values were recorded (figure 5.45),

suggesting that these alterations in chromatin physical properties may represent γ-irradiation-induced chromatin expansion and diffusion within the cells of interest. The most dramatic increase in normalised spot area was recorded in time-lapse series 3 (by 303.9 %), followed by that of series 2 (by 218.6 %).
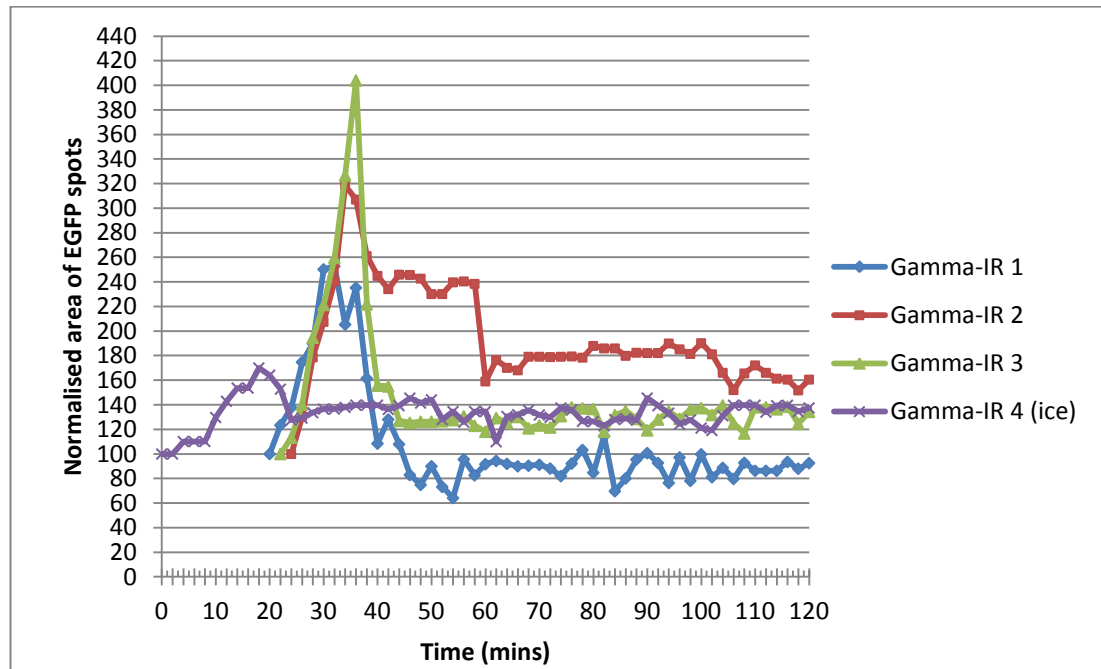

Figure 5.43 Normalised change in area of EGFP spots in CHO-R-O-25 cells exposed to 1 Gy γ-IR
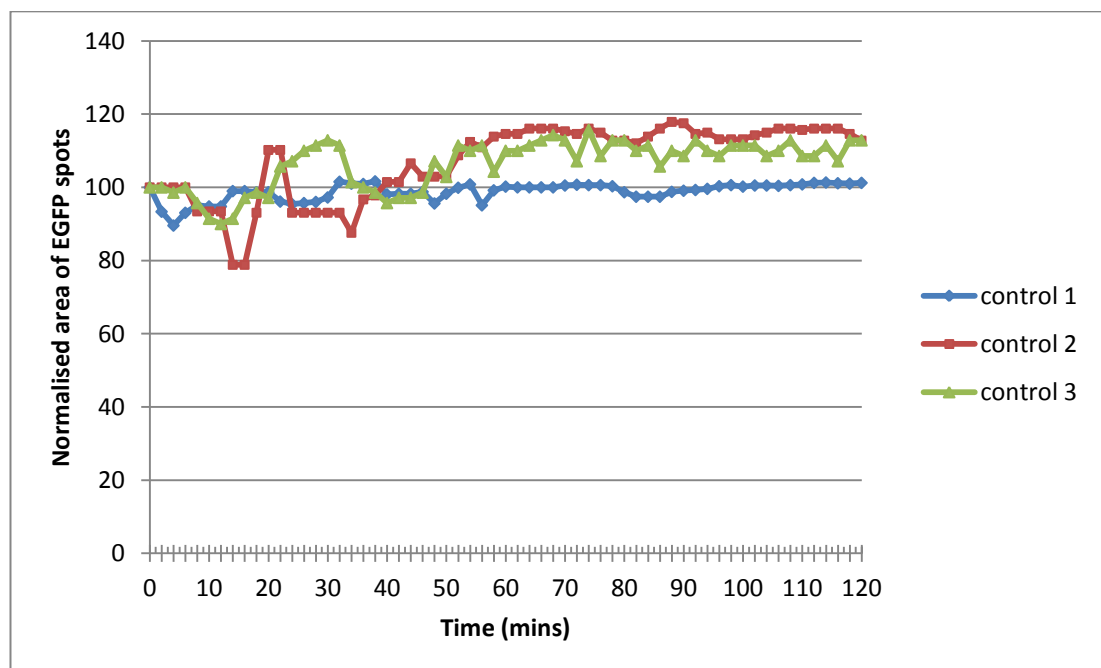
Figure 5.44 Normalised change in area of EGFP spots in untreated CHO-R-O-25 cells

255

Abrupt decreases in the mean intensity of EGFP spots were observed during the first 18, 14, 14 and 16 minutes into acquisition for time-lapse courses 1, 2, 3 and 4, respectively (figure 5.45). These decreases were considerably higher than those of normalised mean intensity values in untreated cells (figure 5.35) and this together with the timing of their appearance after the end of irradiation and their independence from defocusing have implications for DNA damage repair associated events.
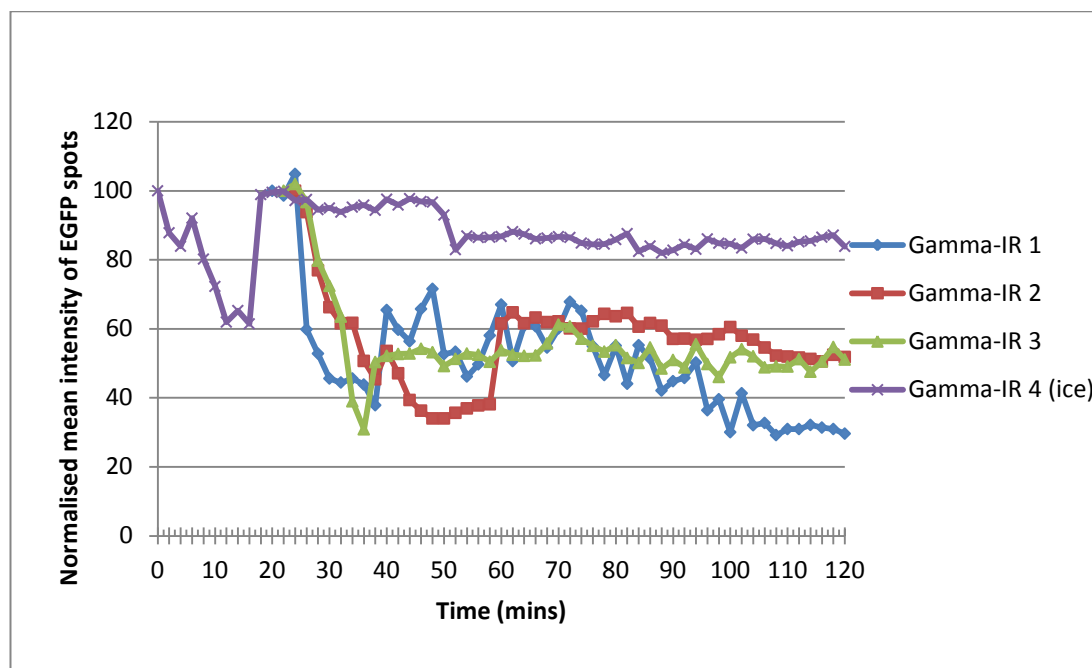
Figure 5.45 Normalised change in mean intensity of EGFP spots in CHO-R-O-25 cells exposed to 1 Gy γ-IR

5.5.5 TIME-LAPSE SERIES OF CELLS EXPOSED TO 4 Gy γ-IRRADIATION

In 4 Gy γ-IR time-lapse series, the first image was acquired 22 minutes after exposure. An abrupt and considerable decrease was recorded during 34 – 56 minutes after exposure (12 – 34 minutes into acquisition), that reduced the normalised total intensity value by 31 % compared to its initial value (figure 5.46). Surprisingly, the steepness of this decrease was less pronounced than the corresponding decreases in pooled H_2O_2, BLM and 1 Gy γ-IR series. Between 58 and 120 minutes after the end of irradiation, the normalised total intensity value remained at the same declined

level that it possessed at 56 minutes. Similar to 1 Gy γ-irradiation series 2 and 4 (figures 5.40 and 5.42, respectively), the increase during 22 – 34 minutes after the end of irradiation is attributed to the more substantial increase in normalised spot area relative to the decrease in normalised mean intensity values during that period of time (compare figures 5.47 and 5.48). The overall normalised total intensity decrease in 4 Gy γ-IR series was more abrupt and considerable than those of pooled untreated, H_2O_2, BLM and 1 Gy γ-IR series. Similar to BLM (figure 5.36) and 1 Gy γ-IR (figure 5.37) pooled series, the biphasic normalised total intensity decrease is evident by the abrupt and more gradual declines during 34 – 56 and 58 - 120 minutes after irradiation, respectively (figure 5.46).
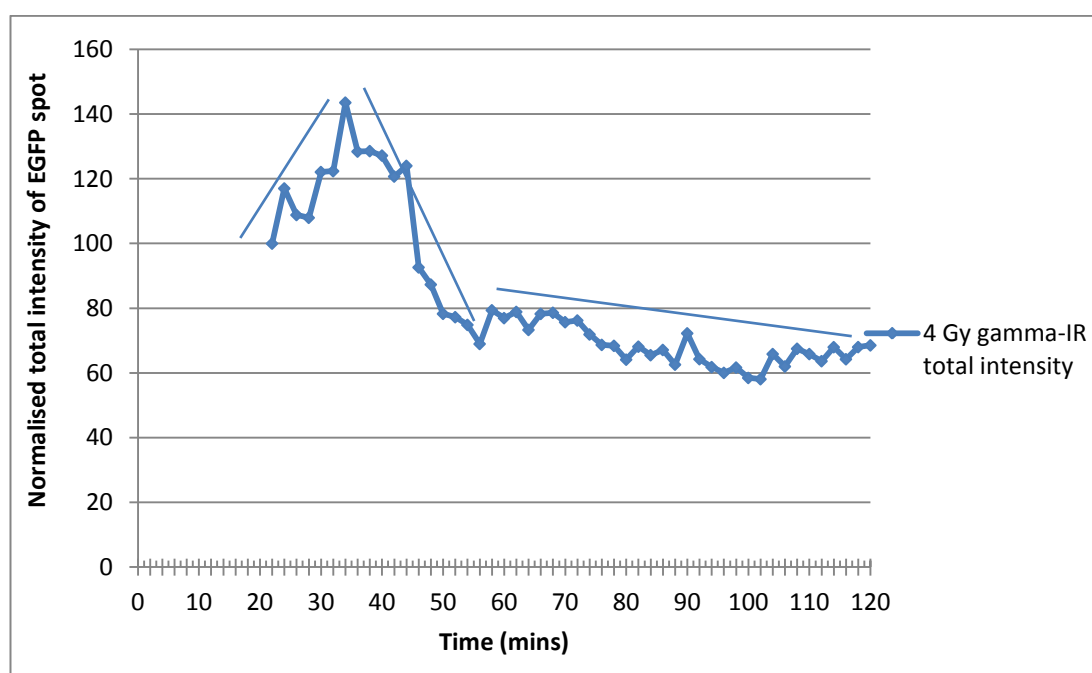
Figure 5.46 Normalised change in total intensity of EGFP spot in CHO-R-O-25 cells exposed to 4 Gy γ-irradiation

5.5.5.1 CHANGES IN PHYSICAL PROPERTIES OF EGFP-LABELLED CHROMATIN IN CELLS EXPOSED TO 4 Gy γ-IR

In this time-lapse series, observation of the normalised change in spot area showed an abrupt increase during the first 12 minutes into acquisition (22 – 34 minutes after irradiation), corresponding to > 60% of the initial value (figure 5.47). The normalised spot area remained at this increased level until 44 minutes, when an abrupt decrease was noted (during 44 – 56 minutes). Thereafter, the spot area was stable at consistent values to the initial until the end of acquisition.
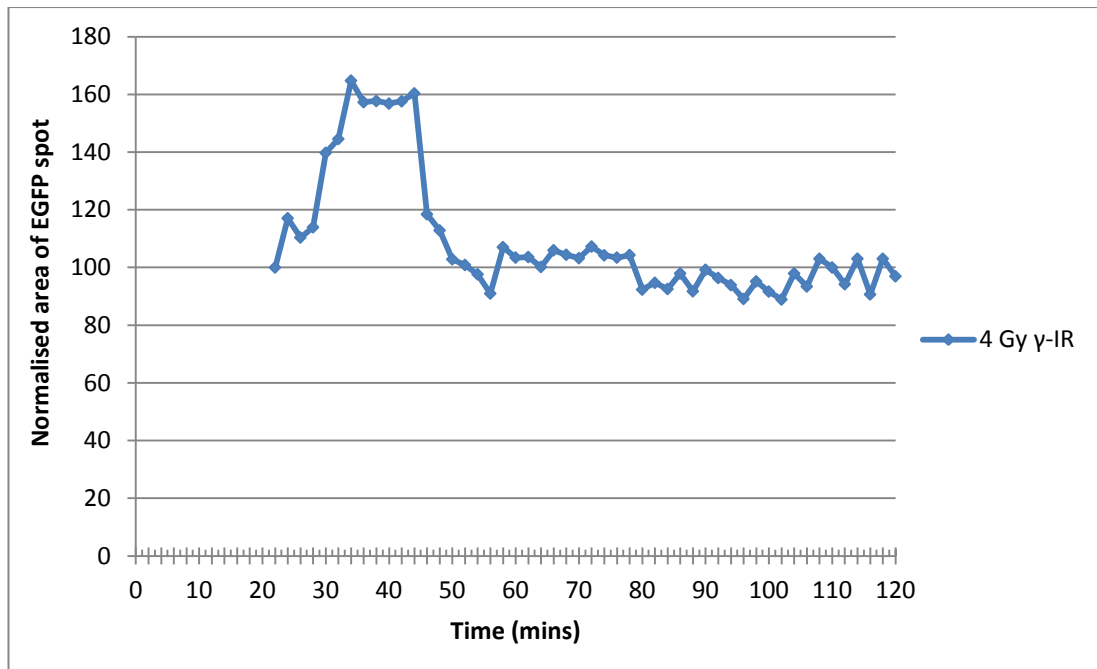
Figure 5.47 Normalised change in EGFP spot area after exposure to 4 Gy γ-IR

During the first 20 minutes into acquisition (22 - 42 minutes after irradiation), there was a ~25% decrease in normalised spot mean intensity (figure 5.48). This decrease occurred simultaneously with an increase in normalised spot area and both of these alterations were greater than those observed in control cells (figures 5.35 and 5.44), suggesting that they were possibly associated with the DNA damage repair process.
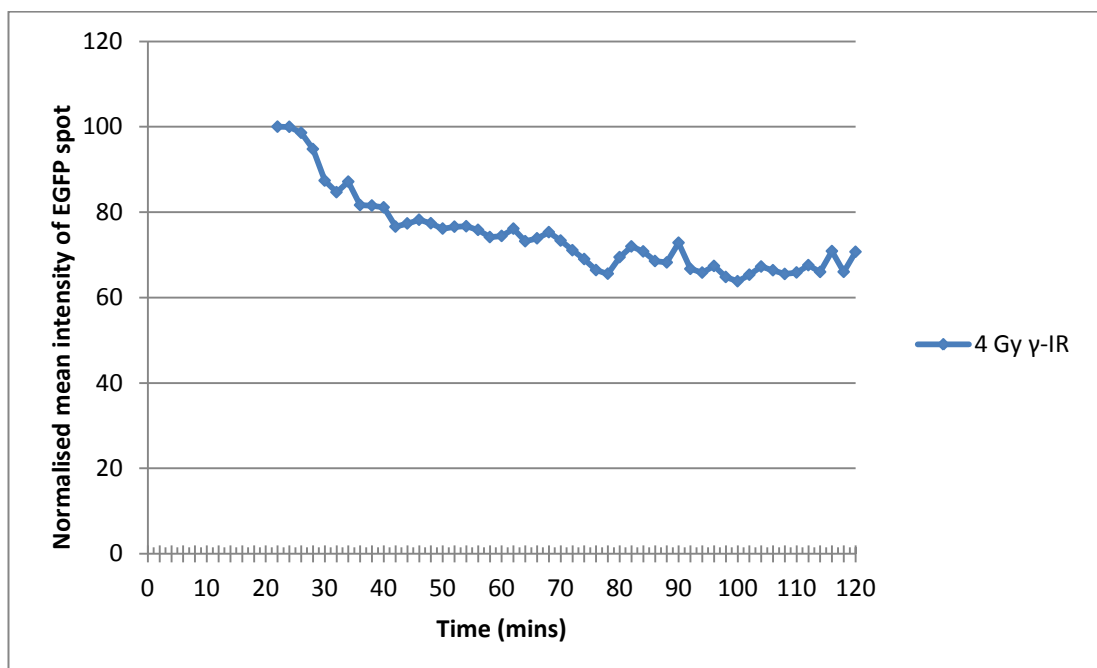
Figure 5.48 Normalised change in EGFP spot mean intensity after exposure to 4 Gy γ-IR

5.5.6 TIME-LAPSE SERIES OF CELLS EXPOSED TO 6 Gy γ-IRRADIATION

The first image in the series was captured 26 minutes after the end of exposure to γ-irradiation. Despite the considerable increase in normalised total intensity during 26 - 46 minutes after the end of exposure (first 20 minutes into acquisition), during 60 – 66 minutes after irradiation there was a decline in normalised total intensity that dropped the value at 66 minutes by 25 % compared to the initial value (figure 5.49). Based on the timing of this decline, no correlation between decrease in normalised spot total intensity and repair can be drawn in this series. However, the possibility that it was due to defocusing is also excluded, as evidenced by the small increase in normalised total intensity value following the refocusing adjustment at 58 minutes. Similar to pooled 1 Gy γ-irradiation series (figure 5.37) and individual 4 Gy γ-irradiation series (figure 5.46), the increase during 26 - 46 minutes after the end of irradiation is attributed to the more considerable increase in normalised spot area relative to the decrease in normalised mean intensity during that period of time (figures 5.50 and 5.51). Between 66 and 120 minutes, the normalised total intensity remained at the same declined level that it possessed at 66 minutes. Consistent with the expectations, the overall normalised total intensity decrease in this series was more abrupt and considerable than those of pooled untreated, H_2O_2, BLM and 1 Gy γ-IR series and individual 4 Gy γ-IR series. However, this is largely owed to the abrupt decrease in normalised total intensity during 60 – 66 minutes and the maintenance of the value at that level until the end of acquisition. Finally, it should be mentioned that similar to pooled 1 Gy γ-IR series, the normalised total intensity pixel change for this series is triphasic, with the three slopes represented by the increase during 26 – 46 minutes, the substantial decline during 60 – 66 minutes and the more gradual decrease during 66 – 120 minutes after exposure (figure 5.49). The latter decrease is consistent with photobleaching.
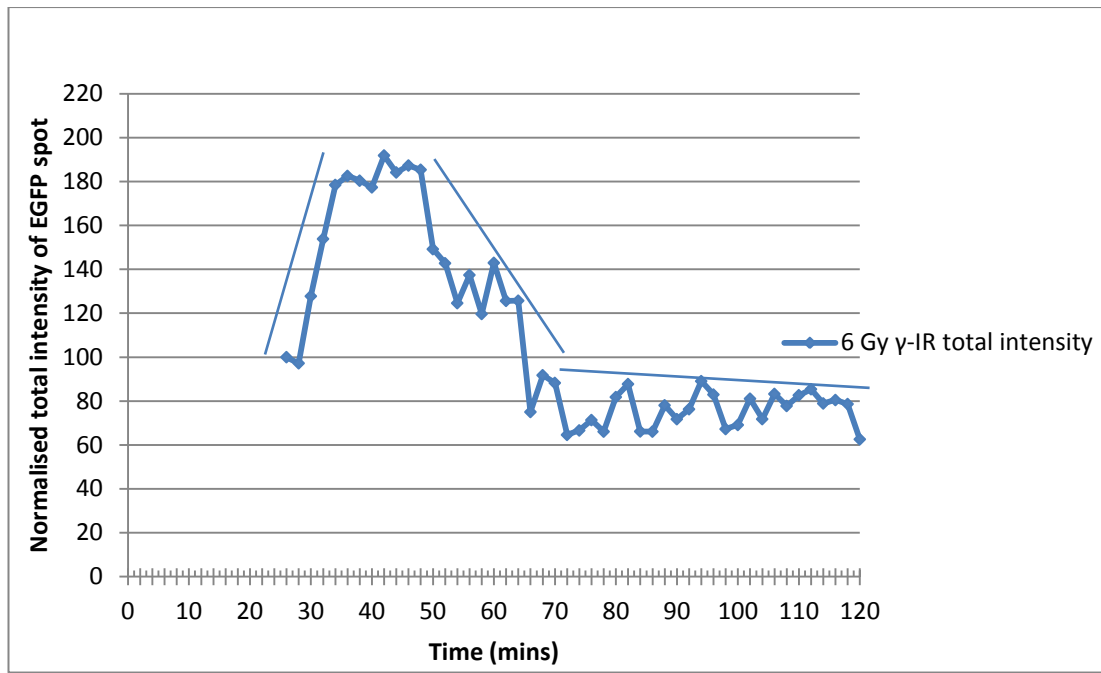
Figure 5.49 Normalised change in total intensity of EGFP spot in CHO-R-O-25 cells exposed to 6 Gy γ-irradiation

5.5.6.1 CHANGES IN PHYSICAL PROPERTIES OF EGFP-LABELLED CHROMATIN IN CELLS EXPOSED TO 6 Gy γ-IR

In this series, over the first 20 minutes into acquisition (26 - 46 minutes after γ-irradiation exposure), the normalised spot area was observed to increase by more than 150 % in comparison to its initial value (figure 5.50).
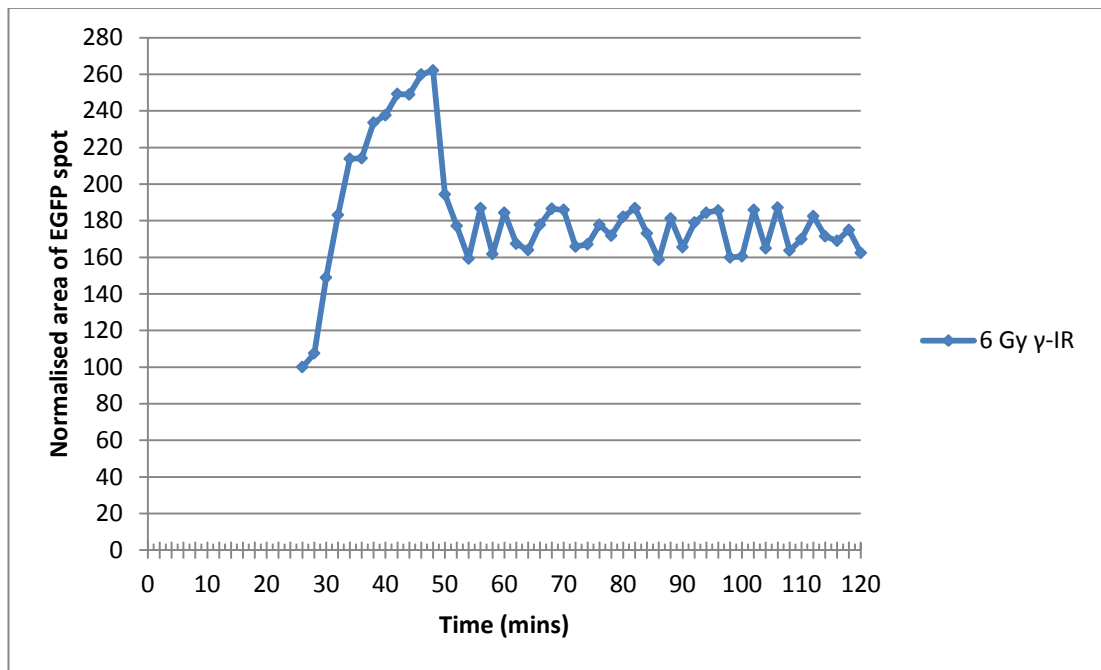
Figure 5.50 Normalised change in EGFP spot area after exposure to 6 Gy γ-IR

Commenting on the normalised spot mean intensity alteration, during the first 20 minutes after exposure (26 – 46 minutes on the graph), mean intensity was decreased (figure 5.51). The increase in normalised spot area in conjunction with the decrease in normalised spot mean intensity during the same period of time, suggests that these two phenomena could be related to chromatin decondensation facilitating DNA damage repair processes. The abrupt decrease in normalised spot mean intensity at 66 minutes was followed by the maintenance of the spot mean intensity value at this declined level during 66 – 120 minutes.
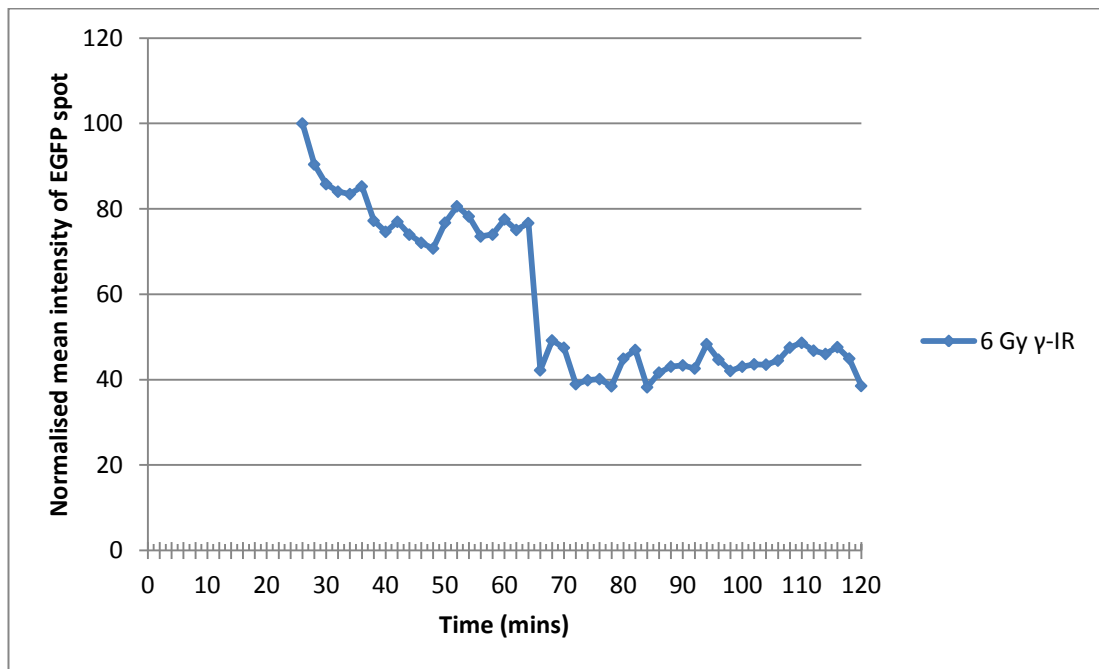
Figure 5.51 Normalised change in EGFP spot mean intensity after exposure to 6 Gy γ-IR

Overall, it should be highlighted that the difference between the normalised total intensity decreases in the pooled series of cells treated with DNA damaging agents and the corresponding decrease in untreated pooled series was independent of defocusing. This in conjunction with the timing of the decline appearances (first 60 minutes after exposure), suggests that they may be related to chromatin relaxation in the vicinity of the EGFP spots, allowing repair processes to operate.

5.6 DISCUSSION

5.6.1 BLM AND H_2O_2 DOSE OPTIMISATION AND IMMUNOSTAINING

Dose optimisation experiments were performed with the aim of identifying the BLM and H_2O_2 concentrations that result in the formation of DSBs, while at the same time retaining cell viability over the time period of time-lapse experimentation. Trypan blue exclusion dye analysis revealed that exposure of CHO DG44 and CHO-R-O-25 cells to concentrations of 20 μg/ml of BLM and 400 μM of H_2O_2 result in 8% and 7.6% of cell death respectively, after exposure to BLM (figure 5.1) and 7.7 % and 8.5 % of cell death respectively, following exposure to H_2O_2 (figure 5.2). These results are consistent with the findings of several research laboratories (86, 119, 275, 276).

PNA-FISH experiments performed by Sanchez et al (2009) have shown that following exposure of log phase CHO cells to a BLM concentration range of 1 – 5 μg/ml for 30 minutes at 37 °C, chromatid and chromosomal aberrations are formed on the interstitial telomeric sequences (ITS) on the chromosomes of these cells. In addition, chromosomal translocations were recorded after exposure to a BLM concentration as low as 2.5 μg/ml at 18 hours after treatment (94). Similarly, on the same cell type Lopez-Larazza et al (2004) have demonstrated that pulse treatment with 1 – 5 μg/ml of BLM for 15 minutes at 37 °C is sufficient to produce significant degradation of DNA, whereas treatment with 10, 50 and 100 μg/ml of BLM also results in DNA degradation with further abolished cell growth after exposure to 100 μg/ml, but not 10 μg/ml of BLM (86). In a separate study that employed the premature chromosome condensation (PCC) technique to assess chromosome aberrations in CHO cells, it was shown that exposure to 25 μg/ml of BLM for 30 minutes at 37 °C results in the formation of chromosomal aberrations including breaks, gaps and exchanges, approximately one third of which are repaired within the first 60 minutes after the end of exposure (90). Further, the effect of BLM has been assessed by autoradiograph observation of DNA samples directly exposed to BLM (74) and DNA samples derived from cells exposed to BLM (95). The exposure of φX174 plasmid DNA to 25 μg/ml of BLM and the exposure of HeLa cell DNA to 250 μg/ml of BLM were shown to induce numerous SSBs and DSBs in addition to preferential cleavage of DNA on G-T and G-C sequences (74). In our study, following exposure of cells to BLM, cells were washed and incubated at 37 °C for 3

hours before staining with trypan blue , as this period of time was believed to be sufficient for the scope of our studies. Therefore, based on these findings, the γ-H2AX foci data (discussed below) and the detail above we elected to expose cells to a concentration of 20 µg/ml of BLM.

Experimental evidence has suggested that H_2O_2 is a highly damaging agent (277). More specifically, in CHO-K1 cells pulse labelled with BrdU in order to study sister chromatid exchange (SCE) formation in S phase, H_2O_2 induced more damage compared to other damaging agents such as mitomycin-C (MMC) and U.V. light (277). In chromosomal aberration studies, the exposure of CHO-K1 cells to $100 – 400$ µM of H_2O_2 resulted in the linear increase in aberration frequency. In contrast, treatment of cells for 3 hours with concentrations in the range of $400 – 800$ µM of H_2O_2 was found to result in a considerable reduction of cell proliferation rates and cause extensive cell death (275). Further, comet assays have suggested that treatment of human thyroid cells with concentrations of H_2O_2 in the range of $200 – 500$ µM for 15 minutes at 37 ^{o}C results in the generation of 225.4 ($\pm$ 42.3) – 241.9 ($\pm$ 23.2) DSBs (276). These authors further suggested that at these concentrations cell death is insignificant (< 1 % of nonviable cells) (276). In separate experiments, immunoblotting analysis demonstrated that incubation of cells with 1 mM of H_2O_2 for 1 hour and 3 hours at 37 ^{o}C results in extensive cell death, as the activation of both caspase-9 and caspase-3 was shown to be enhanced at this concentration (116). On the other hand, experiments in which Jurkat cells were exposed to 70 µM, 150 µM, 250 µM, 500 µM, 750 µM and 1 mM of H_2O_2 for 6 hours at 37 ^{o}C suggested that cleavage and activation of caspases is achieved at H_2O_2 concentrations in the range of 150 - 500 µM, with 500 µM accounting for the maximum effect. At concentrations higher than 500 µM, cleavage and activation of caspases was shown to decline (120). Similarly, the exposure of HeLa cells to $0.06 – 20$ mM of H_2O_2 demonstrated that a concentration of 60 µM of H_2O_2 is more efficient in the generation of aldehydic DNA lesions (ADLs), in comparison to 600 µM and 6 mM. These lesions emerge as a consequence of hydrogen atom subtraction from the deoxyribose sugar chain, following OH$^-$ radical attack on DNA. A Fenton type reaction, including interaction of H_2O_2 with a metal, was suggested to be responsible for this ADL emergence (278). Consistently, Iliakis et al (1992) suggested that a higher number of lesions are produced by lower rather than higher concentrations of H_2O_2 (104). Remarkably, the percentage of nonviable HeLa cells after exposure to

60 μM (~50 %), was only slightly lower than the corresponding percentages at concentrations of 6 mM and 20 mM. The lowest percentage of nonviable cells was recorded after exposure to 600 μM of H_2O_2 (~20 %) (278). It should be added that the sequence-specific cleavage of DNA by H_2O_2 in the presence of Fe^{2+} ions has been reported to be dependent on the concentration of H_2O_2 applied to cells. More specifically, experiments in which plasmid DNA cleavage by H_2O_2 was investigated, suggested that at the concentration of 50 mM of H_2O_2 DNA strand scission preferentially occurs at the bases present at the 5'-end of the third G residue in Pur-GGG (AGGG or TGGG) DNA sequences (running from 5' to 3' direction), whereas following exposure to a concentration of 500 μM of H_2O_2, it occurs at the thymine base in the Pur-GT-Pur DNA sequence (279). As shown by the γ-H2AX data (discussed below), a concentration of 400 μM of H_2O_2 induced an average of 13 foci per nucleus in CHO-R-O-25 cells. Based on the above, it was reasonable to use a concentration of 400 μM of H_2O_2 for the experiments that were performed in this study. Finally, it is worth noting that exposure of human thyroid cells to doses of 1 – 2 Gy and 4 – 5 Gy of γ-IR followed by immediate comet assay analysis has resulted in the formation of 201 (± 6.1) and 244.5 (± 30) DSBs and that the appearance of γ-H2AX foci in the nuclei of cells has been found to be analogous to the γ-IR doses of exposure in the range of 1 – 10 Gy (276). In our study, doses of 1 Gy γ-IR induced an average of 12 [11 – 13] and 10 [9 - 11] foci / nucleus in CHO-R-O-25 and 1 HD cells respectively, while a dose of 4 Gy γ-IR resulted in the appearance of 63 [60 – 66] foci / nucleus in CHO-R-O-25 cells. The number of foci in the work of Driessens et al (2009) was considerably higher compared to our study, because the authors placed the cells on ice immediately after the end of irradiation and commenced comet assay analysis, thereby allowing no time for cells to repair DNA damage (276). By contrast, in our study cells were incubated for 30 minutes at 37 °C after the end of irradiation in order to allow repair to take place before immunostaining.

To assess the frequency of DSB induction after exposure to varying damaging agents, CHO-R-O-25 and CHO-DG44 cells were exposed to H_2O_2, BLM and γ-irradiation (1 and 4 Gy). 1 HD cells were also exposed to 1 Gy γ-IR and stained for γ-H2AX, as a positive control (section 5.2). Overall, γ-H2AX foci were observed in 77 % (± 1.4%) – 96 % (± 1.4%) of analysed nuclei after the varying exposures, compared to only 14 % (± 1.4%) – 15 % (± 2.5%) of nuclei in unexposed cells (figure 5.5). Based on the finding that ~36 % (± 8.3%) of CHO-R-O-25 cells

were demonstrated to be in S and G_1 phases of the cell cycle (section 4.3.1) in conjunction with stalled replication fork-induced DSBs in S phase (142, 280), the background occurrence of γ-H2AX foci in these experiments is consistent with expectations. Moreover, consistent with this is the finding that in unexposed cortical neuronal (281, 282) and other mammalian cell types (283, 284) the percentage of nuclei containing at least 1 focus does not exceed 32 %.

The mean number of foci / nucleus in CHO-R-O-25 nuclei exposed to 400 μM H_2O_2, 20 μg/ml BLM (fixed 30 minutes after the beginning of experiment), 1 Gy and 4 Gy γ-IR (fixed 30 minutes after exposure) were 13 [11 – 15], 19 [18 – 20], 12 [11 – 13] and 63 [60 – 66], respectively and 10 [9 - 11] in 1 HD nuclei exposed to 1 Gy γ-IR and fixed 30 minutes after exposure (figure 5.6). Evidence has suggested that ~40 DSBs per nucleus are generated in mammalian cells exposed to 1 Gy γ-IR and immunostained immediately after treatment [reviewed in (314)]. The number of foci per nucleus in our study is lower due to the fact that cells were allowed 30 minutes to repair damage, before immunostaining. Consistent with the results of our study, Kato et al (2007) demonstrated that 1 hour after exposure of G_0 normal human fibroblast cells to 1 Gy γ-IR the average number of foci / nucleus is within the range of 11.4 – 19.9 with a standard error of ± 0.20 – 0.26 (285). These results come in agreement with our findings, despite the fact that the experiments were carried out in a different cell type. By contrast, immunostaining experiments in human prostate carcinoma cells 30 minutes following exposure to 1 Gy of γ-IR showed the average number of foci per nucleus to be ~ 5 (348). In addition, Staszewski et al (2008) have argued that the average number of foci per nucleus observed 30 minutes after exposure to 1 Gy of γ-IR in CHO-9 cells is 33.8 (286). These data possibly reflect cell type differences, but could also highlight intrinsic differences in inter-laboratory foci counting. We used an automated foci counting script developed in-house (personal communication Andrew McVean), which has been validated to produce reproducible results (McVean et al, unpublished data).

For higher dose exposures of 4 Gy γ-IR, Avondoglio et al (2009) have shown that in human glioblastoma cells fixed 1 hour following exposure, the average number of foci per nucleus is approximately 58 (± 5), supporting the finding of our study that exposure of cells to the same dose in CHO-R-O-25 cells accounts for the emergence of 63 [60 – 66] foci per nucleus (figure 5.6) (287). It should be mentioned however that the comparison above is only indirect, as human glioblastoma cells are

cancerous and therefore their average number of foci per nucleus cannot be directly compared to that of normal cells, such as CHO-R-O-25. For γ-IR doses higher than 4 Gy (6 Gy and 8 Gy), an insignificant difference in the average number of foci per nucleus was seen due to saturation effects (287). In our immunostaining experiments, cells were treated with BLM and H_2O_2 for 30 minutes and then immediately fixed and stained. The average number of foci per nucleus in CHO-R-O-25 cells treated with 20 μg/ml of BLM was found to be 19 [18 – 20; figure 5.6]. In contrast to this finding, Rakiman et al (2008) have reported that in WI-38 cells treated with the same dose of BLM for 3 hours at 37 ^{o}C, the average number of foci per nucleus observed 1 hour after the end of exposure was approximately 3, while the corresponding number in cells that were fixed and immunostained immediately after exposure was ~4 (349). However, the authors argued that the number of foci in different nuclei ranged between 3 and 20 (349). Therefore, the main difference between the results of that study and our study was that WI-38 cells were incubated with the DNA damaging agent for a longer period of time (3 hours) compared to our study, suggestive of a higher incidence of DSB repair before immunostaining compared to our procedure. In addition, in our study stalled replication fork-induced DSBs within the nuclei of cells in S phase that had already been repaired in WI-38 cells before immunostaining, contributes to this higher number of foci per nucleus. Further, Tomilin et al (2001) have shown that exposure of highly proliferating and asynchronised primary human skin fibroblast cells to 200 μg/ml of BLM for 1 hour and incubation for an additional hour in medium devoid of the agent in order to allow repair to occur, results in the appearance of nuclear areas crowded with numerous γ-H2AX foci, reflecting the excessive burden of induced damage (288). Accordingly, it is not surprising that following exposure to a 10-fold lower concentration and incubation for only 30 minutes we obtained an average of 19 foci / nucleus. For nuclei immunostained for γ-H2AX after exposure to 400 μM of H_2O_2, the average number of γ-H2AX foci per nucleus was 13 [11 – 15; figure 5.6]. Driessens et al (2009) have shown a dose effect increase in the number of γ-H2AX foci for the concentration range of 100 μM – 1 mM of H_2O_2 (276), while exposure of NHF human foreskin cells to 100 μM of H_2O_2 for 2 hours has been shown to result in the formation of 2 (± 0.5) foci per nucleus on average, with ~70 % of the nuclei containing at least 1 focus (283). Therefore based on these data, our findings of 13 [11 – 15] γ-H2AX foci per nucleus on average and 86 % (± 1.4 %) of nuclei showing

at least one γ-H2AX focus at the 4-fold higher concentration of 400 μM, seems reasonable.

5.6.2 CONSIDERATIONS FOR DESIGN OF TIME-LAPSE MICROSCOPY

The applicability of time-lapse acquisition for the live-cell examination of cellular and sub-cellular processes is demonstrated by a vast and growing range of studies, using a variety of different cell types. For example, Pinco et al (2002) has tracked α4-GFP fusion protein to provide evidence for α4β1 integrin mediated lamellipodia extensions, after wounding induced by the scraping of living confluent CHO cells (208). In addition, P_tk_1 vertebrate somatic cells have been employed to comprehend the importance of kinetochore attachment to the mitotic spindle for progression from metaphase to anaphase (209, 212) and normal rat kidney epithelial (NRK) cells have been used to study protein dynamics (206, 207).

The culture conditions for cells on stage and the acquisition parameters in time-lapse experiments are dependent upon the specific requirements of the study, both to ensure maintenance of the cell population and to ensure appropriate measure of the research question. For instance, cells need to be maintained in their optimal environmental conditions for the duration of the experiment and images need to be acquired at relevant intervals for a defined period of time. It is important that problems associated with phototoxicity and adverse conditions related to the culturing of cells are avoided (238). Thus, it is important to define the time and acquisition intervals appropriately. In the study of kinetochores, P_tk_1 vertebrate somatic cells were studied over a total period of ~ 2 hours. To achieve this, cells were reseeded on glass slides that were subsequently sealed on Rose chambers, surrounded by heaters keeping the medium at ~37^oC. Specific monitors on the heaters and inside the chambers ensured that there were no deviations in temperature. Using phase-contrast and DIC optics, 15 frames were acquired every minute on an inverted microscope for a total of 2 hours (209, 212). The study carried out by Pinco et al (2002) required images to be acquired every two minutes, over a period of 2-3 hours. For this CHO cells were placed on glass-bottom dishes and imaged on an inverted fluorescence microscope equipped with a CCD camera and a temperature adjustment device, using phase and FITC channels (208). For longer-term time-lapse experiments such as that to study the process of mitotic spindle formation for ~3 days in BSC-1 monkey kidney epithelial cells (212), humidity and

maintenance of respiration products is of even greater importance. For example, the authors constructed a chamber for the cells containing pre-warmed imaging-specific medium composed of HEPES buffer, FCS and fluorocarbon oil that is known to produce oxygen and chelate CO_2 that is released by the cells. Gaps on the chamber were filled with mineral oil, in order to maintain humid conditions (350). Further, different cell cycle stages have been investigated in human cells following the incorporation of CENPB-GFP fusion protein within cell nuclei, using time-lapse confocal microscopy (62). Time-lapse series were obtained during metaphase, anaphase and telophase stages of the mitotic cycle and interphase from one focal plane in each series. During metaphase, the picture series were acquired by averaging the scans, thereby obtaining 6-7 images per minute. One image was obtained every 20 seconds. Images were processed and analysed quantitatively, through the determination of the distance between the centres of α-satellite segments of the two centromeres of a cell in which mobility had been recorded. In anaphase, time-lapse sequences were obtained with one image being acquired every 12 seconds. At the end of anaphase, time-lapse sequences were acquired every 5 minutes until G_1, in order to gain insight into chromosome disintegration during telophase. In interphase, images were acquired every 30 seconds following six centromeres, three of which were characterised by considerable motion (62). Accordingly, here and elsewhere, many individual images were acquired over short-time scales.

In this investigation, time-lapse microscopy was achieved by the acquisition of one image of a selected cell every 2 minutes, over a time interval of 2 hours. Cells were selected on the basis of fluorescent spot characteristics within their nuclei and viewed using a 63x oil immersion objective on an Axiovert 200 M inverted fluorescence microscope equipped with a CCD camera. The choice of this length of acquisition was based on the fact that the majority of DNA damage repair processes take place during the first 30-60 minutes after exposure of cells to DNA damaging agents (126-129, 133, 134). In addition, during the time interval of 2 hours the possibility that the cells under investigation would die off by the agents or U.V. light - induced damage was thought to be minimal. For example, the acquisition of images at frequent time intervals (every 12, 20 and 30 seconds) by Shelby et al (1996) had no negative effect on cell viability for long-term periods (62). In addition, it is worth mentioning that in *Drosophila* and *S. cerevisiae* species wide-field deconvolution 3-

D time-lapse microscopy has been performed by the acquisition of images every 12, 24 and 96 seconds. Furthermore, following topoisomerase II microinjection in *Drosophila*, chromatin motion has been tracked resulting in the generation of 3-D datasets every 20 seconds. At each time point, 16 images were being collected (59). For our experiments, HEPES – supplemented Opti-MEM imaging medium in conjunction with the temperature and gas conditions in the imaging chamber (37 ^{o}C and 5 % CO_2, respectively), supported cell survival ideally until the end of image acquisitions (sections 2.13.1 – 2.13.3 and CD supplementary material). The 2 minute intervals that intervened between the capture of individual images, were associated with the scope of identifying damage-induced changes in chromatin physical properties as soon as these had occurred.

In our time-lapse experiments, the maintenance of temperature at stable levels was monitored by using a temperature sensor, whereas humid conditions during imaging were maintained by placing a trough containing pre-warmed sterile dH_2O into the stage during the acquisition period. Similar to our studies, in the work of Hinchcliffe et al (2005), the chamber on the microscope stage was surrounded by a Plexiglass box (212). While in our experiments the temperature was kept at 37 ^{o}C by the supply of heating into the chamber from the temperature controller device, Hinchcliffe et al (2005) employed a heat gun in order to maintain a temperature of 37 ^{o}C into the interior of the chamber. In their study, acquisition of images was accomplished using wide-field GFP fluorescence and phase-contrast microscopy, with the aid of a CCD camera (212).

5.6.3 ALTERATIONS OF CHROMATIN PHYSICAL PROPERTIES AFTER EXPOSURE TO DNA DAMAGING AGENTS

Evidence has speculated that following DNA damage induction, chromatin structure assumes a more relaxed configuration that serves as a favourable platform for the subsequent recruitment of DNA damage repair proteins to the damaged sites (139, 146-148). Moreover, another widely recognised proposal is that the majority of repair processes occur within the first 60 minutes following DNA damage induction, with the major peak taking place during the first 30 minutes (126-129, 133, 134). In our experimental setup, we imaged cells containing discrete and intense EGFP spots over a period of 2 hours after exposure to sham, H_2O_2, BLM or γ-IR. Each image was then processed enabling the area, mean intensity and total intensity

measurements of fluorescent spots to be tracked within the nuclei of the selected cells. Following t-test performance, it was shown that the entire sets of series corresponding to the same treatments could be pooled into single representative graphs (tables 8.2 – 8.5 in appendix). During the first 60 minutes after exposure we expected to record diffusions of the fluorescent spots, reflected by decreases in pooled normalised total intensity, in cells exposed to DNA damaging agents and not in untreated cells. The comparison between the declining trends of normalised total intensity in these pooled sets of series revealed that during the first 60 minutes and the entire course of acquisition, the declining trends of the graphs corresponding to pooled H_2O_2, BLM, 1 Gy γ-IR series and individual 4 Gy γ-IR series (figures 5.30, 5.36, 5.37 and 5.46 respectively) were more abrupt and pronounced compared to that of untreated pooled set of series (figure 5.29). In pooled H_2O_2 series, two steep decreases in normalised total intensity were recorded during 0 – 10 and 20 – 38 minutes into acquisition. Additionally, in pooled BLM, pooled 1 Gy γ-IR and individual 4 Gy γ-IR series, abrupt decreases were observed during 12 – 52, 32 – 52 and 34 – 56 minutes after exposure, respectively. In individual 6 Gy γ-IR series, the decreasing trend of normalised total intensity values was steeper and more considerable in comparison to pooled untreated series during the entire course of acquisition, but this was not the case during the first 60 minutes after exposure. The major decline in this series occurred during 60 – 66 minutes after irradiation. In this series, DNA damage repair was associated with the initial increase in normalised total intensity during 26 – 46 minutes after exposure (figure 5.49), as explained on pages 274 - 275 below.

While the trend of normalised total intensity decrease in pooled untreated series was monophasic and consistent with photobleaching, different trends of decrease were observed in the pooled series corresponding to cells treated with DNA damaging agents. More specifically, a triphasic decrease was recorded for pooled H_2O_2 series (figure 5.30) and biphasic declines were recorded for pooled BLM (figure 5.36), 1 Gy γ-IR (figure 5.37) series and individual 4 Gy (figure 5.46) and 6 Gy γ-IR (figure 5.49) series. Unlike pooled H_2O_2 and BLM series (figures 5.30 and 5.36, respectively), in pooled 1 Gy γ-IR series and individual 4 Gy and 6 Gy γ-IR series there were increases in normalised total intensity values early in acquisition, during 20 – 32, 22 – 34 and 26 – 46 minutes after exposure, respectively. The peak in normalised total intensity was shown to be higher for the individual time-lapse

series in which cells were exposed to the higher dose of 6 Gy γ-IR (~90 %; figure 5.49) compared to individual 4 Gy γ-IR series (~40 %; figure 5.46) and pooled 1 Gy γ-IR series (~20 %; figure 5.37). As explained in sections 5.5.4 – 5.5.6 above, these total intensity peaks were due to the higher magnitude of increases in area values relative to decreases in mean intensity values in these series (compare figures 5.35, 5.43 – 5.45, 5.47 – 5.48 and 5.50 – 5.51). It is possible that these peaks in normalised total intensity represent the initial response of the DNA damage repair machinery to damage, resulting in the increase in chromatin area and therefore the opening of chromatin structure. This relaxation of chromatin structure might have been so significant that resulted in the increase of normalised total intensity, as opposed to a decrease that would have been expected due to the diffusion of the fluorescent spots under investigation. Consistent with expectations, the overall declines during the 2 hours of acquisition in these series (figures 5.37, 5.46 and 5.49) were more substantial than that of untreated pooled set of sequences (figure 5.29). The explanation provided above for the early normalised total intensity increases in γ-IR series could also apply to the increase of normalised spot total intensity back to its initial value in pooled H_2O_2 series, which occurred during $10 – 18$ minutes and followed the initial decline during the first 10 minutes (figure 5.30).

But, why were these increases in pooled normalised total intensity observed only in time-lapse series corresponding to cells exposed to γ-IR and not in series representing cells treated with H_2O_2 or BLM? In order to answer this question, the extent of DNA damage and the relative proportions of cells containing DSBs after exposure to the aforementioned agents will have to be taken into consideration. In addition, based on the fact that different complexities of DSBs result in different repair responses after damage formation, DSB complexity will have to be taken into account for cells exposed to H_2O_2, BLM and γ-IR. The discussion that follows indicates that a higher extent of aberration formation might be expected after γ-IR in comparison to H_2O_2 or BLM exposure, thereby possibly explaining the considerable initial increase of normalised total intensity in γ-IR series that was absent in pooled H_2O_2 and BLM series. This explanation might also support the finding that the magnitude of this increase within γ-IR time-lapse series is dose-dependent (6 Gy > 4 Gy > 1 Gy).

Line of evidence has suggested that a requirement for H_2O_2 and BLM-induced DNA damage formation is the presence of Fe^{2+} ions and oxygen in proximity with the double helix (79, 80, 83, 99-101, 104). Moreover, comet assays on human peripheral lymphocytes have suggested that exposure to 500 μM of H_2O_2 for 5 minutes results in the generation of DSBs in only 19 ± 3.1 % of cells out of the total population (289). In the same cell type, exposure to 75 μg/ml and 150 μg/ml of BLM resulted in the formation of DSBs in only 7.5 ± 2.1 % and 16.5 ± 3.2 % of cells, respectively (289). While numerous SSBs can be formed by H_2O_2, the number of DSBs that can be generated by this agent alone is low (107, 110, 121, 351). The formation of DSBs after treatment of human, mouse, monkey and hamster cells with H_2O_2 has been reported to require the presence of the amino acid histidine (107, 110, 121). In BLM-treated cells, the sequence specificity (74) and the structure of chromatin (85) are major determinants of the extent of damage that can be induced. BLM has been shown to recognise and exert its damaging effect only at G-T and G-C sequences of the genome and sequences in which the guanine is present at the 3 'end of the pyrimidine (T-G) and (C-G) are not recognized and thus not cleaved by the antibiotic (74). It has also been shown that decondensed chromatin regions of actively transcribed genes are prefered for BLM-induced cleavage over more condensed regions (85). Furthermore, it has been suggested that cell cycle stage plays a role in aberration formation by BLM (90) and that the pathway of damage repair is specific for the specific cell type in which damage has occurred (89). Finally, studies with confluent human fibroblasts have indicated that following BLM exposure the cell membrane acts as a physical barrier for the entry of the agent into the cells, thereby resulting in only a fraction of BLM inducing chromosomal damage (95).

On the other hand, ionising radiation is responsible for the formation of SSBs, DSBs, cross-links between DNA molecules, cross-links between DNA and proteins, damage on the deoxyribose sugar, base damage and base modifications (352). In contrast to H_2O_2 and BLM, exposure of cells to ionising radiation results in the emergence of chromosomal aberrations of high complexity that involve ≥ 3 breaks in two or more chromosomes (70, 163, 290). Anderson et al (2002) have shown that following exposure of PBL to densely ionising high-linear energy transfer (LET) α-particle irradiation, an average of four distinct chromosomes and six distinct breaks participate in aberration events, with the highest number of

chromosomes and breaks observed to be involved being eight and ten, respectively (70). In a seperate study that employed the same cell type, Anderson et al (2006) categorized complex chromosomal aberrations as non-reproducible aberrations that involved one simple re-joining event or sequential exchange complex aberrations that involved multiple cycles of re-joining, with some aberrations being represented by both categories (163). Between two and six distinct chromosomes were demonstrated to be involved in these aberrations (163). Sparsely ionising irradiation such as γ-rays represents the low-LET form of irradiation (291, 292). Evidence has indicated that in human cell lines, an average of 35 - 39 DSBs per nucleus are formed in response to exposure of cells to 1 Gy of low-LET irradiation, with the entire cell population being positive for the presence of DSBs (126, 292). It has also been suggested that including base damage, approximately 50 % of the DSBs that are generated after exposure to low-LET radiation are complex (293, 294). A common feature between high and low-LET ionising radiation is the generation of clusters of damage on exposed DNA within or nearby tracks of radiation (291, 295). These clusters represent ≥ two lesions present on a short DNA fragment corresponding to one or two twists of the DNA double helix (291, 296-298). Clusters of damaged DNA are more predominant in cells exposed to high-LET, but are also present in cells exposed to low-LET radiation (291). They correspond to direct breaks within single radiation tracks and / or indirect breaks created by OH$^-$ radicals that are present in close proximity and opposite to one another on the double helix (291, 293, 299, 300). The complexity of this clustered damage can vary from simple DSBs, to highly complex damage involving DSBs, base damage, SSBs nearby main DSBs and various aberrations in which different chromosomes participate (291, 295). Gulston et al (2002) have demonstrated that exposure of HF19 human fibroblasts and V79-4 CHO fibroblasts to γ-irradiation results in the formation of clustered DNA damage (301). Similarly, in other studies clustered DNA damage has been observed in human breast cancer cells (297, 302), human hematopoietic cells (296) and CHO cells (303, 304), following exposure to γ-irradiation. The DNA damage representing these clusters has been proposed to be more severe in comparison to that produced by ROS (293, 299, 300) in H_2O_2 and BLM exposed cells. Accordingly, the repair of this clustered damage by the cell represents a task that is considerably more difficult (302, 305) compared to the repair of simple DSBs

generated by ROS. The difference in the severity of DNA damage induced by γ-IR compared to that owed to the actions of H_2O_2 and BLM can be proved to be even higher, taking into account the 'non-targeted' effects of ionising radiation (295, 306-310). These include DNA damage owed to initial damage occurring in the cell cytoplasm (309), damage occurring in nuclear locations that are irrelevant from the nuclear sites of the initial insults (306-308) and damage owed to the 'bystander' effect of irradiation within the nuclei of cells that were not originally affected by ionising radiation (307, 308, 310). Therefore based on these findings, it is concluded that the dose-dependent early increases of normalised total intensity in pooled 1 Gy and individual 4 Gy and 6 Gy γ-IR series which reflected a more substantial chromatin area expansion in comparison to pooled H_2O_2 and BLM series, might be consistent with expectations.

A common feature between the biphasic declining trends of the graphs corresponding to pooled BLM, 1 Gy γ-IR and individual 4 Gy γ-IR series was that the first phase of normalised total intensity decrease during the first ~ 60 minutes was steeper and more remarkable, in comparison to the second phase of decline during ~ 60 – 120 minutes after exposure. Similarly, in pooled H_2O_2 series the first two phases of decrease during the initial ~ 60 minutes after irradiation were higher and more abrupt, in comparison to the more gradual decline between ~ 60 and 120 minutes after exposure. In contrast, no such timing correlation could be drawn for the declining trend of the graph corresponding to pooled untreated series. Based on these findings, it is likely that the first phases corresponding to the more abrupt and considerable decreases of normalised total intensity for pooled H_2O_2, BLM, 1 Gy γ-IR and individual 4 Gy γ-IR series during the initial ~ 60 minutes after irradiation, could be attributed to the operation of repair processes on relaxed chromatin regions in the vicinity of the fluorescent spots. The fact that these changes were independent of defocusing strengthens this speculation. In individual 6 Gy γ-IR series, normalised total intensity was decreased below its initial value between 60 and 66 minutes after irradiation. For the latter series however, the operation of repair processes could be linked to the early increase in normalised total intensity during 26 – 46 minutes after exposure, by ~90 % (figure 5.49). This early increase was the result of the increase in normalised spot area during 26 – 46 minutes after exposure (figure 5.50), that

occurred simultaneously with a less pronounced decrease in normalised mean intensity during the same time interval (figure 5.51).

The most common chromatin relaxation event that occurs immediately following DSB induction is histone H2AX phosphorylation and the expansion of γ-H2AX foci over Megabase chromatin regions surrounding DSBs (126, 130, 133, 311). Furthermore, *in vitro* chromatin relaxation generating a favourable environment for the subsequent assembly of DNA damage repair factors has been reported to be carried out by chromatin remodeling machineries that alter chromatin structure [reviewed in (312, 313)]. Following DSB induction, these chromatin remodeling activities are performed by SWI/SNF, P/CAF, INO80, Rad54, SWR1 and RSC enzymes (314-319). In addition, Kruhlak et al (2006) have found that ATP-dependent chromatin decondensation occurs in MEFs and HeLa cells within minutes after DNA damage induction (139). According to the authors, this chromatin relaxation was owed to proteins that are involved in the sensing of damage, thereby altering chromatin structure upstream of repair factor assembly (139). Consistent with this, Falk et al (2007) have demonstrated that between 15 and 40 minutes after γ-irradiation treatment of MCF7 and human fibroblast cells, chromatin decondensation takes place (147). Similarly, Ziv et al (2006) have reported that during the first 15 minutes following DNA damage induction in human osteosarcoma cells there is a global phosphorylation of KAP-1 that is responsible for the genome-wide chromatin decondensation in these cells (148). In agreement with these findings, evidence has suggested that following exposure of mammalian cells to X-ray irradiation, DSB-induced γ-H2AX foci are preferentially generated in relaxed euchromatic rather than compact heterochromatic regions of the genome (146). Characteristic of the requirement for a decondensed chromatin state in order for repair to proceed is the fact that during transcription repair is facilitated by the binding of repair proteins to the more relaxed chromatin regions of transcribed genes [reviewed in (319)].

In pooled H_2O_2, BLM and 1 Gy γ-IR and individual 4 Gy γ-IR time-lapse series, the second phases corresponding to the more gradual declines between ~ 60 and 120 minutes were shown to be consistent with photobleaching. Biologically, this finding may be correlated to the completion of repair represented by the re-appearance of chromatin original structure [reviewed in (311-313)], which could in

turn be associated with the less considerable decreases in normalised total intensity values during this period of time.

A question that arises from the scenario explaining the alterations in chromatin physical properties above, is whether relaxation of chromatin following exposure of cells to genotoxic agents requires damage occurring in the vicinity of the EGFP spots, or it represents a genome-wide alteration in chromatin structure in response to damage, that is independent of the nuclear location of the original lesion. While no definite evidence exists in our study, it seems highly unlikely that in every single time-lapse series of each treatment damage occurred in the vicinity of the fluorescent spot, considering the observed small size of the fluorescent spots in relation to the observed larger sizes of the entire nuclear areas within the cells under investigation. Therefore, a more plausible explanation would be that DSB induction has resulted in a global modification in chromatin conformation within the nuclear area [reviewed in (314, 320-322)]. Indeed, it has been proposed that genome-wide post-translational histone modifications including phosphorylation, acetylation, methylation, ubiquitination and ADP ribosylation alter chromatin conformation, in such a way that enhances the access of repair proteins to the damaged sites [reviewed in (312, 314, 319, 321, 322)].

It is well established that following DSB formation, the core histones H2A, H2B, H3 and H4 become phosphorylated [reviewed in (314)]. In addition, H2AX is phosphorylated by ATM and the resulting γ-H2AX foci are expanded over Megabase regions of the genome surrounding DSBs (126, 130, 133, 311). This expansion has been proposed to promote chromatin decondensation, thereby amplifying the signal required for checkpoint activation, recruitment of larger proportions of repair proteins to the damaged sites and their maintenance at these sites (130, 320). Consistent with this, evidence has suggested that following damage sensing by ATM or ATR and cell cycle checkpoint activation through H2AX phosphorylation, checkpoint effector proteins such as p53 can globally modify chromatin structure, in order to promote DSB detection and accessibility by repair proteins within the nucleus [reviewed in (320)]. It has been proposed that in human, mouse, rat and African green monkey kidney cells, p53 achieves that by complexing with p300 histone acetyltransferase enzyme and acetylating histone proteins over Megabase regions throughout the genome (320, 323, 324). Another phosphorylation

event that results in genome-wide chromatin decondensation is that of serine 824 residue on KAP-1 that is induced by ATM (148). Histone acetylation is known to decondense chromatin through the transfer of acetyl groups on lysine residues of histones, thereby generating a favourable environment for the subsequent assembly of chromatin remodelers in response to DNA damage [reviewed in (311, 313, 314, 325, 326)]. The facilitation of DNA damage repair processes after histone acetylation has been demonstrated after exposure of human fibroblasts to U.V. light and ionising radiation (321, 327-329). The binding of p300 to PCNA has been shown to result in the assembly of p300 at DNA lesions and acetylation of proximal histones, which in turn relaxes chromatin thereby promoting the subsequent recruitment of repair proteins at damaged sites [reviewed in (326)]. Besides p300, other common histone acetyltransferases that are involved in the acetylation of core histones in yeast and mammalian cells are Gcn5, PCAF, TIP60 and CBP [reviewed in (312, 314, 321, 322)]. Moreover, it is worth noting that in yeast cells histone acetyltransferase Esa1-dependent acetylation of core histone H4 has been implicated in the repair of DSBs (330). A similar action of Esa1 mammalian homolog TIP60 in DSB repair has been established from studies in which DSB repair was shown to be defective in cells where TIP60 was devoid of its histone acetyltransferase activity [reviewed in (326)]. Methylation is a post-translational histone modification that involves the transfer of methyl groups on lysine and arginine residues of core histones H3 and H4 [reviewed in (325)]. In mammalian cells, following ionising radiation-induced DSB generation, the methylation of lysines H3K79 and H4K20 on histones H3 and H4 results in the escort of 53BP1 protein to repair foci (325, 331-333). Moreover, following ionising radiation-induced DSB formation in human osteosarcoma and embryonic kidney cells, ubiquitination of H2A and H2AX has been shown to be essential for foci formation, maintenance of an active checkpoint status and the recruitment of BRCA1 and 53BP1 repair factors to damaged sites (334-336). Finally, it is worth mentioning that ADP ribosylation of histones H1 and H2B has been implicated in chromatin relaxation and DNA displacement from the ocatamer of core histones [reviewed in (319)]. Apart from post-translational histone modifications, another way in which chromatin structure can be globally relaxed is the direct removal of histone proteins from nucleosomal complexes, through mechanisms powered by ATP hydrolysis [reviewed in (314, 321, 325)].

Aternatively, nucleosomes can be moved along DNA through their slipping along DNA templates [reviewed in (321, 325)].

6. CONCLUSIONS

Following the successful generation of CHO-R-O clones stably transfected with the p3'SSdimerClonEGFP and pSV2-DHFR8.32 plasmids, it was shown that clone CHO-R-O-25 possesses the desired features and therefore a decision was made to perform subsequent studies on this clone. Several characteristics including the growth rates (short-term and long-term) and fraction of cells in S phase of the cell cycle in this clone were found to be comparable to the corresponding characteristics of control CHO DG44 cells, suggesting that the plasmid integrations within the chromosomes of cells did not interfere with vital cellular processes such as growth rate and DNA replication. Furthermore, FISH revealed that the chromosome harbouring the lac O incorporation is a small metacentric (figure 4.14). While this chromosome is suspected to be normal chromosome 9, the relative positions of the centromeres from our FISH procedure cannot be clearly distinguished at this resolution level and therefore no definite conclusions associated with the identity of CHO-R-O-25 chromosomes in our FISH procedure can be drawn.

The results of this project have revealed that time-lapse fluorescence microscopy can be successfully applied for the assessment of alterations in chromatin physical properties, after DNA damage. These alterations have been measured based on changes in fluorescent spot total intensity over the course of time-lapse acquisitions. Importantly, such measures have the potential to be exploited for addressing relevant questions associated with the comprehension of DNA damage repair responses and possibly exchange formation. It has been shown that especially during the first 60 minutes into acquisition, but also during the entire course of time-lapse acquisition, decreases in fluorescent spot total intensity occur for cells treated with 20 μg/ml of BLM, 400 μM of H_2O_2, 1 Gy and 4 Gy of γ-irradiation. Consistently, these decreases were not observed in the fluorescent spots within the nuclei of untreated cells. Based on the timing of their occurrence, it is highly likely that the aforementioned alterations in fluorescent spot physical properties during the course of these time-lapse series in treated cells were owed to DNA damage –induced chromatin relaxation in the vicinity of the fluorescent spots,

allowing repair to proceed. On the other hand, no such correlation could be drawn for cells exposed to 6 Gy of γ-irradiation, as the decline of normalised total intensity in this series occurred during 60 – 66 minutes after exposure. However, as mentioned in section 5.6.3 above, in this series DNA damage repair could be associated with the substantial initial increase in normalised total intensity during 26 – 46 minutes after exposure. Importantly, the treatment of cells with these DNA damaging agents resulted in the formation of numerous DSBs within the nuclei of cells (section 5.2). In the pooled series corresponding to cells exposed to 1 Gy γ-IR and in individual series of cells exposed to 4 Gy and 6 Gy γ-IR, initial increases in fluorescent spot normalised total intensity were recorded during 20 – 32, 22 – 34 and 26 – 46 minutes after irradiation, respectively. These increases, which were absent in pooled untreated, H_2O_2 and BLM series, were shown to be dependent on the dose of γ-IR exposure. More specifically, the highest increase was recorded in individual 6 Gy γ-IR series (~90 %), followed by that of individual 4 Gy γ-IR series (~40 %) and pooled 1 Gy γ-IR series (~20 %). These increases reflected more substantial increases in the area of the fluorescent spots in comparison with decreases in mean intensity. Based on the reported higher severity of damage occurring after exposure to γ-IR compared to damage appearing after H_2O_2 and BLM treatments, it is speculated that these increases were due to the initial over-pronounced expansion of chromatin in response to γ-IR exposure. Finally, based on the unlikelihood of the possibility that the decreases in normalised total intensity that were observed in pooled H_2O_2, BLM and γ-IR series represented damage that occurred in the vicinity of the spot for every single time-lapse series, it is speculated that these decreases represented genome-wide chromatin decondensation events in response to DSB formation, where the nuclear site of the initial insult was irrelevant of the observed response. This scenario seems more reasonable in comparison to the unlikely possibility that chromatin relaxation in each individual series of each treatment corresponded to damage occurring in the vicinity of the fluorescent spot.

Overall, this study has demonstrated that the time-lapse microscopical investigation of fluorescently labelled chromatin sites in living CHO cells represents a potentially useful model in the comprehension of chromatin organisation in response to a variety of DNA damaging agents such as H_2O_2, BLM and γ-irradiation. The development of CHO cells stably transfected with the p3'SSdimerClonEGFP

and pSV2-DHFR8.32 plasmids provided the tools in our attempt to achieve this scope. While the applicability of this approach in other mammalian cell types has not been tested and the exact implications of the alterations in chromatin physical properties recorded in this study remain obscure, the possibility that these phenomena are correlated to DNA damage repair processes occurring during the first 60 minutes after the end of exposure has been highlighted.

7. FUTURE DIRECTIONS

With regards to the future completion of characterisation of CHO-R-O-25 cells, Southern blotting can be performed, in order to determine the number of lac operator copies that are integrated within the genome of cells. Another future prospect that was not fulfilled in this project is the stable co-transfection of other mammalian cell types such as human cells, with p3'SSdimerClonEGFP and pSV2-DHFR 8.32 plasmids. Based on the fact that the DHFR gene sequence is constitutively expressed only in the genome of CHO DG44 cells, it would be necessary to replace this DNA sequence with another sequence in the pSV2-DHFR8.32 plasmid, to enable the selection of stable transfected cells. In this respect, the blasticidin resistance (Bsr) gene would be a candidate. The advantage of the Bsr gene over other genes is that it can be easily and efficiently introduced into a large plasmid such as pSV2-DHFR8.32, due to its small size. As mentioned in the introductory section of this thesis, line of evidence has suggested that the pSV2-DHFR 8.32 plasmid can be specifically modified, so that defined sequences can be incorporated or removed from the plasmid (173, 177). In order to cut out the DHFR gene from the pSV2-DHFR 8.32 plasmid, restriction digestion with the appropriate restriction enzymes can be performed. Similarly, restriction digestion can be performed on the plasmid that contains the Bsr gene and the band that corresponds to the gene can be subsequently excised from the gel, purified and ligated to the pSV2-DHFR 8.32 plasmid. Similar to the plasmid bulking procedure that was followed in this project, the stability of the insertion of the modified plasmid can be assessed by its introduction into Stbl-2 bacterial cells through heat shock transformation (177). Then, Mini prep can be carried out, in order to isolate a small amount of plasmid DNA. The subsequent restriction digestion will determine whether the Bsr gene has been incorporated efficiently into the plasmid, by observation of the picture of the

gel. In case the Bsr gene has been successfully ligated into the plasmid, Maxi prep can be carried out, in order to isolate a large amount of plasmid DNA. Following co-transfection, selection of stable CHO cell transfectants can take place by culturing the cells in CD DG44 chemically defined medium (Gibco) containing thymidine and hypoxanthine, lacking L-glutamine and supplemented with the antibiotics blasticidin and hygromycin. Stable transfectant cells can be finally isolated and cloned.

The measurement of changes in chromatin physical properties following DNA damage induction by agents that have not been used in our studies yet, represents an intriguing future development for this project that necessitates the performance of time-lapse microscopy. In this respect, fluorescent multi-labelling of chromatin regions within the nuclei of living cells could be performed, using plasmids that contain fluorescent fusion proteins of different colours (170). Useful conclusions associated with the mechanism of chromosomal aberration formation and DSB mobility have been drawn, based on time-lapse series of living MEF cells simultaneously expressing lac – CFP and tet - YFP fusion constructs (170). In addition, multiple DNA damage repair proteins fused to different fluorescent labels have been employed in studies that have sought to address the nature of repair processes following damage formation (147, 334, 337, 338). The transfection of human MCF7 breast cancer cells with both H2B-GFP and 53BP1-RFP fusion proteins has provided useful information associated with the interdependence between chromatin structure and repair processes after exposure to γ-irradiation (147). In addition, Mailand et al (2007) have examined the role of RNF8 ubiquitin ligase in the recruitment of repair factors to damaged sites following the stable transfection of human osteosarcoma cells with MDC1-GFP, 53BP1-GFP, ATR-GFP and NBS1-RFP repair fusion proteins (334). Similarly, the kinetics of 53BP1 recruitment to sites of DSBs after exposure to γ-irradiation has been assessed in human fibrosarcoma cells stably transfected with 53BP1-YFP, through the tracking of this repair fusion protein within the nuclei of cells in time-lapse series (337). Finally, in the same cell type, following stable transfection with 53BP1-GFP, MDC1-GFP, MRE11-GFP, GFP-PARP-1 and MSH2-GFP, the kinetics of detection of DSBs and repair factor assembly at DSBs have been elucidated, after microbeam-induced low-LET and high-LET irradiation (338). Besides repair proteins fused to fluorescent labels, the fusion of centromeric proteins, such as CENP-A to fluorescent tags can provide useful information associated with the operation of repair processes

following damage induction (339). In human embryonic kidney cells transfected with GFP-CENP-A and RFP-SceI-GR construct, the assembly of CENP-A to DSBs has been demonstrated following damage formation by the construct (339). Following the performance of time-lapse microscopy, analyses of the associations and kinetics of such repair proteins fused to fluorescent labels in combination with the elucidation of the behavior of histones fused to separate fluorescent tags, could provide important clues associated with the relationship between chromatin structure and DNA damage repair processes operating within the nuclei of cells.

8. APPENDIX

8.1 STATISTICAL EVIDENCE FOR DATA POOLING – NORMAL DISTRIBUTION AND STUDENT T-TEST

8.1.1 BACKGROUND

The vast majority of time-lapse series of CHO-R-O-25 cells exposed to BLM, H_2O_2 and γ-IR (1 Gy, 4 Gy and 6 Gy) show decreasing trends of total intensity after image J analysis. Visual analysis of the generated plots suggested that the steepness of the declines was greater in the treated compared to control series. Between the three individual control series similar decreasing trends were observed, suggesting that this is a consequence of photobleaching (304, 353).

To compare trends in total intensity between control and exposed cells, individual time points from all series of each treatment were averaged as one single trend, representing that particular treatment. To establish whether individual series can be pooled, the most appropriate statistical test was required to be identified. Taking into consideration that the student t – test can only be performed where the data are normally distributed (i.e.: for data that are parametric), the normal distribution was calculated for each series. In the event that the data were not normally distributed (non-parametric), the chi square (x^2) goodness-of-fit test would be the ideal statistical test to be performed. The tests were performed for both absolute and normalised values in each time-lapse series. The normal distributions

were calculated using the Excel sheet array column of all data points from the first to the last time point in acquisition. The result of each test corresponded to the z mean value (μ) of the test.

8.1.2 PERFORMANCE OF NORMAL DISTRIBUTION TESTS

In summary, the normal distribution results (table 8.1) revealed that the untreated, BLM, H_2O_2 and γ-IR series are normally distributed for both of the absolute and normalised data points. This indicated that the t-test can be reliably performed to assess whether time-lapse sequences of the same type (e.g.: BLM series 1 and BLM series 2) can be pooled into a single graph. Based on these results, there was no requirement to carry out chi square (x^2) analysis.

Table 8.1 Normal distribution tests for control and treated time-lapse series

Treatment	Normal distribution (z mean values)	
	Absolute data points	Normalised data points
Untreated 1	1	1
Untreated 2	1	1
Untreated 3	0.7736	1
H_2O_2 1	1	1
H_2O_2 2	0.995	1
H_2O_2 3	1	1
H_2O_2 4	0.5	0.5
BLM 1	0.5	1
BLM 2	0.5	1
BLM 3	0.5	1
BLM 4	0.5	0.5
1 Gy γ-IR 1	0.5	0.5
1 Gy γ-IR 2	0.5	0.5
1 Gy γ-IR 3	0.5	0.5
1 Gy γ-IR 4	1	1

8.1.2.1 UNTREATED TIME-LAPSE SERIES

The results of the normal distribution test for both absolute and normalised data points suggested that all three series are normally distributed. Regarding the absolute data points, the z mean values were equal to1, 1 and 0.7736 for sequences 1 - 3. The z mean value for the untreated 3 series was <1, but since it was only ~ 0.2 standard deviation away (to the left or to the right) from the mean of series 1 and 2, it was concluded that it was normally distributed with these series. With respect to the normalised data points, the z mean values of series 1 - 3 were all calculated to be equal to 1.

8.1.2.2 H_2O_2 TIME-LAPSE SERIES

Similar to the results of normal distribution tests for untreated series, H_2O_2 series 1 – 4 were also shown to be normally distributed regarding their absolute and normalised data points. For the absolute data points of sequences 1, 2, 3 and 4 the z mean values were found to be 1, 0.995, 1 and 0.5, respectively. Regarding the normalised data points, the z mean values for series 1 - 3 were all equal to 1 and that of series 4 was only half a standard deviation away from the mean of the other three series, as it was equal to 0.5.

8.1.2.3 BLM TIME-LAPSE SERIES

Following the performance of normal distribution tests it was shown that for both absolute and normalised data points, all 4 time-lapse sequences are normally distributed. Regarding the absolute data points, the z mean values for all 4 series were equal to 0.5, while for the normalised data points, the z mean values for series 1 – 3 were all equal to 1. The z mean value for the normalised datapoints of series 4 was 0.5 and therefore, based on the fact that it was only half a standard deviation away from the mean of series 1, 2 and 3, it was concluded that it was normally distributed with these series.

8.1.2.4) 1 Gy γ-IRRADIATION TIME-LAPSE SERIES

Based on the results of normal distribution tests for both absolute and normalised data points, all four series are normally distributed. Regarding the absolute and normalised data points of series 1, 2 and 3, the z mean values were all equal to 0.5, suggesting that these three series are normally distributed. For the absolute and normalised data points of series 4, both z mean values were shown to be equal to 1 and therefore, based on the fact that they were only half a standard deviation away from the mean of the other three sequences, it was concluded that they were normally distributed with series 1, 2 and 3.

8.1.3 PERFORMANCE OF STUDENT T-TEST

8.1.3.1 BACKGROUND

The normal distribution test results suggested that the dependent student t-test would be the most appropriate statistical test to be performed in order to determine whether untreated, BLM, H_2O_2 and 1 Gy γ-IR series of the same type could be pooled, with the aim of developing a single graph for each one of these treatments. As described above, the main objective of this was to compare the trends in total intensity for each of these treatments. The dependent student t-test was performed for all possible pairs of sequences of the same type (e.g.: BLM series 1 and 2, BLM series 1 and 3, BLM series 1 and 4, BLM series 2 and 3, BLM series 2 and 4 and BLM series 3 and 4). Time-lapse series were pooled based on their resulting p value being < 0.05 (meaning that there is a less than 5 % probability that series cannot be pooled).

8.1.3.2 UNTREATED TIME-LAPSE SERIES

According to the results of the t-test (table 8.2) for both absolute and normalised change in total intensity, all 3 series can be pooled into single graphs, as $p < 0.05$ for all three series pairs tested.

Table 8.2 Student t-test for series 1, 2 and 3 corresponding to untreated cells

Treatment / pair of series	Absolute change: p value	Normalised change: p value
Untreated 1 and 2 t-test	9.135×10^{-49}	8.494×10^{-6}
Untreated 1 and 3 t-test	2.712×10^{-58}	1.676×10^{-6}
Untreated 2 and 3 t-test	5.916×10^{-75}	0.0134

8.1.3.3 H_2O_2 TIME-LAPSE SERIES

The results of student t-test (table 8.3) revealed that all 4 series can be pooled in order to construct two graphs of absolute and normalised change in total intensity, as $p < 0.05$ for H_2O_2 1 and 2, H_2O_2 1 and 3, H_2O_2 1 and 4, H_2O_2 2 and 3, H_2O_2 2 and 4 and H_2O_2 3 and 4 series pairs tested.

Table 8.3 Student t-test for series 1, 2, 3 and 4 corresponding to cells exposed to H_2O_2

Treatment / pair of series	Absolute change: p value	Normalised change: p value
H_2O_2 1 and 2 t-test	1.817×10^{-22}	2.99×10^{-12}
H_2O_2 1 and 3 t-test	1.43×10^{-9}	1.798×10^{-5}
H_2O_2 1 and 4 t-test	1.72×10^{-35}	5.51×10^{-23}
H_2O_2 2 and 3 t-test	7.8×10^{-20}	0.0045
H_2O_2 2 and 4 t-test	1.724×10^{-35}	0.023
H_2O_2 3 and 4 t-test	0.031	5.3×10^{-23}

8.1.3.4 BLM TIME-LAPSE SERIES

Based on the results of the student t-test (table 8.4), it was shown that all 4 series can be pooled in order to construct two graphs of absolute and normalised change in total intensity. The p values after comparison between BLM 1 and 2, BLM 1 and 3, BLM 1 and 4, BLM 2 and 3, BLM 2 and 4 and BLM 3 and 4 pairs of series were lower than 0.05 ($p < 0.05$), for both arrays corresponding to absolute and normalised change in total intensity.

Table 8.4 Student t-test for series 1, 2, 3 and 4 corresponding to cells exposed to BLM

Treatment / pair of series	Absolute change: p value	Normalised change: p value
BLM 1 and 2 t-test	7.17×10^{-9}	3.66×10^{-7}
BLM 1 and 3 t-test	1.11×10^{-9}	0.012
BLM 1 and 4 t-test	2.19×10^{-16}	1.26×10^{-22}
BLM 2 and 3 t-test	1.24×10^{-21}	0.00086
BLM 2 and 4 t-test	0.0441	9.25×10^{-11}
BLM 3 and 4 t-test	4.513×10^{-20}	5.7×10^{-26}

8.1.3.5) 1 Gy γ-IRRADIATION TIME-LAPSE SERIES

According to the results of the student t-test (table 8.5), it was established that regarding both absolute and normalised change in total intensity, all four series can be pooled in two representative graphs.

Table 8.5 Student t-test for series 1, 2, 3 and 4 corresponding to cells exposed to 1 Gy γ-irradiation

Treatment / pair of series	Absolute change: p value	Normalised change: p value
Gamma-IR 1 and 2 t-test	8.45×10^{-27}	3.4×10^{-22}
Gamma-IR 1 and 3 t-test	0.0032	2.7×10^{-14}
Gamma-IR 1 and 4 t-test	1.47×10^{-49}	6.35×10^{-25}
Gamma-IR 2 and 3 t-test	2.3×10^{-29}	1.01×10^{-12}
Gamma-IR 2 and 4 t-test	1.4×10^{-36}	0.0014
Gamma-IR 3 and 4 t-test	1.29×10^{-48}	4.38×10^{-15}

8.2 DNA EXTRACTIONS

For single and double transfected clones, DNA extractions were performed with the subsequent aim to identify the copy number and assess the stability of plasmid integrations within the chromosomes of cells, by Southern blotting. They were carried out as described in sections 2.4.2.1 and 2.4.2.2, using either the TRIzol or phenol - chloroform method. Using the former method, RNA was also extracted from single and double transfected cells, for future use in reverse transcription – PCR (RT-PCR) experiments. The samples were stored for future use in the aforementioned procedures. Tables 8.6 and 8.7 below provide information associated with DNA samples from single and double transfected cells, respectively.

Table 8.6 Single transfected CHO-R DNA samples

SAMPLE	DNA CONCENTRATION	TOTAL AMOUNT OF DNA	A_{260}/A_{280} RATIO	A_{260}/A_{230} RATIO	METHOD USED
CHO-R-21 A	0.1307 μg/μl	57.116 μg	1.32	1.79	TRIZOL
CHO-R-21 D	0.1083 μg/μl	47.327 μg	1.33	36.0	TRIZOL
CHO-R-17 A	0.1938 μg/μl	84.691 μg	1.41	2.03	TRIZOL
CHO-R-17 B	0.2001 μg/μl	87.444 μg	1.39	1.76	TRIZOL
CHO-R-02 v	0.3089 μg/μl	135.3 μg	1.60	1.27	TRIZOL
CHO-R-02 iv	0.305 μg/μl	133.59 μg	1.67	2.40	Phenol-Chloroform
CHO-R-02 D	0.1086 μg/μl	52.128 μg	1.53	2.36	Phenol-Chloroform
CHO-R-02 G	0.185 μg/μl	85.1 μg	1.60	2.28	Phenol-Chloroform
CHO-R-02 i (Hyg+)	0.0713 μg/μl	33.511 μg	1.54	1.84	Phenol-Chloroform
CHO-R-02 B	0.0279 μg/μl	13.761 μg	1.92	1.85	Phenol-Chloroform
CHO-R-02 F	0.1183 μg/μl	57.967 μg	1.72	1.08	Phenol-Chloroform
CHO-R-14 A	0.0726 μg/μl	34.1 μg	1.78	1.23	Phenol-Chloroform
CHO-R-14 G	0.0261 μg/μl	12.5 μg	1.80	0.47	Phenol-Chloroform
CHO-R-14 C (Hyg+)	0.0721 μg/μl	33.89 μg	1.88	0.44	Phenol-Chloroform
CHO-R-19 A	0.122 μg/μl	58.56 μg	1.85	0.73	Phenol-Chloroform
CHO-R-19 D (Hyg+)	0.149 μg/μl	71.568 μg	1.85	0.85	Phenol-Chloroform
CHO-R-19 E	0.132 μg/μl	64.68 μg	1.93	0.45	Phenol-Chloroform
CHO-R-09 C (Hyg+)	0.1345 μg/μl	64.56 μg	1.85	1.37	Phenol-Chloroform
CHO-R-09 E	0.430 μg/μl	210.8 μg	1.87	1.46	Phenol-Chloroform
CHO-R-09 H	0.1694 μg/μl	83 μg	1.86	1.26	Phenol-Chloroform

Table 8.7 Double transfected CHO-R-O DNA samples

SAMPLE	DNA CONCENTRATION	TOTAL AMOUNT OF DNA	A_{260}/A_{280} RATIO	A_{260}/A_{230} RATIO	METHOD USED
CHO-R-O-25 (i) (p11)	0.542 µg/µl	265.6 µg	1.95	0.65	PHENOL-CHLOROFORM
CHO-R-O-25 D (p13)	0.0194 µg/µl	95.1 µg	1.62	1.89	TRIZOL
CHO-R-O-25 K (p14) partially digested	0.422 µg/µl	206.78 µg	1.96	0.55	PHENOL-CHLOROFORM
CHO-R-O-25 K (p14) re-extracted	0.313 µg/µl	156.19 µg	1.75	1.73	PHENOL-CHLOROFORM-ISOAMYL ALCOHOL OPTIMISATION
CHO-R-O-25 G (p14)	0.055 µg/µl	253 µg	1.29	2.20	TRIZOL
CHO-R-O-25 H (p17)	0.5127 µg/µl	148.68 µg	1.86	1.19	TRIZOL
CHO-R-O-25 L (p19)	0.6773 µg/µl	196.4 µg	1.82	1.35	TRIZOL
CHO-R-O-167 (p12) failed to be digested	0.4265 µg/µl	212.8 µg	1.77	1.36	PHENOL-CHLOROFORM
CHO-R-O-167 (p12) re-extracted	0.308 µg/µl	153.7 µg	1.88	1.71	PHENOL-CHLOROFORM-ISOAMYL ALCOHOL OPTIMISATION
CHO-R-O-9 (p12) failed to be digested	0.2214 µg/µl	110.5 µg	1.80	1.50	PHENOL-CHLOROFORM
CHO-R-O-9 (p12) re-extracted	0.097 µg/µl	48.4 µg	1.70	1.74	PHENOL-CHLOROFORM-ISOAMYL ALCOHOL OPTIMISATION
CHO-R-O-34 F (p13)	0.3057 µg/µl	88.65 µg	1.83	0.68	TRIZOL
CHO-R-O-34 G	0.4008 µg/µl	116.2 µg	1.86	1.49	TRIZOL
CHO-R-O-36 A (p12)	0.0212 µg/µl	61.5 µg	1.79	1.31	TRIZOL
CHO-R-O-36 D (p13)	0.0232 µg/µl	67.3 µg	1.79	1.46	TRIZOL
CHO-R-O-36 H (p14)	0.0162 µg/µl	79.4 µg	2.04	1.52	TRIZOL
CHO DG44 (control) (p12) partially digested	0.217 µg/µl	106.3 µg	2.00	0.33	PHENOL-CHLOROFORM
CHO DG44 (p12) re-extracted	0.116 µg/µl	56.8 µg	1.76	1.82	ISOAMYL ALCOHOL OPTIMISATION

The DNA concentration of each sample was determined as described in section 2.1.4.1. For double transfected DNA samples, DNA extractions were followed by digestion tests of 1 μg of DNA from each sample with restriction enzymes NheI-HF and SpeI (New England Biolabs), in order to confirm that the samples can be efficiently digested. For samples that failed to be digested due to poor A_{260}/A_{280} and A_{260}/A_{230} ratios, the extraction procedure was optimised as described in section 8.2.1 below.

8.2.1 OPTIMISATION OF PHENOL-CHLOROFORM DNA EXTRACTION

A different phenol-chloroform DNA extraction method was employed for samples that had failed to be digested. Initially, equal amounts of phenol and chloroform were mixed in the fume cupboard and left at RT for 1 hour, in order for the mixture to become equilibrated. An equal volume of phenol-chloroform was added to the volume that DNA was dissolved in and the contents of the eppendorf mixed gently, by placing it on the rotating platform at low speed for 10 minutes. Following centrifugation at 11300 x g for 10 minutes at RT, the upper aqueous phase was removed and transferred to a new eppendorf. An equal volume of 24:1 (v/v) chloroform:isoamyl alcohol (Sigma-Aldrich) was added and the contents of the tube mixed gently on the rotating platform for 10 minutes. Then, centrifugation at 11300 x g for 10 minutes at RT was performed and the upper aqueous phase removed and transferred to a new eppendorf. Afterwards, DNA was precipitated as described in section 2.1.2 and dissolved in sterile dH_2O, before been finally stored in the fridge at 4 ^{o}C. The spectrophotometer readings following re-extraction of DNA samples suggested that the samples were devoid of contaminants, as the A_{260}/A_{280} and A_{260}/A_{230} ratios had been improved (their values were closer to 1.80). Although the clean-up of the samples was achieved, this was performed in the expense of a lower yield of DNA after re-extraction. Commenting on DNA sample CHO-R-O-25 K, after re-extraction the A_{260}/A_{280} and A_{260}/A_{230} ratios were improved from 1.96 and 0.55 to 1.75 and 1.73, respectively. This resulted in its efficient digestion by enzymes Spe I and Nhe I – HF, which before clean-up was partial (table 8.7). Similarly, regarding sample CHO-R-O-167, the A_{260}/A_{280} and A_{260}/A_{230} ratios were improved from 1.77 and 1.36 to 1.88 and 1.71, respectively, after re-extraction. The A_{260}/A_{280} and A_{260}/A_{230} ratios of sample CHO-R-O-9 were altered after re-extraction from 1.80 and 1.50 to 1.70 and 1.74, respectively. This resulted in the efficient

digestion of these samples by the aforementioned restriction enzymes. Finally, the A_{260}/A_{280} and A_{260}/A_{230} ratios of CHO DG44 control DNA sample were optimised from 2.00 and 0.33 before clean – up to 1.76 and 1.82, respectively. Similarly, this sample was efficiently digested by the restriction enzymes, after re-extraction (table 8.7).

9. REFERENCES

1. Bednar J, Horowitz RA, Grigoryev SA, Carruthers LM, Hansen JC, Koster AJ, et al. Nucleosomes, linker DNA, and linker histone form a unique structural motif that directs the higher-order folding and compaction of chromatin. Proc Natl Acad Sci U S A. 1998 Nov 24;95(24):14173-8.

2. Schalch T, Duda S, Sargent DF, Richmond TJ. X-ray structure of a tetranucleosome and its implications for the chromatin fibre. Nature. 2005 Jul 7;436(7047):138-41.

3. Hansen JC. Conformational dynamics of the chromatin fiber in solution: Determinants, mechanisms, and functions. Annu Rev Biophys Biomol Struct. 2002;31:361-92.

4. Santos-Rosa H, Caldas C. Chromatin modifier enzymes, the histone code and cancer. Eur J Cancer. 2005 Nov;41(16):2381-402.

5. Widlak P, Pietrowska M, Lanuszewska J. The role of chromatin proteins in DNA damage recognition and repair. Histochem Cell Biol. 2006 Jan;125(1-2):119-26.

6. Chodaparambil JV, Barbera AJ, Lu X, Kaye KM, Hansen JC, Luger K. A charged and contoured surface on the nucleosome regulates chromatin compaction. Nat Struct Mol Biol. 2007 Nov;14(11):1105-7.

7. Schwarz PM, Felthauser A, Fletcher TM, Hansen JC. Reversible oligonucleosome self-association: Dependence on divalent cations and core histone tail domains. Biochemistry. 1996 Apr 2;35(13):4009-15.

8. Woodcock CL, Dimitrov S. Higher-order structure of chromatin and chromosomes. Curr Opin Genet Dev. 2001 Apr;11(2):130-5.

9. Belmont AS, Sedat JW, Agard DA. A three-dimensional approach to mitotic chromosome structure: Evidence for a complex hierarchical organization. J Cell Biol. 1987 Jul;105(1):77-92.

10. Belmont AS, Bruce K. Visualization of G1 chromosomes: A folded, twisted, supercoiled chromonema model of interphase chromatid structure. J Cell Biol. 1994 Oct;127(2):287-302.

11. Pienta KJ, Coffey DS. A structural analysis of the role of the nuclear matrix and DNA loops in the organization of the nucleus and chromosome. J Cell Sci Suppl. 1984;1:123-35.

12. Bednar J, Horowitz RA, Dubochet J, Woodcock CL. Chromatin conformation and salt-induced compaction: Three-dimensional structural information from cryoelectron microscopy. J Cell Biol. 1995 Dec;131(6 Pt 1):1365-76.

13. Park PC, De Boni U. Dynamics of structure-function relationships in interphase nuclei. Life Sci. 1999;64(19):1703-18.

14. Gerlich D, Hirota T, Koch B, Peters JM, Ellenberg J. Condensin I stabilizes chromosomes mechanically through a dynamic interaction in live cells. Curr Biol. 2006 Feb 21;16(4):333-44.

15. Beaudouin J, Gerlich D, Daigle N, Eils R, Ellenberg J. Nuclear envelope breakdown proceeds by microtubule-induced tearing of the lamina. Cell. 2002 Jan 11;108(1):83-96.

16. Dietzel S, Zolghadr K, Hepperger C, Belmont AS. Differential large-scale chromatin compaction and intranuclear positioning of transcribed versus non-transcribed transgene arrays containing beta-globin regulatory sequences. J Cell Sci. 2004 Sep 1;117(Pt 19):4603-14.

17. Belmont AS, Zhai Y, Thilenius A. Lamin B distribution and association with peripheral chromatin revealed by optical sectioning and electron microscopy tomography. J Cell Biol. 1993 Dec;123(6 Pt 2):1671-85.

18. Raska I, Koberna K, Malinsky J, Fidlerova H, Masata M. The nucleolus and transcription of ribosomal genes. Biol Cell. 2004 Oct;96(8):579-94.

19. Bartova E, Kozubek S. Nuclear architecture in the light of gene expression and cell differentiation studies. Biol Cell. 2006 Jun;98(6):323-36.

20. Spector DL. Macromolecular domains within the cell nucleus. Annu Rev Cell Biol. 1993;9:265-315.

21. Bridger JM, Bickmore WA. Putting the genome on the map. Trends Genet. 1998 Oct;14(10):403-9.

22. Ferreira J, Paolella G, Ramos C, Lamond AI. Spatial organization of large-scale chromatin domains in the nucleus: A magnified view of single chromosome territories. J Cell Biol. 1997 Dec 29;139(7):1597-610.

23. Cremer T, Kurz A, Zirbel R, Dietzel S, Rinke B, Schrock E, et al. Role of chromosome territories in the functional compartmentalization of the cell nucleus. Cold Spring Harb Symp Quant Biol. 1993;58:777-92.

24. Leitch AR, Mosgoller W, Schwarzacher T, Bennett MD, Heslop-Harrison JS. Genomic in situ hybridization to sectioned nuclei shows chromosome domains in grass hybrids. J Cell Sci. 1990 Mar;95 (Pt 3)(Pt 3):335-41.

25. Albiez H, Cremer M, Tiberi C, Vecchio L, Schermelleh L, Dittrich S, et al. Chromatin domains and the interchromatin compartment form structurally defined and functionally interacting nuclear networks. Chromosome Res. 2006 Nov;14(7):707-33.

26. Branco MR, Pombo A. Intermingling of chromosome territories in interphase suggests role in translocations and transcription-dependent associations. PLoS Biol. 2006 May;4(5):e138.

27. Scheuermann MO, Tajbakhsh J, Kurz A, Saracoglu K, Eils R, Lichter P. Topology of genes and nontranscribed sequences in human interphase nuclei. Exp Cell Res. 2004 Dec 10;301(2):266-79.

28. Zink D, Cremer T, Saffrich R, Fischer R, Trendelenburg MF, Ansorge W, et al. Structure and dynamics of human interphase chromosome territories in vivo. Hum Genet. 1998 Feb;102(2):241-51.

29. Zink D, Cremer T. Cell nucleus: Chromosome dynamics in nuclei of living cells. Curr Biol. 1998 Apr 23;8(9):R321-4.

30. Cremer T, Cremer M, Dietzel S, Muller S, Solovei I, Fakan S. Chromosome territories--a functional nuclear landscape. Curr Opin Cell Biol. 2006 Jun;18(3):307-16.

31. Cremer T, Cremer C. Chromosome territories, nuclear architecture and gene regulation in mammalian cells. Nat Rev Genet. 2001 Apr;2(4):292-301.

32. Adkins NL, Watts M, Georgel PT. To the 30-nm chromatin fiber and beyond. Biochim Biophys Acta. 2004 Mar 15;1677(1-3):12-23.

33. Munkel C, Eils R, Dietzel S, Zink D, Mehring C, Wedemann G, et al. Compartmentalization of interphase chromosomes observed in simulation and experiment. J Mol Biol. 1999 Jan 22;285(3):1053-65.

34. Sachs RK, van den Engh G, Trask B, Yokota H, Hearst JE. A random-walk/giant-loop model for interphase chromosomes. Proc Natl Acad Sci U S A. 1995 Mar 28;92(7):2710-4.

35. Yokota H, van den Engh G, Hearst JE, Sachs RK, Trask BJ. Evidence for the organization of chromatin in megabase pair-sized loops arranged along a random walk path in the human G0/G1 interphase nucleus. J Cell Biol. 1995 Sep;130(6):1239-49.

36. Solovjeva L, Svetlova M, Stein G, Chagin V, Rozanov Y, Zannis-Hadjopoulos M, et al. Conformation of replicated segments of chromosome fibres in human S-phase nucleus. Chromosome Res. 1998 Dec;6(8):595-602.

37. Kosak ST, Groudine M. Form follows function: The genomic organization of cellular differentiation. Genes Dev. 2004 Jun 15;18(12):1371-84.

38. Zirbel RM, Mathieu UR, Kurz A, Cremer T, Lichter P. Evidence for a nuclear compartment of transcription and splicing located at chromosome domain boundaries. Chromosome Res. 1993 Jul;1(2):93-106.

39. Cremer T, Kupper K, Dietzel S, Fakan S. Higher order chromatin architecture in the cell nucleus: On the way from structure to function. Biol Cell. 2004 Oct;96(8):555-67.

40. van den Engh G, Sachs R, Trask BJ. Estimating genomic distance from DNA sequence location in cell nuclei by a random walk model. Science. 1992 Sep 4;257(5075):1410-2.

41. Bolzer A, Kreth G, Solovei I, Koehler D, Saracoglu K, Fauth C, et al. Three-dimensional maps of all chromosomes in human male fibroblast nuclei and prometaphase rosettes. PLoS Biol. 2005 May;3(5):e157.

42. Mahy NL, Perry PE, Bickmore WA. Gene density and transcription influence the localization of chromatin outside of chromosome territories detectable by FISH. J Cell Biol. 2002 Dec 9;159(5):753-63.

43. Kurz A, Lampel S, Nickolenko JE, Bradl J, Benner A, Zirbel RM, et al. Active and inactive genes localize preferentially in the periphery of chromosome territories. J Cell Biol. 1996 Dec;135(5):1195-205.

44. Chen TA, Sterner R, Cozzolino A, Allfrey VG. Reversible and irreversible changes in nucleosome structure along the c-fos and c-myc oncogenes following inhibition of transcription. J Mol Biol. 1990 Apr 5;212(3):481-93.

45. Lau LF, Nathans D. Expression of a set of growth-related immediate early genes in BALB/c 3T3 cells: Coordinate regulation with c-fos or c-myc. Proc Natl Acad Sci U S A. 1987 Mar;84(5):1182-6.

46. Cmarko D, Verschure PJ, Martin TE, Dahmus ME, Krause S, Fu XD, et al. Ultrastructural analysis of transcription and splicing in the cell nucleus after bromo-UTP microinjection. Mol Biol Cell. 1999 Jan;10(1):211-23.

47. Verschure PJ, Van Der Kraan I, Enserink JM, Mone MJ, Manders EM, Van Driel R. Large-scale chromatin organization and the localization of proteins involved in gene expression in human cells. J Histochem Cytochem. 2002 Oct;50(10):1303-12.

48. Visser AE, Aten JA. Chromosomes as well as chromosomal subdomains constitute distinct units in interphase nuclei. J Cell Sci. 1999 Oct;112 (Pt 19)(Pt 19):3353-60.

49. Kill IR, Bridger JM, Campbell KH, Maldonado-Codina G, Hutchison CJ. The timing of the formation and usage of replicase clusters in S-phase nuclei of human diploid fibroblasts. J Cell Sci. 1991 Dec;100 (Pt 4)(Pt 4):869-76.

50. Manders EM, Kimura H, Cook PR. Direct imaging of DNA in living cells reveals the dynamics of chromosome formation. J Cell Biol. 1999 Mar 8;144(5):813-21.

51. Visser AE, Eils R, Jauch A, Little G, Bakker PJ, Cremer T, et al. Spatial distributions of early and late replicating chromatin in interphase chromosome territories. Exp Cell Res. 1998 Sep 15;243(2):398-407.

52. Berezney R, Mortillaro MJ, Ma H, Wei X, Samarabandu J. The nuclear matrix: A structural milieu for genomic function. Int Rev Cytol. 1995;162A:1-65.

53. Bridger JM, Boyle S, Kill IR, Bickmore WA. Re-modelling of nuclear architecture in quiescent and senescent human fibroblasts. Curr Biol. 2000 Feb 10;10(3):149-52.

54. Dimitrova DS, Gilbert DM. The spatial position and replication timing of chromosomal domains are both established in early G1 phase. Mol Cell. 1999 Dec;4(6):983-93.

55. Zink D, Bornfleth H, Visser A, Cremer C, Cremer T. Organization of early and late replicating DNA in human chromosome territories. Exp Cell Res. 1999 Feb 25;247(1):176-88.

56. Nakamura H, Morita T, Sato C. Structural organizations of replicon domains during DNA synthetic phase in the mammalian nucleus. Exp Cell Res. 1986 Aug;165(2):291-7.

57. Bornfleth H, Edelmann P, Zink D, Cremer T, Cremer C. Quantitative motion analysis of subchromosomal foci in living cells using four-dimensional microscopy. Biophys J. 1999 Nov;77(5):2871-86.

58. Haaf T, Schmid M. Chromosome topology in mammalian interphase nuclei. Exp Cell Res. 1991 Feb;192(2):325-32.

59. Marshall WF, Straight A, Marko JF, Swedlow J, Dernburg A, Belmont A, et al. Interphase chromosomes undergo constrained diffusional motion in living cells. Curr Biol. 1997 Dec 1;7(12):930-9.

60. Maguire MP. The mechanism of meiotic homologue pairing. J Theor Biol. 1984 Feb 21;106(4):605-15.

61. Manuelidis L. A view of interphase chromosomes. Science. 1990 Dec 14;250(4987):1533-40.

62. Shelby RD, Hahn KM, Sullivan KF. Dynamic elastic behavior of alpha-satellite DNA domains visualized in situ in living human cells. J Cell Biol. 1996 Nov;135(3):545-57.

63. Vazquez J, Belmont AS, Sedat JW. Multiple regimes of constrained chromosome motion are regulated in the interphase drosophila nucleus. Curr Biol. 2001 Aug 21;11(16):1227-39.

64. Chubb JR, Boyle S, Perry P, Bickmore WA. Chromatin motion is constrained by association with nuclear compartments in human cells. Curr Biol. 2002 Mar 19;12(6):439-45.

65. Abney JR, Cutler B, Fillbach ML, Axelrod D, Scalettar BA. Chromatin dynamics in interphase nuclei and its implications for nuclear structure. J Cell Biol. 1997 Jun 30;137(7):1459-68.

66. Buchenau P, Saumweber H, Arndt-Jovin DJ. The dynamic nuclear redistribution of an hnRNP K-homologous protein during drosophila embryo development and heat shock. flexibility of transcription sites in vivo. J Cell Biol. 1997 Apr 21;137(2):291-303.

67. Elliott B, Jasin M. Double-strand breaks and translocations in cancer. Cell Mol Life Sci. 2002 Feb;59(2):373-85.

68. Fornace AJ,Jr, Kohn KW, Kann HE,Jr. DNA single-strand breaks during repair of UV damage in human fibroblasts and abnormalities of repair in xeroderma pigmentosum. Proc Natl Acad Sci U S A. 1976 Jan;73(1):39-43.

69. Hande MP, Azizova TV, Geard CR, Burak LE, Mitchell CR, Khokhryakov VF, et al. Past exposure to densely ionizing radiation leaves a unique permanent signature in the genome. Am J Hum Genet. 2003 May;72(5):1162-70.

70. Anderson RM, Stevens DL, Goodhead DT. M-FISH analysis shows that complex chromosome aberrations induced by alpha -particle tracks are cumulative products of localized rearrangements. Proc Natl Acad Sci U S A. 2002 Sep 17;99(19):12167-72.

71. Bassing CH, Alt FW. H2AX may function as an anchor to hold broken chromosomal DNA ends in close proximity. Cell Cycle. 2004 Feb;3(2):149-53.

72. Umezawa H. Recent studies on bleomycin. Lloydia. 1977 Jan-Feb;40(1):67-81.

73. Umezawa H, Maeda K, Takeuchi T, Okami Y. New antibiotics, bleomycin A and B. J Antibiot (Tokyo). 1966 Sep;19(5):200-9.

74. Takeshita M, Grollman AP, Ohtsubo E, Ohtsubo H. Interaction of bleomycin with DNA. Proc Natl Acad Sci U S A. 1978 Dec;75(12):5983-7.

75. Burger RM, Berkowitz AR, Peisach J, Horwitz SB. Origin of malondialdehyde from DNA degraded by fe(II) x bleomycin. J Biol Chem. 1980 Dec 25;255(24):11832-8.

76. Burger RM, Peisach J, Horwitz SB. Stoichiometry of DNA strand scission and aldehyde formation by bleomycin. J Biol Chem. 1982 Aug 10;257(15):8612-4.

77. Muller WE, Yamazaki Z, Breter HJ, Zahn RK. Action of bleomycin on DNA and RNA. Eur J Biochem. 1972 Dec 18;31(3):518-25.

78. Mirabelli CK, Ting A, Huang CH, Mong S, Crooke ST. Bleomycin and talisomycin sequence-specific strand scission of DNA: A mechanism of double-strand cleavage. Cancer Res. 1982 Jul;42(7):2779-85.

79. Sausville EA, Stein RW, Peisach J, Horwitz SB. Properties and products of the degradation of DNA by bleomycin and iron(II). Biochemistry. 1978 Jul 11;17(14):2746-54.

80. Lown JW, Sim SK. The mechanism of the bleomycin-induced cleavage of DNA. Biochem Biophys Res Commun. 1977 Aug 22;77(4):1150-7.

81. Giloni L, Takeshita M, Johnson F, Iden C, Grollman AP. Bleomycin-induced strand-scission of DNA. mechanism of deoxyribose cleavage. J Biol Chem. 1981 Aug 25;256(16):8608-15.

82. Wu JC, Kozarich JW, Stubbe J. The mechanism of free base formation from DNA by bleomycin. A proposal based on site specific tritium release from poly(dA.dU). J Biol Chem. 1983 Apr 25;258(8):4694-7.

83. Sausville EA, Peisach J, Horwitz SB. Effect of chelating agents and metal ions on the degradation of DNA by bleomycin. Biochemistry. 1978 Jul 11;17(14):2740-6.

84. Murray V, Martin RF. The sequence specificity of bleomycin-induced DNA damage in intact cells. J Biol Chem. 1985 Sep 5;260(19):10389-91.

85. Kuo MT. Preferential damage of active chromatin by bleomycin. Cancer Res. 1981 Jun;41(6):2439-43.

86. Lopez-Larraza DM, Padron J, Ronci NE, Vidal Rioja LA. Chromatin condensation and differential sensitivity of mammalian and insect cells to DNA strand breaks induced by bleomycin. Mutat Res. 2006 Aug 30;600(1-2):93-101.

87. Tien Kuo M, Hsu TC. Biochemical and cytological studies of bleomycin actions on chromatin and chromosomes. Chromosoma. 1978 Sep 1;68(3):229-40.

88. Cloos J, Reid CB, van der Sterre ML, Tobi H, Leemans CR, Snow GB, et al. A comparison of bleomycin-induced damage in lymphocytes and primary oral fibroblasts and keratinocytes in 30 subjects. Mutagenesis. 1999 Jan;14(1):87-93.

89. Okudela K, Ito T, Mitsui H, Hayashi H, Udaka N, Kanisawa M, et al. The role of p53 in bleomycin-induced DNA damage in the lung. A comparative study with the small intestine. Am J Pathol. 1999 Oct;155(4):1341-51.

90. Hittelman WN, Rao PN. Bleomycin-induced damage in prematurely condensed chromosomes and its relationship to cell cycle progression in CHO cells. Cancer Res. 1974 Dec;34(12):3433-9.

91. Cohen AM, Philips FS, Sternberg SS. Studies on the cytotoxicity of bleomycin in the small intestine of the mouse. Cancer Res. 1972 Jun;32(6):1293-300.

92. Barranco SC, Humphrey RM. The effects of bleomycin on survival and cell progression in chinese hamster cells in vitro. Cancer Res. 1971 Sep;31(9):1218-23.

93. Watanabe M, Takabe Y, Katsumata T, Terasima T. Effects of bleomycin on progression through the cell cycle of mouse L-cells. Cancer Res. 1974 Apr;34(4):878-81.

94. Sanchez J, Bianchi MS, Bolzan AD. Effect of bleomycin on interstitial telomeric sequences of immortalized chinese hamster ovary cells. Mutat Res. 2009 Jun 18.

95. Sidik K, Smerdon MJ. Bleomycin-induced DNA damage and repair in human cells permeabilized with lysophosphatidylcholine. Cancer Res. 1990 Mar 1;50(5):1613-9.

96. Hsie AW, Recio L, Katz DS, Lee CQ, Wagner M, Schenley RL. Evidence for reactive oxygen species inducing mutations in mammalian cells. Proc Natl Acad Sci U S A. 1986 Dec;83(24):9616-20.

97. Brink A, Richter I, Lutz U, Wanek P, Stopper H, Lutz WK. Biological significance of DNA adducts: Comparison of increments over background for various biomarkers of genotoxicity in L5178Y tk(+/-) mouse lymphoma cells treated with hydrogen peroxide and cumene hydroperoxide. Mutat Res. 2009 Jun 16.

98. Fridovich I. Superoxide radicals, superoxide dismutases and the aerobic lifestyle. Photochem Photobiol. 1978 Oct-Nov;28(4-5):733-41.

99. Meneghini R, Hoffmann ME. The damaging action of hydrogen peroxide on DNA of human fibroblasts is mediated by a non-dialyzable compound. Biochim Biophys Acta. 1980 Jun 27;608(1):167-73.

100. Mello Filho AC, Meneghini R. In vivo formation of single-strand breaks in DNA by hydrogen peroxide is mediated by the haber-weiss reaction. Biochim Biophys Acta. 1984 Feb 24;781(1-2):56-63.

101. Halliwell B. Superoxide-dependent formation of hydroxyl radicals in the presence of iron salts is a feasible source of hydroxy radicals in vivo. Biochem J. 1982 Aug 1;205(2):461-3.

102. Mello Filho AC, Hoffmann ME, Meneghini R. Cell killing and DNA damage by hydrogen peroxide are mediated by intracellular iron. Biochem J. 1984 Feb 15;218(1):273-5.

103. Doulias PT, Christoforidis S, Brunk UT, Galaris D. Endosomal and lysosomal effects of desferrioxamine: Protection of HeLa cells from hydrogen peroxide-induced DNA damage and induction of cell-cycle arrest. Free Radic Biol Med. 2003 Oct 1;35(7):719-28.

104. Iliakis GE, Pantelias GE, Okayasu R, Blakely WF. Induction by H2O2 of DNA and interphase chromosome damage in plateau-phase chinese hamster ovary cells. Radiat Res. 1992 Aug;131(2):192-203.

105. Tenopoulou M, Doulias PT, Barbouti A, Brunk U, Galaris D. Role of compartmentalized redox-active iron in hydrogen peroxide-induced DNA damage and apoptosis. Biochem J. 2005 May 1;387(Pt 3):703-10.

106. Ueda J, Shimazu Y, Ozawa T. Reactions of copper(II)-oligopeptide complexes with hydrogen peroxide: Effects of biological reductants. Free Radic Biol Med. 1995 May;18(5):929-33.

107. Cantoni O, Sestili P, Brandi G, Cattabeni F. The L-histidine-mediated enhancement of hydrogen peroxide-induced cytotoxicity is a general response in cultured mammalian cell lines and is always associated with the formation of DNA double strand breaks. FEBS Lett. 1994 Oct 10;353(1):75-8.

108. Sestili P, Cattabeni F, Cantoni O. The L-histidine-mediated enhancement of hydrogen peroxide-induced DNA double strand breakage and cytotoxicity does not involve metabolic processes. Biochem Pharmacol. 1995 Nov 27;50(11):1823-30.

109. Sestili P, Cattabeni F, Cantoni O. Simultaneous determination of DNA double strand breaks and DNA fragment size in cultured mammalian cells exposed to hydrogen peroxide/histidine or etoposide with CHEF electrophoresis. Carcinogenesis. 1995 Apr;16(4):703-6.

110. Sestili P, Guidarelli A, Cattabeni F, Murray D, Cantoni O. AG8 cells, which are highly resistant to hydrogen peroxide, display collateral sensitivity to the combination of hydrogen peroxide and L-histidine. Carcinogenesis. 1996 Apr;17(4):885-8.

111. Ollinger K, Brunk UT. Cellular injury induced by oxidative stress is mediated through lysosomal damage. Free Radic Biol Med. 1995 Nov;19(5):565-74.

112. Yu Z, Persson HL, Eaton JW, Brunk UT. Intralysosomal iron: A major determinant of oxidant-induced cell death. Free Radic Biol Med. 2003 May 15;34(10):1243-52.

113. Persson HL, Yu Z, Tirosh O, Eaton JW, Brunk UT. Prevention of oxidant-induced cell death by lysosomotropic iron chelators. Free Radic Biol Med. 2003 May 15;34(10):1295-305.

114. Ramirez DC, Gomez Mejiba SE, Mason RP. Mechanism of hydrogen peroxide-induced cu,zn-superoxide dismutase-centered radical formation as explored by immuno-spin trapping: The role of copper- and carbonate radical anion-mediated oxidations. Free Radic Biol Med. 2005 Jan 15;38(2):201-14.

115. Fatokun AA, Stone TW, Smith RA. Cell death in rat cerebellar granule neurons induced by hydrogen peroxide in vitro: Mechanisms and protection by adenosine receptor ligands. Brain Res. 2007 Feb 9;1132(1):193-202.

116. Lee YA, Shin MH. Mitochondrial respiration is required for activation of ERK1/2 and caspase-3 in human eosinophils stimulated with hydrogen peroxide. J Investig Allergol Clin Immunol. 2009;19(3):188-94.

117. Antunes F, Cadenas E, Brunk UT. Apoptosis induced by exposure to a low steady-state concentration of H2O2 is a consequence of lysosomal rupture. Biochem J. 2001 Jun 1;356(Pt 2):549-55.

118. Li W, Yuan X, Nordgren G, Dalen H, Dubowchik GM, Firestone RA, et al. Induction of cell death by the lysosomotropic detergent MSDH. FEBS Lett. 2000 Mar 17;470(1):35-9.

119. Kim DK, Cho ES, Um HD. Caspase-dependent and -independent events in apoptosis induced by hydrogen peroxide. Exp Cell Res. 2000 May 25;257(1):82-8.

120. Barbouti A, Amorgianiotis C, Kolettas E, Kanavaros P, Galaris D. Hydrogen peroxide inhibits caspase-dependent apoptosis by inactivating procaspase-9 in an iron-dependent manner. Free Radic Biol Med. 2007 Nov 15;43(10):1377-87.

121. Cantoni O, Giacomoni P. The role of DNA damage in the cytotoxic response to hydrogen peroxide/histidine. Gen Pharmacol. 1997 Oct;29(4):513-6.

122. Cantoni O, Sestili P, Palomba L, Guidarelli A, Cattabeni F, Murray D. Isolation and preliminary characterization of a chinese hamster ovary cell line with high-degree resistance to hydrogen peroxide. Biochem Pharmacol. 1996 Apr 26;51(8):1021-9.

123. Jackson SP. Sensing and repairing DNA double-strand breaks. Carcinogenesis. 2002 May;23(5):687-96.

124. Kanaar R, Hoeijmakers JH, van Gent DC. Molecular mechanisms of DNA double strand break repair. Trends Cell Biol. 1998 Dec;8(12):483-9.

125. Meaburn KJ, Misteli T, Soutoglou E. Spatial genome organization in the formation of chromosomal translocations. Semin Cancer Biol. 2007 Feb;17(1):80-90.

126. Rogakou EP, Pilch DR, Orr AH, Ivanova VS, Bonner WM. DNA double-stranded breaks induce histone H2AX phosphorylation on serine 139. J Biol Chem. 1998 Mar 6;273(10):5858-68.

127. Paull TT, Rogakou EP, Yamazaki V, Kirchgessner CU, Gellert M, Bonner WM. A critical role for histone H2AX in recruitment of repair factors to nuclear foci after DNA damage. Curr Biol. 2000 Jul 27-Aug 10;10(15):886-95.

128. An J, Huang YC, Xu QZ, Zhou LJ, Shang ZF, Huang B, et al. DNA-PKcs plays a dominant role in the regulation of H2AX phosphorylation in response to DNA damage and cell cycle progression. BMC Mol Biol. 2010 Mar 6;11:18.

129. Stiff T, O'Driscoll M, Rief N, Iwabuchi K, Lobrich M, Jeggo PA. ATM and DNA-PK function redundantly to phosphorylate H2AX after exposure to ionizing radiation. Cancer Res. 2004 Apr 1;64(7):2390-6.

130. Celeste A, Fernandez-Capetillo O, Kruhlak MJ, Pilch DR, Staudt DW, Lee A, et al. Histone H2AX phosphorylation is dispensable for the initial recognition of DNA breaks. Nat Cell Biol. 2003 Jul;5(7):675-9.

131. Wilson PF, Nham PB, Urbin SS, Hinz JM, Jones IM, Thompson LH. Inter-individual variation in DNA double-strand break repair in human fibroblasts before and after exposure to low doses of ionizing radiation. Mutat Res. 2010 Jan 5;683(1-2):91-7.

132. Spycher C, Miller ES, Townsend K, Pavic L, Morrice NA, Janscak P, et al. Constitutive phosphorylation of MDC1 physically links the MRE11-RAD50-NBS1 complex to damaged chromatin. J Cell Biol. 2008 Apr 21;181(2):227-40.

133. Rogakou EP, Boon C, Redon C, Bonner WM. Megabase chromatin domains involved in DNA double-strand breaks in vivo. J Cell Biol. 1999 Sep 6;146(5):905-16.

134. Nelms BE, Maser RS, MacKay JF, Lagally MG, Petrini JH. In situ visualization of DNA double-strand break repair in human fibroblasts. Science. 1998 Apr 24;280(5363):590-2.

135. Goldberg M, Stucki M, Falck J, D'Amours D, Rahman D, Pappin D, et al. MDC1 is required for the intra-S-phase DNA damage checkpoint. Nature. 2003 Feb 27;421(6926):952-6.

136. Kinner A, Wu W, Staudt C, Iliakis G. Gamma-H2AX in recognition and signaling of DNA double-strand breaks in the context of chromatin. Nucleic Acids Res. 2008 Oct;36(17):5678-94.

137. Stewart GS, Wang B, Bignell CR, Taylor AM, Elledge SJ. MDC1 is a mediator of the mammalian DNA damage checkpoint. Nature. 2003 Feb 27;421(6926):961-6.

138. Kobayashi J, Tauchi H, Sakamoto S, Nakamura A, Morishima K, Matsuura S, et al. NBS1 localizes to gamma-H2AX foci through interaction with the FHA/BRCT domain. Curr Biol. 2002 Oct 29;12(21):1846-51.

139. Kruhlak MJ, Celeste A, Dellaire G, Fernandez-Capetillo O, Muller WG, McNally JG, et al. Changes in chromatin structure and mobility in living cells at sites of DNA double-strand breaks. J Cell Biol. 2006 Mar 13;172(6):823-34.

140. Lukas C, Melander F, Stucki M, Falck J, Bekker-Jensen S, Goldberg M, et al. Mdc1 couples DNA double-strand break recognition by Nbs1 with its H2AX-dependent chromatin retention. EMBO J. 2004 Jul 7;23(13):2674-83.

141. Stucki M, Jackson SP. MDC1/NFBD1: A key regulator of the DNA damage response in higher eukaryotes. DNA Repair (Amst). 2004 Aug-Sep;3(8-9):953-7.

142. Ward IM, Chen J. Histone H2AX is phosphorylated in an ATR-dependent manner in response to replicational stress. J Biol Chem. 2001 Dec 21;276(51):47759-62.

143. Downs JA. Chromatin structure and DNA double-strand break responses in cancer progression and therapy. Oncogene. 2007 Dec 10;26(56):7765-72.

144. Fraga MF, Ballestar E, Villar-Garea A, Boix-Chornet M, Espada J, Schotta G, et al. Loss of acetylation at Lys16 and trimethylation at Lys20 of histone H4 is a common hallmark of human cancer. Nat Genet. 2005 Apr;37(4):391-400.

145. Seligson DB, Horvath S, Shi T, Yu H, Tze S, Grunstein M, et al. Global histone modification patterns predict risk of prostate cancer recurrence. Nature. 2005 Jun 30;435(7046):1262-6.

146. Cowell IG, Sunter NJ, Singh PB, Austin CA, Durkacz BW, Tilby MJ. gammaH2AX foci form preferentially in euchromatin after ionising-radiation. PLoS ONE. 2007 Oct 24;2(10):e1057.

147. Falk M, Lukasova E, Gabrielova B, Ondrej V, Kozubek S. Chromatin dynamics during DSB repair. Biochim Biophys Acta. 2007 Oct;1773(10):1534-45.

148. Ziv Y, Bielopolski D, Galanty Y, Lukas C, Taya Y, Schultz DC, et al. Chromatin relaxation in response to DNA double-strand breaks is modulated by a novel ATM- and KAP-1 dependent pathway. Nat Cell Biol. 2006 Aug;8(8):870-6.

149. Chowdhury D, Keogh MC, Ishii H, Peterson CL, Buratowski S, Lieberman J. Gamma-H2AX dephosphorylation by protein phosphatase 2A facilitates DNA double-strand break repair. Mol Cell. 2005 Dec 9;20(5):801-9.

150. Chowdhury D, Xu X, Zhong X, Ahmed F, Zhong J, Liao J, et al. A PP4-phosphatase complex dephosphorylates gamma-H2AX generated during DNA replication. Mol Cell. 2008 Jul 11;31(1):33-46.

151. Nakada S, Chen GI, Gingras AC, Durocher D. PP4 is a gamma H2AX phosphatase required for recovery from the DNA damage checkpoint. EMBO Rep. 2008 Oct;9(10):1019-26.

152. Bryant PE. Repair and chromosomal damage. Radiother Oncol. 2004 Sep;72(3):251-6.

153. Chadwick KH, Leenhouts HP. Radiation induced chromosome aberrations: Some biophysical considerations. Mutat Res. 1998 Aug 3;404(1-2):113-7.

154. Chadwick KH, Leenhouts HP. The rejoining of DNA double-strand breaks and a model for the formation of chromosomal rearrangements. Int J Radiat Biol Relat Stud Phys Chem Med. 1978 Jun;33(6):517-29.

155. Radford IR. Transcription-based model for the induction of interchromosomal exchange events by ionizing irradiation in mammalian cell lines that undergo necrosis. Int J Radiat Biol. 2002 Dec;78(12):1081-93.

156. Bryant PE. The signal model: A possible explanation for the conversion of DNA double-strand breaks into chromatid breaks. Int J Radiat Biol. 1998 Mar;73(3):243-51.

157. REVELL SH. The accurate estimation of chromatid breakage, and its relevance to a new interpretation of chromatid aberrations induced by ionizing radiations. Proc R Soc Lond B Biol Sci. 1959 Sep 1;150:563-89.

158. Savage JR. Cancer. proximity matters. Science. 2000 Oct 6;290(5489):62-3.

159. Haber JE, Leung WY. Lack of chromosome territoriality in yeast: Promiscuous rejoining of broken chromosome ends. Proc Natl Acad Sci U S A. 1996 Nov 26;93(24):13949-54.

160. Lisby M, Mortensen UH, Rothstein R. Colocalization of multiple DNA double-strand breaks at a single Rad52 repair centre. Nat Cell Biol. 2003 Jun;5(6):572-7.

161. Aten JA, Stap J, Krawczyk PM, van Oven CH, Hoebe RA, Essers J, et al. Dynamics of DNA double-strand breaks revealed by clustering of damaged chromosome domains. Science. 2004 Jan 2;303(5654):92-5.

162. Wu H, Durante M, Lucas JN. Relationship between radiation-induced aberrations in individual chromosomes and their DNA content: Effects of interaction distance. Int J Radiat Biol. 2001 Jul;77(7):781-6.

163. Anderson RM, Papworth DG, Stevens DL, Sumption ND, Goodhead DT. Increased complexity of radiation-induced chromosome aberrations consistent with a mechanism of sequential formation. Cytogenet Genome Res. 2006;112(1-2):35-44.

164. Sachs RK, Chen AM, Brenner DJ. Review: Proximity effects in the production of chromosome aberrations by ionizing radiation. Int J Radiat Biol. 1997 Jan;71(1):1-19.

165. Savage JR. Insight into sites. Mutat Res. 1996 Nov;366(2):81-95.

166. Richardson C, Jasin M. Frequent chromosomal translocations induced by DNA double-strand breaks. Nature. 2000 Jun 8;405(6787):697-700.

167. Liang F, Romanienko PJ, Weaver DT, Jeggo PA, Jasin M. Chromosomal double-strand break repair in Ku80-deficient cells. Proc Natl Acad Sci U S A. 1996 Aug 20;93(17):8929-33.

168. Rogakou EP, Nieves-Neira W, Boon C, Pommier Y, Bonner WM. Initiation of DNA fragmentation during apoptosis induces phosphorylation of H2AX histone at serine 139. J Biol Chem. 2000 Mar 31;275(13):9390-5.

169. Celeste A, Difilippantonio S, Difilippantonio MJ, Fernandez-Capetillo O, Pilch DR, Sedelnikova OA, et al. H2AX haploinsufficiency modifies genomic stability and tumor susceptibility. Cell. 2003 Aug 8;114(3):371-83.

170. Soutoglou E, Dorn JF, Sengupta K, Jasin M, Nussenzweig A, Ried T, et al. Positional stability of single double-strand breaks in mammalian cells. Nat Cell Biol. 2007 Jun;9(6):675-82.

171. Downs JA, Jackson SP. A means to a DNA end: The many roles of ku. Nat Rev Mol Cell Biol. 2004 May;5(5):367-78.

172. Nikiforova MN, Stringer JR, Blough R, Medvedovic M, Fagin JA, Nikiforov YE. Proximity of chromosomal loci that participate in radiation-induced rearrangements in human cells. Science. 2000 Oct 6;290(5489):138-41.

173. Robinett CC, Straight A, Li G, Willhelm C, Sudlow G, Murray A, et al. In vivo localization of DNA sequences and visualization of large-scale chromatin organization using lac operator/repressor recognition. J Cell Biol. 1996 Dec;135(6 Pt 2):1685-700.

174. Solovei I, Cavallo A, Schermelleh L, Jaunin F, Scasselati C, Cmarko D, et al. Spatial preservation of nuclear chromatin architecture during three-dimensional fluorescence in situ hybridization (3D-FISH). Exp Cell Res. 2002 May 15;276(1):10-23.

175. Mongelard F, Vourc'h C, Robert-Nicoud M, Usson Y. Quantitative assessment of the alteration of chromatin during the course of FISH procedures. fluorescent in situ hybridization. Cytometry. 1999 Jun 1;36(2):96-101.

176. Mora-Bermudez F, Ellenberg J. Measuring structural dynamics of chromosomes in living cells by fluorescence microscopy. Methods. 2007 Feb;41(2):158-67.

177. Belmont AS, Li G, Sudlow G, Robinett C. Visualization of large-scale chromatin structure and dynamics using the lac operator/lac repressor reporter system. Methods Cell Biol. 1999;58:203-22.

178. Kanda T, Sullivan KF, Wahl GM. Histone-GFP fusion protein enables sensitive analysis of chromosome dynamics in living mammalian cells. Curr Biol. 1998 Mar 26;8(7):377-85.

179. Raap AK, Marijnen JG, Vrolijk J, van der Ploeg M. Denaturation, renaturation, and loss of DNA during in situ hybridization procedures. Cytometry. 1986 May;7(3):235-42.

180. Miyawaki A, Sawano A, Kogure T. Lighting up cells: Labelling proteins with fluorophores. Nat Cell Biol. 2003 Sep;Suppl:S1-7.

181. Marshall WF, Marko JF, Agard DA, Sedat JW. Chromosome elasticity and mitotic polar ejection force measured in living drosophila embryos by four-dimensional microscopy-based motion analysis. Curr Biol. 2001 Apr 17;11(8):569-78.

182. Belmont AS. Visualizing chromosome dynamics with GFP. Trends Cell Biol. 2001 Jun;11(6):250-7.

183. Belmont AS, Braunfeld MB, Sedat JW, Agard DA. Large-scale chromatin structural domains within mitotic and interphase chromosomes in vivo and in vitro. Chromosoma. 1989 Aug;98(2):129-43.

184. Zink D, Sadoni N, Stelzer E. Visualizing chromatin and chromosomes in living cells. Methods. 2003 Jan;29(1):42-50.

185. Tobey RA, Oishi N, Crissman HA. Cell cycle synchronization: Reversible induction of G2 synchrony in cultured rodent and human diploid fibroblasts. Proc Natl Acad Sci U S A. 1990 Jul;87(13):5104-8.

186. Arndt-Jovin DJ, Jovin TM. Fluorescence labeling and microscopy of DNA. Methods Cell Biol. 1989;30:417-48.

187. Labas YA, Gurskaya NG, Yanushevich YG, Fradkov AF, Lukyanov KA, Lukyanov SA, et al. Diversity and evolution of the green fluorescent protein family. Proc Natl Acad Sci U S A. 2002 Apr 2;99(7):4256-61.

188. Prasher DC, Eckenrode VK, Ward WW, Prendergast FG, Cormier MJ. Primary structure of the aequorea victoria green-fluorescent protein. Gene. 1992 Feb 15;111(2):229-33.

189. SHIMOMURA O, JOHNSON FH, SAIGA Y. Extraction, purification and properties of aequorin, a bioluminescent protein from the luminous hydromedusan, aequorea. J Cell Comp Physiol. 1962 Jun;59:223-39.

190. Matz MV, Fradkov AF, Labas YA, Savitsky AP, Zaraisky AG, Markelov ML, et al. Fluorescent proteins from nonbioluminescent anthozoa species. Nat Biotechnol. 1999 Oct;17(10):969-73.

191. Griesbeck O, Baird GS, Campbell RE, Zacharias DA, Tsien RY. Reducing the environmental sensitivity of yellow fluorescent protein. mechanism and applications. J Biol Chem. 2001 Aug 3;276(31):29188-94.

192. Nagai T, Ibata K, Park ES, Kubota M, Mikoshiba K, Miyawaki A. A variant of yellow fluorescent protein with fast and efficient maturation for cell-biological applications. Nat Biotechnol. 2002 Jan;20(1):87-90.

193. Baird GS, Zacharias DA, Tsien RY. Biochemistry, mutagenesis, and oligomerization of DsRed, a red fluorescent protein from coral. Proc Natl Acad Sci U S A. 2000 Oct 24;97(22):11984-9.

194. Campbell RE, Tour O, Palmer AE, Steinbach PA, Baird GS, Zacharias DA, et al. A monomeric red fluorescent protein. Proc Natl Acad Sci U S A. 2002 Jun 11;99(12):7877-82.

195. Snapp EL, Hegde RS, Francolini M, Lombardo F, Colombo S, Pedrazzini E, et al. Formation of stacked ER cisternae by low affinity protein interactions. J Cell Biol. 2003 Oct 27;163(2):257-69.

196. Kimura H, Cook PR. Kinetics of core histones in living human cells: Little exchange of H3 and H4 and some rapid exchange of H2B. J Cell Biol. 2001 Jun 25;153(7):1341-53.

197. Minden JS, Agard DA, Sedat JW, Alberts BM. Direct cell lineage analysis in drosophila melanogaster by time-lapse, three-dimensional optical microscopy of living embryos. J Cell Biol. 1989 Aug;109(2):505-16.

198. Hiraoka Y, Minden JS, Swedlow JR, Sedat JW, Agard DA. Focal points for chromosome condensation and decondensation revealed by three-dimensional in vivo time-lapse microscopy. Nature. 1989 Nov 16;342(6247):293-6.

199. Swedlow JR, Platani M. Live cell imaging using wide-field microscopy and deconvolution. Cell Struct Funct. 2002 Oct;27(5):335-41.

200. Platani M, Goldberg I, Swedlow JR, Lamond AI. In vivo analysis of cajal body movement, separation, and joining in live human cells. J Cell Biol. 2000 Dec 25;151(7):1561-74.

201. Piston DW. Imaging living cells and tissues by two-photon excitation microscopy. Trends Cell Biol. 1999 Feb;9(2):66-9.

202. Kapoor TM, Lampson MA, Hergert P, Cameron L, Cimini D, Salmon ED, et al. Chromosomes can congress to the metaphase plate before biorientation. Science. 2006 Jan 20;311(5759):388-91.

203. Tumbar T, Sudlow G, Belmont AS. Large-scale chromatin unfolding and remodeling induced by VP16 acidic activation domain. J Cell Biol. 1999 Jun 28;145(7):1341-54.

204. Salmon ED. VE-DIC light microscopy and the discovery of kinesin. Trends Cell Biol. 1995 Apr;5(4):154-8.

205. Rieder CL, Cole RW. Perfusion chambers for high-resolution video light microscopic studies of vertebrate cell monolayers: Some considerations and a design. Methods Cell Biol. 1998;56:253-75.

206. Murata-Hori M, Tatsuka M, Wang YL. Probing the dynamics and functions of aurora B kinase in living cells during mitosis and cytokinesis. Mol Biol Cell. 2002 Apr;13(4):1099-108.

207. Wheatley SP, Hinchcliffe EH, Glotzer M, Hyman AA, Sluder G, Wang Y. CDK1 inactivation regulates anaphase spindle dynamics and cytokinesis in vivo. J Cell Biol. 1997 Jul 28;138(2):385-93.

208. Pinco KA, He W, Yang JT. Alpha4beta1 integrin regulates lamellipodia protrusion via a focal Complex/focal adhesion-independent mechanism. Mol Biol Cell. 2002 Sep;13(9):3203-17.

209. Rieder CL, Khodjakov A, Paliulis LV, Fortier TM, Cole RW, Sluder G. Mitosis in vertebrate somatic cells with two spindles: Implications for the metaphase/anaphase transition checkpoint and cleavage. Proc Natl Acad Sci U S A. 1997 May 13;94(10):5107-12.

210. Rieder CL, Schultz A, Cole R, Sluder G. Anaphase onset in vertebrate somatic cells is controlled by a checkpoint that monitors sister kinetochore attachment to the spindle. J Cell Biol. 1994 Dec;127(5):1301-10.

211. Straight AF, Belmont AS, Robinett CC, Murray AW. GFP tagging of budding yeast chromosomes reveals that protein-protein interactions can mediate sister chromatid cohesion. Curr Biol. 1996 Dec 1;6(12):1599-608.

212. Hinchcliffe EH. Using long-term time-lapse imaging of mammalian cell cycle progression for laboratory instruction and analysis. Cell Biol Educ. 2005 Winter;4(4):284-90.

213. Hakansson S, Morisaki H, Heuser J, Sibley LD. Time-lapse video microscopy of gliding motility in toxoplasma gondii reveals a novel, biphasic mechanism of cell locomotion. Mol Biol Cell. 1999 Nov;10(11):3539-47.

214. Shlyakhtenko LS, Lushnikov AY, Lyubchenko YL. Dynamics of nucleosomes revealed by time-lapse atomic force microscopy. Biochemistry. 2009 Aug 25;48(33):7842-8.

215. Yodh JG, Lyubchenko YL, Shlyakhtenko LS, Woodbury N, Lohr D. Evidence for nonrandom behavior in 208-12 subsaturated nucleosomal array populations analyzed by AFM. Biochemistry. 1999 Nov 30;38(48):15756-63.

216. Yodh JG, Woodbury N, Shlyakhtenko LS, Lyubchenko YL, Lohr D. Mapping nucleosome locations on the 208-12 by AFM provides clear evidence for cooperativity in array occupation. Biochemistry. 2002 Mar 19;41(11):3565-74.

217. Nikova DN, Pope LH, Bennink ML, van Leijenhorst-Groener KA, van der Werf K, Greve J. Unexpected binding motifs for subnucleosomal particles revealed by atomic force microscopy. Biophys J. 2004 Dec;87(6):4135-45.

218. Dimitrova N, Chen YC, Spector DL, de Lange T. 53BP1 promotes non-homologous end joining of telomeres by increasing chromatin mobility. Nature. 2008 Nov 27;456(7221):524-8.

219. Rubio N, Rajadurai A, Held KD, Prise KM, Liber HL, Redmond RW. Real-time imaging of novel spatial and temporal responses to photodynamic stress. Free Radic Biol Med. 2009 Aug 1;47(3):283-90.

220. Collins TJ. ImageJ for microscopy. BioTechniques. 2007 Jul;43(1 Suppl):25-30.

221. Fay FS, Taneja KL, Shenoy S, Lifshitz L, Singer RH. Quantitative digital analysis of diffuse and concentrated nuclear distributions of nascent transcripts, SC35 and poly(A). Exp Cell Res. 1997 Feb 25;231(1):27-37.

222. Costes SV, Daelemans D, Cho EH, Dobbin Z, Pavlakis G, Lockett S. Automatic and quantitative measurement of protein-protein colocalization in live cells. Biophys J. 2004 Jun;86(6):3993-4003.

223. van Steensel B, van Binnendijk EP, Hornsby CD, van der Voort HT, Krozowski ZS, de Kloet ER, et al. Partial colocalization of glucocorticoid and mineralocorticoid receptors in discrete compartments in nuclei of rat hippocampus neurons. J Cell Sci. 1996 Apr;109 (Pt 4)(Pt 4):787-92.

224. Eliceiri KW, Rueden C. Tools for visualizing multidimensional images from living specimens. Photochem Photobiol. 2005 Sep-Oct;81(5):1116-22.

225. Rajwa B, McNally HA, Varadharajan P, Sturgis J, Robinson JP. AFM/CLSM data visualization and comparison using an open-source toolkit. Microsc Res Tech. 2004 Jun 1;64(2):176-84.

226. Li Q, Lau A, Morris TJ, Guo L, Fordyce CB, Stanley EF. A syntaxin 1, galpha(o), and N-type calcium channel complex at a presynaptic nerve terminal: Analysis by quantitative immunocolocalization. J Neurosci. 2004 Apr 21;24(16):4070-81.

227. Khanna R, Li Q, Sun L, Collins TJ, Stanley EF. N type Ca2+ channels and RIM scaffold protein covary at the presynaptic transmitter release face but are components of independent protein complexes. Neuroscience. 2006 Jul 21;140(4):1201-8.

228. Sage D, Unser M, Salmon P, Dibner C. A software solution for recording circadian oscillator features in time-lapse live cell microscopy. Cell Div. 2010 Jul 6;5:17.

229. Swedlow JR, Sedat JW, Agard DA. Multiple chromosomal populations of topoisomerase II detected in vivo by time-lapse, three-dimensional wide-field microscopy. Cell. 1993 Apr 9;73(1):97-108.

230. Latt SA. Microfluorometric detection of deoxyribonucleic acid replication in human metaphase chromosomes. Proc Natl Acad Sci U S A. 1973 Dec;70(12):3395-9.

231. McNeil PL, Warder E. Glass beads load macromolecules into living cells. J Cell Sci. 1987 Dec;88 (Pt 5)(Pt 5):669-78.

232. Brown M, Figge J, Hansen U, Wright C, Jeang KT, Khoury G, et al. Lac repressor can regulate expression from a hybrid SV40 early promoter containing a lac operator in animal cells. Cell. 1987 Jun 5;49(5):603-12.

233. Hu MC, Davidson N. The inducible lac operator-repressor system is functional in mammalian cells. Cell. 1987 Feb 27;48(4):555-66.

234. Chao MV, Martinson HG, Gralla JD. Lac operator nucleosomes. 2. lac nucleosomes can change conformation to strengthen binding by lac repressor. Biochemistry. 1980 Jul 8;19(14):3260-9.

235. Belmont AS, Straight AF. In vivo visualization of chromosomes using lac operator-repressor binding. Trends Cell Biol. 1998 Mar;8(3):121-4.

236. Subramani S, Mulligan R, Berg P. Expression of the mouse dihydrofolate reductase complementary deoxyribonucleic acid in simian virus 40 vectors. Mol Cell Biol. 1981 Sep;1(9):854-64.

237. Fieck A, Wyborski DL, Short JM. Modifications of the E.coli lac repressor for expression in eukaryotic cells: Effects of nuclear signal sequences on protein activity and nuclear accumulation. Nucleic Acids Res. 1992 Apr 11;20(7):1785-91.

238. Strukov YG, Belmont AS. Development of mammalian cell lines with lac operator-tagged chromosomes. Cold Spring Harbor Protocols. 2008 January 1;2008(2):pdb.prot4903.

239. Hamada F, Oshima Y, Horiuchi T. Dissociation of the lac repressor into subunits. J Biochem. 1973 Jun;73(6):1299-302.

240. Chen J, Matthews KS. Deletion of lactose repressor carboxyl-terminal domain affects tetramer formation. J Biol Chem. 1992 Jul 15;267(20):13843-50.

241. Li G, Sudlow G, Belmont AS. Interphase cell cycle dynamics of a late-replicating, heterochromatic homogeneously staining region: Precise choreography of condensation/decondensation and nuclear positioning. J Cell Biol. 1998 Mar 9;140(5):975-89.

242. Sasmor HM, Betz JL. Specific binding of lac repressor to linear versus circular polyoperator molecules. Biochemistry. 1990 Sep 25;29(38):9023-8.

243. Delidakis C, Swimmer C, Kafatos FC. Gene amplification: An example of genome rearrangement. Curr Opin Cell Biol. 1989 Jun;1(3):488-96.

244. Urlaub G, Mitchell PJ, Kas E, Chasin LA, Funanage VL, Myoda TT, et al. Effect of gamma rays at the dihydrofolate reductase locus: Deletions and inversions. Somat Cell Mol Genet. 1986 Nov;12(6):555-66.

245. Dietzel S, Belmont AS. Reproducible but dynamic positioning of DNA in chromosomes during mitosis. Nat Cell Biol. 2001 Aug;3(8):767-70.

246. Boggs SS, Gregg RG, Borenstein N, Smithies O. Efficient transformation and frequent single-site, single-copy insertion of DNA can be obtained in mouse erythroleukemia cells transformed by electroporation. Exp Hematol. 1986 Nov;14(10):988-94.

247. Barsoum J. Introduction of stable high-copy-number DNA into chinese hamster ovary cells by electroporation. DNA Cell Biol. 1990 May;9(4):293-300.

248. Neumann E, Schaefer-Ridder M, Wang Y, Hofschneider PH. Gene transfer into mouse lyoma cells by electroporation in high electric fields. EMBO J. 1982;1(7):841-5.

249. Batard P, Jordan M, Wurm F. Transfer of high copy number plasmid into mammalian cells by calcium phosphate transfection. Gene. 2001 May 30;270(1-2):61-8.

250. Kjer KM, Fallon AM. Efficient transfection of mosquito cells is influenced by the temperature at which DNA-calcium phosphate coprecipitates are prepared. Arch Insect Biochem Physiol. 1991;16(3):189-200.

251. Chen C, Okayama H. High-efficiency transformation of mammalian cells by plasmid DNA. Mol Cell Biol. 1987 Aug;7(8):2745-52.

252. Dyba M, Hell SW. Focal spots of size lambda/23 open up far-field fluorescence microscopy at 33 nm axial resolution. Phys Rev Lett. 2002 Apr 22;88(16):163901.

253. Albrecht B, Failla AV, Schweitzer A, Cremer C. Spatially modulated illumination microscopy allows axial distance resolution in the nanometer range. Appl Opt. 2002 Jan 1;41(1):80-7.

254. Dietzel S, Eils R, Satzler K, Bornfleth H, Jauch A, Cremer C, et al. Evidence against a looped structure of the inactive human X-chromosome territory. Exp Cell Res. 1998 May 1;240(2):187-96.

255. Esa A, Coleman AE, Edelmann P, Silva S, Cremer CG, Janz S. Conformational differences in the 3-D nanostructure of the immunoglobulin heavy-chain locus, a hotspot of chromosomal translocations in B lymphocytes. Cancer Genet Cytogenet. 2001 Jun;127(2):168-73.

256. Bridger JM, Kill IR, Lichter P. Association of pKi-67 with satellite DNA of the human genome in early G1 cells. Chromosome Res. 1998 Jan;6(1):13-24.

257. Derouazi M, Martinet D, Besuchet Schmutz N, Flaction R, Wicht M, Bertschinger M, et al. Genetic characterization of CHO production host DG44 and derivative recombinant cell lines. Biochem Biophys Res Commun. 2006 Feb 24;340(4):1069-77.

258. Wang CY, Sugden B. Identifying a property of origins of DNA synthesis required to support plasmids stably in human cells. Proc Natl Acad Sci U S A. 2008 Jul 15;105(28):9639-44.

259. Nanbo A, Sugden A, Sugden B. The coupling of synthesis and partitioning of EBV's plasmid replicon is revealed in live cells. EMBO J. 2007 Oct 3;26(19):4252-62.

260. Straight AF, Marshall WF, Sedat JW, Murray AW. Mitosis in living budding yeast: Anaphase A but no metaphase plate. Science. 1997 Jul 25;277(5325):574-8.

261. Siemering KR, Golbik R, Sever R, Haseloff J. Mutations that suppress the thermosensitivity of green fluorescent protein. Curr Biol. 1996 Dec 1;6(12):1653-63.

262. Kaether C, Gerdes HH. Visualization of protein transport along the secretory pathway using green fluorescent protein. FEBS Lett. 1995 Aug 7;369(2-3):267-71.

263. Ogawa H, Inouye S, Tsuji FI, Yasuda K, Umesono K. Localization, trafficking, and temperature-dependence of the aequorea green fluorescent protein in cultured vertebrate cells. Proc Natl Acad Sci U S A. 1995 Dec 5;92(25):11899-903.

264. Pines J. GFP in mammalian cells. Trends Genet. 1995 Aug;11(8):326-7.

265. Heim R, Cubitt AB, Tsien RY. Improved green fluorescence. Nature. 1995 Feb 23;373(6516):663-4.

266. Garrick D, Fiering S, Martin DI, Whitelaw E. Repeat-induced gene silencing in mammals. Nat Genet. 1998 Jan;18(1):56-9.

267. McBurney MW, Mai T, Yang X, Jardine K. Evidence for repeat-induced gene silencing in cultured mammalian cells: Inactivation of tandem repeats of transfected genes. Exp Cell Res. 2002 Mar 10;274(1):1-8.

268. Chen D, Huang S. Nucleolar components involved in ribosome biogenesis cycle between the nucleolus and nucleoplasm in interphase cells. J Cell Biol. 2001 Apr 2;153(1):169-76.

269. Molenaar C, Abdulle A, Gena A, Tanke HJ, Dirks RW. Poly(A)+ RNAs roam the cell nucleus and pass through speckle domains in transcriptionally active and inactive cells. J Cell Biol. 2004 Apr 26;165(2):191-202.

270. Deaven LL, Petersen DF. The chromosomes of CHO, an aneuploid chinese hamster cell line: G-band, C-band, and autoradiographic analyses. Chromosoma. 1973;41(2):129-44.

271. Urlaub G, Chasin LA. Isolation of chinese hamster cell mutants deficient in dihydrofolate reductase activity. Proc Natl Acad Sci U S A. 1980 Jul;77(7):4216-20.

272. Urlaub G, Kas E, Carothers AM, Chasin LA. Deletion of the diploid dihydrofolate reductase locus from cultured mammalian cells. Cell. 1983 Jun;33(2):405-12.

273. Majors BS, Arden N, Oyler GA, Chiang GG, Pederson NE, Betenbaugh MJ. E2F-1 overexpression increases viable cell density in batch cultures of chinese hamster ovary cells. J Biotechnol. 2008 Nov 25;138(3-4):103-6.

274. Xiao M, Inal CE, Parekh VI, Chang CM, Whitnall MH. 5-androstenediol promotes survival of gamma-irradiated human hematopoietic progenitors through induction of nuclear factor-kappaB activation and granulocyte colony-stimulating factor expression. Mol Pharmacol. 2007 Aug;72(2):370-9.

275. Santoro A, Lioi MB, Monfregola J, Salzano S, Barbieri R, Ursini MV. L-carnitine protects mammalian cells from chromosome aberrations but not from inhibition of cell proliferation induced by hydrogen peroxide. Mutat Res. 2005 Nov 10;587(1-2):16-25.

276. Driessens N, Versteyhe S, Ghaddhab C, Burniat A, De Deken X, Van Sande J, et al. Hydrogen peroxide induces DNA single- and double-strand breaks in thyroid cells and is therefore a potential mutagen for this organ. Endocr Relat Cancer. 2009 Sep;16(3):845-56.

277. Albanesi T, Polani S, Cozzi R, Perticone P. DNA strand methylation and sister chromatid exchanges in mammalian cells in vitro. Mutat Res. 1999 Oct 19;429(2):239-48.

278. Nakamura J, Purvis ER, Swenberg JA. Micromolar concentrations of hydrogen peroxide induce oxidative DNA lesions more efficiently than millimolar concentrations in mammalian cells. Nucleic Acids Res. 2003 Mar 15;31(6):1790-5.

279. Henle ES, Han Z, Tang N, Rai P, Luo Y, Linn S. Sequence-specific DNA cleavage by Fe2+-mediated fenton reactions has possible biological implications. J Biol Chem. 1999 Jan 8;274(2):962-71.

280. Pascucci B, Russo MT, Crescenzi M, Bignami M, Dogliotti E. The accumulation of MMS-induced single strand breaks in G1 phase is recombinogenic in DNA polymerase beta defective mammalian cells. Nucleic Acids Res. 2005 Jan 12;33(1):280-8.

281. Kim SJ, Kim JE, Moon IS. Paraquat induces apoptosis of cultured rat cortical cells. Mol Cells. 2004 Feb 29;17(1):102-7.

282. Crowe SL, Movsesyan VA, Jorgensen TJ, Kondratyev A. Rapid phosphorylation of histone H2A.X following ionotropic glutamate receptor activation. Eur J Neurosci. 2006 May;23(9):2351-61.

283. Sedelnikova OA, Horikawa I, Zimonjic DB, Popescu NC, Bonner WM, Barrett JC. Senescing human cells and ageing mice accumulate DNA lesions with unrepairable double-strand breaks. Nat Cell Biol. 2004 Feb;6(2):168-70.

284. Sedelnikova OA, Rogakou EP, Panyutin IG, Bonner WM. Quantitative detection of (125)IdU-induced DNA double-strand breaks with gamma-H2AX antibody. Radiat Res. 2002 Oct;158(4):486-92.

285. Kato TA, Wilson PF, Nagasawa H, Fitzek MM, Weil MM, Little JB, et al. A defect in DNA double strand break processing in cells from unaffected parents of retinoblastoma patients and other apparently normal humans. DNA Repair (Amst). 2007 Jun 1;6(6):818-29.

286. Staszewski O, Nikolova T, Kaina B. Kinetics of gamma-H2AX focus formation upon treatment of cells with UV light and alkylating agents. Environ Mol Mutagen. 2008 Dec;49(9):734-40.

287. Avondoglio D, Scott T, Kil WJ, Sproull M, Tofilon PJ, Camphausen K. High throughput evaluation of gamma-H2AX. Radiat Oncol. 2009 Aug 24;4:31.

288. Tomilin NV, Solovjeva LV, Svetlova MP, Pleskach NM, Zalenskaya IA, Yau PM, et al. Visualization of focal nuclear sites of DNA repair synthesis induced by bleomycin in human cells. Radiat Res. 2001 Oct;156(4):347-54.

289. Benitez-Bribiesca L, Sanchez-Suarez P. Oxidative damage, bleomycin, and gamma radiation induce different types of DNA strand breaks in normal lymphocytes and thymocytes. A comet assay study. Ann N Y Acad Sci. 1999;887:133-49.

290. Anderson RM, Sumption ND, Papworth DG, Goodhead DT. Chromosome breakpoint distribution of damage induced in peripheral blood lymphocytes by densely ionizing radiation. Int J Radiat Biol. 2006 Jan;82(1):49-58.

291. Goodhead DT. Mechanisms for the biological effectiveness of high-LET radiations. J Radiat Res (Tokyo). 1999 Dec;40 Suppl:1-13.

292. Ward JF. DNA damage produced by ionizing radiation in mammalian cells: Identities, mechanisms of formation, and reparability. Prog Nucleic Acid Res Mol Biol. 1988;35:95-125.

293. Nikjoo H, O'Neill P, Wilson WE, Goodhead DT. Computational approach for determining the spectrum of DNA damage induced by ionizing radiation. Radiat Res. 2001 Nov;156(5 Pt 2):577-83.

294. Nikjoo H, O'Neill P, Terrissol M, Goodhead DT. Quantitative modelling of DNA damage using monte carlo track structure method. Radiat Environ Biophys. 1999 May;38(1):31-8.

295. Goodhead DT. Energy deposition stochastics and track structure: What about the target? Radiat Prot Dosimetry. 2006;122(1-4):3-15.

296. Georgakilas AG, Bennett PV, Wilson DM,3rd, Sutherland BM. Processing of bistranded abasic DNA clusters in gamma-irradiated human hematopoietic cells. Nucleic Acids Res. 2004 Oct 19;32(18):5609-20.

297. Peddi P, Francisco DC, Cecil AM, Hair JM, Panayiotidis MI, Georgakilas AG. Processing of clustered DNA damage in human breast cancer cells MCF-7 with partial DNA-PKcs deficiency. Cancer Lett. 2008 Sep 28;269(1):174-83.

298. Asaithamby A, Hu B, Chen DJ. Unrepaired clustered DNA lesions induce chromosome breakage in human cells. Proc Natl Acad Sci U S A. 2011 May 17;108(20):8293-8.

299. Nikjoo H, Bolton CE, Watanabe R, Terrissol M, O'Neill P, Goodhead DT. Modelling of DNA damage induced by energetic electrons (100 eV to 100 keV). Radiat Prot Dosimetry. 2002;99(1-4):77-80.

300. Nikjoo H, O'Neill P, Goodhead DT, Terrissol M. Computational modelling of low-energy electron-induced DNA damage by early physical and chemical events. Int J Radiat Biol. 1997 May;71(5):467-83.

301. Gulston M, Fulford J, Jenner T, de Lara C, O'Neill P. Clustered DNA damage induced by gamma radiation in human fibroblasts (HF19), hamster (V79-4) cells and plasmid DNA is revealed as fpg and nth sensitive sites. Nucleic Acids Res. 2002 Aug 1;30(15):3464-72.

302. Hair JM, Terzoudi GI, Hatzi VI, Lehockey KA, Srivastava D, Wang W, et al. BRCA1 role in the mitigation of radiotoxicity and chromosomal instability through repair of clustered DNA lesions. Chem Biol Interact. 2010 Nov 5;188(2):350-8.

303. Terato H, Tanaka R, Nakaarai Y, Nohara T, Doi Y, Iwai S, et al. Quantitative analysis of isolated and clustered DNA damage induced by gamma-rays, carbon ion beams, and iron ion beams. J Radiat Res (Tokyo). 2008 Mar;49(2):133-46.

304. Boucher D, Testard I, Averbeck D. Low levels of clustered oxidative DNA damage induced at low and high LET irradiation in mammalian cells. Radiat Environ Biophys. 2006 Nov;45(4):267-76.

305. Goodhead DT, Thacker J, Cox R. Weiss lecture. effects of radiations of different qualities on cells: Molecular mechanisms of damage and repair. Int J Radiat Biol. 1993 May;63(5):543-56.

306. Kadhim MA, Macdonald DA, Goodhead DT, Lorimore SA, Marsden SJ, Wright EG. Transmission of chromosomal instability after plutonium alpha-particle irradiation. Nature. 1992 Feb 20;355(6362):738-40.

307. Morgan WF. Non-targeted and delayed effects of exposure to ionizing radiation: I. radiation-induced genomic instability and bystander effects in vitro. Radiat Res. 2003 May;159(5):567-80.

308. Morgan WF. Non-targeted and delayed effects of exposure to ionizing radiation: II. radiation-induced genomic instability and bystander effects in vivo, clastogenic factors and transgenerational effects. Radiat Res. 2003 May;159(5):581-96.

309. Wu LJ, Randers-Pehrson G, Xu A, Waldren CA, Geard CR, Yu Z, et al. Targeted cytoplasmic irradiation with alpha particles induces mutations in mammalian cells. Proc Natl Acad Sci U S A. 1999 Apr 27;96(9):4959-64.

310. Prise KM, Folkard M, Michael BD. A review of the bystander effect and its implications for low-dose exposure. Radiat Prot Dosimetry. 2003;104(4):347-55.

311. Gontijo AM, Green CM, Almouzni G. Repairing DNA damage in chromatin. Biochimie. 2003 Nov;85(11):1133-47.

312. Verger A, Crossley M. Chromatin modifiers in transcription and DNA repair. Cell Mol Life Sci. 2004 Sep;61(17):2154-62.

313. Green CM, Almouzni G. When repair meets chromatin. first in series on chromatin dynamics. EMBO Rep. 2002 Jan;3(1):28-33.

314. Pandita TK, Richardson C. Chromatin remodeling finds its place in the DNA double-strand break response. Nucleic Acids Res. 2009 Apr;37(5):1363-77.

315. Osley MA, Shen X. Altering nucleosomes during DNA double-strand break repair in yeast. Trends Genet. 2006 Dec;22(12):671-7.

316. van Attikum H, Fritsch O, Hohn B, Gasser SM. Recruitment of the INO80 complex by H2A phosphorylation links ATP-dependent chromatin remodeling with DNA double-strand break repair. Cell. 2004 Dec 17;119(6):777-88.

317. Morrison AJ, Highland J, Krogan NJ, Arbel-Eden A, Greenblatt JF, Haber JE, et al. INO80 and gamma-H2AX interaction links ATP-dependent chromatin remodeling to DNA damage repair. Cell. 2004 Dec 17;119(6):767-75.

318. van Attikum H, Fritsch O, Gasser SM. Distinct roles for SWR1 and INO80 chromatin remodeling complexes at chromosomal double-strand breaks. EMBO J. 2007 Sep 19;26(18):4113-25.

319. Meijer M, Smerdon MJ. Accessing DNA damage in chromatin: Insights from transcription. Bioessays. 1999 Jul;21(7):596-603.

320. Koundrioukoff S, Polo S, Almouzni G. Interplay between chromatin and cell cycle checkpoints in the context of ATR/ATM-dependent checkpoints. DNA Repair (Amst). 2004 Aug-Sep;3(8-9):969-78.

321. Dinant C, Houtsmuller AB, Vermeulen W. Chromatin structure and DNA damage repair. Epigenetics Chromatin. 2008 Nov 12;1(1):9.

322. Moggs JG, Orphanides G. The role of chromatin in molecular mechanisms of toxicity. Toxicol Sci. 2004 Aug;80(2):218-24.

323. Avantaggiati ML, Ogryzko V, Gardner K, Giordano A, Levine AS, Kelly K. Recruitment of p300/CBP in p53-dependent signal pathways. Cell. 1997 Jun 27;89(7):1175-84.

324. Lill NL, Grossman SR, Ginsberg D, DeCaprio J, Livingston DM. Binding and modulation of p53 by p300/CBP coactivators. Nature. 1997 Jun 19;387(6635):823-7.

325. Johnson AB, Barton MC. Hypoxia-induced and stress-specific changes in chromatin structure and function. Mutat Res. 2007 May 1;618(1-2):149-62.

326. Hasan S, Hottiger MO. Histone acetyl transferases: A role in DNA repair and DNA replication. J Mol Med (Berl). 2002 Aug;80(8):463-74.

327. Ramanathan B, Smerdon MJ. Changes in nuclear protein acetylation in u.v.-damaged human cells. Carcinogenesis. 1986 Jul;7(7):1087-94.

328. Ramanathan B, Smerdon MJ. Enhanced DNA repair synthesis in hyperacetylated nucleosomes. J Biol Chem. 1989 Jul 5;264(19):11026-34.

329. Ikura T, Ogryzko VV, Grigoriev M, Groisman R, Wang J, Horikoshi M, et al. Involvement of the TIP60 histone acetylase complex in DNA repair and apoptosis. Cell. 2000 Aug 18;102(4):463-73.

330. Bird AW, Yu DY, Pray-Grant MG, Qiu Q, Harmon KE, Megee PC, et al. Acetylation of histone H4 by Esa1 is required for DNA double-strand break repair. Nature. 2002 Sep 26;419(6905):411-5.

331. Botuyan MV, Lee J, Ward IM, Kim JE, Thompson JR, Chen J, et al. Structural basis for the methylation state-specific recognition of histone H4-K20 by 53BP1 and Crb2 in DNA repair. Cell. 2006 Dec 29;127(7):1361-73.

332. Kim J, Daniel J, Espejo A, Lake A, Krishna M, Xia L, et al. Tudor, MBT and chromo domains gauge the degree of lysine methylation. EMBO Rep. 2006 Apr;7(4):397-403.

333. Huyen Y, Zgheib O, Ditullio RA,Jr, Gorgoulis VG, Zacharatos P, Petty TJ, et al. Methylated lysine 79 of histone H3 targets 53BP1 to DNA double-strand breaks. Nature. 2004 Nov 18;432(7015):406-11.

334. Mailand N, Bekker-Jensen S, Faustrup H, Melander F, Bartek J, Lukas C, et al. RNF8 ubiquitylates histones at DNA double-strand breaks and promotes assembly of repair proteins. Cell. 2007 Nov 30;131(5):887-900.

335. Huen MS, Grant R, Manke I, Minn K, Yu X, Yaffe MB, et al. RNF8 transduces the DNA-damage signal via histone ubiquitylation and checkpoint protein assembly. Cell. 2007 Nov 30;131(5):901-14.

336. Kolas NK, Chapman JR, Nakada S, Ylanko J, Chahwan R, Sweeney FD, et al. Orchestration of the DNA-damage response by the RNF8 ubiquitin ligase. Science. 2007 Dec 7;318(5856):1637-40.

337. Asaithamby A, Chen DJ. Cellular responses to DNA double-strand breaks after low-dose gamma-irradiation. Nucleic Acids Res. 2009 Jul;37(12):3912-23.

338. Giesen U, Langner F, Mielke C, Mosconi M, Dirks WG. Online imaging of initial DNA damages at the PTB microbeam. Radiat Prot Dosimetry. 2011 Feb;143(2-4):349-52.

339. Zeitlin SG, Baker NM, Chapados BR, Soutoglou E, Wang JY, Berns MW, et al. Double-strand DNA breaks recruit the centromeric histone CENP-A. Proc Natl Acad Sci U S A. 2009 Sep 15;106(37):15762-7.

340. Mashanov GI, Tacon D, Peckham M, Molloy JE. The spatial and temporal dynamics of pleckstrin homology domain binding at the plasma membrane measured by imaging single molecules in live mouse myoblasts. J Biol Chem. 2004 Apr 9;279(15):15274-80.

341. David Secko. The cell cycle: A universal cellular division program. The Science creative Quarterly, August 2003

342. K. Sax. Types and frequencies of chromosomal aberrations induced by X-rays. Cold Spring Harb. Symp. Quant. Biol. 1941; 9: 93 - 103

343. A.S. Serebrovski. A general scheme for the origin of mutations Am. Nat. 1929; 63: 374 - 378

344. Rose, G.G. Cinemicrography in Cell Biology. New York:

Academic Press 1963

345. Bajer, A.S. and Bajer, J.M. Spindle dynamics and chromosome

movements. Int. Rev. Cytol. Supp. 1972; 3: 1–271.

346. Abramoff, M. D., P. J. Magalhaes and S. J. Sam. Image processing with ImageJ. Biophot. Int. 2004; 36-42

347. Vladimir A. Trifonov, Nadezhda N. Vorobieva and Willem Rens. FISH with and without COT1 DNA Fluorescence In Situ Hybridization (FISH) – Application Guide 2009 Chapter 9; Thomas Liehr (ed.) Spinger Protocols

348. Amir Lavaf, Shibo Fu1, Sheila Peters, Yen-Nien Hou, Barry S. Rosenstein, and Johnny Kao. ATM Phosphorylation Kinetics as a Biological Reporter of Cellular Radiosensitivity J. Cancer Mol. 2009 5(1): 9-14

349. Imdadhu Rakiman, M. Chinnadurai, U. Baraneedharan, Solomon F.D. Paul and P. Venkatachalam γ-H2AX assay: a technique to quantify DNA double strand breaks Advanced Biotech. 2008 Jul; 39 - 42 (Tools and Techniques)

350. G. Sluder, J. Nordberg, F. Miller and E. Hinchcliffe. A sealed preparation for long-term observations of cultured cells (chapter 18). Live Cell Imaging – A laboratory manual (2005), edited by Robert D. Goldman and David L. Spector. Cold Spring Harbor Laboratory Press

351. McMillan, T.J. and Steel, G.G. Molecular aspect of radiation

biology. In: Basic and clinical radiobiology, 1st edn., pp.
211-224. Editor: G. Gordon Steel. Edward Arnold, London,1993.

352. Steel, G.G. 2002. Basic Clinical Radiobiology. Oxford University Press. London–New York.

353. Fluorescence Microscopy interactive Java Tutorials – Photobleaching; Molecular Expressions^{TM} Optical Microscopy Primer Specialized Techniques (http://micro.magnet.fsu.edu/primer/java/fluorescence/photobleaching) Contributing authors: Brian Herman - Department of Cellular and Structural Biology, University of Texas Health Science Center, 7703 Floyd Curl Drive, San Antonio, Texas 78229; Matthew J. Parry-Hill, Ian D. Johnson, and Michael W. Davidson - National High Magnetic Field Laboratory, 1800 East Paul Dirac Dr., The Florida State University, Tallahassee, Florida, 32310